KU LEUVEN
FACULTEIT BIOMEDISCHE WETENSCHAPPEN
BEELDVORMING EN CARDIOVASCULAIRE DYNAMICA
Herestraat 49, 3000 Leuven (België)

SEGMENTATIE VAN DE LINKER HARTKAMER IN REAL-TIME 3D ECHOCARDIOGRAFIE

Promotors:

Prof. dr. Jan D'HOOGE
Prof. dr. ir. Olivier BERNARD

Examencommissie:

Prof. dr. Werner Budts (voorzitter)
Prof. dr. ir. Dirk Vandermeulen
Prof. dr. ir. Sofie Pollin
Prof. dr. ir. Johan G. Bosch

Proefschrift voorgedragen tot het behalen van het doctoraat in de Biomedische Wetenschappen

door

João PEDROSA

Oktober 2018

KU LEUVEN
FACULTY OF BIOMEDICAL SCIENCES
CARDIOVASCULAR IMAGING AND DYNAMICS
Herestraat 49, 3000 Leuven (Belgium)

LEFT VENTRICULAR SEGMENTATION OF THE HEART IN REAL-TIME 3D ECHOCARDIOGRAPHY

Promotors:

Prof. Jan D'HOOGE, PhD
Prof. Olivier BERNARD, PhD

Examination committee:

Prof. Werner Budts, MD, PhD (chair)
Prof. Dirk Vandermeulen, PhD
Prof. Sofie Pollin, PhD
Prof. Johan G. Bosch, PhD

Dissertation presented in partial fulfilment of the requirements for the degree of Doctor in Biomedical Sciences

by

João PEDROSA

October 2018

Acknowledgements

Firstly, I would like to express my gratitude to the institutions that made this work possible, namely the European Research Council through the European Union's Seventh Framework Program for funding this project and giving me this opportunity to grow and then also the KU Leuven for receiving me into this great institution which I have grown to love.

Secondly, to all the jury members, thank you for your willingness to devote time to this work by reading this manuscript and wishing to make it better through your comments and questions. I must especially thank Dirk Vandermeulen and Sofie Pollin for your continuous efforts during this PhD to assess the progress that was being made and discuss what should be the next steps.

Third, to my advisors throughout this project, Jan D'hooge and Olivier Bernard, I cannot thank you enough for your help throughout these four years. Jan, you have stood beside me since day one and it's been a pleasure to work by your side. Thank you for giving me the support I needed to believe in myself at the many times I doubted what I was doing. On the academic world and outside of it you have been an example through your calm but firm approach to every problem that appeared. To see that what drives you forward (and all of us with you) is the simple almost childlike desire to know more and show it to others made every challenge that much easier. To Olivier Bernard, thank you for the insight you gave throughout this PhD and the many meetings we had. It was always useful to get a look from outside the lab to know what we missed and where to go next. To Daniel Barbosa, thank you for the BEAS legacy you left me and for the guidance in the first few months of the PhD. In a way, this PhD would have never been possible without you.

Looking back at this PhD it is inevitable to see others in myself and in how I've found my way through the challenges that appeared and my family has, more than anyone, made me who I am. The willingness to jump up to every challenge as a means to grow and help others in the process is perhaps one of the biggest lessons I have been taught. Thank you for all the love you have given me always and for teaching me how to love others. To my mother, thank you for teaching me so much, about the world and the wonders that fill it from deep down under to the skies and beyond, for teaching me to love to learn and giving me this burning desire to find out what lies after the next turn. To my father, thank you for teaching me to find simple solutions to complex problems and to make things from nothing with my bare hands and to feel proud on what I had achieved every time. To my sister,

thank you showing me how to find myself and fight for what I believe in. You have been there from the very start and I will follow you, always.

To Helena, my partner through every struggle and every conquest, thank you so much for everything. You have carried me every step of the way with a patience and faith in me I cannot find in myself. I am blessed to receive your love and your example of love and care for all those around you is something I can only hope to achieve. You are the most perfect of companions, sending me flying to heights I never dreamed of and putting my feet on the ground at the same time. Thank you for launching yourself into this great adventure with me. I can only hope that we will share many many more, preferably with less than 1485km between us.

To all my colleagues and friends at the Louvre, thank you for all the long days and nights spent together but also for the fun, the coffee breaks, conferences, winter and summer schools and everything else. To Bidisha, my doctorate sister, I am so proud and lucky to have shared this time in the Louvre with you going through the same struggles together, laughing, travelling and learning together. To Adriyana, thank you for teaching so much about the world to the innocent privileged boy that I am next to you. To Pedro and Nuno, my home away from home, it was always a laugh with both of you from the first day (or night) and I hope we will bump into each other many times back in tiny little Portugal. To Anna, you are the sunshine! Thank you for all the laughter we shared together. To Brecht, thank you for teaching me everything about how to be a true Flemish and for giving me the passion for cycling I have found in me. To all of you, to Alejandra, Carolina, Martino, Margot, Raja, Natalia, Mahdi, Hang, Natasa, Antonio, Vangjush, Nadya, Miaomiao, Mahvish, Sandro, Morais, Aravind, Wentao, Alessandro, Olivia, Sofie, Arun, Marta and Helena and also to Jürgen, Monica, Marta, Aniela, Ahmed, Blazej and Razvan and also to Dzemila, I will miss you and remember you always.

To all the friends and wonderful people I was fortunate to meet in Leuven, thank you for the happiness and experience you brought into my life. To Hanna, Jonas and Robby, thank you for all the moments and dinners we shared, especially during the first year. It was difficult but good to see that we all grew beyond ourselves to become more than what we were four years ago. To Clarissa, my dearest friend, I admire you deeply and you know that I will miss your company the most. Your passion for life and all things beautiful really makes you shine and most days it was just enough to bask under that warm glow. On the difficult days, remember that hope for something better lies just a warm cozy plate of food away. To Carla, thank you for all those evenings spent together sharing the pieces of our lives. Thank you for giving me the strength to push on and believe in myself; you have done much more than you might ever imagine. To Oli and Jade, thank you for all the happiness that comes barging through everytime you are near, thank you for giving me the gift of making the benches together. To all of you and also to Marie, Anaïs, Chiara, Lucía, Katja and Michiel thank you for enriching my Leuven these four years.

To all of those above and the ones I have forgotten to mention my greatest of thank you's!

João Pedrosa

Abstract

Left Ventricular Segmentation of the Heart in Real-Time 3D Echocardiography

Cardiovascular diseases account for more deaths than any other cause [1] and are projected to remain the single leading cause of death [2]. Echocardiography plays a crucial role in clinical cardiology with diagnostic, prognostic and interventional value. This is potentiated by its excellent temporal resolution, safety, good spatial resolution and low cost, making it the cardiac imaging exam of reference in daily practice. Though 2D echocardiography remains the predominant modality for cardiac assessment, 3D echocardiography has the advantage of allowing for a 3D rendering of the anatomical structures thus discarding the need for the geometrical assumptions inherent to 2D echocardiography. Nevertheless, the analysis of 3D images is challenging and time consuming, fueling the need for software tools that enable a fast, accurate analysis that reduces the burden on the clinician while at the same time reducing the inter- and intra observer variability of the clinical indices extracted. This thesis aims to address these issues with a number of technical contributions from which a fast and robust framework for automatic full cycle 3D left ventricular myocardial segmentation emerges. This was possible based on the B-spline Explicit Active Surfaces framework [3], a formulation of Active Geometric Functions [4] exploring the link between explicit and implicit formulations for image segmentation. The starting point for this thesis was a previous implementation of this framework for left ventricular segmentation and tracking which proved very promising, outperforming other state-of-the-art methods. In this thesis, a hybrid energy for segmentation and tracking is introduced, allowing for more accurate full cycle segmentation; robust left ventricular myocardial segmentation is made possible by an efficient coupling between the endo- and epicardial surfaces; automatic short axis orientation of the left ventricle is proposed, allowing for additional information to be extracted; a Statistical Shape Model built from cardiac magnetic resonance imaging is used to improve the robustness of the segmentation by providing information on the expected shapes of the left ventricle when image information is low or unreliable. At each step of the development thorough validation of the methods was performed, leading to the final framework for fast, automatic and robust full heart cycle 3D left ventricular myocardial segmentation. This framework was then implemented in a user-friendly distributable software application to potentiate its application in future studies. The added value of 3D echocardiography is further highlighted through a method for myocardial performance mapping

through the study of the stress-strain relationships validated against nuclear imaging. Finally, the application of the developed framework in real-time is considered by implementing it in an experimental system for 2D left ventricular segmentation for anatomical imaging, as to obtain high frame rate imaging and study short lived myocardial dynamics.

Segmentatie van de Linker Hartkamer in Real-Time 3D Echocardiografie

Hart- en vaatziekten zijn verantwoordelijk voor meer sterfgevallen dan enige andere oorzaak [1] en zullen naar verwachting ook de belangrijkste doodsoorzaak blijven [2]. Echocardiografie speelt een cruciale rol in klinische cardiologie met diagnostische, prognostische en interventionele waarde. Dit wordt versterkt door zijn uitstekende temporele resolutie, veiligheid, goede ruimtelijke resolutie en lage kost, waardoor het het cardiale beeldvormingsonderzoek bij uitstek is in de dagelijkse praktijk. Hoewel 2D echocardiografie de meest gebruikte modaliteit blijft voor cardiale beoordeling, heeft 3D echocardiografie het voordeel dat een 3D weergave van de anatomische structuren mogelijk is, waardoor de noodzaak voor de geometrische aannames inherent aan 2D-echocardiografie wordt weggenomen. Desalniettemin is de analyse van 3D beelden moeilijk en tijdrovend, wat de behoefte aan software tools aanwakkert die een snelle, nauwkeurige analyse mogelijk maken. Dit zou de werk belasting voor de clinicus verminderen, terwijl tegelijkertijd de inter- en intra-waarnemervariabiliteit van de klinische indices verminderen. Dit proefschrift beoogt deze problemen aan te pakken met een aantal technische bijdragen waaruit een snel en robuust raamwerk voor automatische 3D linkerventrikelmyocardiale segmentatie naar voren komt voor de volledige hartcyclus. Dit was mogelijk op basis van het B-spline Explicit Active Surfaces raamwerk [3], een formulering van Active Geometric Functions [4] met behulp van de koppeling tussen expliciete en impliciete formuleringen voor beeldsegmentatie. Het uitgangspunt voor dit proefschrift was een eerdere implementatie van dit raamwerk voor linkerventrikel segmentatie en tracking, dat veelbelovend bleek te zijn en beter presteerde dan andere state-of-the-art methoden. In dit proefschrift wordt er een hybride energie voor segmentatie en tracking geïntroduceerd, waardoor een meer nauwkeurige volledige hartcyclus segmentatie mogelijk wordt; robuuste linkerventrikel myocardiale segmentatie wordt mogelijk gemaakt door een efficiënte koppeling tussen de endo- en epicardiale oppervlakken; er wordt een automatische korte as oriëntatie van de linkerventrikel voorgesteld, waardoor aanvullende informatie kan worden geëxtraheerd; een Statistical Shape Model gebouwd met behulp van cardiale magnetische resonantie beeldvorming wordt gebruikt om de robuustheid van de segmentatie te verbeteren door informatie te verschaffen over de verwachte vormen van het linkerventrikel wanneer de beeldinformatie onbetrouwbaar is. Bij elke stap van de ontwikkeling werd er een grondige validatie van de methoden uitgevoerd, leidend tot het definitieve raamwerk voor snelle, automatische en robuuste volledige hartcyclus 3D linkerventrikelmyocardiale segmentatie. Dit raamwerk werd vervolgens geïmplementeerd in een gebruiksvriendelijke, distribueerbare softwareapplicatie om de toepassing ervan in toekomstige studies te vergemakkelijken. De toegevoegde waarde van 3D

echocardiografie wordt verder benadrukt door de ontwikkeling van een methode om myocardiale performantie te verkrijgen door de studie van de stress-strain relaties die gevalideerd is tegen nucleaire beeldvorming. Ten slotte wordt het ontwikkelde raamwerk geïmplementeerd in een experimenteel systeem voor 2D linkerventrikel segmentatie in real-time voor anatomische beeldvorming, om beeldvorming met een hoge beeldsnelheid te verkrijgen en kortstondige myocarddynamiek te bestuderen.

List of acronyms

1D	One dimensional
2D	Two dimensional
2DE	Two dimensional echocardiography
2S	Two-step
3D	Three dimensional
4D	Four dimensional
AAM	Active appearance model
AL-PM	Anterolateral-posteromedial
AV	Aortic valve
A-P	Anterior-posterior
BEAS	B-spline explicit active surfaces
cMRI	Cardiac magnetic resonance imaging
CRT	Cardiac resynchronization therapy
CT	Computed tomography
DW	Diverging waves
EB	Endocardial based
ECG	Electrocardiogram
ED	End diastole
EDV	End diastolic volume
EF	Ejection fraction
ES	End systole
ESV	End systolic volume
FDG-PET	18F-fluorodeoxyglucose positron emission tomography
FOV	Field of view
FPGA	Field-programmable gate array
FR	Frame rate

HD	Hausdorff distance
HTc	Hough transform for circles
ICP	Iterative closest point
LA	Left atrium
lAAOF	Localized anatomical affine optical flow
LAx	Long-axis
LV	Left ventricle
LVOT	Left ventricle outflow tract
MA	Mitral annulus
MAD	Mean absolute distance
MLA	Multi-line acquisition
MLT	Multi-line transmit
MM	Mid-myocardial
MV	Mitral valve
NRIR	Non-rigid image registration
PET	Positron emission tomography
PVA	Polyvinyl alcohol
RA	Right atrium
ROI	Region of interest
RT3DE	Real-time three dimensional echocardiography
RV	Right ventricle
SAx	Short-axis
SNR	Signal-to-noise ratio
SPECT	Single photon emission computed tomography
SSM	Statistical shape model
SV	Stroke volume
TEE	Transesophageal echocardiography
TTE	Transthoracic echocardiography
UN	Uncoupled

Contents

Chapter 1

Motivation, Objectives and Outline

Motivation

Analysis of cardiac function, and specifically of left ventricle (LV) function, is an important part of clinical cardiology for patient management, diagnosis, risk stratification and therapy selection [5–7]. Among the different cardiac imaging modalities, ultrasound stands out due to its safety, portability, low cost, competitive spatiotemporal resolution and real-time capability. While 2D echocardiography (2DE) remains the predominant modality for cardiac assessment, real-time 3D echocardiography (RT3DE) has inherent advantages, namely the imaging of the 3D geometry and motion of the heart, which cannot be directly assessed in 2DE. Numerous validation studies support the claim that valuable clinical information can be extracted through RT3DE, based on comparison with the current gold standard for volumetric assessment, cardiac magnetic resonance imaging (cMRI). Nevertheless, manual 3D image analysis is challenging and time consuming and, to answer this problem, extensive research towards more automated solutions for LV segmentation and tracking in RT3DE have been conducted with a similar trend in commercial solutions. In spite of this, at the beginning of this project, there was no satisfactory software package available that provided fast and fully automatic LV volume/function assessment in a robust way.

Thesis objectives

The overall goal of this thesis was to investigate and develop novel techniques for LV segmentation in 3D echocardiographic images. The optimal LV segmentation framework should fulfill the following requirements:

- The framework should work in *real-time* or close to real-time. The computational burden should be compatible with a realistic application of the method, thereby enhancing the bedside real-time nature of echocardiography.
- The framework should require *minimal or no user input*. This not only maximizes its applicability to large databases but also removes the inter- and intra-observer variability inherent to user interaction.
- The framework should perform *full-cycle* segmentation. In order to assess the dynamics of a moving object such as the heart, a full 4D segmentation must be possible and must be performed in a way as to preserve temporal coherence.
- The framework should perform *full myocardial* segmentation. Besides endocardial segmentation, epicardial segmentation is also extremely important to obtain further clinical information but also as a first step in further analysis of the cardiac tissue.
- The framework should be *robust* and widely applicable. RT3DE often presents challenging image quality with acoustic shadowing and local dropouts and, as such, the optimal framework must be able to cope with these conditions. Furthermore, it should be applicable to virtually any 3D echocardiographic image, independent of the vendor or imaging system.

Moreover, the direct application of the methods developed in this thesis was considered and the following additional goals were defined:

1. Implement the methods developed in this thesis in a software application so as to allow its application in future studies. The software application should be user-friendly and interactive, allowing for easy extraction of 4D LV geometry.
2. Develop a method for myocardial performance mapping based on 4D LV segmentation by using the local LV geometry and strain to assess local LV stress-strain relationships.
3. Study the feasibility of real-time anatomical imaging by applying 2D real-time LV segmentation to limit the field of view (FOV) to the anatomically relevant regions of the image, achieving a higher frame rate (FR).

Thesis outline

The thesis is divided into two main parts, the first part addressing the segmentation methodologies developed (Chapters 3-7) and the second part addressing the application of those methodologies to clinical and/or technical challenges (Chapters 8-10). A brief summary of the 11 chapters which compose this thesis is given below:

Chapter 2 presents an introduction to the cardiovascular system and the importance of LV morphology/function assessment. This is followed by an introduction to ultrasonic imaging as the imaging method of choice and a literature review of

state-of-the-art methods for LV segmentation and tracking, both in research and in commercial software. Finally, the key rationale of the thesis is presented and a detailed description of B-spline Explicit Active Surfaces (BEAS), the segmentation framework used throughout this thesis, is given. Chapter 2 is based on a peer-reviewed publication (item 1 of the journal publications on the List of Publications).

Chapter 3 presents a method for hybrid LV segmentation and tracking using BEAS and anatomical affine optical flow. This method allows for robust full-cycle segmentation by combining both segmentation and tracking clues in an efficient manner. Though this framework was initially proposed in the PhD work of Daniel Barbosa, the author of this thesis played a determinant role in the finalization and publication of the validation results obtained. Chapter 3 is based on a peer-reviewed publication (item 3 of the journal publications on the List of Publications).

Chapter 4 presents a method for short-axis (SAx) orientation of the LV based on the detection of the right ventricular (RV) insertion point. This orientation allows for a point-to-point correspondence between the mesh and the cardiac anatomy, thereby providing information on the orientation of the LV. Chapter 4 is based on conference proceedings (item 3 of the proceedings publications on the List of Publications).

Chapter 5 presents a method for LV segmentation and tracking with increased robustness by combining BEAS with a statistical shape model (SSM) and the hybrid segmentation/tracking approach used in Chapter 3. The SSM provides LV shape clues, thus acting as a regularization of BEAS. It is shown that this method outperforms all currently available state-of-the-art methods on LV endocardial segmentation. Chapter 5 is based on a peer-reviewed publication (item 5 of the international journals listed on the List of Publications).

Chapter 6 addresses one of the fundamental issues in myocardial segmentation - the definition of the two surfaces, i.e. endo- and epicardium, as well as to which degree they are connected. For this purpose, different coupling models are tested and an ideal coupling model for myocardial segmentation is proposed. Chapter 6 is based on a peer-reviewed publication (item 4 of the journal publications on the List of Publications).

Chapter 7 extends the framework from Chapter 5 to perform LV myocardial segmentation by taking advantage of the coupling models studied in Chapter 6 and applying them with a myocardial SSM. Chapter 7 is based on a peer-reviewed publication (item 7 of the journal publications on the List of Publications).

Chapter 8 brings the tools developed in the aforementioned chapters together in a user-friendly distributable software application. This allows users to easily apply the developed methods in future studies.

Chapter 9 focusses on the application of the method developed in Chapter 7 to obtain myocardial performance maps. By performing 3D myocardial segmentation and tracking, local geometry and strain are obtained which are used to assess local LV stress-strain relationships, a measure of myocardial work. This method is validated against 18F-fluorodeoxyglucose positron emission tomography (FDG-PET),

the reference method to assess local metabolism clinically. Chapter 7 is based on a peer-reviewed publication (item 7 of the journal publications on the List of Publications).

Chapter 10 investigates the feasibility of in-vivo anatomical scanning in 2DE. A 2D version of the framework developed in Chapter 7 is implemented on an experimental scanner to perform real-time segmentation. By obtaining information on the position of the myocardium in the image, the scanning sequence is modified to focus on the myocardial region only, thus increasing FR. It is shown that a minimum FR gain of 1.5 can be obtained without degrading image quality, which could be further increased through the use of advanced beamforming techniques. Chapter 10 is based on conference proceedings (item 4 of the proceedings publications on the List of Publications).

Finally, Chapter 11 discusses the contributions of this thesis, including future developments for the methodologies proposed in this thesis and its future applications.

Appendix A proposes a method for mitral valve (MV) segmentation in transthoracic echocardiography (TTE). It takes advantage of the LV segmentation framework proposed in Chapter 5 to localize the MV in the image and uses BEAS to perform MV segmentation, further refined by the use of an atlas of segmented MV shapes. Appendix A is based on conference proceedings (item 8 of the proceedings publications on the List of Publications).

Chapter 2

Introduction

Sections of this chapter are based on a paper published in *Current Pharmaceutical Design*: **Pedrosa J.**, Barbosa D., Almeida N., Bernard O., Bosch J., D'hooge J.. Cardiac Chamber Volumetric Assessment Using 3D Ultrasound - A Review. *Curr Pham Des*, 2016;22(1):105-21.

Abstract

This chapter provides a global overview of the main topics covered in this thesis. First, the basic concepts of the cardiovascular system are reviewed, with special emphasis on the left ventricle (LV). The value of cardiac morphology and function are then explained, as well as the available imaging modalities. Given the topic of this thesis, a chapter is dedicated to ultrasonic imaging, starting from its fundamental concepts and going into further detail in emerging techniques, namely high frame rate (FR) imaging and real-time 3D echocardiography (RT3DE) and their potential applications. Finally, the analysis of echocardiographic images is considered in a state-of-the-art review of LV segmentation/tracking methods, both in the research setting and the commercial tools available. The validation of these tools and of 3D LV assessment in general is also considered at this point. The final section of this chapter draws on the contextualization from the previous sections to give a final overview on the remaining challenges that this thesis addresses.

2.1 The Heart

2.1.1 Cardiovascular Anatomy and Function

The cardiovascular system is an organ system that enables the circulation of blood and transports nutrients, hormones and cells within the body, providing nourishment but also playing a role in other tasks such as fighting disease and maintaining homeostasis. It is composed of the heart, blood vessels, blood and the lymphatic system, which circulates lymph [8].

The heart is the organ responsible for pumping the blood throughout the body, thus playing a crucial role. The human heart is located between the lungs, near the center of the thoracic cavity, where it is suspended by its attachment to the great vessels within the pericardium, a fibrous sac that protects the heart from infection and provides lubrication. The heart is a muscular organ with four main chambers - LV, left atrium (LA), right ventricle (RV) and right atrium (RA) (Figure 2.1). These four chambers, divided into left and right side, work as two separate pumping systems, where the blood flows from the veins into the atria where the blood is pumped into the ventricles and from there into the arteries. The right side receives deoxygenated blood through the vena cava from the systemic circulation and pumps it through the pulmonary artery into the lungs where it is oxygenated. The left side then receives the oxygenated blood through the pulmonary veins and forwards it through the aorta into the systemic circulation where the blood provides oxygen to the cells and becomes deoxygenated thus completing the cycle. In order to maintain a unidirectional blood flow, four valves separate the atria and the ventricles and the main arteries, opening and closing in close coordination with the pumping of the chambers.

This complex pumping motion is achieved by the contraction and expansion of the chambers, which occurs in a cyclic coordinated manner. This coordination is

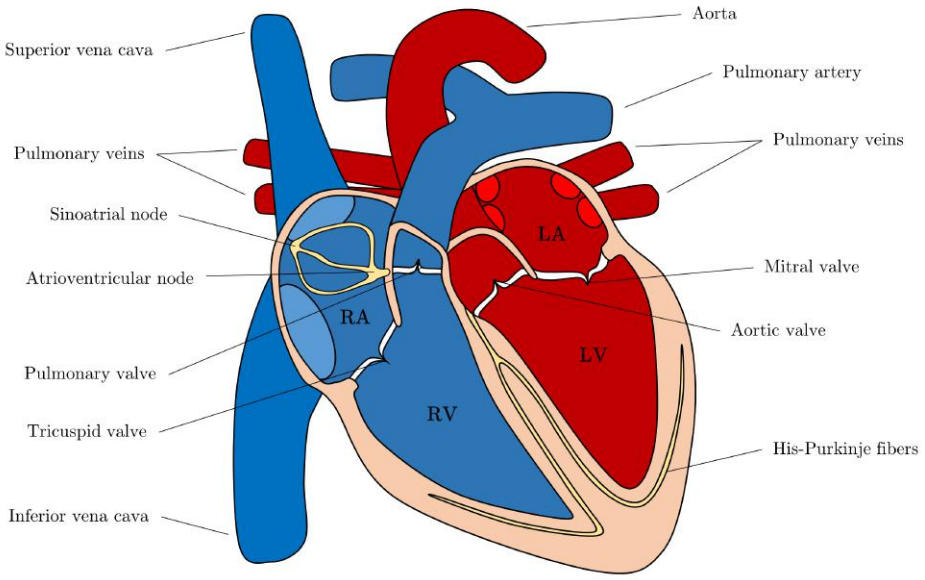

Figure 2.1: The heart and its main anatomical constituents.

assured by the conduction system, making the heart an efficient pump. The sinoatrial node creates and sustains the cardiac rhythm, generating an action potential that is carried radially via Bachmann's bundle causing the contraction of the LA and RA. From the atrioventricular node the signal is then propagated throughout the His-Purkinje network to the ventricles, causing them to contract. The contraction itself is performed by the cardiac muscular tissue, the myocardium, composed of cardiac myocytes arranged into fibers with a complex orientation distribution across the wall.

The cardiac cycle is divided into systole and diastole, the active contraction and relaxation phases respectively (Figure 2.2). Systole begins with the active contraction of the ventricular myocardium. The rise of the ventricular pressure above the atrial pressure causes the rapid closure of the mitral valve (MV) and tricuspid valve, leading to a quick buildup of pressure in the ventricles. This phase is known as the isovolumic contraction. As soon as the ventricular pressure surpasses the arterial pressure, the aortic (AV) and pulmonary valves open, leading the blood into the systemic and pulmonary circulations. This is known as the ejection phase. As the ventricular contraction decreases and pressure drops, the AV and pulmonary valves close, ending the systole. Diastole begins with the isovolumic relaxation, when the myocardium relaxes and pressure falls rapidly given that all valves are closed. This phase ends as the ventricular pressure falls below the atrial pressure and the MV and tricuspid valves open, letting the blood flow into the ventricles. Due to the difference of pressures, a passive filling of the ventricles occurs, followed by an active filling as the sinoatrial node is triggered, leading to the contraction of the atria. The signal from the sinoatrial node is then propagated to the ventricles,

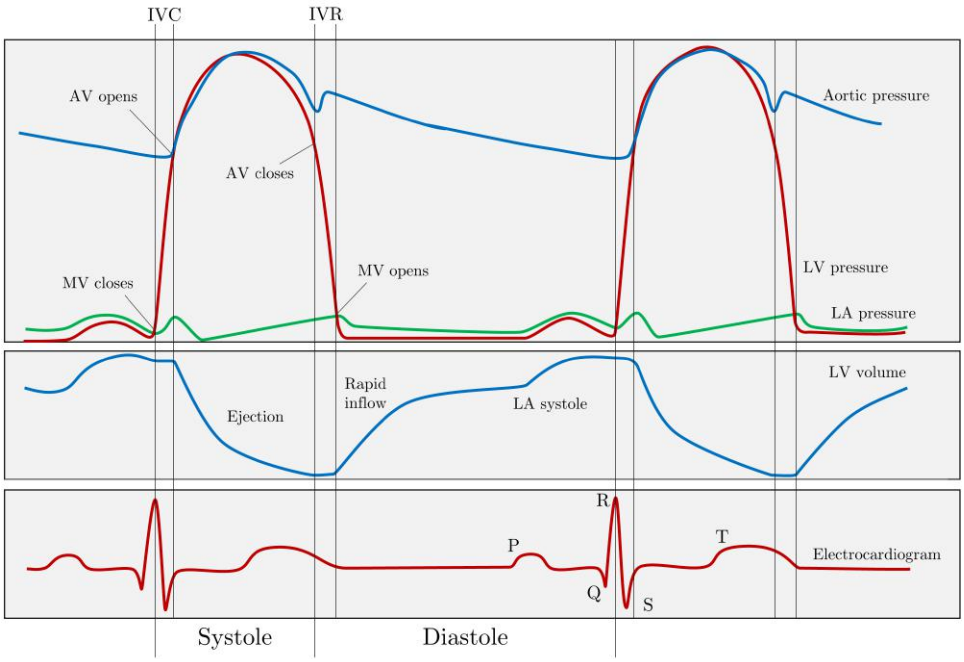

Figure 2.2: Wiggers diagram showing the key events of the cardiac cycle. IVC - Isovolumic contraction; IVR - Isovolumic relaxation. Adapted under CC BY-SA 4.0. [9]

leading to their contraction and thus restarting the systolic phase.

2.1.2 The Left Ventricle

The LV is one of the chambers of the heart and, perhaps for symbolic reasons as the driver of the systemic circulation, is by far the most studied both in anatomy, function and pathology. It sits below the LA, separated by the MV at the mitral annulus (MA), and shares the septal wall with the RV (Figure 2.1). Together with the RV, they form the apex of the heart. The LV connects with the systemic circulation through the aorta, separated by the AV. Inside the LV itself, one can identify the main chamber, as well as the LV outflow tract (LVOT) on the anteroseptal side, which leads to the AV. Due to its role driving the systemic circulation, the LV has thicker myocardial walls than the remaining chambers to pump blood throughout the body. The inner and outer surfaces of the myocardial walls are designated as the endo- and epicardium respectively. Rather than a smooth surface, the endocardium is covered in rounded irregular muscular columns, the trabeculae, which are thought to play a role in hemodynamics. One can also identify the papillary muscles, on the anterior and posterior walls, which attach to each of the MV's leaflets through chordae tendineae and prevent the inversion or prolapse of the MV when pressure in the LV builds up during systole.

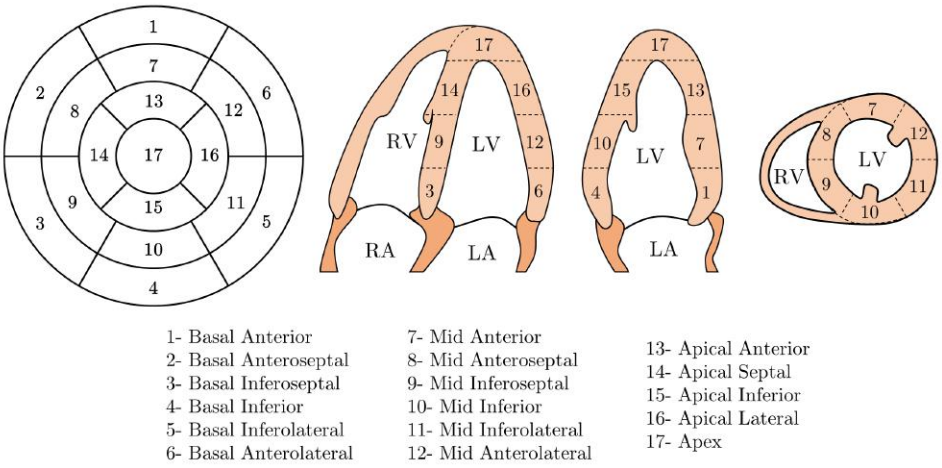

Figure 2.3: 17 segment division of the LV and long axis and short axis views of the LV showing the location of the different segments.

The LV is commonly divided into 17 different segments (Figure 2.3): longitudinally these are divided into the basal, mid-cavity and apical segments and the apical cap and circumferentially into the anterior, anteroseptal, inferoseptal, inferior, inferolateral and anterolateral segments [10].

2.2 Left Ventricular Assessment

The current global status of cardiovascular diseases, accounting for more deaths than any other cause [1] and projected to remain the leading global cause of death [2], makes the assessment of cardiac volume and function a topic of extreme importance not only in the clinical field for patient diagnosis and follow-up but also in research as new therapies are developed and tested.

Besides linear measurements of the LV dimensions such as the LV diameter, the most common indices extracted to characterize both cardiac morphology and global function are those from the volume traces at end diastole (ED) and end systole (ES), namely the ED and ES volumes (EDV and ESV). Furthermore, other cardiac global functional indices can be extracted from the volume traces. Stroke volume (SV=EDV-ESV) is the effective amount of blood ejected by a cavity. The LV SV, when multiplied by the heart rate, gives the total cardiac output. As a measure of pumping efficiency, one can estimate the ejection fraction (EF=(SV/EDV)x100%), as proposed originally by Pombo et al. [11], which is still probably the most widely used parameter to assess the global status of cardiac function in LV [12].

2.2.1 Prognostic Value in Clinical Practice

Extensive research has been directed at determining the prognostic value of volumetric indices for different illnesses and conditions. A brief review of some of these studies is presented here to illustrate the importance of cardiac volume and function assessment. Patient survival after myocardial infarction and its relation to LV function has been thoroughly described in literature. It was first associated with LV ESV by White et al. [13] and Norris et al. [14]. In a study by Burns et al., it was shown that LV EF had even a superior prognostic value than LV ESV for survival after myocardial infarction [15]. Numerous other studies have given further evidence on the prognostic value of LV EF on both short- and long-term survival after myocardial infarction [16–20]. Furthermore, LV EF has been linked to cardiac arrest events [19], heart failure [21], and arrhythmia suppression and cardiac events [22] in survivors of myocardial infarction. More generally, mortality in patients with coronary artery disease has also been associated with LV EF by Buxton et al. [23].

The prognostic value of LV EF for the mortality in patients with heart failure has also been a subject of much research as well as controversy with different studies reaching different conclusions as to which population, preserved or reduced LV EF, represents a higher mortality risk [24, 25]. More recently, two meta-analysis studies, one by Somaratne et al. and a second by a large-scale project (MAGGIC), analyzed data from 17 and 31 studies respectively demonstrating that a higher risk of death is present in patients with heart failure and reduced LV EF [26, 27].

LV function has also been used as a predictor of survival in dilated cardiomyopathy [28, 29]. Furthermore, LV EF has been associated to mortality in patients with LV dysfunction [30] and to mortality in end-stage renal disease patients on starting hemodialysis [31]. Some works have also been dedicated to the study of stress and post-stress LV volumes. In Sharir et al. post-exercise LV EF and ESV were associated to cardiac death [32] and in Coletta et al. dobutamine stress testing was used to link stress LV EDV to cardiac events in patients with coronary heart disease [33].

2.2.2 Available Imaging Modalities

It is thus clear that the assessment of cardiac volumes throughout the cardiac cycle and its associated indices is a fundamental task in diagnostic cardiology routine. Furthermore, these indices can be of paramount importance in the design of studies to show the efficacy of new therapies. To this end, there is a large array of imaging modalities that provide insight to cardiac chamber size and function, with some examples shown in Figure 2.4.

Magnetic resonance imaging, and more specifically cardiac magnetic resonance imaging (cMRI), is long considered the gold standard for assessment of cardiac anatomy and analysis of global cardiac function and shape [34]. The key limitations of cMRI are the high cost of the imaging system and the long acquisition times.

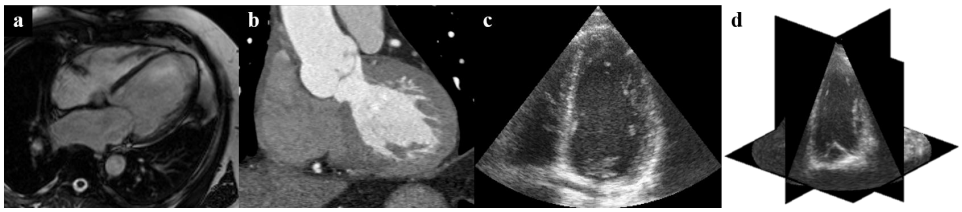

Figure 2.4: Examples of different cardiac imaging modalities: cMRI (a), CT (b), 2DE (c) and RT3DE (d). CT image courtesy of Walter Coudyzer, Department of Radiology, UZ Leuven, Belgium.

This last problem is particularly relevant for cardiac imaging, given the fast dynamics of a beating heart. Computed tomography (CT) is one of the fastest evolving imaging modalities. Cardiac CT, which requires the use of contrast agents, offers superb definition of the boundary between the myocardium and the blood pool, excellent spatial resolution (<1mm) and good temporal resolution. However, it involves exposure to ionizing radiation and is expensive. Other imaging modalities used include cardiac single photon emission computed tomography (SPECT) and multiple gated imaging strategies, also known as radionuclide ventriculography [35, 36], positron emission tomography (PET) [37] and other nuclear imaging techniques [38]. However, these techniques require the injection of radioactive tracers, thus involving exposure to ionizing radiation, and the imaging systems are very expensive.

With the exception of standard X-ray exams, ultrasound is the leading imaging modality worldwide [39]. As key imaging advantages, the excellent temporal resolution clearly sets echocardiography apart from the remaining modalities. Other important advantages, such as its safety, good spatial resolution and low cost, also contribute to the widespread use of echocardiography as the cardiac imaging diagnostic exam of reference in daily practice.

2.3 Ultrasonic Imaging

The history of medical ultrasound first started during World War I, when military investment fast-tracked the technology, first as a means for detection of submarines and later for nondestructive testing of metals [40]. In the medical field, ultrasound was first applied as a theurapeutic tool in physiotherapy and cancer treatment. It was only in 1942 that ultrasound was first used as a diagnostic tool for brain tumour localization. Diagnostic ultrasound was then further developed leading to the first 2D grayscale images in the 1950s and the first cardiac examination in 1953 by Inge Edler and Carl H. Hertz [41]. Since then, diagnostic ultrasound kept evolving, with the introduction of real time imaging in 1965 and electronic beam steering in 1968, as well as overall improvements in image quality and acquisition and processing techniques in the following decades [40].

The use of echocardiography to assess cardiac chamber size and function dates

to the advent of this technology. Popp et al. investigated the variation of cardiac dimensions during the cardiac cycle using M-mode echocardiography [42]. Feigenbaum et al. used these changes to assess LV function and correlated it to angiography [43]. Wyatt et al. showed that volumetric indices extracted from 2D B-mode images were superior to their M-mode counterparts, especially in asymmetrical hearts [44, 45]. Currently, biplane area assessment using 2DE is the standard tool for assessment of LV volumetric indices but recent developments in RT3DE have allowed to entirely visualize the morphology of the cardiac chambers.

2.3.1 Fundamental Physical Concepts

The term ultrasonic refers to sound waves with frequencies above those audible by humans. This ranges from 20kHz onwards but, typically, medical (non-invasive) ultrasound operates within the 1-20MHz range depending on the application. Ultrasonic waves are progressive compression waves, which means that the particles are displaced in a direction parallel to the direction of wave motion. This forms regions of high and low particle density which in turn propagate the wave forward as the elasticity and inertia of the medium counteract to return the medium's particles to their original positions [40]. Ultrasonic imaging depends on the interactions between the tissue and the propagating ultrasonic wave.

As the ultrasonic wave travels through the tissue, it meets a multitude of different structures which lead to different phenomena. When a wave meets the boundary between two media of different density and/or sound velocity, part of the energy of the wave is *reflected* and the remaining is *refracted* through the boundary into the second media. The reflection/transmission ratio depend on the acoustic impedances of the two media, where mismatched acoustic impedances lead to a high reflection of the ultrasonic wave. While a perfectly smooth boundary will cause a pure *specular reflection*, where the reflected wave has a single direction, this is usually not the case and irregularities at the boundary will lead to a *diffuse reflection* in a wide range of directions. Furthermore, tissue inhomogeneities due to local variations of density and/or compressibility cause similar diffuse reflections - *scattering*. It is this property that gives ultrasound its particular grainy appearance, called *speckle*, which reflects the inhomogeneous nature of each of the tissues in the image.

However, as the ultrasonic wave travels through the tissue, there is a loss of acoustic energy mainly due to the conversion of acoustic energy into heat. This *attenuation* causes the wave amplitude to decay exponentially as it travels, thus limiting the depth to which imaging is possible. Finally, *nonlinear distortion* may occur for high amplitude ultrasonic waves due to the nonlinear mechanic characteristics of the medium, changing the original shape of the transmitted ultrasonic pulse as it travels through the tissue.

2.3.2 Acquisition System and Image Formation

Typically, ultrasonic waves are generated by means of a piezoelectric crystal, which, when excited with an oscillating electric field, expand and contract at the

same frequency as the electrical field creating a compression wave. This very same phenomenon is used to receive the signal, where compression waves that hit the piezoelectric crystal are converted into an electrical field. The concept of pulse-echo is thus typically used in medical ultrasound where the same transducer, composed of an array of piezoelectric crystals, is used to first transmit the ultrasonic pulse and then receive its reflections as it travels through the tissue.

The electrical field generated by the piezoelectric crystal can then be amplified, filtered and converted to a digital signal. Envelope detection is then performed to the raw data obtained to remove the high frequency oscillations and the amplitude is corrected for the attenuation effects, a process known as time gain compensation. Usually, the signal is then log-compressed to decrease the differences in amplitude between the specular and scatter reflections, which gives additional information on the tissue texture. Such a pipeline provides the simplest ultrasound imaging mode, the A-mode (for amplitude), where the magnitude along a single direction is acquired and plotted as a function of depth, and subsequently overwritten. If the transducer is static and multiple A-lines are acquired at subsequent time points, the signals obtained can then be plotted in 2D, with depth and time as dimensions, providing an insight into the motion of tissue in time. This is known as M-mode (for motion).

To obtain a 2D ultrasound image, multiple A-lines have to be acquired successively from different directions, forming the B-mode. This can be done by translating or tilting the transducer mechanically but is usually performed by changing the transmit profile along the different piezoelectric crystals in the transducer. In echocardiography applications, where the imaging window is relatively narrow due to the position of the ribs, this is typically done by introducing delays to the transmits of each piezoelectric crystal such that the beams are steered from one side to the other. Because this process provides A-lines in a polar grid, a final interpolation is needed to obtain the 2D cartesian image. An example of an A-, M- and B-mode are shown in Figure 2.5.

2.3.3 High Frame Rate Imaging

Given that conventional B-mode acquisition relies on single line acquisition, where each beam direction is acquired at a time, there is an intrinsic trade-off between temporal resolution and the number of lines acquired (and thus spatial resolution). As such, improving the temporal resolution through advanced beamforming techniques has long been an active topic of research in the field. Multiple techniques have thus been proposed which enable an increase in temporal resolution with more or less impact on spatial resolution and image contrast.

A straightforward method to improve temporal resolution is to perform a multi-beat acquisition. This strategy consists in dividing the whole image into different sections and acquiring each of those sections in a consecutive number of beats [46]. This technique depends however on the patient having a stable heartbeat and keeping a breathhold during the whole acquisition which might not be straightforward for some patients.

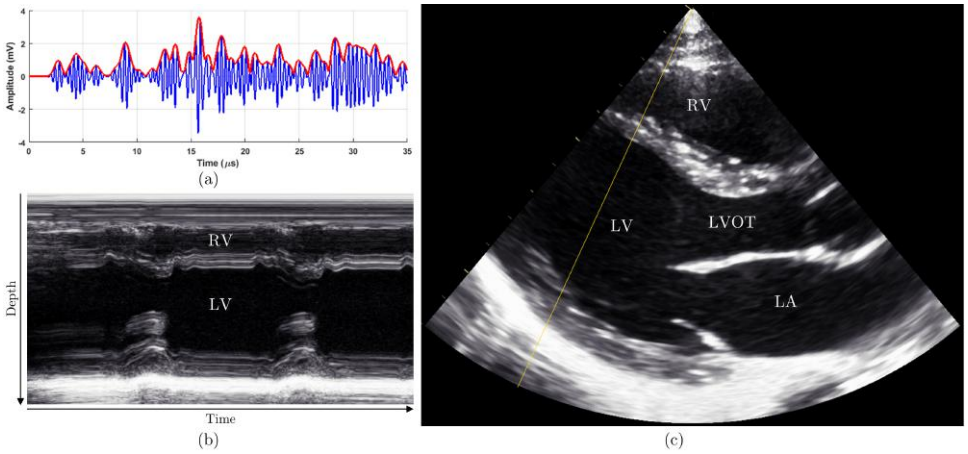

Figure 2.5: A-, M- and B-mode examples. (a) Acquired ultrasound signal (blue) and corresponding A-mode (red). (b) Parasternal long axis M-mode of the heart for assessment of cardiac wall motion during contraction. The dark regions are blood, the bright reflection is the pericardium and the gray region is between is the heart muscle itself. (c) Parasternal long axis B-mode of the heart showing the different cardiac chambers. Yellow line shows acquisition line used to produce the M-mode in (b).

Shattuck and Weinshenker first introduced the concept of parallel receive beamforming, now know as multi-line acquisition (MLA) [47]. This allows to reconstruct multiple lines from the same transmit beam, given the fact that the transmit beam is sufficiently broad to enclose multiple receive beams. This allows to double the FR in 2D and quadruple it in 3D without loss in image quality, but further gains can be increasing by broadening the transmit beam. MLA preserves a good spatial resolution, signal-to-noise ratio (SNR) and penetration and together with multi-beat acquisition for 3D ultrasound is a technique commonly implemented in clinical ultrasound systems to improve temporal resolution.

While MLA increases the FR by receive parallelization, multi-line transmit (MLT) allows transmit parallelization, thus transmitting multiple beams simultaneously in different directions [48, 49]. This allows to increase the FR a number of times equal to the number of beams per transmit event. As the individual beams are virtually unchanged, the resolution and penetration properties are preserved. There is a possibility of crosstalk between the different beams but it has been shown that these effects can be minimized through appropriate strategies thus giving an image quality comparable to that of single line acquisition [50]. Further FR gains can be obtained by combining MLT and MLA. An example could be a 16MLT/4MLA setup for RT3DE which would give a FR 64 times higher than single line acquisition with comparable image quality [51].

As an alternative to the methods discussed above, the use of unfocused transmissions has also been proposed [52]. For linear scanning, the use of plane waves [53]is especially appealing, while diverging waves (DW) [54–56] are more often used in

cardiac applications to match the sector scan geometry. DWs use the full transducer array to create a wave that insonifies the whole volume at once, thus allowing to reconstruct a full volume in a single transmission. This comes, however, at the expense of lateral resolution, SNR and penetration, as well as possible side lobe issues. For these reasons, coherent compounding of DWs is usually performed by combining insonifications with different orientations [57]. Motion of the probe or the tissue being imaged can however be problematic if a high number of transmissions are compounded and motion correction has been proposed to compensate this effect [58].

Besides offsetting the trade-off between spatial and temporal resolution, thus improving the imaging of dynamic structures such as the heart, increasing the temporal resolution would undoubtedly find multiple applications in clinical cardiology of both diagnostic and prognostic value and an extensive review on this topic can be found in [59] and [60]. Motion and deformation imaging in 3D and with high temporal resolution can be especially interesting to get a full 3D contextual information of cardiac events, especially short lived ones [61]. Electromechanical wave imaging is such an example where following local myocardial motion/deformation as the myocardium depolarizes and begins to contract, would provide information about the cardiac activation sequence and allow to build electroanatomical maps non-invasively [62, 63].

2.3.4 Three-Dimensional Echocardiography

While 2D B-mode remains the predominant modality for cardiac assessment, the fact that it is a 2D slice of a 3D anatomical structure makes it an inherently flawed diagnostic tool [64]. First, because the fact that only a 2D slice is obtained at a time means that to make any statement about the 3D anatomy, strong geometrical assumptions must be made which inevitably lead to innacuracies. Moreover, attempts at mentally transforming a series of 2D slices to get a 3D impression of a structure are extremely subjective and innefficient. Secondly, the fact that a particular 2D slice for analysis must be chosen from a 3D structure is problematic in itself. Finding the correct anatomical slice can be difficult and foreshortening - slicing the heart obliquely so that not the whole length of the LV is represented - leads to wrong geometrical assumptions. Even with a definition of standard anatomical views, it is challenging, at best, to obtain the same image plane at different points in time, thus making it difficult to make exact statements on the evolution of a given structure over time. In comparison, the acquisition of 3D ultrasonic imaging would give access to the full geometry of the heart thus solving the aforementioned limitations.

Dekker et al. [65] were the first to scan the human heart in 3D by using a robotic arm to move a transducer with five degrees of freedom. Later attempts relied on 1D transducer arrays moved mechanically to obtain multiple 2D image planes which could then be rendered into a single 3D volume [66–71]. However it was with the development of 2D matrix transducers, enabling 3D electronic steering in the seminal work of S. Smith, H. Pavy, and O. von Ramm [72, 73], that the

technology was able to mature. Further advances in design and engineering led to the commercialization of RT3DE technology [74].

Nevertheless, due to the intrinsic trade-off between temporal and spatial resolution in ultrasound, RT3DE acquisition is often challenging. In fact, to acquire a volume encompassing the whole heart a volume of 75˚x75˚with a 15cm range is typically required. For adequate lateral resolution, approximately 85x85 lines would be required and for each line the sound must travel twice the 15cm range. This then means that a single volume would take 1.4 seconds, giving a FR of 0.7Hz. While this value is clearly insufficient to assess a dynamic organ such as the heart, different strategies can be implemented to improve FR. First of all, the field of view (FOV) can be decreased to encompass only the structure of interest. However, that might not be possible, especially in the case of dilated hearts. Secondly, the line density can be decreased, which however degrades the overall image quality. Third, a multi-beat acquisition can be performed, a strategy implemented in most clinical scanners. Finally, any of the advanced beamforming techniques mentioned for high frame rate imaging might be used to offset the trade-off between spatial and temporal resolution, thereby increasing the FR in RT3DE.

Furthermore, the fact that 2D probes present a larger footprint makes the acquisition more challenging as the intercostal space varies between patients and can obstruct the ultrasound path. The processing of RT3DE data is also a challenge as manual contouring of 3D data is time consuming and automatization has only recently been made available in commercial solutions. The intrinsic more challenging acquisition and processing of the data has thus led to a delay of the introduction of RT3DE to clinical practice.

In spite of the limitations of RT3DE, the fact that the 3D anatomy of the heart can be assessed without assumptions directly translates into increased agreement of RT3DE against the current gold-standard method (i.e. cMRI) when compared to conventional 2DE. Summing this to the intrinsic advantages of ultrasound imaging against other modalities and the continuous technical advances in both image acquisition and processing, RT3DE will likely become the standard echocardiographic examination of the future.

2.4 Echocardiographic Image Analysis

Additionally to the imaging acquisition, the extraction of the relevant information from the data must be considered. The assessment of volumetric, functional and morphologic indices poses two main problems. First, a clear identification of the myocardial anatomy is needed, through the delineation of the endo- and epicardial surfaces at a given time point. Furthermore, the position of these boundaries throughout the cardiac cycle is needed to recover the underlying motion of the cardiac chamber and capture the volume changes. However, ultrasound image processing poses several challenges [75]. The image quality is strongly affected by the acquisition conditions which can lead to low SNR and different artifacts such as dropouts resulting in missing boundaries. Furthermore, the very contrast between

structures of interest is often low. The inherent speckle pattern of ultrasound image can also be a confounder. Moreover, the manual delineation of boundaries in 3D data is a cumbersome and time-consuming task, making the introduction of semi- or fully automated cardiac image processing methods of great importance.

2.4.1 Left Ventricular Segmentation/Tracking Methods

Several methods have thus been proposed to address these problems and a categorization of these methods is possible dividing into geometrical models, shape-free methods, statistical models, classification approaches and tracking [76]. Each of these categories is briefly described in this section. For a more comprehensive description of these methods, the interested reader can refer to the extensive review by Leung and Bosch [76].

Geometrical models are the most common border detection approaches and consist of the representation of a border in terms of a curved surface influenced by geometrical constraints. This surface is initialized interactively or automatically and evolves iteratively according to image features such as the local intensity or edge information. Most geometrical models use energy-based optimization where a mathematical energy function is defined according to the image features and other regularization terms and optimized iteratively [3, 77–81]. Given the surface representation that is used, the main disadvantage of these models lies in finding a balance between a surface that is too smooth and one that becomes implausible.

Shape-free methods are, as the name implies, methods with little or no dependency on the shape of the final object. As such, they are heavily dependent on low-level image information such as pixel intensity, gradients, edges and corners and motion vectors. The two main families with this category are clustering and level sets. Clustering is, simply put, a categorization of each pixel of the image into groups, for example myocardial tissue and blood pool [82–85]. Level sets are similar to geometrical models with the main difference that the shape of the object is not restricted, which can often result in multiple disconnected surfaces [86–90]. Due to the low level of shape restrictions imposed, these techniques are quite susceptible to image artifacts such as shadowing or dropouts.

Statistical models are population based methods that model the statistical variations of patient data according to borders manually contoured by experts. This is done by finding a relatively simple mathematical model with but a few parameters that can express the patient variability from an average. By varying these parameters one can then synthesize a large number of shapes. Different sources of information can be used to build such a model. Active shape models use the manually contoured borders [91–93], whereas active appearance models (AAM) use a combination of the manually contoured borders and the image intensity information [94–96]. Given their origin from real examples this method can only find plausible results. However, this is also its downfall as the accuracy of the model will always be dependent on the quality of the original database and its extension throughout both healthy and pathological populations.

Classification approaches are also dependent on large sets of data contoured by experts, with however a different approach than statistical models [97–100]. According to the database information, a classifier is trained to distinguish the objects of interest into classes using appropriate features. In practice, parts of an image are then classified by selecting regions of different sizes in the image in different positions and determining its class following a coarse-to-fine scheme. Though the training procedure is extremely time consuming, the detection can be very fast. Classification approaches suffer from the same disadvantage as statistical models due to its dependency on the original database. However, even larger datasets are typically needed than for statistical models. Recently, classification approaches have received increasingly more attention following the advent of machine learning and deep learning techniques. The continuous increase in computational power and data storage have increased the feasibility of these methods and it should be expected that, as in other computer vision problems, these methods should in the future prove very effective given their direct access to a wide range of data.

Finally, tracking approaches are the most different from the other approaches as they do not aim at the border detection itself but at the estimation of the motion of an object throughout time. Thus, tracking approaches have a more dynamic nature. Since tracking approaches are mostly dependent on image information such as pixel intensity, the results can be especially sensitive to the presence of artifacts. This makes the introduction of information such as cardiac motion patterns particularly interesting. The existing tracking approaches are usually based on either registration or speckle tracking. In registration approaches the spatial correspondence between sequential images is found by measuring and optimizing a measure of similarity between them [79, 101–104]. Speckle tracking approaches aim at finding a correspondence between speckle patterns throughout time [105–113].

Given the many different approaches proposed in literature, it can be extremely overwhelming to draw conclusions over which segmentation tools seem to be the best and most promising. As such, benchmarking efforts such as the one recently published in Bernard et al. [114] are extremely important. By providing a thorough and equal validation to all segmentation methods, a just comparison can be performed and conclusions drawn over the evaluated strategies. In the study by Bernard et al., B-spline Explicite Active Surfaces (BEAS) [115] was the most accurate automatic segmentation tool both in distance metrics but also in the clinical indices evaluated. In terms of computational time, it was also one of the fastest methods, surpassed only by the Kalman filtering method by Smistad et al. [116]. It is also worth noting that the shape information or modelling provided to the segmentation model seems to play a big role in determining the behaviour of a given segmentation tool, probably due to the challenging aspects of ultrasound in terms of shadowing and dropout artifacts.

2.4.2 Available Commercial Technology

From the aforementioned methods, some of them have been adapted or developed into commercial software packages designed to introduce at least some form

of automation for 3D LV segmentation and, ultimately, aid the clinician.

Tomtec Imaging Systems (Unterschleissheim, Germany) was the first company presenting commercial tools for 3D volume quantification, taking advantage of its expertise on image processing and visualization. Their current product, TomTec 4D LV-Analysis©, performs an automatic orientation of the LV longitudinal axis to display three apical and three short axis (SAx) views. If necessary, these can be adjusted by the user to avoid foreshortening and modify the AV landmark orientation. The entire 3D endocardial surface of the LV is then contoured by the software in ES and, using 3D speckle tracking, propagated throughout the heart cycle [117]. This same tool is also available under TomTec's software solution 4D LV-Function^{TM}.

Contrarily to the purely offline approach offered by TomTec, Philips Healthcare (Best, Netherlands) introduced the possibility of both offline and online analysis with their QLAB – 3DQ Advance (3DQA) software suit [118, 119]. First, the longitudinal axes must be aligned in the 4-chamber and 2-chamber views at the ED phase. Five anatomical landmarks must then be marked, which are used to initialize a deformable shell model [77]. This model is afterwards deformed towards the LV boundaries, with the option for manual correction. The same process must be completed for the ES phase [119]. Philips Healthcare has recently introduced a new commercial tool, the HeartModel^{AI}, available on their EPIQ7 system. The HeartModel^{AI} is a fully automatic knowledge-based model which detects ED and ES instances, performs localization and tracking of the four chambers and also alignment of the apical 4-, 3- and 2-chamber views [120]. Refinement of the results is also possible through manual correction of the contours. The tool returns then the LV and LA volumes at ED and ES.

More recently, also General Electric (GE Vingmed, Horten, Norway) introduced a software package, 4D AutoLVQ, which allows both fully or semi-automated segmentation and volume quantification of the LV [117]. In this product, an initial alignment of the axis is needed so as to avoid foreshortening. This can be performed either automatically or manually by pivoting and translating the planes. In the semi-automatic version, the user is required to mark the location of the apex and the MA at ED and ES. After this, the 3D endocardial surface is automatically detected at these instances. In the fully automatic version no initialization points are required. After the conclusion of the segmentation the user is allowed to manually edit the contours.

Toshiba Medical Systems (Tokyo, Japan) has entered the RT3DE realm with its Artida^{TM} system, which was complemented with a software tool for chamber quantification by RT3DE speckle tracking, 3D Wall Motion Tracking (3D-WMT) [119, 121, 122]. This computational platform performs an automatic selection of apical 4-chamber and 2-chamber views, as well as 3 SAx views at different LV levels. The user is then required to place six markers: at the edge of the MV and at the apex in each of the apical planes. These points are then used to automatically segment the endocardium. The epicardial contour is defined either by a predetermined thickness or through manual contouring. The final shape of the LV can then be corrected manually by the user. A 3D block matching algorithm [123] is then used to track the wall motion throughout the cardiac cycle in a fully automatic manner.

The development of a fully automatic image analysis software package has been one of the main strategic investments of Siemens Medical Solutions (Mountain View, California) while developing their Acuson SC2000^{TM} RT3DE system, resulting in the software tool eSie LVA^{TM}. This tool is based on a comprehensive database of manually annotated RT3DE exams (over 4000) covering both healthy and typical pathological cases in clinical practice. The offline learning process was performed using a Probabilistic Boosting Tree [124] to obtain the final classifier. Given an input volume, this classifier sequentially estimates position, position-orientation and full similarity to locate the object and finally performs both an orientation according to standard planes [100] and also the contouring of the LV using boundary detectors [125] and statistical shape models (SSM). The final endocardial contours can be refined by the user through manual correction.

2.4.3 3D Left Ventricular Volume Assessment Validation

The enthusiasm generated in the medical community by 2D matrix transducers and RT3DE is well demonstrated by the numerous validation studies for this imaging modality over the past decade. Although validation on other experimental setups has been done (e.g. water balloons of known volume [126], intracavity balloon measurement in canine models [127], in vitro porcine heart models [128]), the primary and more generalized validation route for the existing software suites for volumetric measurement is to perform direct comparison of the volumetric indices extracted from RT3DE exams against reference values extracted from cMRI, which remains the generally accepted gold standard method for volumetric assessment of cardiac chamber dimensions. Alternatively, some studies report a direct comparison between automated vs. manual contouring of RT3DE data, thus providing insight on the ability of automating the contouring process. The most relevant studies are summarized in this sub-section and Table 2.1 provides an overview of the corresponding main results.

The earlier studies focused on software tools that relied mostly on a computer-assisted 3D manual contouring paradigm, either requiring manual delineation of the endocardial boundary in several long axis (LAx) planes or requiring significant user input in semi-automatic segmentation algorithms. The performance of the pioneer Volumetrics system was analyzed by both Schimdt et. al [129] and Lee et al. [130]. Both studies found excellent correlation between cMRI-derived volumetric indices and the ones extracted from RT3DE data by manually contouring in different azimuthally equidistant LAx images. Note that Kühl et al. had already demonstrated that the truly 3D nature of RT3DE data enabled LAx contouring in contrast to the SAx, sum-of-disk approaches initially inherited from cMRI [131]. Mannaerts et al. performed a similar study with an ATL® HDI 5000 system and manually contouring the endocardium using one of the first TomTec tools, EchoView. Mannaerts et al. reported good correlation as well as the first evidence of a negative bias of 3D echocardiographic volumes with respect to cMRI [132]. Kühl et al. performed the first clinical validation on the second generation of 2D (i.e. fully sampled) matrix transducers, showing excellent correlation against cMRI, in a

cohort of 24 good image quality patients [133]. In this study, a manual contouring paradigm was compared against an early semi-automatic algorithm, showing that the tested semi-automated approach enabled full 4D delineation but required longer analysis times and showed larger bias and wider limits of agreement. Jenkins et al. further validated the same system in a larger study (#=50) using a semi-automatic approach provided in an earlier version of TomTec's 4D LV-Analysis© [134]. The tool required the placement of landmarks in 12 azimuthally equidistant LAx views which were used to fit an ellipse to the endocardial borders. This was then followed by manual refinement. In addition to low bias and acceptable limits of agreement, RT3DE showed lower test-retest and intra/inter-observer variability than its 2D counterpart. The same semi-automatic approach was validated by Sugeng et al. with excellent correlation against cMRI and low bias though with wider limits of agreement [135]. Van den Bosch et al. carried out the first clinical validation of RT3DE-derived LV volumes in congenital heart disease patients, whose challenging cardiac shapes had been previously reported as a difficulty [136]. Their results showed excellent correlation/agreement for LV volumetric analysis using a fully manual contouring approach. However, when applying the same semi-automatic contouring software tool as used in [134], the results highlighted that this tool relied too much on a purely elliptical shape prior, thus having a poor performance. Despite the strong resilience of the multi-planar contouring paradigm in the early clinical validation, a more 3D-oriented vision has been introduced with the algorithm proposed by Corsi et al. [87], which was further validated by Caiani et al. in a clinical setting [90].

Jacobs et al. were the first to validate the concept of rapid, online measurement of LV volumes from RT3DE data [118], using the tool provided by Philips, QLAB – 3DQA. Indeed, online volumetric analysis within the imaging system without the need to export data to an external computer for tracing and 3D reconstruction further reduces time load. Very strong correlation and acceptable limits of agreement were found for all volumetric indices, despite the significant bias for EDV and ESV. Additionally, the comparison between the volumetric indices extracted online correlated strongly and had good agreement against the offline semi-automatic contouring approach proposed in [133]. Nonetheless, in a study by Jenkins et al., the offline approach by TomTec was compared to Philips' QLAB – 3DQA showing that offline approaches remain superior to the online quantification of LV volumetric indices, at the expense of longer analysis times [137]. A similar study was conducted by Soliman et al. using a newer version of TomTec's 4D LV-Analysis© in which only the manual contouring of three orthogonal planes is needed and similar results as those by Jenkins et al were obtained [138]. In a different study by Soliman et al., two different versions of TomTec's 4D LV-Analysis© are compared to volumes obtained through cMRI showing strong correlation for both methods and a clear superiority of the newer version dependent on full volume reconstruction [139].

Despite the convincing results of the previous validation studies, a clearer understanding of possible sources of errors was required for optimal clinical usage. To this end, Mor-Avi et al. have studied the source of variation between volumetric indices measured with RT3DE and cMRI, showing that the fundamental difference

is the inability of RT3DE to resolve the separation between trabeculae and myocardium. Indeed, including the trabecular region outside of the blood pool during cMRI contouring in the blood pool significantly reduced the RT3DE vs. cMRI bias, as well as the limits of agreement [126]. This fact sums up with the blurring effect caused by the point spread function of the acquired ultrasound signal, which pushes the apparent blood-tissue interface towards the blood pool, as shown by Mor-Avi et al. in balloon phantoms.

More recently, a shift towards more advanced software suites has enabled more automated analysis of RT3DE data, allowing a more efficient workflow for the extraction of clinically relevant information from RT3DE data. Indeed, the previously cited studies have mostly focused on semi-automatic software tools that provide at most computer-aided manual delineation of the LV cavity. Typical time of analysis ranged from around 2 [118] to 10 minutes [90, 134], although several studies report analysis times around 5 minutes per dataset [126,138]. Note that Jacobs et al. have shown that online LV volumetric analysis can provide accurate results in less than 2 minutes per volume [118] but they stress that manual adjustments were required in 42% of the analyzed cases using an online quantification tool, increasing the analysis time from 2 minutes to up to 5 minutes per volume.

With this in mind, a strong research effort has been directed towards more efficient software packages, incorporating advanced computer algorithms enabling a faster, more efficient and more accurate processing of RT3DE volumes. Hansegård et al. [140] and Muraru et al. [141] used GE's AutoLVQ and TomTec's 4D LV-Analysis© to show that a more advanced, automated software package can reduce the average time of analysis when compared with standard semi-automated strategies, while keeping comparable accuracy. Muraru et al. [141] have equally shown that fully automated (i.e. only manual initialization on ED and ES frames, with subsequent automatic delineation) is feasible. However, their results show that a noticeable increased agreement can be achieved by manually adjusting the results from an automated method, at the cost of doubling the total analysis time. Kleijn et al. have validated another highly automated software tool, Toshiba's 3D-WMT [142]. Despite only moderately good results for the LV volume assessment, the EF results showed excellent correlation and remarkably low bias and limits of agreement, indicating that more advanced tracking methods can positively influence the quality of the extracted surfaces when compared to pure contour-extraction approaches. Similar results have been reported by Kawamura et al. [122]. To test the potential of RT3DE in a realistic clinical scenario, Miller et al. analyzed 60 consecutive patients to determine the effect of image quality in RT3DE volume quantification performance [143]. Despite reporting lower agreement with cMRI measurements than previously found, the authors stress that the degree of error is intrinsically linked with image quality.

Using Siemens' eSie LVA^{TM} tool, Thavendiranathan et al. demonstrated that fully automatic analysis of RT3DE is possible and presents extremely encouraging results [144]. Note that Thavendiranathan et al. point out that the patients undergoing RT3DE exams in the analyzed dataset were selected for good acoustical windows, thus having good imaging quality. The authors have applied the same

computational automatic analysis algorithm to the reconstructed cMRI datasets and have found slightly higher bias and limits of agreement against the manual delineation on cMRI data than when using the same software on RT3DE data ($-0.8 \pm 4.7\%$ vs. $-0.3 \pm 2.5\%$). This seems to point towards the excellent image quality of the analyzed RT3DE dataset. Similar results were also found by Zhang et al. [145]. Using the same tool, Chang et al. [146] reported slightly lower correlations and the Bland-Altman analysis on EF estimates revealed much larger bias and limits of agreement than reported by Thavendiranathan et al. in [144]. Nonetheless, it is important to stress that the dataset corresponded to consecutive patients, although previously selected based on 2DE image quality and the user was allowed to manually correct the automatically detected contours. It should also be noticed that Chang et al. report that automatic results were considered excellent in 11% of the cases (i.e. not requiring any adjustment), good (i.e. five or fewer manual corrections required) in 34% of the cases and it failed completely (i.e. required manual delineation) in 10% of the cases. Regarding the influence of manual correction, Shibayama et al. have evaluated the same system, performing first fully automatic analysis and then allowing the user to proceed to manual corrections, in a cohort of 44 consecutive patients [147]. Their results reinforce the findings of Muraru et al. for a different system, thus highlighting that even state-of-the-art software packages are not yet able to consistently perform fully automated/automatic analysis of RT3DE data. Indeed, Shibayama et al. show that fully automatic results are significantly improved through manual interaction. Nonetheless, manual correction increased the total analysis time by a factor of 10. Using Philips' HeartModel^{AI} tool, Tsang et al. analyzed 46 patients achieving similar results to those reported with other fully automatic approaches without performing manual correction of the contours [148].

The key summary of the literature on the clinical validation of RT3DE volumetric assessment against cMRI can also be appreciated in the recent meta-analysis studies of Shimada and Shiota [149] and Dorosz et al. [150]. Shimada and Shiota's meta-analysis included 3055 subjects in 95 studies, focusing not only on 2D matrix transducers but also earlier systems based on mechanical steering. A key evidence is the significant underestimation bias of LV volumes (both EDV and ESV) by RT3DE compared with cMRI. On the other hand, no statistically significant bias for estimation of EF was found. Sources of error included gender and presence of congenital heart disease, which were associated with larger underestimation in the analysis. Semi-automatic border detection and the use of matrix-array transducers were associated with a smaller degree of underestimation. As key conclusion, the studied literature supports the role of RT3DE as both accurate and reproducible in assessing LV volumes and EF, although it is not interchangeable with other radiologic modalities. On the meta-analysis study by Dorosz et al., an additional perspective on how RT3DE compares with conventional 2DE is given in parallel to the central comparison of RT3DE-derived volumetric indices against cMRI. Their main conclusion is that RT3DE underestimates volumes and has wide limits of agreement, but compared with traditional 2D methods, it is more accurate (i.e. smaller bias) for volumes (EDV and ESV) and more precise (i.e. tighter limits of agreement) for EDV, ESV and EF measurements. One of the key benefits of RT3DE is the

reduction in intra/interobserver variability, which is important for clinical practice, since disease progression in a patient will most likely be assessed serially by different readers. Dorosz et al. also highlight the natural influence of image quality on the estimation of LV volumetric indices. Indeed, an analysis of those studies that accepted all 3D datasets, instead of selecting patients for image quality, shows that the 95% limits of agreement against cMRI raise from ±34 to ±38ml for EDV, ±30 to ±34ml for ESV and ±12 to ±15% for EF.

Finally, the first step towards effective clinical integration of RT3DE volume measurements is the population-based assessment of normal values, as acknowledged recently by Marwick in the editorial note of a leading cardiovascular imaging journal [151]. Several studies, including the work of Aune et al. [152], Kaku et al. [153], Fukuda et al. [154], Chahal et al. [155] and Muraru et al. [156], have been filling this gap, providing clinicians one of the last pieces of the path towards clinical integration of RT3DE examination in daily routine. An ongoing large-scale project (EchoNoRMAL) is aiming to define the echocardiographic normal ranges of the LV, through a collaborative effort meta-analysis approach [157, 158].

2.5 Towards Robust Left Ventricular Segmentation

In spite of the significant research efforts related to LV segmentation and tracking in echocardiography, at the beginning of this project, no satisfactory software package was available that provided fast and fully automatic LV assessment in a robust way. While significant advances have been made in terms of increasing robustness and automatization, commercial software packages at the beginning of this project relied heavily on user interaction and the findings of Bernard et al. [114] showed that there is still a gap in accuracy between state of the art methods and interobserver variability. Even today, commercial software packages, such as Siemens eSie LVA^{TM} or Philips HeartModel^{AI}, are proprietary and subject to the inherent image characteristics and meta-information of those systems. As such, the goal of the present work was to develop a tool for 3D echocardiographic LV assessment and to make it available to clinicians by incorporating it in a graphical user interface. This tool should perform LV assessment along the *full heart cycle* in a coherent way. To provide all the necessary clinical parameters the tool should perform *myocardial* segmentation - besides the endocardial volumes, epicardial segmentation can be especially interesting to study myocardial mass and as an initial step for further post-processing applications. Additionally, the ideal tool should be automatic, with *minimal/no user input*. Furthermore, the tool should do so in *real-time* or close to real-time, as the immediate access to the information is one of the strongest assets of echocardiography. Finally, the ideal tool should be extremely *robust* and be able to cope with images from different imaging systems. In this context, experimental systems can be especially challenging as the image quality is likely to be worse than in conventional systems. Yet, it is also in this setting that an automatic tool would be especially important to streamline applicational research such as that briefly

described in section 2.3.3.

Given the requirements defined in the previous paragraph, it becomes clear that the method chosen for segmentation must be flexible and robust, but also fast. As such, and according to the findings of Bernard et al. [114] as discussed in section 2.4.1, the tool chosen was BEAS as it showed excellent performance and can easily be modelled to perform epicardial segmentation as well [159]. Furthermore, to increase robustness in poor image quality cases, shape/landmark information should be further included in the framework as this was shown to play a significant role in determining the behaviour of the segmentation.

2.6 B-spline Explicit Active Surfaces

2.6.1 Framework Fundamentals

The fundamental concept of BEAS is to represent the interface Γ as an explicit function of its coordinates, i.e. one of the coordinates of the points along Γ is expressed as a function of the remaining coordinates [3]. As such, a point $\mathbf{x} \in \mathbb{R}^n$ of coordinates $\{x_1, ..., x_n\}$ belonging to surface Γ in an n-dimensional space can be expressed explicitly as $x_1 = \psi(x_2, ..., x_n)$. In this framework, ψ is defined as a linear combination of B-spline basis functions [160], i.e.:

$$x_1 = \psi(x_2, ..., x_n) = \sum_{\mathbf{k} \in \mathbb{Z}^{n-1}} c[\mathbf{k}] \beta^d \left(\frac{\mathbf{x}^*}{h} - \mathbf{k} \right), \tag{2.1}$$

where $\mathbf{x}^* \in \mathbb{R}^{n-1}$ is a point of coordinates $\{x_2, ..., x_n\}$ and $\beta^d(\cdot)$ is the uniform $(n–1)$-dimensional B-spline of degree d. The knots of the B-splines are located on a rectangular grid defined on the chosen coordinate system, with a regular spacing given by h. The coefficients of the B-spline representation are gathered in $c[\mathbf{k}]$. This allows for a smooth representation of any surface with the limitation that it must respect the coordinate system in which ψ is expressed. In the case of a spherical coordinate system for example, the surface represented should be a closed surface around the origin in which every point must be 'seen' from the origin, i.e. a straight line from the origin to any point in the surface does not intersect with the surface at any other point.

2.6.2 Energy Formulation

Given the formulation of BEAS as a geometrical model, the explicit function ψ is first initialized and then evolved by the minimization of an energy criterion E. This energy term can be defined according to any desired criterion and is often a combination of multiple terms that reflect the properties of the object to be segmented. The term corresponding to image features typically uses a localized region-based formulation due to its low sensitivity to noise and suitability for segmentation of heterogeneous objects [161]. These terms use the specific image characteristics on

either side of the boundary to drive the segmentation and are localized, meaning that these carachteristics are only considered in a region around the boundary. Such a formulation can be written as:

$$E = \int_{\Omega} \delta_{\phi}(\mathbf{x}) \int_{\Omega} B(\mathbf{x}, \mathbf{y}) \cdot F(\mathbf{y}, H_{\phi}(\mathbf{y}))\, d\mathbf{y} d\mathbf{x}, \tag{2.2}$$

where $F(\mathbf{y}, H_{\phi}(\mathbf{y}))$ is the image criterion and $B(\mathbf{x}, \mathbf{y})$ is the mask function in which the local parameters that drive the evolution are estimated. $\delta_{\phi}(\mathbf{x})$ is the Dirac operator applied to the level set function $\phi(\mathbf{x}) = \Gamma(\mathbf{x}^*) - x_1$, which is defined over the image domain Ω and $H_{\phi_j}(\mathbf{y}) = H(\phi_j(\mathbf{y}))$ with H being the Heaviside function.

To maintain low computational costs, the region B is restricted to the normal direction at $\mathbf{x}$, thus:

$$B(\mathbf{x}, \mathbf{y}) = \begin{cases} 1, & if \quad \mathbf{y} = \mathbf{x} + k\mathbf{N}(\mathbf{x}), k \in [-\rho, \rho] \\ 0, & otherwise \end{cases} \tag{2.3}$$

where $\mathbf{N}(\mathbf{x})$ is the normal to the interface at position $\mathbf{x}$ and ρ the radius of the local neighborhood considered.

Given the BEAS formulation, the minimization of 2.2 can then be done with respect to each B-spline coefficient $c[\mathbf{k_i}]$ and can be shown [3] to be:

$$\frac{\partial E}{\partial c[\mathbf{k}_i]} = \int_{\Gamma} \bar{g}(\mathbf{x}^*) \beta^d \left(\frac{\mathbf{x}^*}{h} - \mathbf{k}_i \right) d\mathbf{x}^*, \tag{2.4}$$

where $\bar{g}(\mathbf{x}^*)$ represents the feature functions that drive the minimization of energy E.

2.6.3 Algorithm Implementation

Because any object to be described by BEAS must be described through the explicit function in terms of its coordinates, the choice of an appropriate coordinate system is extremely important as it determines the topology of the final segmented object. For a 3D closed object such as the LV, the spherical coordinate system would be appropriate, giving the radius of the surface points in function of the azimuth and elevation angles ($r = \psi(\theta, \phi)$). This implies of course that an appropriate coordinate system origin and orientation are set before the segmentation is started so that every surface point can be "seen" from the origin. An example of this representation through an explicit function is shown on Figure 2.6.

A second consideration must be the discretization of the interface and the B-spline spacing h. Given that the explicit function ϕ is defined over an $n-1$ dimensional grid, this grid must be discretized in a uniform way. Adjusting these two parameters allows one to adjust to the complexity of the shape, as the number of points must be sufficient to represent the level of surface details necessary, but also to control the smoothing of the surface through the B-spline spacing h.

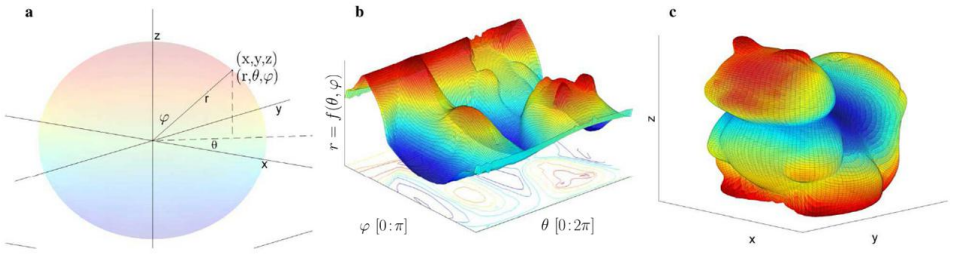

Figure 2.6: Illustrative 3D surface representation through an explicit function in the spherical domain. (a) Correspondence between the cartesian and spherical domains. (b) Explicit function in the spherical domain. (c) Explicit function converted to the cartesian space. Reproduced from [3].

In order to minimize the energy criterion, a modified gradient descent with feedback step adjustment algorithm is applied [162] so that the B-spline coefficients evolve according to:

$$c[\mathbf{k}]^{t+1} = c[\mathbf{k}]^t + \lambda \frac{\partial E}{\partial c[\mathbf{k}]^t}, \tag{2.5}$$

where λ is the step size and t the current iteration of BEAS. A description of the operating principle of BEAS is shown on Table 2.2.

2.6.4 Application to 3D Left Ventricular Segmentation

BEAS was first applied to 3D LV segmentation in the seminal BEAS publication by Barbosa et al. [3]. The segmentation was manually initialized at the first temporal frame by using an ellipsoid and the segmentation driven using the Chan-Vese energy functional [163]:

$$F(\mathbf{y}, H_\phi(\mathbf{y})) = (I(\mathbf{y}) - u_{in})^2 + (I(\mathbf{y}) - u_{out})^2, \tag{2.6}$$

where $I(\mathbf{y})$ is the image intensity at point $\mathbf{y}$ and u_{in} and u_{out} are the localized means inside and outside the surface defined according to:

$$\begin{cases} u_{in} = \dfrac{\int_\Omega B(\mathbf{x},\mathbf{y}) H_\phi(\mathbf{y}) I(\mathbf{y}) d\mathbf{y}}{\int_\Omega B(\mathbf{x},\mathbf{y}) H_\phi(\mathbf{y}) d\mathbf{y}}, \\ u_{out} = \dfrac{\int_\Omega B(\mathbf{x},\mathbf{y})(1 - H_\phi(\mathbf{y})) I(\mathbf{y}) d\mathbf{y}}{\int_\Omega B(\mathbf{x},\mathbf{y})(1 - H_\phi(\mathbf{y})) d\mathbf{y}}. \end{cases} \tag{2.7}$$

The minimization of E according to $c[\mathbf{k}]$ can then be expressed through 2.4 where

$$\bar{g}(\mathbf{x}^*) = (\bar{I}(\mathbf{x}) - u_{in})^2 - (\bar{I}(\mathbf{x}) - u_{out})^2, \tag{2.8}$$

and $\bar{I}(\mathbf{x})$ corresponds to the image intensity at position $\mathbf{x} = \{\psi(\mathbf{x}^*), x_2, ..., x_n\}$.

The segmentation result at each frame was then used to initialize the following frame, thus segmenting a full 4D echocardiographic dataset. Each frame took in average 12.5ms to segment thus demonstrating the potential of BEAS for real-time LV assessment.

Barbosa et al. [164] then validated BEAS against a prereleased commercial software package, eSieLVA$^{\text{TM}}$, for ED and ES LV segmentation by initializing at each frame, placing points at the MA and LV apex. It was thus shown by Barbosa et al. that BEAS achieves similar accuracy and reproducibility as state-of-the-art commercial tools.

The BEAS framework was later extended and improved in [165] by the addition of automatic initialization and a novel localized energy term for endocardial segmentation in ultrasound.

The automatic initialization proposed in [165] was inspired by the work of van Stralen et al. [166] and relies on the sequential detection of the LV LAx and the MV base to fit a spheroid to the endocardial boundaries. In brief, the endocardial boundaries are first detected in several C-planes (i.e. planes parallel to the transducer surface) using phase-based edge operators. The Hough transform for circles (HTc) is then used to find the probability of each point being the center of a circle of radius r, where $r \in$[15,35]mm. Multi-dimensional dynamic programming is then used to find the optimal path that maximizes the center probabilities along the depth direction [167]. This will give a smoothed path corresponding to the set of positions that have a high probability of being the center of a circle. A straight line is then fit to this path, thus determining the LAx. Next, a plane is slid along the LAx retrieving the average gray-level for each position. A merit function sensitive to a dark-to-bright transition and a brighter appearance is then used to find the MV position. Finally, a spheroid is fit using the radius probability information from HTc to maximize a sum of probabilities according to the LAx and MV position determined.

The localized energy term proposed in [165] is a variation of the Yezzi localized energy which aims to maximize the difference in mean intensity inside and outside the surface:

$$F(\mathbf{y}, H_\phi(\mathbf{y})) = -(u_{in} - u_{out})^2. \tag{2.9}$$

In [165], this energy was adapted to be sensitive to the expected intensities of the endocardial surface. Since the blood pool is usually darker than the myocardial tissue, the energy functional can be expressed as:

$$F(\mathbf{y}, H_\phi(\mathbf{y})) = u_{in} - u_{out}. \tag{2.10}$$

The minimization of E according to $c[\mathbf{k}]$ can then be expressed through 2.4 where:

$$\bar{g}(\mathbf{x}^*) = \frac{\bar{I}(\mathbf{x}) - u_{in}}{A_{in}} - \frac{\bar{I}(\mathbf{x}) - u_{out}}{A_{out}}, \tag{2.11}$$

where A_j is the area of region j used to estimate the local mean u_j.

A first step towards a motion coherent full cycle LV segmentation framework was presented in [168]. This was done by first using the result of the segmentation of frame $t-1$ to initialize the segmentation of frame t and then regularizing this result in a contrast dependent manner, thus allowing to improve the LV segmentation in areas of low contrast. A later approach by the same authors used a global affine optical flow to estimate cardiac motion from one frame to the subsequent, which is then locally refined using recursive block matching [115].

A framework for myocardial segmentation using BEAS was also presented by Barbosa et al. [159], though this work was limited to 2D SAx parasternal views. Nevertheless, the model showed promising results. Rather than defining the endo- and epicardium as two separate surfaces, the two surfaces were coupled by defining them in function of two common explicit functions such that:

$$\Gamma_{endo}(\mathbf{x}^*) = \psi_{mid\text{-}myocardium}(\mathbf{x}^*) - \psi_{half\text{-}thickness}(\mathbf{x}^*), \tag{2.12}$$

$$\Gamma_{epi}(\mathbf{x}^*) = \psi_{mid\text{-}myocardium}(\mathbf{x}^*) + \psi_{half\text{-}thickness}(\mathbf{x}^*). \tag{2.13}$$

This definition couples the evolution of both surfaces such that the segmentation of each of the surfaces depends on the other.

2.7 Concluding Remarks

The current status of cardiovascular disease as the leading global cause of death has established cardiac, and specifically, LV volume and function assessment as an essential task in clinical practice. While different imaging modalities are available to image the heart, ultrasound clearly stands out due to its high temporal resolution, safety, low cost and portability. While 2DE is the predominant modality for cardiac assessment, the full 3D anatomy of the heart can only be imaged using RT3DE. However, manual LV assessment in RT3DE is a challenging and time consuming task. As such, numerous methods have been proposed for automatic or semi-automatic LV segmentation in RT3DE. Nevertheless, a fast and fully automatic robust method for full-cycle myocardial LV segmentation was not available at the beginning of this project, thus motivating the present work. BEAS, as a flexible, fast and successful framework for LV segmentation in RT3DE was selected as the tool of choice.

Table 2.1: Validation of RT3DE and commercial software tools for LV volumetric assessment (#: number of exams; Ref: reference measurements taken from cMRI or manual contouring of RT3DE data (3DM); T: average frame processing time (s); R: correlation coefficient; BA: Bland-Altman analysis; NR: not reported).

Study	Imaging System	Analysis System	User Input	#	Ref	T	R			BA($\mu \pm 2\sigma$)		
							EDV	ESV	EF	EDV	ESV	EF
Schimdt et al. 1999 [129]	Volumetrics	-	A(NR)	25	cMRI	120-180	0.88	0.82	NR	NR	NR	NR
Lee et al. 2001 [130]	Volumetrics	-	A(7)	25	cMRI	NR	0.99	0.99	0.92	NR	NR	NR
Mannaerts et al. 2003 [132]	ATL® HDI 5000+P4	TomTec EchoView 4.2	A(9)	28	cMRI	1200-1800	0.79	0.90	0.87	-27.9±45.7	-34.4±45.5	1.2±15.8
Kühl et al. 2004 [133]	Sonos 7500+X4	-	C(24,2)	24	cMRI	720±300	0.98	0.98	0.98	-13.6±37.8	-12.8±41.0	0.9±8.8
Kühl et al. 2004 [133]	Sonos 7500+X4	-	C(24,2)	24	3DM	720±300	0.99	0.99	0.98	-1.3±17.2	-0.2±10.8	-0.1±5.4
Jenkins et al. 2004 [134]	Sonos 7500+X4	TomTec 4DLVA	C(36,2)+R	50	cMRI	630±60	NR	NR	NR	-4±58	-3±36	0±14
Caiani et al. 2004 [90]	Sonos 7500+X4	-	B(4)+R	44	cMRI	∼300	0.97	0.97	0.93	-4.1±30	-3.5±34	-0.8±14
Jacobs et al. 2005 [118]	Sonos 7500+X4	QLAB - 3DQA	C(5,2)+R	50	cMRI	120-420	0.96	0.97	0.93	-14±34	-6.5±32	-1±12.8
Bosch et al. 2006 [136]	Sonos 7500+X4	TomTec EchoView 5.2	A(8)	29	cMRI	1020±300	0.97	0.98	0.94	-2.9±12	0.9±9.9	-1.4±7.2
Bosch et al. 2006 [136]	Sonos 7500+X4	TomTec 4DLVA 1.2	C(24,2)	29	cMRI	360±120	0.79	0.84	0.54	NR	NR	NR
Jenkins et al. 2006 [137]	Sonos 7500+X4	TomTec 4DLVA	C(36,2)+R	110	cMRI	630±60	0.86	0.91	0.81	-15±56	-10±44	1±16
Jenkins et al. 2006 [137]	Sonos 7500+X4	QLAB - 3DQA	C(5,2)+R	110	cMRI	240±20	0.78	0.86	0.64	-44±70	-21±56	-2±20
Sugeng et al. 2006 [135]	Sonos 7500+X4	TomTec 4DLVA	C(18,2)+R	31	cMRI	NR	0.97	0.96	0.96	-5±53	-6±53	0.3±8
Soliman et al. 2007 [138]	Sonos 7500+X4	TomTec 4DLVA 2.0	B(3)+R	41	cMRI	360±120	0.99	0.99	0.98	-9.4±8.9	-4.8±10.1	0.3±4.7
Soliman et al. 2007 [138]	Sonos 7500+X4	QLAB - 3DQA	C(5,2)+R	41	cMRI	240±20	0.99	0.98	0.97	-16.4±13.4	-8.5±14.2	0.7±6.3
Soliman et al. 2007 [139]	Sonos 7500+X4	TomTec 4DLVA 1.2	C(24,2)+R	53	cMRI	900±300	0.96	0.98	0.95	-24.0±9.4	-11.3±17.2	0.8±6.4
Soliman et al. 2007 [139]	Sonos 7500+X4	TomTec 4DLVA 2.0	B(3)+R	53	cMRI	360±120	0.99	0.99	0.98	-9.9±8.4	-5.0±9.6	0.6±4.8
Mor-Avi et al. 2008 [126]	iE33+X3-1	QLAB - 3DQA	C(5,2)+R	92	cMRI	∼300	0.91	0.92	0.81	-67±92	-41±92	-3±22
Muraru et al. 2010 [141]	Vivid7+3V	4D AutoLVQ	C(9,2)	23	cMRI	48±24	0.77	0.72	0.64	-32.3±43.6	-13.9±30.7	-1.5±12.8
Muraru et al. 2010 [141]	Vivid7+3V	4D AutoLVQ	C(9,2)+R	23	cMRI	112±30	0.93	0.95	0.85	-11.0±24.2	-9.1±14.2	-2.9±8.4
Muraru et al. 2010 [141]	Vivid7+3V	TomTec 4DLVA 2.0	B(3)+R	23	cMRI	226±84	0.96	0.94	0.85	-8±19	-7±13	-2.8±8.4
Chang et al. 2011 [146]	SC2000+4Z1c	eSie LVA™	D+R	91	cMRI	NR	0.91	0.94	0.91	-41.38±37.2	-7.91±33.7	-8.26±13.0
Thavendiranathan et al. 2012 [144]	SC2000+4Z1c	eSie LVA™	D	91	cMRI	30-60	0.90	0.96	0.98	-17.6±53.4	-9.8±35.8	-0.3±5.0
Kleijn et al. 2012 [142]	Artida4D+PST-25SX	3D-WMT	C(5,2)	45	cMRI	∼300(w/acq)	0.75	0.81	0.91	-34±50	-13±22	-0.6±2.4
Miller et al. 2012 [143]	iE33+X3-1	QLAB - 3DQA	C(5,2)+R	42	cMRI	306±60	0.83	0.84	0.77	-45±70	-11±48	-7±18
Shibayama et al. 2013 [147]	SC2000+4Z1c	eSie LVA™	D	41	cMRI	36±8	0.80	0.85	0.54	-22.2±73.0	-18.0±64.2	1.2±23.3
Shibayama et al. 2013 [147]	SC2000+4Z1c	eSie LVA™	D+R	41	cMRI	371±116	0.96	0.97	0.9	-4.4±34.9	-5.0±27.7	0.9±15.2
Tsang et al. 2013 [148]	X5-1	HeartModel^{AI}	D	46	cMRI	<5	0.89	0.94	0.93	-35.05±90.34	-24.95±86.84	0.55±11.62
Zhang et al. 2013 [145]	SC2000	eSie LVA™	D	60	cMRI	NR	0.89	0.93	0.71	-3.5±43.5	-0.07±33.2	-2.7±15.7
Kawamura et al. 2013 [122]	Artida™	3D-WMT	C(5,2)+R	64	cMRI	NR	0.86	0.85	0.74	-19.0±76.5	-10.1±70.4	-0.3±13.1

User input: A(X): Computer assisted delineation of the 3D surface via manual contouring of X 2D planes; B(X): Semi-automatic segmentation, with manual initialization by contouring in X 2D planes; C(L,F): Automated segmentation, with user input of L anatomical landmarks in F time frames; D: Fully automatic segmentation without any user intervention; R: Manual refinement of segmentation results.

Table 2.2: BEAS algorithm operating principle description. Adapted from [3].

Initialization	• Choose appropriate coordinate system • Define the origin and orientation of the coordinate system • Initialize $\psi(\mathbf{x}^*)$ and sample according to discretization grid • Set the gradient descent parameters λ_i, η_f and It_T
Segmentation	**While** $It < It_{max}$ and $ctr < It_T$ • Estimate image feature $\bar{g}(\mathbf{x}^*)$ at the current surface position • Compute the energy gradient ∂E with respect to $c[\mathbf{k}]$ • Update the B-spline coefficients $c[\mathbf{k}]$ • Update $\psi(\mathbf{x}^*)$ to get the new interface points **If** the update leads to a decrease in E ◦ $ctr = 0$ ◦ $\lambda = \lambda_i$ ◦ $\psi_{final}(\mathbf{x}^*) = \psi(\mathbf{x}^*)$ **Else** ◦ $ctr = ctr + 1$ ◦ $\lambda = \lambda/\eta_f$ • It=It+1

λ_i is the initial step size, η_f is the step size update factor and It_T the maximum number of iterations allowed without finding a new energy optimum.

Part I

Segmentation Methodologies

Chapter 3

heartBEATS: A Hybrid Energy Approach for Real-Time B-spline Explicit Active Tracking of Surfaces

This chapter is based on a paper published in *Computerized Medical Imaging and Graphics*: Barbosa D., **Pedrosa J.**, Heyde B., Dietenbeck T., Friboulet D., Bernard O., D'hooge J.. heartBEATS: A hybrid energy approach for real-time B-spline explicit active tracking of surfaces. *Computerized Medical Imaging and Graphics.* 2017 Dec 1;62:26-33.

Abstract

In this chapter a novel method is presented for left ventricular (LV) tracking in real-time 3D echocardiography (RT3DE) data using a hybrid approach combining segmentation and tracking-based clues. This is accomplished by coupling an affine motion model to an existing LV segmentation framework and introducing an energy term that penalizes the deviation to the affine motion estimated using a global Lucas-Kanade algorithm. The hybrid nature of the proposed solution can be seen as using the estimated affine motion to enhance the temporal coherence of the segmented surfaces, by enforcing the tracking of consistent patterns, while the underlying segmentation algorithm allows to locally refine the estimated global motion. The proposed method was tested on a dataset composed of 24 4D ultrasound sequences from both healthy volunteers and diseased patients. The proposed hybrid tracking platform offers a competitive solution for fast assessment of relevant LV volumetric indices, by combining the robustness of affine motion tracking with the low computational burden of the underlying segmentation algorithm.

3.1 Introduction

Despite the existence of several functional indices, ejection fraction (EF) remains the most widely used parameter to assess global cardiac function [12]. While cardiac magnetic resonance imaging (cMRI) remains the gold standard to assess cardiac morphology and function, it is still impractical for large patient throughput. Thanks to the technological maturation of 2D matrix array transducers, 3D ultrasonic imaging systems have been gradually introduced into clinical practice over the past decade. When compared with conventional 2D echocardiography (2DE), RT3DE offers some important advantages. Indeed, it overcomes several known limitations of conventional 2DE imaging, since it avoids foreshortening, out-of-plane motion and the need of geometric assumptions for volume estimation. As a result, it has already been shown that RT3DE offers superior performance in the assessment of global morphology and function than 2DE, when compared against cMRI measurements [141]. Thus, the ability of combining accurate 3D volumetric assessment of cardiac morphology and function with the intrinsic benefits of ultrasound imaging makes RT3DE a very useful and promising tool for clinical daily routine.

It should be noted that the added dimensionality of RT3DE data also poses some challenges in the data analysis pipeline, when compared with conventional 2DE. The manual analysis of RT3DE data remains cumbersome and time consuming, which has triggered the development of several software suites in order to reduce the burden on the operating physician while extracting relevant cardiac diagnostic information. However, even state-of-the-art commercial solutions still require some degree of user interaction both at the initialization step and for correction of the segmentation/tracking results [141].

Nonetheless, several relevant methods have been proposed in order to increase the automation degree and decrease the total analysis time of RT3DE data. For

instance, Dikici and Orderud [169] have recently extended the Kalman-based, computationally efficient tracking framework initially introduced in [170], in order to account for advanced edge detectors to track the position of the LV endocardial border throughout the cardiac cycle. Leung et al. [171] proposed a fully automatic method for RT3DE data segmentation based on 3D active appearance models (AAM). The same authors have equally proposed a tracking framework able to take into account statistical cardiac motion models to improve the performance of an optical flow based tracking algorithm [172]. Yang et al. [173] have proposed a computational framework targeted to robust and fast 3D tracking of deformable objects without any user interaction, by combining the input of multiple collaborative trackers. Different commercial solutions also exist in the field, typically dependent on user interaction for single frame segmentation which is then propagated throughout the heart cycle using different tracking strategies as for example in Tomtec's and Toshiba's commercial tools described in Chapter 2 On the other hand, other approaches such as the newest available tools from Siemens and Philips, use large statistical models to perform the segmentation in 4D.

Despite the promising results of B-spline Explicit Active Surfaces (BEAS) on the segmentation of RT3DE data in both end diastolic (ED) and end systolic (ES) frames, as described in Section 2.6, the direct application of this algorithm to track the LV throughout the cardiac cycle has some intrinsic flaws. Indeed, segmentation-oriented energy functionals are designed to recover objects from a background in static images. Although they can be used in multi-static scenarios to perform tracking on subsequent images, there is no guarantee that the temporal coherence of the patterns being tracked will be captured.

With this in mind, a novel hybrid framework which combines both segmentation as well as motion-oriented clues is proposed. This is accomplished by coupling an affine motion model to the segmented LV surface and introducing an energy term that penalizes the deviation to the affine motion estimated using a global Lucas-Kanade algorithm. The hybrid nature of the proposed solution can be seen as using the estimated affine motion to enhance the temporal coherence of the segmented surfaces, by enforcing the tracking of consistent patterns, while the underlying segmentation algorithm allows to locally refine the estimated global motion. The proposed solution offers a competitive approach for fast assessment of relevant LV volumetric indices, by combining the robustness of affine motion tracking with the low computational burden of BEAS.

The present chapter is structured as follows. First, the method for LV affine motion estimation is presented, while also introducing the key novelty of this work, a hybrid tracking platform relying on both segmentation-based energies and tracking-oriented clues. It is shown that this coupling can be done via affine transformation of the coordinate system associated with the segmented LV surface. The key parameter values chosen in the implementation of the proposed algorithm are then addressed. In the Results section, an evaluation of the performance of the method using a dataset composed of 24 4D ultrasound exams is performed. In the Discussion, the main findings of the experiments are discussed and the performance of the proposed algorithm is compared against the most relevant prior work in literature. Finally,

the Conclusions section gives the main conclusions and perspectives of this work.

3.2 Methodology

3.2.1 B-spline Explicit Active Surfaces

In this Chapter, the modified version of the localized means separation energy is used as introduced in 2.9, which takes advantage of the darker appearance of blood with respect to the myocardial tissue. Given the volumetric nature of the object of interest, ψ is defined in the spherical space, i.e. $r = \psi(\phi, \theta)$. Further details regarding the fundamental formalism of BEAS and the derivation of the segmentation energy minimization strategy are described in Section 2.6.

3.2.2 Fast left ventricular affine motion estimation

3D cardiac motion assessment is a very active research field and different algorithms have been proposed. While block-matching is a very popular approach in current commercial software suites [174], the recent trends in the research community show a tendency towards solutions based on elastic registration and optical flow algorithms, as highlighted in the recent comparative study by De Craene et al. [175]. In the present manuscript, a global 3D extension of the method proposed by Sühling et al. [176] for the estimation of the local affine motion is used, as introduced in [177].

As noted in the seminal work of Lucas and Kanade [178], the least squares solution of the optical flow equation is equivalent to the first order Taylor expansion of the minimization of the sum of squared differences between two subsequent frames. Therefore, optical flow motion estimation algorithms build upon the assumption that the intensity of a particular point in a moving pattern does not change over time and thus any difference in the local appearance of a region over a sequence is uniquely defined by the underlying motion. Let $I(x_1, x_2, x_3, t)$ denote the pixel intensity at location $\vec{x} = [x_1, x_2, x_3]$ and time t in a 4D image dataset. This assumption can then be formulated as [179]:

$$I_{x_1}(\vec{x}, t)u(\vec{x}, t) + I_{x_2}(\vec{x}, t)v(\vec{x}, t) + I_{x_3}(\vec{x}, t)w(\vec{x}, t) + I_T(\vec{x}, t) = 0, \tag{3.1}$$

where $\nabla I = [I_{x_1}, I_{x_2}, I_{x_3}]$ is the local image spatial gradient and I_T corresponds to the temporal derivative. u, v and w are the x_1-, x_2- and x_3-components of the optical flow that are to be estimated.

Taking the affine motion model as defined in [176], the 3D affine motion on frame t can be estimated by minimizing the following energy term:

$$E_M(t) = \int \mathcal{W}(x_1 - c_1, x_2 - c_2, x_3 - c_3)(I_{x_1}u + I_{x_2}v + I_{x_3}w + I_T)^2 \mathrm{d}\vec{x}, \tag{3.2}$$

where $\mathcal{W}$ is a local window function centered in the position $\vec{c} = [c_1, c_2, c_3]$ and

$$u(\vec{x}, t) = u_0 + u_1(x_1 - c_1) + u_2(x_2 - c_2) + u_3(x_3 - c_3), \tag{3.3}$$

$$v(\vec{x}, t) = v_0 + v_1(x_1 - c_1) + v_2(x_2 - c_2) + v_3(x_3 - c_3), \tag{3.4}$$

$$w(\vec{x}, t) = w_0 + w_1(x_1 - c_1) + w_2(x_2 - c_2) + w_3(x_3 - c_3), \tag{3.5}$$

encode the local motion field along respectively x_1, x_2 and x_3. Parameters u_0, v_0 and w_0 correspond to the motion at the window center and u_1, u_2, u_3, v_1, v_2, v_3, w_1, w_2 and w_3 are respectively the first order spatial derivatives of u, v and w. These parameters then define the affine transform for frame t associated with the local motion field $[u, v, w]$ as expressed by the augmented matrix

$$\vec{M}_t = \begin{bmatrix} 1+u_1 & u_2 & u_3 & u_0 \\ v_1 & 1+v_2 & v_3 & v_0 \\ w_1 & w_2 & 1+w_3 & w_0 \\ 0 & 0 & 0 & 1 \end{bmatrix}. \tag{3.6}$$

By differentiating equation 3.2 with respect to the affine motion field components, it can be shown that the minimization of the weighted least-squares criterion can be expressed as the solution of $A^T \mathcal{W} A \vec{d} = A^T \mathcal{W} b$, whose components are expanded at the bottom of the page. Note that $< a, b >$ denotes the continuous analogue of the dot product, expressed as $\int a(\vec{x}) b(\vec{x}) \mathrm{d}\vec{x}$ and that $\vec{A}$, $\vec{d}$ and $A^T \vec{\mathcal{W}} b$ are functions of $(\vec{x}, t)$ though this was ommitted for simplicity.

A global formulation of the algorithm introduced by Sühling et al. could be employed by considering $\mathcal{W}(\vec{p}) = 1$, $\forall \vec{p}$. Such an assumption would yield the global affine transform between the two subsequent images. Nonetheless, increasing the span of the window function $\mathcal{W}$ intrinsically hampers the underlying assumption that the affine motion model is constant within this region. This is particularly problematic in the case of echocardiographic data, since it is known that the motion patterns of the blood and the surrounding tissues (e.g. pericardium and valves) are significantly different from the ones within the myocardium, thus violating the fundamental assumption of constant motion within the region of interest (ROI). In order to allow estimating the global affine transformation of the LV between subsequent frames, the existing segmentation framework will be used and the formalism introduced in [177] to define a ROI only around the segmented surface from the convolution expanded so that:

$$\mathcal{W}(\vec{x}) = \delta_\phi(\vec{x}) \ * \ N(\vec{x}), \tag{3.7}$$

where $\delta_\phi(\vec{x})$ implicitly defines the segmented surface and $N(\vec{x})$ is simply a neighborhood function defined as a 3D cube centered in $\vec{x}$. An example of the resulting

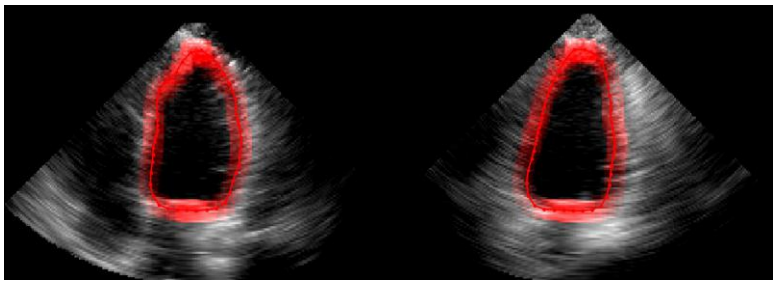

Figure 3.1: Anatomical ROI for affine motion estimation.

$\mathcal{W}(\vec{x})$ is shown in Figure 3.1.

3.2.3 Hybrid framework for fast left ventricle tracking

The integration of the motion information estimated with the aforementioned optical flow algorithm within the BEAS segmentation framework will enhance its tracking performance. This is achieved since the temporal coherence of the patterns being tracked is the fundamental driver of affine motion estimation, whereas the existing segmentation framework is mostly relying on the identification of salient features in static images. By combining the two, a hybrid framework will allow a synergistic collaboration between tracking-based and segmentation-based clues, increasing the overall performance and robustness. In the present sub-section the manner through which the hybrid tracking strategy can be implemented via affine deformation of the coordinate system associated with the segmented LV surface is described. A conceptual description of the proposed approach is illustrated in Figure 3.2.

First, the inherent characteristics of the BEAS segmentation framework should be recalled: BEAS models the LV object (in 3D) through an explicit function ψ_t in the spherical coordinate system, thus a function of azimuthal and elevation angles θ and φ. As such, to translate this explicit function ψ_t into the LV surface $\vec{S_t}$ in the Cartesian coordinate system, not only does the spherical to Cartesian conversion need to be performed, but the orientation and position of the spherical coordinate system (in which the BEAS surface is defined) relative to the Cartesian system have to be taken into account. The LV surface can thus be defined as:

$$\vec{S_t} = \vec{S}(\vec{T_t}, \psi_t) = \vec{T_t} \begin{bmatrix} \psi_t(\theta,\varphi)cos(\theta)sin(\varphi) \\ \psi_t(\theta,\varphi)sin(\theta)sin(\varphi) \\ \psi_t(\theta,\varphi)cos(\varphi) \end{bmatrix}, \tag{3.8}$$

$$\vec{A} = \begin{bmatrix} I_{x_1} \\ I_{x_2} \\ I_{x_3} \\ x_1 I_{x_1} \\ x_2 I_{x_1} \\ x_3 I_{x_1} \\ x_1 I_{x_2} \\ x_2 I_{x_2} \\ x_3 I_{x_2} \\ x_1 I_{x_3} \\ x_2 I_{x_3} \\ x_3 I_{x_3} \end{bmatrix}, \quad [A^T \vec{\mathcal{W}} A]_{ij} = <A_i \mathcal{W}, A_j>, \quad \vec{d} = \begin{bmatrix} u_0 \\ v_0 \\ w_0 \\ u_1 \\ u_2 \\ u_3 \\ v_1 \\ v_2 \\ v_3 \\ w_1 \\ w_2 \\ w_3 \end{bmatrix}, \quad A^T \vec{\mathcal{W}} b = - \begin{bmatrix} <\mathcal{W}, I_{x_1} I_T> \\ <\mathcal{W}, I_{x_2} I_T> \\ <\mathcal{W}, I_{x_3} I_T> \\ <x_1\mathcal{W}, I_{x_1} I_T> \\ <x_2\mathcal{W}, I_{x_1} I_T> \\ <x_3\mathcal{W}, I_{x_1} I_T> \\ <x_1\mathcal{W}, I_{x_2} I_T> \\ <x_2\mathcal{W}, I_{x_2} I_T> \\ <x_3\mathcal{W}, I_{x_2} I_T> \\ <x_1\mathcal{W}, I_{x_3} I_T> \\ <x_2\mathcal{W}, I_{x_3} I_T> \\ <x_3\mathcal{W}, I_{x_3} I_T> \end{bmatrix}$$

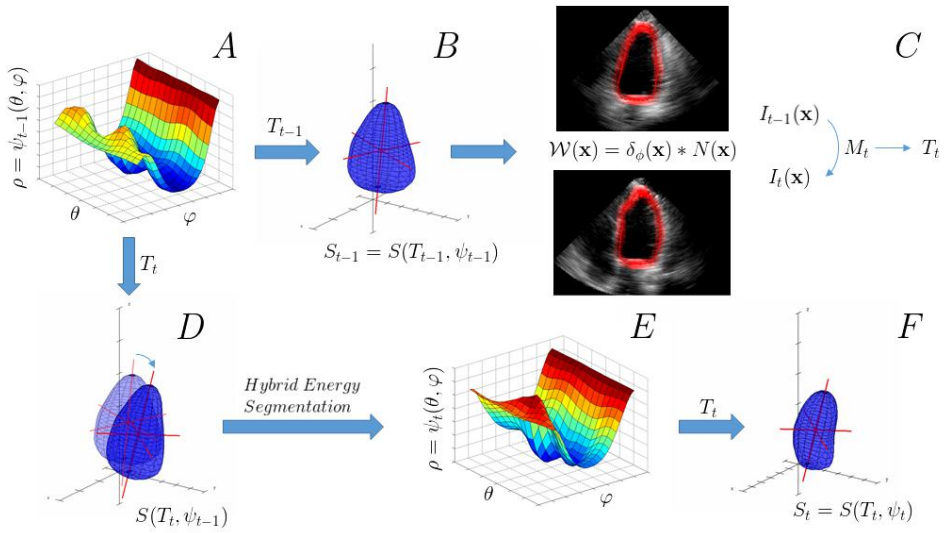

Figure 3.2: Conceptual description of the proposed hybrid algorithm. The explicit function ψ_{t-1} (A) defining the LV surface $\vec{S_{t-1}}$ through $\vec{T_{t-1}}$ (B) is used to the estimate the affine transformation $\vec{M_t}$ between two consecutive frames in the anatomical ROI $\mathcal{W}(\mathbf{x})$ (C). This gives $\vec{T_t}$, the LV global pose for frame t. This affine deformation is then applied to $\vec{S_{t-1}}$ (shown in greater transparency) giving $\vec{S}(\vec{T_t}, \psi_{t-1})$ (D). Hybrid energy segmentation is then applied to evolve ψ_{t-1} according to equation 3.12 to obtain ψ_t (E), which, through $\vec{T_t}$, defines the final LV surface for frame t, $\vec{S_t}$ (F).

where $\vec{T_t}$ is the augmented matrix comprising the orientation of the LV long axis (LAx) and its center position on frame t. This relationship is evident in Figure 2-A and B, where the explicit function ψ_{t-1} is transformed into $\vec{S_{t-1}}$ by employing equation 3.8. In this equation it is clear that, though ψ_t controls the local shape of the LV surface, this surface can also be globally deformed through $\vec{T_t}$.

Given that the estimated motion field can be expressed as an affine transformation, the estimated affine transformation between subsequent frames, $\vec{M_t}$, will be coupled to the underlying spherical to Cartesian transformation, using the recursive formulation:

$$\vec{T_t} = \vec{M_t}\vec{T_{t-1}}, \tag{3.9}$$

where $\vec{T_1}$ is the augmented matrix of orientation and center position of the LV in the ED frame. By applying the current estimate of $\vec{T_t}$ to the underlying spherical to Cartesian transformation, the entire surface can be intrinsically deformed according to the estimated affine transformation through translation, rotation and scaling. This is in fact the equivalent of deforming the original coordinate frame of the LV object according to the global affine motion estimated with the anatomical optical flow algorithm detailed previously, as illustrated in Figure 3.3. In the proposed

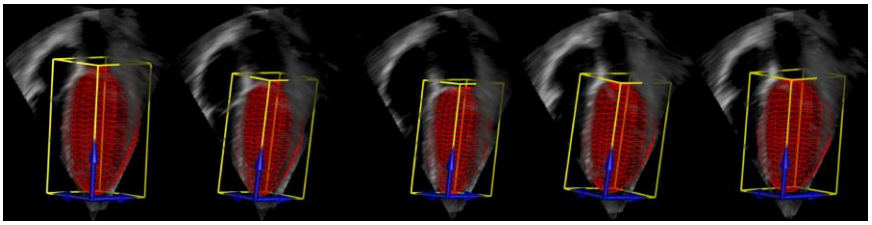

Figure 3.3: Affine deformation of the LV surface along time. For clarity sake, the coordinate system associated with the LV object was translated to the corner of the bounding box to facilitate its visualization.

hybrid framework, the LV surface $S_{t-1}^{\vec{}}$ (Figure 3.2-B) is used to determine $\mathcal{W}(\vec{x})$ which in turn is used to estimate the affine transformation $\vec{M}_t$ and obtain the new LV surface pose $\vec{T}_t$ (Figure 3.2-C). This augmented matrix $\vec{T}_t$ is then applied to ψ_{t-1} to deform the LV surface according to the affine motion estimated as shown in Figure 3.2-D.

In order to balance the contribution between tracking and segmentation-based clues, a hybrid segmentation is then performed to this deformed surface. For that purpose, an energy term that penalizes the deviation between the current surface position, $\vec{S}(\vec{T}_t, \psi_t)$, and the one initialized by applying the affine transformation to the previous segmentation result, i.e. $\vec{S}(\vec{T}_t, \psi_{t-1})$, is proposed:

$$E_A(t) = \int_\Gamma \left(\vec{S}(\vec{T}_t, \psi_t(\theta, \varphi)) - \vec{S}(M_t \vec{T}_{t-1}, \psi_{t-1}(\theta, \varphi)) \right)^2 \, d\mathbf{x}^*, \tag{3.10}$$

which, because the global pose $T_t = \vec{M}_t T_{t-1}$ is shared between the two LV surfaces, can be simplified to:

$$E_A(t) = \int_\Gamma \left(\psi_t(\theta, \varphi) - \psi_{t-1}(\theta, \varphi) \right)^2 \, d\mathbf{x}^*. \tag{3.11}$$

The global energy term for optimization can then be defined as:

$$E(t) = E_d(t) + \lambda E_A(t), \tag{3.12}$$

where λ is a hyperparameter controlling the balance between the data attachment term E_d and the tracking-based energy E_A. The energy criterion E can be minimized directly wrt. the B-spline coefficients controlling the shape of ψ_t:

$$\frac{\partial E(t)}{\partial c[\mathbf{k}_i]} = \frac{\partial E_d(t)}{\partial c[\mathbf{k}_i]} + \lambda \frac{\partial E_A(t)}{\partial c[\mathbf{k}_i]}, \tag{3.13}$$

where $\partial E_d(t)/\partial c[\mathbf{k}_i]$ is defined according to equation 2.11 and $\partial E_d(t)/\partial c[\mathbf{k}_i]$ can be expressed through equation 2.4 where

$$\bar{g}(\mathbf{x}^*) = \psi_t(\theta, \varphi) - \psi_{t-1}(\theta, \varphi). \tag{3.14}$$

Note that even though the affine transform parameters are not explicitly stated through $E(t)$, these are present in the term $E_A(t)$ as shown in equation 3.10. This term penalizes the deviation from the LV surface position after the affine deformation, guaranteeing that the data attachment term from the segmentation energy functional only modifies the segmented LV surface in regions where strong image content is available. Thus, LV regions with reduced image content are preferably tracked with the global affine deformations via optical flow estimation, while regions with rich image content rely mostly on the image data. Therefore, there is an intrinsic trade-off between global, robust tracking and localized, accurate surface positioning.

By performing this hybrid segmentation, the explicit function ψ_t is then obtained (Figure 3.2-E), which, through $\vec{T}_t$, defines the final LV surface for frame t, $\vec{S}_t$ (Figure 3.2-F) and thus enabling to restart the process for the next frame.

3.2.4 Implementation Details

In order to speed-up the estimation of $\mathcal{W}(\vec{x})$, the convolution expressed in equation 3.7 defining the anatomical ROI where E_M is evaluated was simplified by assuming that $\delta_\phi(\vec{x})$ is different from zero only in the positions of the discretized BEAS surface. N was defined as a 11x11x11 cube centered in the target point. The image gradient ∇I was estimated using a Gaussian derivative kernel with $\sigma = 1$, implemented as a separable convolution operation. Since differential optical flow approaches are best suited to estimate small displacements, the optimization of $E_M(t)$ was performed using an iterative displacement refinement scheme to improve the accuracy and robustness of the affine motion $\vec{M}_t$ estimation [180]. Five iterations were used in all experiments.

The hyperparameter λ controlling the balance between the segmentation and tracking-based terms in equation 3.12 was empirically set to 0.25. As in previous BEAS implementations for the LV [165], the angular discretization of the boundary ϕ was set to 24×16 and the B-spline scale h to 2^1. The mask function $B(\vec{x}, \vec{y})$ was restricted to the points along the normal direction of the surface at a distance smaller than 16mm as in [165]. The optimization of the global segmentation energy $E(t)$ was implemented in a modified gradient descent with feedback step adjustment as in previous BEAS implementations [165].

3.3 Experiments and Results

Twenty-four RT3DE exams were acquired using a Siemens Acuson SC2000 rev. 1.5 (Siemens Ultrasound, Mountain View, CA) using a 4Z1c matrix transducer.

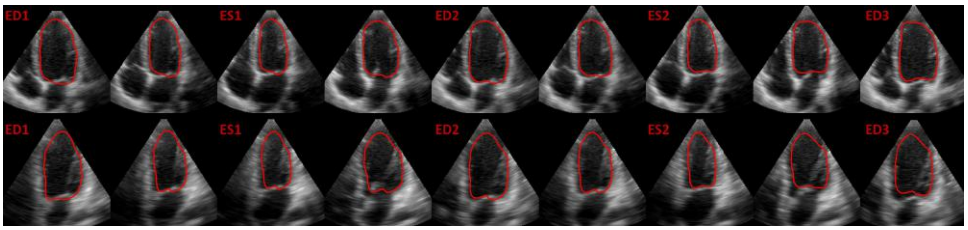

Figure 3.4: Tracking of the LV in a RT3DE dataset using the proposed hybrid approach (top: apical 4 chambers view, bottom: apical 2 chamber view).

Volume sequences were acquired during apical scanning and the sonographer aimed at the inclusion of the entire LV within the pyramidal field of view (FOV). Volume rates ranged from 20 to 40 volumes per second. Each sequence was analyzed by three experts using eSie LVA pre-release software (Siemens, Mountain View), who provided manual delineation of the LV chamber at both ED and ES frames. From these, the corresponding ED and ES volumes were calculated. The stroke volume (SV) and EF were posteriorly computed from the ED volume (EDV) and ES volume (ESV). The mean value of the three experts was taken as the reference for the aforementioned LV volumetric indices. The described protocol was approved by the institutional review board and patients signed an informed consent.

The proposed tracking framework was automatically initialized in the ED frame with the algorithm introduced in [165]. In order to demonstrate the synergistic interaction of the segmentation and tracking-based clues, the proposed solution was compared with the pure segmentation-based approach, by setting λ to zero in (3.12), and also with a pure global tracking approach, by keeping ψ fixed and adjusting $\vec{T}_t$ over time.

The summary of the results for the LV volumetric indices extracted using the proposed hybrid framework against the manual references can be found in Table 3.1. In the same table, the performances for both the pure affine tracking-based solution and the pure segmentation solution are also reported. An example of a RT3DE exam segmented using the proposed hybrid tracking algorithm is given in Figure 3.4, for 2 consecutive cardiac cycles. The segmentation of the first frame, which included the automatic initialization step, took approximately 1s , while the tracking between subsequent frames was done in 30ms, in a C++ implementation running on an Intel i7 laptop.

The key parameter to be tuned in the proposed algorithm is the hyperparameter λ controlling the balance between the contribution of the segmentation-based and tracking-based terms in equation 3.13. In order to test the sensitivity of the empirically chosen value, i.e. $\lambda = 0.25$, the value of λ was varied between 0 and 0.5, in steps of 0.05 and its corresponding LV tracking results observed. This allowed to assess the influence of removing the tracking-based term from equation 3.13 on the bottom side of the variation range, while the upper variation range corresponded to doubling the influence of the tracking-based clues. Additionally, the pure global tracking approach, where the influence of the tracking-based clues tend to infinity,

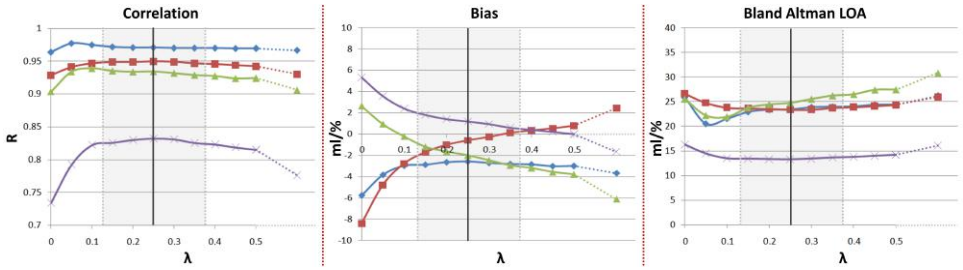

Figure 3.5: Influence of the balance between the segmentation and tracking-based terms in the overall performance of the proposed hybrid tracking algorithm (left to right: Pearson correlation coefficient, Bland-Altman bias (μ) and limits of agreement (1.96σ); EDV: blue; ESV: red; SV: green; EF: purple). The chosen value of λ is marked as a vertical gray line, while the range corresponding to a $\pm 50\%$ variation of its numeric value is shaded in light gray. Note that the leftmost data points in each plot correspond to a pure segmentation-based approach, while the rightmost ones correspond to a pure tracking approach.

Table 3.1: LV volumetric indices extracted using the proposed hybrid approach versus the pure segmentation-based (PS) tracking and the pure global affine optical flow algorithm (LOA: limits of agreement; *, $p<0.05$, paired t-test against zero).

	Correlation Coefficient (R)			**Bland-Altman Analysis LOA** ($bias \pm 1.96\sigma$)		
	PS	Affine	Hybrid	PS	Affine	Hybrid
EDV (ml)	0.964	0.966	0.971	-5.76*±25.9	-3.68±26.2	-2.58±23.4
ESV (ml)	0.929	0.930	0.950	-8.40*±26.6	2.43±26.0	-0.60±23.4
SV (ml)	0.904	0.906	0.934	2.64±25.6	-6.11±30.8	-1.99±24.8
EF (%)	0.734	0.776	0.833	5.35*±16.3	-1.65±16.1	1.20±13.3

was also tested. The results of this sensitivity analysis are given in Figure 3.5.

3.4 Discussion

The proposed hybrid tracking framework offers competitive performance for the fully automatic quantification of relevant volumetric cardiac indices used in daily practice for assessment of LV morphology and global function. This is supported by the strong correlation for all the estimated volumetric indices. Furthermore, low, non-statistically significant bias and tight limits of agreement were observed by Bland-Altman analysis. Comparing the results from the proposed hybrid approach to the pure segmentation and pure tracking strategies shown on Table 3.1 it becomes clear that the proposed hybrid approach outperforms both the pure segmentation and the pure tracking approach. There is thus a significant advantage on bringing

together the segmentation- and tracking-based clues within the same approach.

Furthermore, the proposed approach compares positively against the pure affine motion estimation algorithm used to estimate the global LV deformation previously introduced in [177]. This clearly indicates the advantages of the refinement stage using a hybrid combination of both segmentation and tracking-based clues. Indeed, despite the small inter-frame differences between the pure affine tracking and the proposed hybrid approach, a cumulative effect over the entire cardiac cycle leads to a significant improvement in tracking performance. Such observation is supported by the appreciable reduction in both bias and limits of agreement of SV estimation, to which sums up the strong increase in the EF correlation against the reference measurements. Therefore, even if visually the added value of the proposed hybrid strategy is not strikingly evident between two frames, the accumulation over the entire cycle improves the tracking performance significantly. Furthermore, the comparison against the previously proposed strategy based on sequential segmentation [168], whose results are included in the performance comparison in the following section, clearly highlights the synergistic effect between the tracking-oriented clues and segmentation-based energy terms.

Interestingly, the proposed affine coupling allows to deform the spherical discretization grid used to represent the segmented surface according to the estimated LV deformation. This enables capturing valuable information regarding both longitudinal and circumferential global motion of the heart which could not be properly evaluated with the previous segmentation framework. This opens the path towards the extraction of other cardiac global functional indices, such as global longitudinal and circumferential strain. Furthermore, the inclusion of the longitudinal/circumferential deformation via affine transformation of the coordinate system associated with the segmented LV surface provides a seamless integration on the previous formal framework, therefore not requiring any special modification to the underlying mathematical foundations.

The results of the sensitivity analysis demonstrate its robustness towards the chosen value for the hyperparameter λ controlling the balance between the tracking-based and segmentation-based terms in equation 3.13. Indeed, a modification of $\pm 50\%$ of its nominal value does not lead to appreaciable modifications in the correlation values for any of the LV volumetric indices considered in the present work. A similar trend is observed for the width of the limits of agreement for the EDV, SV and EF estimates. Nonetheless, the influence of λ is particularly visible in the performance of the ESV estimation. Such observation is explained by the opposite bias of the pure tracking-based and segmentation-based approaches. Indeed, while the pure segmentation-based approach overestimates the true ESV volume, the pure tracking-based affine optical flow method underestimates it.

3.4.1 Performance comparison

Although the proposed hybrid tracking approach offers promising results, a careful comparison with the values reported in the literature has been done in order to evaluate its competitiveness against currently available solutions. This comparison

does not aim to be extensive, but rather informative to the reader on how the proposed fully automatic framework for LV volume analysis compares with existing relevant methods. An overview of the results of the proposed algorithm and its comparison with other methods reported in the literature is shown in Table 3.2. Nonetheless, it should be noted that a fair and quantitative comparison is not trivial, due to differences in patient population and image quality and due to different acquisition conditions and equipment. We have selected relevant algorithms ranging from pure segmentation-based approaches to more oriented tracking strategies. However, methods with a similar validation approach (i.e. where the segmentation results were compared with manual segmentation of RT3DE data) were selected.

Table 3.2 also shows that the proposed algorithm presents a competitive performance when compared with the most relevant algorithms presented in the literature, both in terms of accuracy and overall computational load. Indeed, performance-wise only the algorithm of [172] and [173] provide clearly more accurate results than the ones provided by the developed algorithm. Nonetheless, both these algorithms are not able to run in real-time and rely on statical shape models (SSM) and motion models. While prior knowledge is a very powerful tool to deal with missing information scenarios, which is often the case in RT3DE data where some of the boundaries are missing, care should be taken to not infer wrong estimations due to excessive influence of the priors. Furthermore, the ability to deal with unseen data is typically related with the amount of different patterns included in the initial learning phase, which implies very tedious and labor-intensive stages towards building such statistical databases. It should also be noted that the algorithm in [172] is tracking-oriented and, thus, requires LV delineation at ED. While the same authors also propose an automatic ED segmentation algorithm in [171], the validation of their complete segmentation/tracking framework remains to be done.

In terms of overall running time, only the works of Orderud and Hansegård et al. [93, 170, 181] and the framework of Duan et al. [4] are able to compete with the proposed algorithm, which yields an average computing time of 30 ms per processed frame. On the other hand, level-set based algorithms, such as the ones in [86] and [182], require a significantly larger computational power due to the implicit representation of the evolving interface, with a direct trade-off between shape topology freedom and computational burden. Furthermore, in the current implementation of heartBEATS there are redundant computations introduced within the anatomical ROI in equation 3.7, since there are overlapping regions. This sums up to the high degree of parallelism in the key algorithmic blocks of the proposed method, which opens the path to further implementation optimizations which would allow to further reduce overall computational time. Therefore, there is still a considerable margin to improve the processing speed of heartBEATS, which will allow the method to be prepared to deal with higher frame rate (FR) 3D acquisitions, currently a hot topic in the ultrasound community [55, 183].

The comparison against the recent work of Zhang et al. [184] also supports the competitive performance of the proposed algorithm. Despite validating their algorithm in a dataset composed of patients selected for cardiac resynchronization therapy (CRT), relative volume errors of $4.2 \pm 17.4\%$ and $-1.3 \pm 16.8\%$ ($\mu \pm \sigma$) are

reported for the segmented LV surfaces considering the input of two different users. In the current study, the proposed algorithm yielded $-4.7 \pm 14.1\%$ considering both EDV and ESV values. Thus, heartBEATS presents a competitive performance when compared to the active shape model-based method of Zhang et al. [184], while doing so without any kind of user input.

Table 3.2: Proposed vs. state-of-the-art algorithms (#: number of exams; ΔT_f: average frame processing time (s); R: correlation coefficient; BA: Bland-Altman analysis; FC: full cycle, NR: not reported).

Study	**Algorithm/Frames /User Input**	**#**	$\mathbf{\Delta T_f}$	**R**			**BA**($\mu \pm 2\sigma$)		
				EDV	ESV	EF	EDV	ESV	EF
Prior work									
Angelini et al. 2005 [86]	PS/ED+ES/I	10	NR	0.63	0.62	0.45	16.1±50	6.6±34	0.5±22
Hansegård et al. 2007 [93]	MSS/FC/0	21	0.008	0.91	0.91	0.74	-5.9±21	6.2±19	-7.7±12
Leung et al. 2010 [171]	PS/ED/0	99	NR	0.95	NR	NR	-1.47±40	NR	NR
Leung et al. 2011 [172]	PT/FC/II	35	6	0.982		NR	1.9±14		NR
Yang et al. 2011 [173]	HST/FC/0	67	1.5	NR	NR	NR	1.32±12		1.0±10
Rajpoot et al. 2011 [182]	PS/ED+ES/I	34	NR	NR	NR	NR	-5.0±49	1.2±26	-0.7±14
Rajpoot et al. 2011 [182]	PT/FC/II	34	NR	NR	NR	NR	NR	4.0±40	-3.3±25
Barbosa et al. 2012 [168]	MSS/FC/0	24	0.05	0.98	0.92	0.78	-3.9±22	-5.0±27	3.4±15
Zhang et al. 2013 [184]	MSS/FC/II	34	10	0.84		NR	NR	NR	NR
Proposed									
heartBEATS	HST/FC/0	24	0.03	0.97	0.95	0.83	-2.6±23	-0.6±23	1.2±13

Note that PS, MSS, PT and HST stand for the algorithm class, namely pure segmentation, multi-static segmentation, pure tracking and hybrid segmentation and tracking. Regarding user input, 0 stands for a fully automatic method, I for minor user input (such as few anatomical landmarks) and II for significant user input, such as manual contouring at the ED frame.

3.5 Conclusions

The proposed hybrid segmentation/tracking framework (heartBEATS) combines both segmentation-oriented image information with global tracking clues, for enhanced performance on the tracking of the LV surface throughout the cardiac cycle. Furthermore, it allows assessing the motion components tangential to the LV boundaries, which was a limitation of the existing segmentation algorithm. Lastly, the computational burden is low, pointing towards the feasibility of accurate real-time online tracking.

Chapter 4

Automatic Short Axis Orientation of the Left Ventricle in 3D Ultrasound Recordings

This chapter is based on a paper published in the proceedings of the *2016 SPIE Medical Imaging: Ultrasonic Imaging and Tomography*: **Pedrosa, J.**, Heyde, B., Heeren, L., Engvall, J., Zamorano, J., Papachristidis, A., Edvardsen, T., Claus, P. and D'hooge, J.; Automatic short axis orientation of the left ventricle in 3D ultrasound recordings. *2016 SPIE Medical Imaging proceedings*, Vol.9790, 9790E.

Abstract

The recent advent of real-time 3D echocardiography (RT3DE) has led to an increased interest from the scientific community in left ventricle (LV) segmentation frameworks for cardiac volume and function assessment. An automatic orientation of the segmented LV mesh is an important step to obtain a point-to-point correspondence between the mesh and the cardiac anatomy. Furthermore, this would allow for an automatic division of the LV into the standard 17 segments and, thus, fully automatic per-segment analysis, e.g. regional strain assessment. In this work, a method for fully automatic short axis (SAx) orientation of the segmented LV is presented. The proposed framework aims at detecting the inferior right ventricular (RV) insertion point. 211 RT3DE images were used to validate this framework by comparison to manual annotation of the inferior RV insertion point. A mean unsigned error of $8.05° \pm 18.50°$ was found, whereas the mean signed error was $1.09°$. Large deviations between the manual and automatic annotations ($> 30°$) only occurred in 3.79% of cases. The average computation time was 666ms in a non-optimized MATLAB environment, which allows for real-time application. In conclusion, a successful automatic real-time method for orientation of the segmented LV is proposed.

4.1 Introduction

LV segmentation has become an essential task in cardiovascular medicine for cardiac volume and function assessment. The recent advent of RT3DE has made this modality especially promising for clinical practice and attracted the attention of the scientific community for the development of segmentation frameworks [76]. Nevertheless, to take full advantage of the information obtained from LV segmentation, an orientation of the segmented mesh is an essential step. This allows for a point-to-point correspondence between the mesh and the cardiac anatomy and, as such, makes an automatic division of the LV into its 17 segments possible. This is especially significant for the application of post-processing techniques such as regional strain assessment [185] or shape feature based statistical models [186].

While several approaches for LV long axis (LAx) orientation have been proposed in literature, little attention has been given to SAx orientation of the LV and approaches looking beyond LAx orientation tend to focus only on the detection of the standard view planes (i.e. 2-, 3- and 4-chamber views). [100, 187–189] Though this is a similar problem, these methods do not give a precise SAx orientation as the standard view planes are quite loosely defined within an interval.

As such, a method for fully automatic real-time SAx orientation of the LV is proposed in the present work. The proposed method relies on a prior LV segmentation, which is performed using the B-spline Explicit Active Surfaces (BEAS) framework [3]. The SAx orientation itself depends on the detection of the inferior RV insertion using both image intensity and structural information.

4.2 Methodology

The automatic LAx orientation and LV initialization and segmentation were performed according to the method of Barbosa et al. [165] as detailed in Section 2.6.

4.2.1 Short Axis Orientation

Due to the near cylindrical symmetry of the LV, SAx orientation cannot rely on the LV shape but must rely on the detection of particular landmarks such as the RV and its insertion points, the aortic valve (AV) or the papillary muscles. From these, the inferior RV insertion point is especially promising as it can be seen even in lower quality images and can be found throughout the longitudinal extension of the LV, making its detection less susceptible to artifacts. As such, the inferior RV insertion point was selected as the preferred landmark for the SAx orientation framework proposed.

The proposed framework can be divided into two modules. The first consists of the extraction of the image intensity information around the LV to detect candidates for the insertion point. The second uses the Hough transform for circles (HTc) as in the initialization to locate the RV and right atrium (RA) around the LV. The results from the two modules are then joined to choose a final candidate. A schematic diagram of this SAx orientation framework is shown in Figure 4.1.

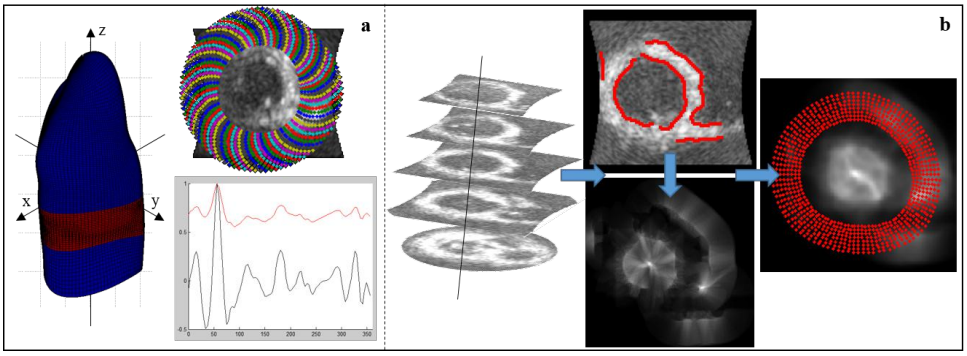

Figure 4.1: Schematic diagram of the SAx orientation framework. (a) Image intensity profile extraction: The region of interest (ROI) from the segmented LV mesh is selected (shown in red) and the intensity outside the LV is extracted in several C-planes along the individually colored curves shown. The intensities are then averaged to obtain a single circumferential intensity profile (red) and its associated Laplacian (black). (b) Structure information extraction using HTc: Equally spaced C-planes along the LAx are selected and edge detection is performed in each plane, followed by HTc. Alignment according to the LAx gives an averaged HTc from which the intensity is extracted (red points) to then obtain a circumferential HTc profile.

The extraction of the image intensity takes advantage of the BEAS structure

from the segmentation, namely the spherical domain distribution of points along the surface and the surface normals at each point. As such, the intensity outside the surface is extracted. However, as shown in the C-planes in Figure 4.1, the RV is naturally curved towards the septal side, resembling a sail. As such, instead of extracting the intensity along the normals, the intensity is extracted along a curve as shown in Figure 4.1. This allows to adapt to the curvature of the RV "sail" thus allowing to pinpoint the RV insertion point more precisely and avoid a bias towards the septal side. The intensity information extracted was limited to a radial distance of 10-40mm from the endocardium and to the region at one third of the distance from the base to the apex. This allows to focus on the LV region where the RV insertion is most visible and avoid the complexity of the basal region. The extracted intensity values are then averaged in the radial and azimuthal directions to obtain a circumferential profile of the intensities outside the LV. Finally, a Laplacian filter is used to highlight the intensity peaks from the background.

The structural information module is inspired on the LV initialization framework proposed by Barbosa et al. [165] and detailed in Section 2.6. Similarly to the LAx alignment framework, the HTc is used to retrieve information from pre-processed C-planes. However, the HTc radius interval is now set to [8,25]mm to limit the response to other anatomical structures, namely the RV and RA. Since in most images only part of the RV is visible, the lower radius in the interval will allow to get a response even from the RV "sail". This module operates thus from the LV mid-cavity to 35mm below the base to be able to retrieve information from both the RV and RA. The LAx is then used to align the different C-planes and, as for the intensity information, the HTc probabilities are averaged in the radial and azimuthal direction to obtain a circumferential profile.

Finally, the information from both circumferential profiles is used to select the RV insertion point. From the normalized HTc profile, the peaks above a threshold of 0.6 are considered as candidates for the RV/RA cavities. For each HTc peak, the maximum intensity peak within an interval of 10° to 55° towards the inferior side is considered as an RV insertion point candidate. The pair of HTc and intensity peaks with the maximum summed value is then selected as the RV insertion point. Figure 4.2 shows an example of HTc and intensity profiles and the respective RV insertion candidates.

4.3 Experiments

With the purpose of validating the proposed methodology, 211 real-time RT3DE exams were randomly selected from a large multi-center clinical study, DOPPLER-CIP [190], which was aimed at patients whose profile corresponds to suspected chronic ischemic heart disease. The datasets used in this study were collected in five centers across Europe. From the 211 datasets, 129 were acquired using a GE Vivid E9 scanner and the remaining 82 were acquired with a Philips iE33 or EPIQ 7C scanner. In each image, an expert annotated the inferior RV insertion point at one third of the distance from the base to the apex after BEAS segmenta-

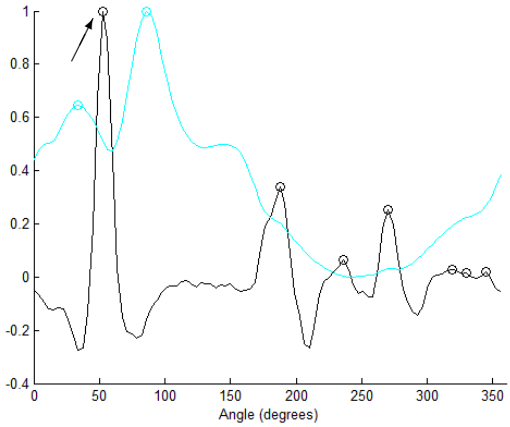

Figure 4.2: Laplacian of intensity (black) and HTc (cyan) profile example. Candidate peaks are marked by circles and the chosen peak is indicated by the arrow. X-axis represents angle in degrees relative to image x-axis.

tion using an in-house developed software package (Speqle3D, KU Leuven).

The angle between the manual and automatic annotations of the RV insertion point was measured to validate the proposed framework. A positive angle represents a deviation towards the inferior side from the manual annotation. One sample t-test was used to find the statistical significance of the results.

4.4 Results

Figure 4.3 shows the comparison between manual and automatic annotation of the inferior RV insertion for SAx orientation. The mean unsigned error was $8.05° \pm 18.50°$ and deviations from the manual annotation larger than 30° only occurred in 3.79% (8) of the cases. Figure 4.4 shows the best and worst results comparing the manual and automatic orientation. The average computation time was of 666ms.

4.5 Discussion

Analyzing the results shown in Figure 4.3, it is clear that the proposed algorithm is successful at finding the RV insertion point without significant bias. Furthermore, the mean unsigned error is small in comparison to the 60° width of the segments in the 17-segment model and deviations larger than half the segments' width only occur on a small percentage of the data.

The image quality of the datasets in the DOPPLER-CIP database is evident in Figure 4.4. Because this database is acquired using a protocol as close as possible

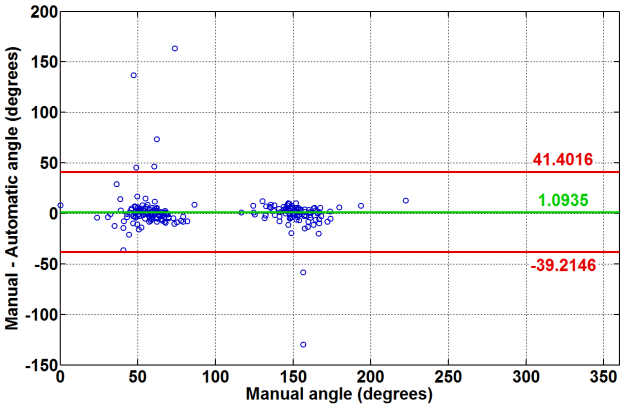

Figure 4.3: Bland-Altman plot comparing manual and automatic annotation of SAx orientation (green: bias (*, $p < 0.05$), red: limits of agreement ($\mu \pm 1.96\sigma$). Absolute manual angles were computed in comparison to the image x-axis.

to clinical practice and with multiple vendors, operators and in different centers, the datasets found are very close to clinical reality. This makes the results shown in Figure 4.3 even more significant as they reflect what is expected in clinical practice.

Looking at each of the cases in Figure 4.4, it becomes clear that even within the four best cases there are images of low quality and even significant artifacts as in the third case. When looking at the four worst cases, it is clear that, in the first case, the RV insertion point is outside the image sector, thus making any detection impossible. For the remaining cases, it seems that other artifacts caused the large deviations observed. Nevertheless, these large deviations only occurred in 3.79% (8) of the cases, in spite of the challenging database presented here. Furthermore, this low image quality is challenging not only for the orientation but also for the automatic segmentation done previously, which will negatively influence the orientation framework.

The strength of this method lies in its simplicity, as it relies on a single reliable landmark. This becomes, however, the very limitation of the method, as it depends too much on one landmark. The knowledge of additional landmarks such as the LV outflow tract (LVOT) could help when the information from the RV insertion point is not clear. Nevertheless, the extraction of reliable information of additional landmarks is challenging, especially when image quality is lower. One possible approach would then be to use a machine learning approach and extract all possible shape and landmark cues to find the SAx orientation.

Regarding the computation time, it can be observed that this approach would allow for a real-time application as an optimized version in a dedicated system would reduce the computation time and, furthermore, part of the structural information module overlaps the initialization needed for BEAS and would not need to be recomputed.

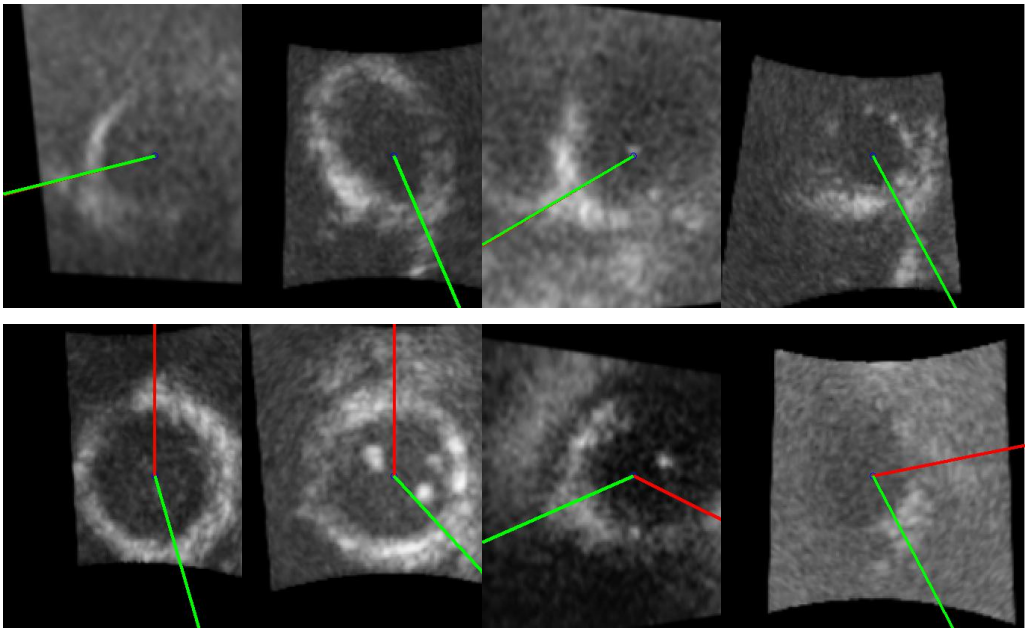

Figure 4.4: Four best (top row) and worst (bottom row) results obtained with automatic SAx orientation (red) compared to manual annotation by expert (green). The planes shown are orthogonal to the LAx and at one third of the distance from the base to the apex.

4.6 Conclusions

In conclusion, the proposed approach is able to perform automatic real-time orientation of a segmented LV mesh by accurately detecting the inferior RV insertion point. The proposed method is applicable to images even with low image quality acquired in a clinical setting. This is due to the simple approach depending on a reliable landmark, the inferior RV insertion point.

Chapter 5

Fast and Fully Automatic Left Ventricular Segmentation and Tracking in Echocardiography Using Shape-Based B-Spline Explicit Active Surfaces

This chapter is based on a paper published in *IEEE Transactions on Medical Imaging*: **Pedrosa J.**, Queirós S., Bernard O., Engvall J., Edvardsen T., Nagel E., D'hooge J.. Fast and Fully Automatic Left Ventricular Segmentation and Tracking in Echocardiography Using Shape-Based B-Spline Explicit Active Surfaces. *IEEE Transactions on Medical Imaging* 2017 Nov;36(11):2287-96.

Abstract

Cardiac volume/function assessment remains a critical step in daily cardiology and 3D ultrasound plays an increasingly important role. Fully automatic left ventricle (LV) segmentation is, however, a challenging task due to the artifacts and low contrast-to-noise ratio of ultrasound imaging. In this chapter, a fast and fully automatic framework for full cycle endocardial LV segmentation is proposed. This approach couples the advantages of the B-spline Explicit Active Surface (BEAS) framework, a purely image information approach, to those of statistical shape models (SSM) to give prior information about the expected shape for an accurate segmentation. The segmentation is propagated throughout the heart cycle using a localized anatomical affine optical flow (lAAOF). It is shown that this approach not only outperforms other state-of-the-art methods in terms of distance metrics with mean absolute distance (MAD) of 1.81 ± 0.59 mm and 1.98 ± 0.66 mm at end diastole (ED) and end systole (ES) respectively but is computationally efficient (in average 11 seconds per 4D image) and fully automatic.

5.1 Introduction

Analysis of cardiac function, and specifically of LV function, is an important part of clinical cardiology for patient management, disease diagnosis, risk stratification or therapy selection [5–7]. Among the different cardiac imaging modalities, real-time 3D echocardiography (RT3DE) stands out as a low-cost, portable, risk-free and non-invasive technique with good space and time resolution. However, RT3DE poses several challenges due to its low contrast-to-noise ratio, the presence of artifacts and the dependence on the acquisition conditions [76].

In spite of the challenges presented, numerous approaches have been proposed for automatic or semi-automatic chamber assessment in RT3DE, both in the research community and in the form of commercial solutions as can be appreciated in Chapter 2. LV endocardial segmentation has been particularly well studied and a number of approaches have been proposed as can be appreciated in the review of Leung and Bosch [76]. This is especially true when compared to other chambers such as the right ventricle (RV) and left atrium (LA) which have received significantly less attention though some methods have been proposed [191, 192]. Given the different frameworks proposed for the same problem of LV segmentation, initiatives such as the CETUS challenge [114] play an extremely important role in allowing the benchmarking of different frameworks [115, 116, 193–195] on the same datasets using the same evaluation tools. Though the highest ranked solution of the challenge was a purely image information approach by Barbosa et al. [115] using the BEAS framework, later approaches using shape and/or appearance clues proved to be more successful. Such approaches by Oktay et al. [196] and van Stralen et al. [197] came to prove the pre-existing idea that RT3DE is inherently challenging to segment due to its many artifacts and that prior information is key to an accurate segmentation. Nevertheless, the gap between state-of-the-art technologies and

interobserver variability is still present and, as such, new approaches joining the advantages of successful basic segmentation frameworks such as BEAS with tools that provide prior information about the LV are of much interest.

In the present work, a framework for fast and fully automatic segmentation and tracking of the LV in RT3DE is proposed. A shape-based deformable model based on the BEAS framework [3] using a SSM as in Queirós et al. [198] is used for segmentation at ED. This assures that both image information and shape-based clues are used, thus increasing the robustness of this approach when compared to BEAS or other methods based solely on image information. This segmentation is then propagated to the rest of the cardiac cycle using lAAOF [199]. To further refine the results from the lAAOF, the shape-based BEAS framework is applied at ES, again allowing for the combination of both image information and shape-based clues for the final segmentation result.

The main novelty of the presented study lies in the algorithmic design and validation of the proposed method. Joining different and independent algorithmic tools, the authors were able to build a single efficient framework capable of performing fast, fully automatic and robust full-cycle segmentation and validate it in a representative dataset that allows direct comparison to other state-of-the-art methods. Furthermore, the shape-based regularization introduced in [198] was extended in this study, from the original formulation based on a 1D SSM of Queirós et al. which would not be applicable to the LV to a full 2D oriented SSM.

5.2 Methodology

5.2.1 B-spline Explicit Active Surfaces

Given the volumetric nature of the object of interest, the B-spline representation was created on a spherical coordinate system thus defining the active geometric functions as $r = \psi(\phi, \theta)$. As in previous implementations of BEAS for LV segmentation [165], the angular discretization of the boundary representation was set empirically at 24×16 (elevation×azimuth) and the B-spline scale to 2^1 for both angular coordinates.

The evolution of the model is defined by the minimization of an energy criterion E. This energy is expressed by the sum of the data attachment term E_d and a regularization term E_r:

$$E = E_d + E_r. \tag{5.1}$$

The data attachment energy function E_d follows a variation of the localized Yezzi energy adapted for endocardial segmentation [165] detailed in Section 2.6. The neighborhood region limit ρ was set to 16 mm as in Barbosa et al. [115].

5.2.2 Statistical Shape Model

5.2.2.1 Data Preprocessing

In order to provide accurate shape information to the proposed shape-based approach, a sufficiently broad and numerous dataset of 3D LV shapes is needed. For that purpose, a broad dataset of cardiac magnetic resonance imaging (cMRI) was gathered. cMRI has excellent spatial and temporal resolution but has the drawback of artifacts (in particular slice misalignment) due to unequal breath holds. Though this does not pose a problem for a typical cMRI analysis that uses a sum-of-disks approach to measure volumes, it does raise concerns when building 3D shapes. The correction of slice misalignment in cMRI has been previously studied by different authors [200–204]. Though using different methodologies, these methods are based on the use of image information on the points of intersection between the different slices to guide the alignment. This is however a relatively complex approach and it can be problematic as the comparison of image intensities between long axis (LAx) and short axis (SAx) slices often shows marked differences. Moreover, implementations of these methods were not freely available. As such, the method used is based on the 3D alignment of the contours using an iterative closest point (ICP) strategy [205].

The dataset used to collect 3D LV shapes is composed of 318 cMRI datasets from a large multi-center clinical study, DOPPLER-CIP [190]. This study was aimed at patients whose profile corresponds to suspected chronic ischemic disease and thus encompasses patients of a broad clinical spectrum. For each case, the endo- and epicardial borders on both SAx and LAx slices were contoured by experts at ED and ES. The mitral annulus (MA) points were annotated on the LAx slices at ED and ES in order to obtain the basal plane. An example of the LV contours at ED on SAx and LAx slices and their misalignment is shown in Figure 5.1 (a) and (b).

Due to the fact that in the acquisition protocol used, the LAx sequences were taken subsequently in the beginning of the acquisition, the misalignments between them were limited and were thus assumed to be negligible. In this way, the SAx

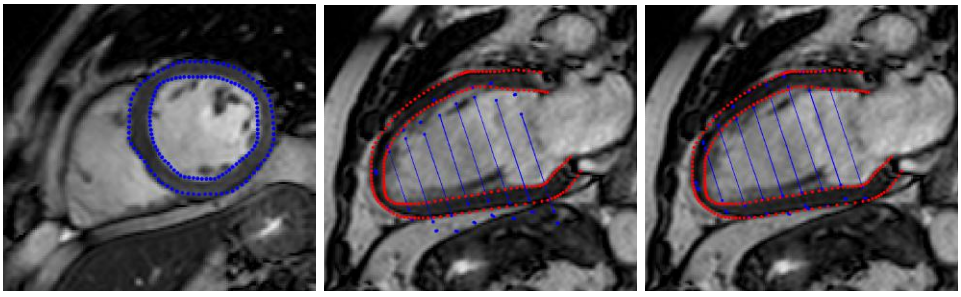

(a) (b) (c)

Figure 5.1: Example of endo- and epicardial contours for cMRI dataset. (a) SAx contours; (b) LAx contours (red) and intersection of the original SAx contours (blue); (c) LAx contours (red) and intersection of the aligned SAx contours (blue).

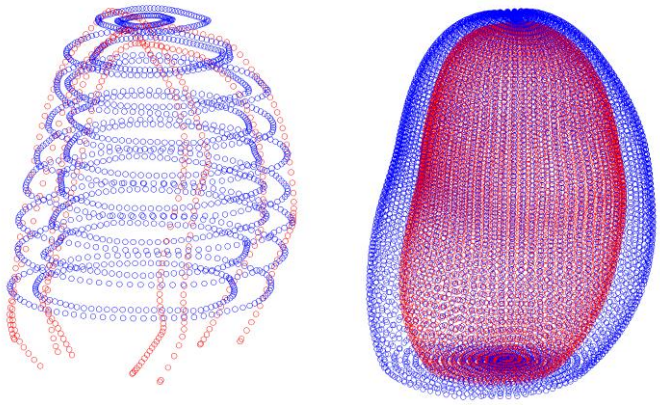

(a) (b)

Figure 5.2: Example of aligned endo- and epicardial contours in 3D (a) and corresponding mesh (b).

slices could be aligned with respect to the LAx contours. Each SAx slice was allowed to move independently in-plane but out-of-plane movement was restricted so that it would be applied to all slices equally. In this way, overfitting of the contours was avoided. Figure 5.1 (c) shows an example of the intersection of the SAx contours with an LAx slice after ICP alignment. After alignment of all cases, a total of 29 cases were excluded, either because there were insufficient LAx slices (less than two) or because the available LAx slices were found to be misaligned and could thus not be used as a reference for the SAx.

After correction of the misalignment between slices, the 2D contours were used to create a 3D mesh of the endo- and epicardial surfaces. This mesh was created using the BEAS framework [3] by considering the contour points as attractors to guide the surface [206]. The angular discretization of the surface representation was set empirically at 24×24 and the B-spline scale to 2^2 as this was found to give the best balance between a smooth surface and an accurate representation of the contours being meshed. Figure 5.2 shows an example of the aligned endo- and epicardial contours in 3D and the mesh obtained from these contours.

5.2.2.2 Statistical Shape Model Construction

As in the work of Queirós et al. [198], the SSM was built in the BEAS coordinate system; in this case in spherical coordinates. The SSM shapes are then represented by their B-spline representation coefficients $c[\mathbf{k}]$. Because such a representation assumes that the position and orientation of the coordinate system is identical for every shape, the position and orientation of the training shapes have to be aligned, which can be done according to the centroid and direction of largest variance of each shape.

Starting from the aligned 3D LV shapes in BEAS space, the first step to build

the SSM is to scale all shapes so that equivalent points from different shapes can be compared without the influence of the LV size. Considering $c_s[\mathbf{k}]$ the s^{th} shape of all N shapes, this is done by: calculating the mean of all shapes $\bar{c}[\mathbf{k}] = \frac{1}{N}\sum_{s=1}^{N} c_s[\mathbf{k}]$, scaling each shape to the current mean $\bar{c}[\mathbf{k}]$ and then repeating these steps until the process converges [207]. The scaling step is done according to:

$$c_{scaled}[\mathbf{k}] = c[\mathbf{k}]\frac{\sum\limits_{i} w[\mathbf{k}_i]\bar{c}[\mathbf{k}_i]c[\mathbf{k}_i]}{\sum\limits_{i} w[\mathbf{k}_i]c[\mathbf{k}_i]c[\mathbf{k}_i]}, \tag{5.2}$$

where $w[\mathbf{k}]$ is a set of weights chosen to give more significance to the points that tend to be most stable:

$$w[\mathbf{k}_i] = \left(\sum_{s=1}^{N} Variance(c_s[\mathbf{k}_i])\right)^{-1}. \tag{5.3}$$

Principal component analysis can then be applied to extract the shape variability of the LV B-spline coefficients [207]. Through singular value decomposition [208], it is then possible to obtain the eigenvectors $\mathbf{p}_i$ and the corresponding eigenvalues λ_i of the covariance matrix:

$$\mathbf{S} = \frac{1}{N}\sum_{s}^{N} \left(c_s[\mathbf{k}_i] - \bar{c}[\mathbf{k}_i]\right)\left(c_s[\mathbf{k}_i] - \bar{c}[\mathbf{k}_i]\right)^T. \tag{5.4}$$

Since most of the variation can be explained by a small number of eigenvectors, only a portion of the original set is kept, corresponding to the number of eigenvectors t whose sum represents 90% of the total variance of all variables. In this way, any shape from the dataset can be approximated by:

$$c[\mathbf{k}] \approx \bar{c}[\mathbf{k}] + \mathbf{P}\mathbf{b}, \tag{5.5}$$

where $\mathbf{P}$ is the matrix of the first t eigenvectors and $\mathbf{b}$ is a vector of t weights which for any given shape corresponds to $\mathbf{b} = \mathbf{P}^T\left(c[\mathbf{k}] - \bar{c}[\mathbf{k}]\right)$.

To be able to model both ED and ES separately, two different SSMs were created according to the methodology described above. The mean shapes for each of these models are shown in Figure 5.3. Note that since these models are scaled according to equation 5.2 only shape variations can be observed in this figure. Additional description of each of the SSMs, namely the shape variations described by each component, are provided in the link given in the footnote.

5.2.3 SSM-Based Regularization

To then use the SSM with BEAS for the segmentation of new images, two different regularization energies were defined so that the segmented shapes are regularized according to those observed in the training set. These two regularizations, a hard

https://kuleuven.box.com/s/bii3yf4o5v4rz3295ua6ctyijjokzy1k

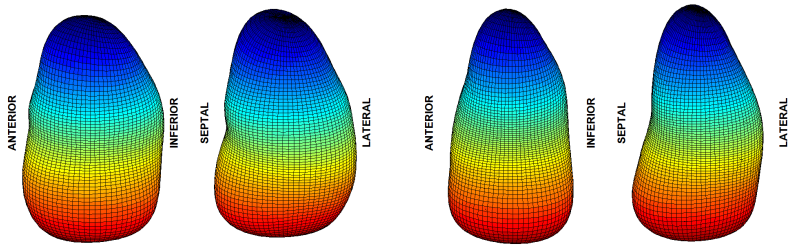

(a) (b)

Figure 5.3: SSM mean models at ED (a) and ES (b).

and a soft SSM-based regularization, were first proposed by Queirós et al. [198]. In the present study, those regularization energies were adapted to regularize the B-spline coefficients $c[\mathbf{k}]$ of a 3D shape.

The hard SSM-based regularization restricts the segmented shape to the shape variability observed in the training set. At each iteration, the weights $\mathbf{b}$ are computed and each is restricted to $\pm m\sqrt{\lambda_i}$, where m defines the limits to the variability from the mean [207]. m is typically set between 2 and 3 since most of the population lies within three standard deviations and was set at 2.5 in this study. Through equation 5.5, a new regularized shape $c_{reg}[\mathbf{k}]$ is then obtained [198]. To include this hard SSM-based term in the BEAS framework, the energy functional can be defined as:

$$E_{hard} = \int_{\Gamma} \frac{1}{2}(c[\mathbf{k}] - c_{reg}[\mathbf{k}])^2 d\mathbf{x}^*. \tag{5.6}$$

The minimization of this energy according to the B-spline coefficients gives:

$$\frac{\partial E_{hard}}{\partial c[\mathbf{k}]} = \int_{\Gamma} (c[\mathbf{k}] - c_{reg}[\mathbf{k}]) d\mathbf{x}^*. \tag{5.7}$$

The soft SSM-based regularization follows the rationale that it is much more probable to find an average shape than a shape which is close to the variability limits. In that way, the soft SSM-based regularization penalizes high values of b_i and is defined as the squared Mahalanobis distance to the training shapes [207], thus:

$$E_{soft} = \sum_{i=1}^{t} \frac{b_i^2}{\lambda_i} = \int_{\Gamma} (c[\mathbf{k}] - \bar{c}[\mathbf{k}])^T \mathbf{S}^{-1} (c[\mathbf{k}] - \bar{c}[\mathbf{k}])\, d\mathbf{x}^*. \tag{5.8}$$

Following the derivation shown in Queirós et al. [198], the minimization of E_{soft} gives:

$$\frac{\partial E_{soft}}{\partial c[\mathbf{k}]} = \int_{\Gamma} 2\mathbf{P}\mathbf{D}^{-1}\mathbf{b}\, d\mathbf{x}^*, \tag{5.9}$$

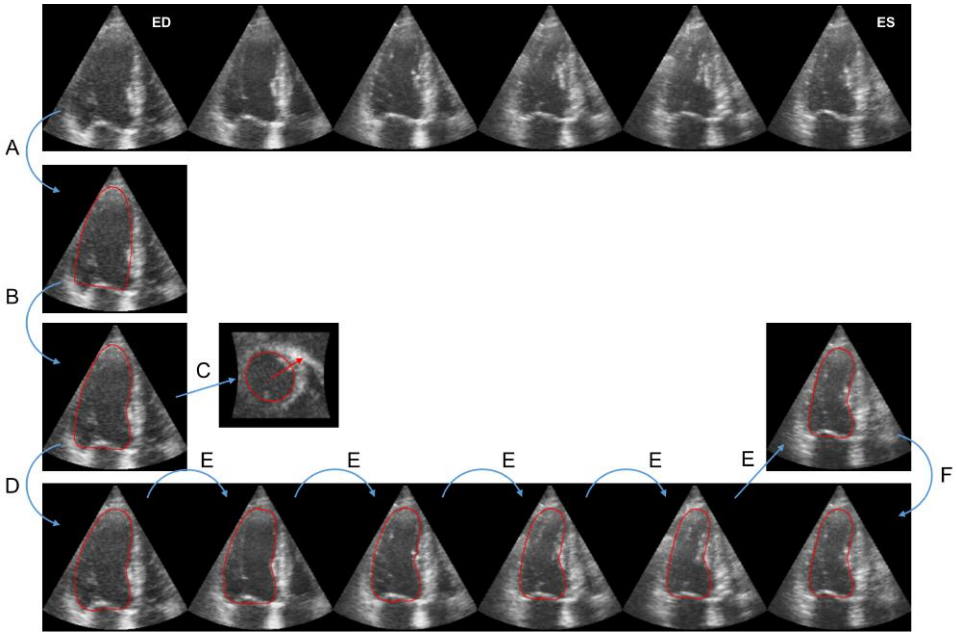

Figure 5.4: Conceptual description of the proposed segmentation and tracking framework. First, automatic initialization is applied to the ED frame (A). The first stage of segmentation is then performed using BEAS (B). The result from this segmentation is used to detect the SAx orientation (C) and this information is then used to perform the second stage of segmentation using BEAS and the ED SSM (D). The final ED segmentation is then propagated frame to frame using the lAAOF (E) and a final refinement to the ES frame is performed using BEAS and the ES SSM (F).

where $\mathbf{D}$ is the diagonal matrix of t eigenvalues λ.

To incorporate these two energies into BEAS, the regularization term E_r is defined as:

$$E_r = \alpha E_{hard} + \beta E_{soft}, \tag{5.10}$$

where α and β are hyperparameters controlling the relative weight between the two terms.

5.2.4 Framework Description

A conceptual description of the proposed framework is shown in Figure 5.4.

5.2.4.1 Automatic Initialization

The automatic initialization algorithm used was first introduced in Barbosa et al. [165] and is detailed in Chapter 2. This initialization will provide the initial estimation of the LAx and center for BEAS and the SSM.

5.2.4.2 Automatic SAx Orientation

The SAx orientation method is detailed on Chapter 4.

The SAx orientation is crucial to correctly position the SSM, given that different sides of the LV have different shape characteristics. However, this orientation algorithm depends on a previous estimate of the LV surface and the result from the initialization is too rough as it relies on the fitting of an ellipsoid. As such, the automatic SAx orientation is only applied after an initial stage of segmentation with BEAS.

5.2.4.3 Segmentation at ED

The segmentation at ED is composed of two stages. Initially, BEAS is used without the SSM, so that the energy criterion E is equal to E_d, the data attachment term. This provides an initial segmentation of the LV, which is used for the SAx orientation estimation but also to refine the initial estimates of LAx orientation and center according to the centroid and direction of largest variance of the segmented mesh. With the center position and both the LAx and SAx orientation well defined, it is then possible to use BEAS with the SSM regularization according to equation 5.10 to further refine the segmentation.

5.2.4.4 Localized Anatomical Affine Optical Flow (lAAOF)

lAAOF is then used to propagate the result from ED to the remaining frames. The lAAOF method was proposed in [199] and relies on an affine optical flow approach which independently estimates the motion at each point in the surface based on an anatomically constrained neighborhood. A detailed description of this method can be found in the original paper by Queirós et al. [199]. The parameters used to tune the lAAOF were replicated from [199].

5.2.4.5 Segmentation at ES

Segmentation at ES is used to further refine the result from the lAAOF, thus bringing together intensity and shape-based clues. In order to balance the contribution between tracking and segmentation clues, an energy term was added to penalize the deviation between the result of the lAAOF and the segmentation. Such an approach is equivalent to that detailed in Chapter 3. The regularization energy

criterion is then expressed as:

$$E_r = \alpha E_{hard} + \beta E_{soft} + \gamma E_A, \tag{5.11}$$

where E_A is defined according to 3.11 and γ is a hyperparameter used to define the balance between tracking and intensity/shape-based information.

5.3 Experiments

5.3.1 Data Description

The proposed framework was tested on the CETUS challenge data [114]. This challenge comprises 45 sequences of RT3DE volumes of one cardiac cycle from 45 patients acquired in three different hospitals and ultrasound machines from three different vendors. On each dataset, the LV endocardium was contoured by three experts at ED and ES until consensus was achieved between the three. Fifteen datasets are available as training with the corresponding reference meshes at ED and ES, while the remaining 30 datasets correspond to the testing set and only the RT3DE images are available.

5.3.2 Segmentation Performance

First, the 15 training datasets were used to tune the hyperparameters β and γ needed respectively for the SSM regularization and for the balance between the segmentation and tracking information. This tuning was performed empirically by visual inspection of the results. The hyperparameters α, β and γ were set respectively to 1, 0.0005 and 0.25. Note that the value of β is directly related to the absolute value of eigenvalues λ as defined in (5.8), thus justifying its relative small value.

Using these settings, the framework was then tested on the 30 testing datasets. The evaluation of the results was conducted using the online MIDAS platform of the CETUS challenge, thus assuring that the proposed method can be directly compared to other state-of-the-art methods. The accuracy of the segmentation was evaluated at ED and ES through different distance metrics: MAD [209], which measures the average distance at any point between the segmented and reference meshes; Hausdorff distance (HD) [210], which measures the maximum distance between the segmented and reference meshes; and Dice [211], which is a measure of the overlap between the segmented and reference meshes. Because the meshes obtained from BEAS are sampled in the spherical coordinate system, causing the point density to be different along the surface, which could bias the error metrics to specific regions, the segmented meshes were remeshed to assure greater smoothness and more uniform mesh point density. Clinical indices were also studied, namely the Pearson correlation coefficient and limits of agreement of ED volume (EDV), ES volume (ESV) and ejection fraction (EF).

Mean computational times of the proposed framework were also obtained using MATLAB code running on an Intel® Xeon® E5-1650v2@3.5GHz with 32GB RAM.

5.3.3 Position/Orientation Performance and Sensitivity

Because the characteristics of the SSM are closely related to the position and orientation (LAx and SAx) of the BEAS coordinate system, it is important to determine the error in the estimation of these parameters. For that purpose, the position, LAx orientation and SAx orientation of the CETUS training set reference meshes were compared to those obtained with the proposed method.

Furthermore, the sensitivity of the segmentation results to variations of these parameters was studied. This was performed by introducing variations from the reference position or orientation on each of these parameters and evaluating the segmentation performance. In this way, to evaluate, for example, the sensitivity to the position, BEAS was initialized at a random position at a distance D from the reference mesh position and with the reference SAx and LAx orientation. The segmentation result was then evaluated on MAD, HD and Dice. To prevent sporadic results from this random positioning, each image was started from three different random positions each time and the results averaged.

5.3.4 Parameter Sensitivity Assessment

To study the robustness and stability of the proposed framework with respect to the multiple parameters involved, a parameter sensitivity assessment was conducted. As such, the balance of the different energies, namely α, β and γ, was studied. Each parameter was varied from their empirically determined preset by 50% of its value and its impact studied in terms of MAD, HD and Dice. To further analyse the contribution of each component of the framework, the segmentation performance was analysed when each of these energy parameters was set to zero. To highlight the importance of the lAAOF, the segmentation performance of the framework without the lAAOF was also studied by using the ED segmentation result for initialization of the ES segmentation.

5.3.5 Statistical Analysis

Paired t-tests were used to analyse the significance of differences between the proposed method and other methods in literature and to analyse the parameter sensitivity of the proposed method. Results are denoted as mean ± standard deviation.

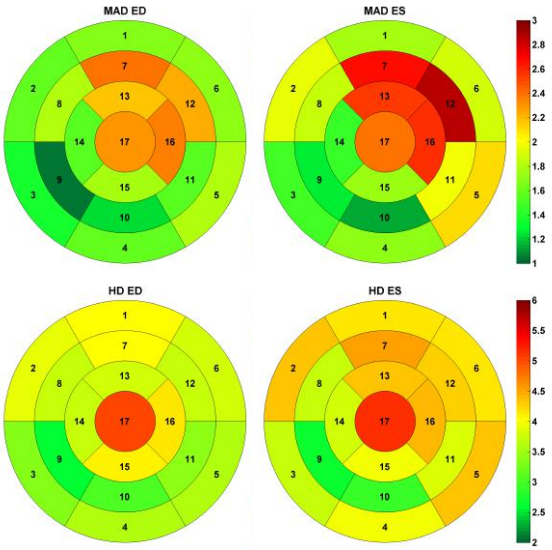

Figure 5.5: Bullseye plots of average MAD and HD at every region for ED and ES for the training datasets. Measures in mm.

5.4 Results

5.4.1 Segmentation Performance

Tables 5.1 and 5.2 show the segmentation and tracking results for the proposed approach, as well as the performance obtained with other state-of-the-art methods and inter-observer variability from manual contouring. Those obtained by Queirós et al. [199] and Barbosa et al. [115] also use BEAS as the segmentation tool but neither use shape-based information. Queirós et al. used the same lAAOF tracking whereas Barbosa et al. used a global anatomically constrained optical flow approach followed by block matching refinement instead of the lAAOF. The other approaches presented were chosen as they are, to the author's knowledge, the ones presenting the best segmentation results on the CETUS dataset.

A regionwise analysis of error was also conducted by dividing the LV into the 17-segment model [10], using the LAx as reference and dividing the LV into basal (35%), mid-cavity (35%) and apical (30%) regions. The average MAD and HD at ED and ES for the training datasets is shown in Figure 5.5. It can be observed that the greatest errors occur on the apical region and on the anterior side of the LV. Figure 5.6 shows examples of the fully automatic segmentation results compared to the consensus manual contours by experts.

Regarding computational time, the proposed framework took on average 0.9 s for the initialization, 0.6 s for the SAx orientation and a combined time of 1.1 s for the two stages of ED segmentation. The tracking took on average 0.8 s/frame and the final ES segmentation 0.4 s. The total time for a fully automatic ED/ES

segmentation was on average 11 s. All data was processed in a non-optimized MATLAB implementation.

5.4.2 Position/Orientation Performance and Sensitivity

At initialization, the position and LAx orientation errors were respectively 3.7 ± 2.1 mm and $5.0 \pm 2.8°$. After refinement at the first stage of ED BEAS segmentation, the position and LAx orientation errors were reduced to respectively 2.4 ± 1.0 mm and $4.4 \pm 2.4°$. Automatic SAx orientation failed in one of the cases due to low image quality giving an error of $120.2°$ compared to manual annotation of the RV insertion point. On the remaining datasets the SAx orientation error was $6.9 \pm 4.4°$.

Figure 5.7 shows the influence on the segmentation performance of the position and orientation of the automatically defined BEAS coordinate system with respect to the position and orientation of the reference meshes. It can be observed that the position and LAx orientation have the most influence on the segmentation results, where a distance above 2mm from the reference mesh centroid or an LAx angle deviation greater than $8°$ give an error larger than what was obtained with the fully automatic method used in this study.

5.4.3 Parameter Sensitivity Assessment

Figure 5.8 shows the influence of the parameters α, β and γ on the segmentation results at ED and ES. For the interval considered from 50% to 150% of the preset value, none of the observed changes were statistically significant at a $p < 0.01$ level and only the MAD at ES showed several statistically significant changes at a $p < 0.05$ level when changing β. When parameters β and γ are set to 0, the difference is statistically significant at a $p < 0.001$ level whereas for α the difference is not statistically significant. When removing the lAAOF, the ES segmentation presents an MAD, HD and Dice of 2.91 ± 1.08mm, 9.81 ± 2.92mm and 0.861 ± 0.054 respectively (all statistically significant at a $p < 0.001$ level).

5.5 Discussion

A fully automatic LV segmentation and tracking framework is proposed, combining the strengths of image information from BEAS and shape-based clues from an SSM for segmentation and lAAOF to perform tracking. The way in which the SSM is represented on the BEAS space, through the corresponding B-spline representation coefficients $c[\mathbf{k}]$, brings BEAS and the SSM closer together, avoiding steps such as conversion between the spherical and Cartesian coordinate systems and scaling/translation operations. It also avoids one of the fundamental problems with SSM, the point correspondence between different training shapes and with testing shapes. This approach assumes however that the position and orientation of the coordinate system is identical for every shape. For the training shapes, it is

trivial to match the position and orientation of every shape, making the previous assumption valid. When trying to fit the SSM to a new image, the center and both the LAx and SAx orientations have to be guessed from image features.

5.5.1 Segmentation Performance

From Table 5.1 it is clear that the proposed automatic method shows excellent segmentation and tracking performance and outperforms any other of the state-of-the-art approaches applied to the same database. Compared to other approaches using BEAS [115,199], the impact of the SSM regularization on ED segmentation is statistically significant. With a better starting point at ED for the lAAOF, together with the SSM regularization at ES, the ES segmentation results are also improved, thereby outperforming other state-of-the-art methods. While a hybrid segmentation and tracking framework as that proposed in Chapter 3 would be possible, the fact that a local rather than global deformation is used in this Chapter means that the complex deformation of the LV can be captured by the tracking alone and it was observed that no significant improvement in terms of segmentation accuracy was obtained from adding a hybrid segmentation and tracking method.

In comparison to other state-of-the-art approaches, it is difficult to say with certainty what is the reason behind the differences in performance given the different strategies used in each framework but the following possible reasons can be considered: regarding the semi-automatic method of Bernier et al. [193] using graph cuts, this method lacks a source of prior information needed to give an accurate segmentation when image information is low or incongruous. For both van Stralen et al. [166] and Oktay et al. [196] that information is provided, respectively, by an active appearance model (AAM) and a multi-atlas approach. However, both these approaches use ultrasound data as a prior which can be more variable than cMRI, especially for reduced datasets. Moreover, both these methods intend to model the appearance of the image, which can be particularly difficult due to the differences between vendors, bad acquisition window or the presence of artifacts. Regarding the clinical indices on Table 5.2, the proposed method has a performance similar to the remaining state-of-the-art methods.

Regarding the regionwise analysis shown in Figure 5.5, there could be two possible explanations for the regions with larger error: either there are inherent image characteristics that make segmentation more difficult or there are framework specific characteristics that cause these errors, such as a systematic error on the LAx detection. However, regionwise error analysis in different frameworks and on manual contouring by experts replicate this trend of larger errors at the apical and anterolateral regions [114], which points to inherent image characteristics that make the segmentation more difficult. Indeed, at the apex, image information is low due to noise in the near field, whereas for the anterolateral region, dropout in this region is common due to its position and proximity to lung tissue.

As for the computational speed, the proposed framework continues to be computationally efficient, especially if compared to other state-of-the-art approaches. Oktay et al. [196] reported an average time of 16min per image and Van Stralen et

al. [166] reported an average segmentation time of 15s in a C++ environment [213] to which the tracking time must be added (not reported). Furthermore, one can consider ways of decreasing the computational burden of the proposed method by changing to a more efficient implementation in C++, where it has been shown that 3D endocardial segmentation can be done using BEAS in approximately 12.5 ms [3].

5.5.2 Position/Orientation Performance and Sensitivity

As predicted, moving the position and orientation away from the reference has a strong impact on the performance. The fact that SAx orientation has a smaller effect than center position and LAx orientation can be explained by the fact that, though the LV is far from being symmetric, the shape differences between the different sides are much less pronounced than the shape difference between the apex and base of the LV or those resulting from representing the LV shape from a wrong position. As such, a compromise between the image information and the SSM can more easily be found for an incorrect SAx orientation than from an incorrect center position or LAx orientation.

Figure 5.7 also shows that one of the bottlenecks of this method is the positioning and orientation of the LV. It can be seen that when the reference position and orientation is used, the error decreases considerably (MAD: 1.38 mm; HD: 4.86 mm; Dice: 0.959). As such, it would be important, in future work, to focus on better automatic initialization methods that, ideally, would provide the true center of the LV and the LAx and SAx orientation. This would imply however to move away from the current initialization, which roughly delineates the LV using the Hough transform for circles (HTc), to more complex methodologies, possibly involving machine learning or other more abstract approaches.

5.5.3 Parameter Sensitivity Assessment

Overall, the parameter sensitivity assessment showed that the performance of the proposed method is not significantly impaired within a wide range of the parameter settings. The parameters related to the SSM regularization seem to have a higher impact as they control the balance between the image information and the SSM. The parameter related to the balance between segmentation and tracking has, as expected, no impact on ED segmentation since γ is not used at ED, and little impact on ES segmentation performance. When each of the parameters is set to zero, thus turning off the corresponding energy contribution, the performance contribution of each energy becomes clear and both β and γ are crucial for the results obtained. The contribution of α is, however, less pronounced. This is due to the fact that the soft energy term already penalizes shapes away from the mean shape, making it less likely for the segmented shape to deviate to the hard set limits at m=2.5. Nevertheless, it can be argued that the hard energy term is important to effectively limit the maximum deviation from the mean shape (if $\alpha = 1$) and in more challenging images where image artifacts could make it easier for the segmented shape to deviate from the mean.

Regarding the lAAOF, it is shown that it also plays an important role in following the endocardial surface from ED to ES to initialize the segmentation at ES, as the results without the lAAOF are significantly worse than the proposed method. Nevertheless, in spite of the fact that in this study the lAAOF was chosen to track the endocardial surface, other tracking methods could equally be applied in a straightforward manner and, if proven to be more effective in tracking the LV, could potentially improve the ES segmentation results further.

Though in this study only the parameters related to the balance of the different energies were studied, the performance of BEAS and the lAAOF also depend on different parameters. Nonetheless, these have been studied before [165,199] and the optimal settings found were used in this study.

5.5.4 Limitations and Future Work

In spite of the promising results shown in this paper, there are limitations which must be addressed in the future. First, as mentioned in Section 5.5.2, the positioning and orientation of the LV is a limiting factor of the accuracy of the proposed framework and its improvement would directly lead to better segmentation results. Secondly, the parameter tuning performed in this study was quite limited. While in this study only parameters β and γ were subject to parameter tuning, there are other parameters that could be further tuned and which were not directly addressed. Even though some of these have been tuned before on the same dataset such as the BEAS [115] and lAAOF [199] parameters, a tuning of all parameters together could prove beneficial, especially for the framework elements identified as crucial such as the initialization. Thirdly, in this study only the endocardial border was considered. Nevertheless, the epicardial border is also of importance to study clinical indices, such as LV mass, and is an essential step for automatic cardiac strain measurements through the definition of a region of interest (ROI). As such, it would be interesting to build an SSM that would describe both the endo- and epicardial borders so that the current framework could be applied for full myocardial segmentation. However, the validation of such a framework cannot be done with the CETUS challenge dataset, as no epicardial contours are provided and, to the author's knowledge, there are no other freely available and reliable datasets of RT3DE data with both endo- and epicardial manual contours.

The dataset used for the SSM must also be considered. First, it could be argued that the cMRI shapes used are not ideal as they are derived from 2D slices rather than from true 3D data. However, that would imply that replacing the current SSM by one built from true 3D data would only further improve the results as more accurate data would be embedded into the SSM. Secondly, the very population targeted by the study from where the shapes were obtained is not ideal. Given that DOPPLER-CIP targeted patients suspected of chronic ischemic disease, one cannot consider that the dataset used represents a normal population. However, as before, that would imply that replacing this population with a more representative one would only improve results as the SSM is more well suited for the purpose for which it is intended.

5.6 Conclusion

In this work, a novel fast and fully automatic LV segmentation and tracking framework based on shape-based BEAS and lAAOF is proposed. The proposed approach outperforms all other state-of-the-art methods for LV segmentation evaluated on the MICCAI CETUS challenge. Moreover, it outperforms other methods in terms of computational speed, being able to perform ED/ES segmentation and tracking in a few seconds in a non-optimized implementation. The main strengths of the proposed framework result from the combination of image and shape information through the balance of the image information from BEAS and the SSM regularization and the combination of tracking and segmentation clues for an efficient ES segmentation.

Table 5.1: Performance on the CETUS testing datasets. MAD, HD and Dice of the proposed framework, other state-of-the-art approaches and inter-observer variability. All values in mean ± standard deviation (*NR* stands for not reported). $\star$, † and ‡ indicate respectively that the difference to the proposed framework was statistically significant at a $p < 0.05$, $p < 0.01$ and $p < 0.001$ level. Note that for methods [193, 196, 197, 212] a comparison is not possible as the data is not publicly available.

Method	**MAD (mm)**		**HD (mm)**		**Dice**	
	ED	**ES**	**ED**	**ES**	**ED**	**ES**
Proposed	1.81 ± 0.59	1.98 ± 0.66	6.31 ± 1.69	6.95 ± 2.14	0.909 ± 0.034	0.875 ± 0.046
Queirós et al. [199]	$2.26 \pm 0.72^{\ddagger}$	$2.45 \pm 0.85^{\ddagger}$	$8.10 \pm 2.62^{\ddagger}$	$8.19 \pm 3.03^{\star}$	$0.894 \pm 0.040^{\ddagger}$	$0.861 \pm 0.054^{\star}$
Barbosa et al. [115]	$2.26 \pm 0.72^{\ddagger}$	$2.43 \pm 0.89^{\ddagger}$	$8.10 \pm 2.62^{\ddagger}$	$8.29 \pm 3.01^{\star}$	$0.894 \pm 0.040^{\ddagger}$	$0.856 \pm 0.056^{\ddagger}$
Bernier et al. [193]	$2.37 \pm NR$	$2.64 \pm NR$	$9.41 \pm NR$	$9.34 \pm NR$	$0.882 \pm NR$	$0.837 \pm NR$
van Stralen et al. [197]	$1.91 \pm NR$	$2.48 \pm NR$	$6.66 \pm NR$	$7.38 \pm NR$	$0.910 \pm NR$	$0.862 \pm NR$
Oktay et al. [196]	1.94 ± 0.55	2.23 ± 0.60	7.00 ± 1.99	7.53 ± 2.23	0.904 ± 0.02	0.874 ± 0.04
Inter-observer [212]	1.01 ± 0.30	1.01 ± 0.38	3.37 ± 0.87	3.30 ± 0.94	0.949 ± 0.15	0.938 ± 0.21

Table 5.2: Performance on the CETUS testing datasets. Pearson correlation coefficient (R) and limits of agreement (LOA) (mean ± standard deviation) in comparison to the reference cardiac indices (EDV, ESV and EF) of the proposed framework, other state-of-the-art approaches and inter-observer variability. Volumes obtained with the proposed method were not statistically significantly different at a $p<0.05$ level when compared to [115, 199]. Note that for methods [193, 196, 197, 212] a comparison is not possible as the data is not publicly available.

Method	**EDV (ml)**		**ESV (ml)**		**EF (%)**	
	R	**LOA**	**R**	**LOA**	**R**	**LOA**
Proposed	0.953	-3.29 ± 19.03	0.960	-4.84 ± 16.09	0.911	1.7 ± 5.18
Queirós et al. [199]	0.965	-4.99 ± 17.66	0.971	-5.83 ± 13.14	0.927	2.30 ± 4.20
Barbosa et al. [115]	0.965	-4.99 ± 17.66	0.967	-6.78 ± 13.86	0.889	2.88 ± 5.24
Bernier et al. [193]	0.979	2.74 ± 13.87	0.968	2.18 ± 13.73	0.811	0.05 ± 7.84
van Stralen et al. [197]	0.958	-4.86 ± 18.08	0.965	-15.39 ± 15.08	0.751	8.40 ± 7.72
Oktay et al. [196]	0.961	-4.14 ± 17.35	0.973	-3.47 ± 13.62	0.892	0.48 ± 5.50
Inter-observer Variability [212]	0.981	-0.64 ± 9.27	0.987	-0.50 ± 7.35	0.959	0.13 ± 3.10

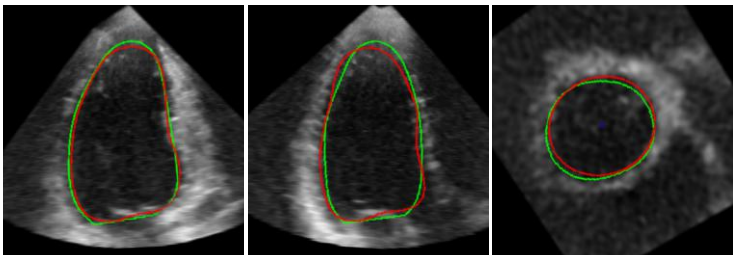

(a)

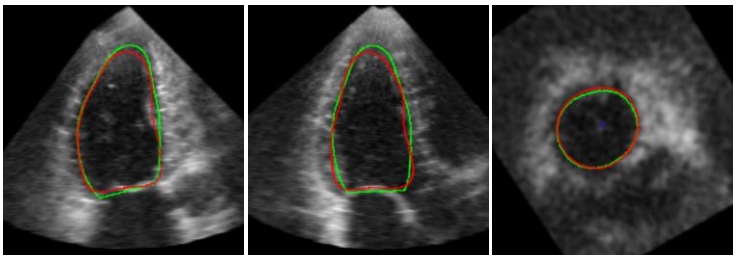

(b)

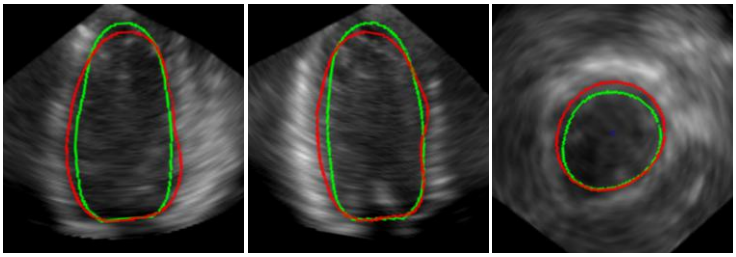

(c)

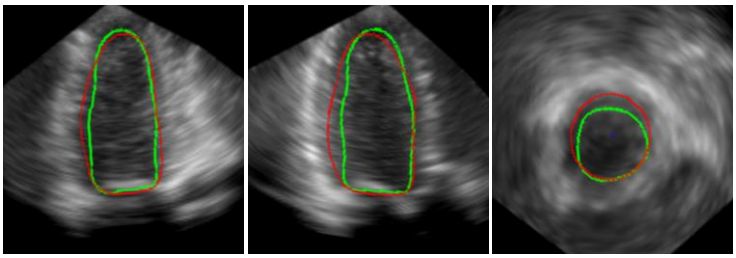

(d)

Figure 5.6: Best (a,b) and worst (c,d) automatic segmentation results (red) compared to manual contours by experts (green) at ED (a,c) and ES (b,d) from the CETUS training set. The three orthogonal planes shown for each 3D image were chosen according to the automatically defined LAx/SAx orientation.

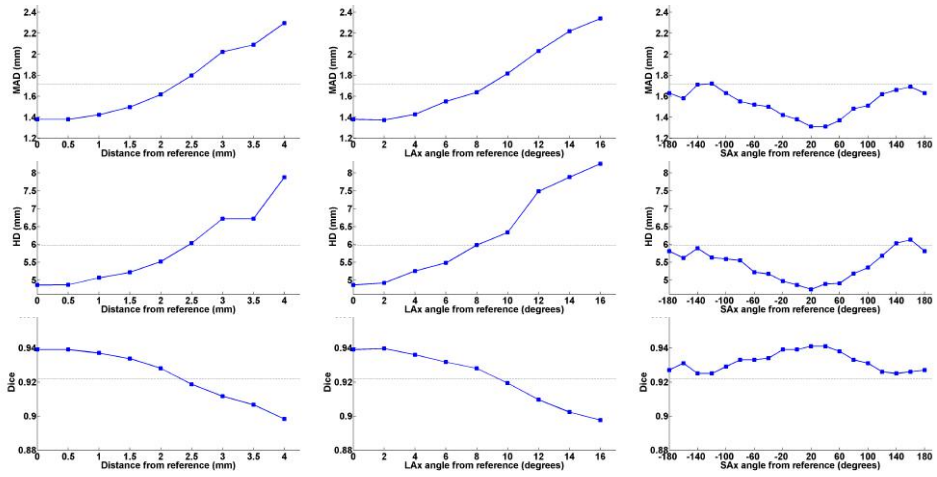

Figure 5.7: Influence of the distance and angle error from the reference position and orientation on the distance metrics (MAD, HD and Dice) at ED. Horizontal dotted line indicates the performance obtained with the proposed automatic framework on the CETUS training set.

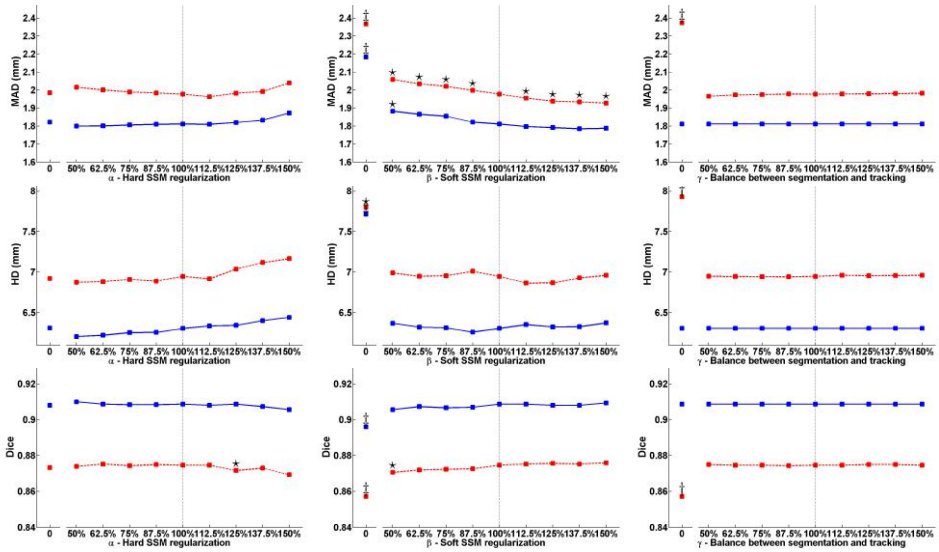

Figure 5.8: Influence of the variation of each of the considered parameters α, β and γ on the distance metrics (MAD, HD and Dice) at ED (blue) and ES (red dotted). Vertical dotted line indicates the preset parameter value. $\star$, † and ‡ indicate respectively that the difference to the result with the preset values was statistically significant at a $p < 0.05$, $p < 0.01$ and $p < 0.001$ level.

Chapter 6

Left Ventricular Myocardial Segmentation in 3D Ultrasound Recordings: Effect of Different Endocardial and Epicardial Coupling Strategies

This chapter is based on a paper published in *IEEE Transactions on Ultrasonics, Ferroelectrics, and Frequency Control*: **Pedrosa J.**, Barbosa D., Heyde B., Schnell F., Rösner A., Claus P., D'hooge J.. Left ventricular myocardial segmentation in 3-D ultrasound recordings: effect of different endocardial and epicardial coupling strategies. *IEEE Transactions on Ultrasonics, Ferroelectrics, and Frequency Control* 2017 Mar; 64(3):525-36.

Abstract

Cardiac volume/function assessment remains a critical step in daily cardiology and real-time 3D echocardiography (RT3DE) plays an increasingly important role. Though development of automatic endocardial segmentation methods has received much attention, the same cannot be said about epicardial segmentation, in spite of the importance of full myocardial segmentation. In this chapter, different ways of coupling the endo- and epicardial segmentation are contrasted and compared to uncoupled segmentation. For this purpose, the B-spline Explicit Active Surfaces (BEAS) framework was used. Twenty-seven RT3DE images were used to validate the different coupling strategies which were compared to manual contouring of the endo- and epicardial borders performed by an expert. It is shown that an independent segmentation of the endocardium followed by an epicardial segmentation coupled to the endocardium is the most advantageous. In this way, a framework for fully automatic 3D myocardial segmentation is proposed using a novel coupling strategy.

6.1 Introduction

Cardiovascular diseases are a group of disorders of the heart and blood vessels that together account for more deaths than any other cause [1] and are projected to remain the single leading cause of death [2]. Analysis of cardiac function, and more specifically, left ventricular (LV) function is an important factor in terms of patient management, outcome and long-term survival of cardiovascular disease patients [13]. Besides global cardiac function, regional cardiac morphology also contains important information for the detection of regional dysfunction. Among the different cardiac imaging modalities, ultrasonic imaging stands out as a low-cost, portable, risk-free and non-invasive technique with good space and time resolution. With the recent advent of RT3DE, several limitations of conventional 2D echocardiography (2DE) were overcome, opening a path for more accurate volumetric analysis of cardiac function and regional morphology. Nevertheless, the intrinsic increase of the amount of data makes manual delineation much more time consuming and thus the importance of automatic LV segmentation frameworks is increasing.

Ultrasound image processing poses however several challenges. The image quality is strongly affected by the acquisition conditions and speckle and a number of artefacts complicate the segmentation task [75]. In spite of this, numerous approaches have been presented aiming at automated or semi-automated border detection in RT3DE as can be appreciated in the review of Leung and Bosch [214]. Most of these approaches focus, however, on the segmentation of the LV endocardial border and full myocardial segmentation (i.e. segmentation of both endo- and epicardium) has received much less attention [75]. The same trend can be found in the available commercial solutions for LV segmentation, which focus mostly on the endocardium and define the epicardium by rudimentary methods such as setting a fixed thickness from the endocardium [215]. This trend is not only a consequence of

Table 6.1: State-of-the-art algorithms for full myocardial segmentation ($\Delta\mathbf{T_f}$: average frame processing time (s); #: number of datasets; NA: not applicable; NR: not reported).

Study	Imaging Modality	Algorithm / User Input	Surface Interaction	#	$\Delta\mathbf{T_f}$
Feng et al. [220]	2D SAx	PS/0	None	2	NR
Chalana et al. [209]	2D SAx	PS/II	Constraints	44	0.6
Dias and Leitão [221]	2D SAx	PS/I	Constraints	1	2.4
Caiani et al. [222]	3D	PS/II	None	19	190
Walimbe et al. [216]	3D	MSS/0	Constraints	5	30
Garson et al. [223]	2D SAx	MSS/II	Constraints	3	36-72
Orderud et al. [217]	3D	MSS/0	Coupling	5	0.0095
Lempitsy et al. [219]	3D	PS/0	NA	14	2.1
Barbosa et al. [159]	2D SAx	PS/I	Coupling	10	1
Zhu et al. [224]	3D	MSS/II	Constraints	11	NR
Verhoek et al. [218]	3D	PT/0	NA	25	120
Dietenbeck et al. [225]	2D	PS/I	Constraints	80	30-60
Butakoff et al. [226]	3D	PS/I	Coupling	19	NR

Note that PS, MSS and PT stand for the algorithm class, namely pure segmentation, multi-static segmentation and pure tracking. Regarding user input, 0 stands for a fully automatic method, I for minor user input (such as few anatomical landmarks) and II for significant user input (such as manual contouring in one frame or extensive landmarking). Surface interaction regards the interactions, if any, between the endo- and epicardial surfaces.

the relatively higher importance of endocardial segmentation, but also due to the intrinsic challenge of epicardial segmentation, especially in apical views where contrast tends to be low [75]. Epicardial segmentation is, nevertheless, extremely useful to study clinical indices such as LV mass. It is also an essential step in automatic cardiac strain measurements through the definition of a region-of-interest and to perform transmural differentiation of strain. This has motivated the development of a small number of epicardial segmentation methods.

An overview of the full myocardial segmentation methods available in literature is given in Table 6.1. Although earlier approaches focused on short axis (SAx) 2DE, more recent approaches have tackled 3D apical echocardiography as well, with promising results. Most methods rely on single-frame (i.e. static) segmentation, thus without using any temporal information. A few of these have been adapted to perform multi-static segmentation: performing segmentation on one frame and transporting it to the following in order to obtain a full cycle segmentation. Among these, the studies from Walimbe et al. [216] and Orderud et al. [217] stand out for being fully automatic and both report good accuracy. The latter has the additional advantage of real-time processing. A tracking approach was proposed by Verhoek et al. [218], where optical flow is used to propagate the results of the single-frame random forest segmentation from Lempitsky et al. [219].

In terms of the interaction between the endo- and epicardial surfaces, most methods use constraints to control the two surfaces and improve segmentation. These

constraints can be, for example, setting limits to the thickness of the myocardium to keep it in a plausible interval as in Chalana et al. [209] and Dias and Leitão [221]. Additionally, one can consider shape constraints as in Dietenbeck et al. [225]. Other constraints can only be considered in multi-static segmentation methods, such as conservation of myocardial volume or thickness [224]. Besides these methods, intrinsic coupling of the two surfaces can be considered so that a joint evolution of the two surfaces is obtained without the need to join them through constraints. This is the case with the method of Butakoff et al. [226] in which the two surfaces are coupled, as they are part of the same statistical shape model (SSM). Coupling can, however, also be applied to geometrical model approaches. In Orderud et al. [217], the global pose between the two surfaces is coupled such that the two surfaces evolve together. Barbosa et al. [159] takes this concept further by coupling not only the pose but also the shape of the two surfaces by defining the endo- and epicardium through two geometric functions - the myocardial wall position and the myocardial thickness. However, it remains unclear in what way the coupling strategy chosen influences the segmentation accuracy. Indeed, although it has been pointed out that epicardial segmentation is more difficult in 3D apical ultrasound imaging, it could be the case that epicardial information can help endocardial segmentation when there is little to no information from the endocardium.

For that purpose, in the present work, the effect of coupling is investigated and different methods of coupling are proposed and contrasted in the setting of an active contour approach for single-frame full myocardial segmentation of RT3DE images. From the methods described above, the BEAS framework used in Barbosa et al. [159] was chosen as it is a fully automatic and potentially real-time method with flexibility to encompass several coupling approaches. Additionally, a new energy better suited for a coupled endo- and epicardial segmentation is proposed. Based on the results of these comparisons, the paper concludes by proposing a method for fully automatic real-time myocardial segmentation in RT3DE recordings.

6.2 Methodology

Four different coupling strategies were tested and compared. First, a fully uncoupled (UN) model can be considered that allows the two surfaces to evolve independently from each other. Secondly, the mid-myocardial (MM) model, as proposed in [159], enables full coupling with equal contributions from endo- and epicardial information. Third, an endocardial based (EB) model (q.v. Section 6.2.3) that ensures full coupling of the two surfaces but puts more emphasis on the endocardial information. Finally, a two-step (2S) model in which the endocardial surface is segmented first, followed by a coupled epicardial segmentation while keeping the endocardial segmentation fixed, to ensure preservation of shape and pose.

6.2.1 Automatic Initialization

The endocardial borders were initialized according to the method of Barbosa et al. [165] presented in Chapter 2. The epicardial boundaries were initialized at a 15mm distance in the normal direction from the endocardial boundaries. Given that the endocardial initialization usually underestimates the border of the endocardium, the 15mm distance to the epicardium ensures that the epicardial surface is not attracted to the endocardium.

6.2.2 B-Spline Explicit Active Surfaces

6.2.2.1 Region-Based Energy Formulations

The evolution of the model is defined by the minimization of an energy criterion E. This energy is expressed by the sum of the data attachment term E_d and a regularization term E_r:

$$E = E_d + E_r. \tag{6.1}$$

The region-based representation of the segmentation problem is shown in Figure 6.1. The endo- and epicardial surfaces, respectively Γ_{endo} and Γ_{epi}, act as interfaces between the blood pool (*in*), the myocardium (*myo*) and the surrounding structures (*out*). Given this topology of the segmentation problem, the data attachment energy functional can be defined as:

$$\begin{aligned} E_d = &\int_\Omega \delta_{\phi_{endo}}(\mathbf{x}) \int_\Omega B(\mathbf{x},\mathbf{y}) \cdot F_{endo}(\mathbf{y})\, d\mathbf{y} d\mathbf{x} + \\ &\int_\Omega \delta_{\phi_{epi}}(\mathbf{x}) \int_\Omega B(\mathbf{x},\mathbf{y}) \cdot F_{epi}(\mathbf{y})\, d\mathbf{y} d\mathbf{x}, \end{aligned} \tag{6.2}$$

where $F_j(\mathbf{y})$ is the image criterion for surface j and $B(\mathbf{x},\mathbf{y})$ is the mask function in which the local parameters that drive the evolution are estimated. $\delta_{\phi_j}(\mathbf{x})$ is the Dirac operator applied to the level set function $\phi_j(\mathbf{x}) = \Gamma_j(\mathbf{x}^*) - x_1$, which is defined over the image domain Ω.

In this study, two different localized region-based energies were used, according to the characteristics of the endo- and epicardium. These region-based energies will be given through the localized means according to $B(\mathbf{x},\mathbf{y})$ in each of the regions, thus:

$$\begin{cases} u_{in} = \dfrac{\int_\Omega B(\mathbf{x},\mathbf{y}) H_{\phi_{endo}}(\mathbf{y}) I(\mathbf{y}) d\mathbf{y}}{\int_\Omega B(\mathbf{x},\mathbf{y}) H_{\phi_{endo}}(\mathbf{y}) d\mathbf{y}}, \\ u_{myo} = \dfrac{\int_\Omega B(\mathbf{x},\mathbf{y}) (H_{\phi_{epi}}(\mathbf{y}) - H_{\phi_{endo}}(\mathbf{y})) I(\mathbf{y}) d\mathbf{y}}{\int_\Omega B(\mathbf{x},\mathbf{y}) (H_{\phi_{epi}}(\mathbf{y}) - H_{\phi_{endo}}(\mathbf{y})) d\mathbf{y}}, \\ u_{out} = \dfrac{\int_\Omega B(\mathbf{x},\mathbf{y}) (1 - H_{\phi_{epi}}(\mathbf{y})) I(\mathbf{y}) d\mathbf{y}}{\int_\Omega B(\mathbf{x},\mathbf{y}) (1 - H_{\phi_{epi}}(\mathbf{y})) d\mathbf{y}}, \end{cases} \tag{6.3}$$

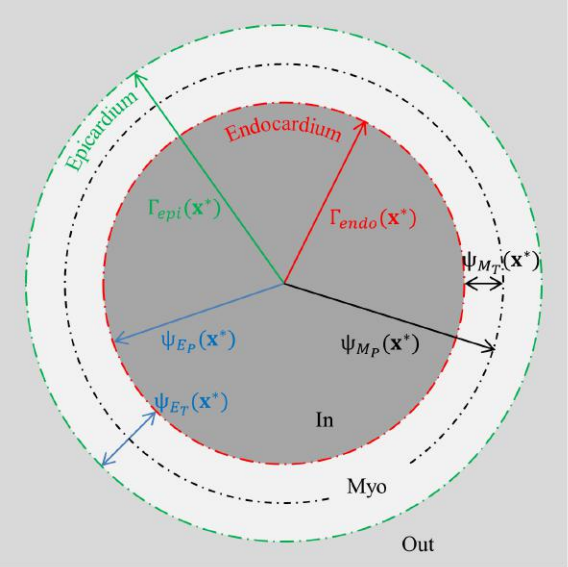

Figure 6.1: Conceptual diagram of the region-based representation of the blood pool, myocardium and pericardium (*in*, *myo* and *out*). The active geometric functions for the MM model are shown in black while the EB model is shown in blue.

where $I(\mathbf{y})$ is the image intensity at point $\mathbf{y}$ and $H_{\phi_j}(\mathbf{y}) = H(\phi_j(\mathbf{y}))$ with H being the Heaviside function.

Because the epicardial interface will separate the myocardium from the external structures, which are quite heterogeneous in intensity, an energy functional flexible enough to accomodate these different situations must be used. The localized Yezzi energy (equation 2.9) was therefore used.

The endocardium is however a much more predictable interface as the blood pool is usually darker than the myocardial tissue. The variation of the localized Yezzi energy adapted for endocardial segmentation introduced in 2.10 takes into account the expected intensities of the blood pool and the endocardium but, given the coupled framework between endo- and epicardium, cannot be used as is. While the localized Yezzi formulation evolves in a quadratic fashion according to the mean difference, the Barbosa formulation evolves linearly. If these two different formulations were combined for the energy minimization, the epicardial surface energy would have a larger influence on the overall energy than the endocardial surface. In order to solve this problem, a novel energy formulation is proposed:

$$F_{endo}(\mathbf{y}) = \frac{(u_{in} - u_{myo})^3}{|u_{in} - u_{myo}|}. \tag{6.4}$$

Note that this formulation maintains both the specificity of the Barbosa formulation for endocardial segmentation converging for a solution where the mean from the myocardial region (u_{myo}) will be larger than the mean from the blood pool

(u_{in}) but also has the same quadratic evolution as the Yezzi formulation used for the endocardium.

The minimization of the data attachment energy term in equation 6.2 can then be performed through optimization of the B-spline coefficient $c[\mathbf{k}_i]$, thus:

$$\frac{\partial E_d}{\partial c[\mathbf{k}_i]} = \int_{\Gamma_{endo}} \bar{g}_{endo}(\mathbf{x}^*)\beta^d\left(\frac{\mathbf{x}^*}{h} - \mathbf{k}_i\right) d\mathbf{x}^* + \int_{\Gamma_{epi}} \bar{g}_{epi}(\mathbf{x}^*)\beta^d\left(\frac{\mathbf{x}^*}{h} - \mathbf{k}_i\right) d\mathbf{x}^*, \tag{6.5}$$

where $\bar{g}_{endo}(\mathbf{x}^*)$ and $\bar{g}_{epi}(\mathbf{x}^*)$ are the feature functions that drive the minimization of the energy E_d:

$$\bar{g}_{epi}(\mathbf{x}^*) = -2(u_{myo} - u_{out})\left(\frac{\bar{I}(\mathbf{x}^*) - u_{myo}}{A_{myo}} + w_{out}\frac{\bar{I}(\mathbf{x}^*) - u_{out}}{A_{out}}\right), \tag{6.6}$$

$$\bar{g}_{endo}(\mathbf{x}^*) = 2\,|u_{in} - u_{myo}|\left(w_{in}\frac{\bar{I}(\mathbf{x}^*) - u_{in}}{A_{in}} + \frac{\bar{I}(\mathbf{x}^*) - u_{myo}}{A_{myo}}\right), \tag{6.7}$$

where A_j is the area of region j used to estimate the local mean u_j. $\bar{I}(\mathbf{x}^*)$ corresponds to the image value at the position $\mathbf{x} = \{\Gamma_j(\mathbf{x}^*), x_2, ..., x_n\}$ and j is the interface being considered.

Note that additionally to the differentiation, and according to what was proposed in [227], the energy functionals were modified by adding weights to the inner and outer regions of the endocardial and epicardial interfaces, w_{in} and w_{out} respectively. These weights can be used to control the balance between the forces exerted by the inner and outer regions of each surface. A weight w_{in} larger than 1 will increase the influence of the inner region attracting the endocardial contour inwards while a weight w_{out} larger than 1 will increase the influence of the outer region attracting the epicardial contour outwards and away from the myocardium. This can be especially important to mimic the physicians' behaviour in the drawing of the contours.

6.2.2.2 Mask Region Definition

In equation 6.2, $B(\mathbf{x}, \mathbf{y})$ was defined as the mask function in which the local parameters that drive the evolution are estimated. This was set according to equation 2.3, where the neighborhood region limit ρ was set at 16mm as in Barbosa et al. [115].

6.2.2.3 Regularization Terms

Although the coupling strategies will help the sharing of information from one surface to the other, additional constraints as those proposed in other studies should further guide the surfaces. To ensure that the segmentation will be limited to

plausible solutions in terms of thickness and curvature, the regularization term E_r is given by:

$$E_r = w_t E_t + w_\kappa (E_\kappa + E_{\kappa_B}), \tag{6.8}$$

where E_t, E_κ and E_{κ_B} are the three energy terms dedicated to constraining the local thickness, local curvature and local curvature at the base respectively and w_t and w_κ are weights given to each of the regularization terms to balance with the data attachment term.

A local thickness term has been proposed before but in other application dependent formulations [209, 216, 221]. Dietenbeck et al. [225] proposed a local energy term to penalize thickness values under a certain minimum and Queirós et al. [227] followed this approach and implemented it to the BEAS framework using a gradual penalization. The same approach was used here to constrain both the minimum t_m and maximum thickness t_M giving:

$$\begin{aligned}\frac{\partial E_t}{\partial c_{W_T}[\mathbf{k}_i]} = &\int_\Gamma ((\psi_T - t_m)H(t_m - \psi_T) + \\ &(\psi_T - t_M)H(\psi_T - t_M))\beta^d\left(\frac{\mathbf{x}^*}{h} - \mathbf{k}_i\right) d\mathbf{x}^*,\end{aligned} \tag{6.9}$$

where ψ_T corresponds to the thickness of the myocardium. The parameters t_m and t_M were set at 1px and 15mm respectively. This ensures that the two surfaces do not merge and prevents the surface from drifting away without being too constrictive.

A similar gradual configuration was used for E_κ to constrain the local mean curvature $\kappa(\mathbf{x}^*)$ (the usual symbol H was not used to avoid confusion with the Heaviside function). This constraint aims at penalizing the negative local mean curvature since the heart cavity is, at least for a large part, of positive curvature as it closes on itself. The analytic computation of the local mean curvature is straightforward within the BEAS framework using the first and second fundamental forms [228], making this an efficient method of regularization.

The evolution equation, inspired by mean curvature motion is given by:

$$\frac{\partial E_\kappa}{\partial c_{W_P}[\mathbf{k}_i]} = \int_\Gamma \kappa(\mathbf{x}^*)H(-\kappa(\mathbf{x}^*))\beta^d\left(\frac{\mathbf{x}^*}{h} - \mathbf{k}_i\right) d\mathbf{x}^*. \tag{6.10}$$

Finally, the term E_{κ_B} is added to prevent leakage through the base by penalizing curvatures different from zero in the basal region. The region will then tend to be flat. Given that in E_κ the curvature is already constrained to be positive, only a term for negative curvature is needed, giving:

$$\frac{\partial E_{\kappa_B}}{\partial c_{W_P}[\mathbf{k}_i]} = \int_\Gamma R_B(\mathbf{x}^*)\kappa(\mathbf{x}^*)H(\kappa(\mathbf{x}^*))\beta^d\left(\frac{\mathbf{x}^*}{h} - \mathbf{k}_i\right) d\mathbf{x}^*, \tag{6.11}$$

where $R_B(\mathbf{x}^*)$ is a mask region defining the surface points closest to the base. This region was defined taking advantage of the long axis (LAx) definition given by the

automatic initialization [165] and the consequent B-spline grid projection using this reference. The points closest to the base were thus defined as the ones with polar angle $\phi \geq 5\pi/12$ according to the LAx definition. $R_B(\mathbf{x}^*)$ is then one for these points and zero otherwise.

The regularization term weights w_t and w_κ were set empirically at 2 and 30 respectively by visually evaluating their impact on the contour evolution.

6.2.3 Coupling Strategies

6.2.3.1 Uncoupled Model

As seen earlier, the most common way to define the endo- and epicardial boundaries, especially in active contour formulations, is by defining them separately and controlling their evolution through additional penalties or constraints. To achieve this fully UN model, a simple definition of the two surfaces as separate explicit functions $\psi_{U_{endo}}$ and $\psi_{U_{epi}}$ is required:

$$\Gamma_{endo}(\mathbf{x}^*) = \psi_{U_{endo}}(\mathbf{x}^*), \tag{6.12}$$

$$\Gamma_{epi}(\mathbf{x}^*) = \psi_{U_{epi}}(\mathbf{x}^*). \tag{6.13}$$

Such an approach might however not be the best, as limited information is shared between two surfaces that, anatomically, are connected.

6.2.3.2 Mid-Myocardial Model

In [159], a different approach for LV segmentation has been proposed where the two boundaries are defined as a combination of two explicit functions representing the MM wall position ($\psi_{M_P}(\mathbf{x}^*)$) and half the wall thickness ($\psi_{M_T}(\mathbf{x}^*)$) thus coupling the two surfaces in its pose and shape:

$$\Gamma_{endo}(\mathbf{x}^*) = \psi_{M_P}(\mathbf{x}^*) - \psi_{M_T}(\mathbf{x}^*), \tag{6.14}$$

$$\Gamma_{epi}(\mathbf{x}^*) = \psi_{M_P}(\mathbf{x}^*) + \psi_{M_T}(\mathbf{x}^*). \tag{6.15}$$

This MM model, has also been used for LV segmentation in cardiac magnetic resonance imaging (cMRI) [227]. The evolution equations for the minimization of the data attachment term can be obtained as shown in [227], thus giving:

$$\frac{\partial E_d}{\partial \psi_{M_P}} = \frac{\partial E_d}{\partial \Gamma_{endo}} + \frac{\partial E_d}{\partial \Gamma_{epi}}, \tag{6.16}$$

$$\frac{\partial E_d}{\partial \psi_{M_T}} = -\frac{\partial E_d}{\partial \Gamma_{endo}} + \frac{\partial E_d}{\partial \Gamma_{epi}}. \tag{6.17}$$

The evolution of the explicit functions, given the B-spline formulation of BEAS, is then given by replacing the endo- and epicardial terms above by those from equation 6.5. The same is true for the remaining coupling strategies.

Analysing equations 6.14-6.17, it becomes clear that both surfaces give equal contributions to the evolution of each other. However, and due to the fact that epicardial border detection is much more challenging in apical views, it may be more advantageous to have a coupling strategy in which the endocardial information has a greater influence than the epicardial.

6.2.3.3 Endocardial Based Model

A change to the MM model is proposed in this chapter in order to form the EB model. Hereto, the two explicit functions are defined as the endocardial boundary position ($\psi_{E_P}(\mathbf{x}^*)$) and the full myocardial wall thickness ($\psi_{E_T}(\mathbf{x}^*)$) thus giving:

$$\Gamma_{endo}(\mathbf{x}^*) = \psi_{E_P}(\mathbf{x}^*), \tag{6.18}$$

$$\Gamma_{epi}(\mathbf{x}^*) = \psi_{E_P}(\mathbf{x}^*) + \psi_{E_T}(\mathbf{x}^*). \tag{6.19}$$

Again, following the derivation shown in Queirós et al. [227], the evolution equations for the minimization of the data attachment term can be obtained:

$$\frac{\partial E_d}{\partial \psi_{E_P}} = \frac{\partial E_d}{\partial \Gamma_{endo}}, \tag{6.20}$$

$$\frac{\partial E_d}{\partial \psi_{E_T}} = -\frac{\partial E_d}{\partial \Gamma_{endo}} + \frac{\partial E_d}{\partial \Gamma_{epi}}. \tag{6.21}$$

A schematic representation of both the EB and MM models is shown in Figure 6.1. This EB model maintains the key advantages of the MM model, namely the joint evolution of both contours and also the control over the myocardial wall properties. It has however a greater independence of the endocardial surface as can be seen in equation 6.20.

6.2.3.4 2-Step Model

Nevertheless, in the EB model, there is still an influence of the epicardial information to the endocardial evolution, as the thickness of the myocardium will influence the region of interest (ROI) that is used to evolve the endocardium according to equation 6.3.

As such, a fourth strategy is proposed in which the EB model is used but in a 2S approach to guarantee full endocardial independence from the epicardium. First, the endocardium segmentation is performed in an uncoupled manner until a final endocardial solution is obtained. Secondly, the EB model is initialized and coupled segmentation of the epicardial surface is performed without, however, evolving the endocardium any further. This can also be seen as first running the EB model with a fixed thickness until endocardial convergence, and only then performing the epicardial segmentation per se. In any case, this 2S model will allow for an endocardial segmentation which is completely independent but which will guide the epicardial segmentation in both pose and shape.

6.2.4 Implementation Details

Given the volumetric nature of the object of interest, the B-spline representation was created on a spherical coordinate system. The active geometric functions will thus be defined as $r = \psi(\phi, \theta)$. The angular discretization of the boundary representation was set empirically at 24×16. This was found to be a good balance between a dense enough representation of the interface and a low computational cost. The B-spline scale h was set at 2^1 for the position functions (UN, endocardial and MM positions) and at 2^3 for the thickness functions. This spacing controls the smoothness of the surfaces and allows overcoming problems such as the presence of the papillary muscles or low contrast. The larger scale for the thickness functions allows a greater uniformity of the thickness along the myocardium. As in previous BEAS implementations, the energy criterion minimization was performed through a modified version of the gradient descent with feedback step adjustment algorithm [162].

Finally, to accomodate the characteristics inherent to the basal region and to match the usual definition of the endo- and epicardium in segmentation, a base plane was fit to the mesh after the segmentation evolution so that a perfectly flat base was obtained. Though a regularization term (E_{κ_B}) to prevent leakage to the atrium was already introduced earlier, and this relies on setting the curvature to zero, this final step was necessary to obtain a fully flat base.

6.3 Experiments

6.3.1 Data acquisition

Twenty-seven RT3DE exams were used in the present study. The data was acquired using a GE E9 scanner (GE Vingmed, Horten, Norway) equipped with a 4V transducer using harmonic imaging (i.e. transmit frequency of 1.67MHz). The datasets used are part of a large multi-center clinical study, DOPPLER-CIP, aimed at patients whose profile corresponds to suspected chronic ischemic disease [190]. The twenty-seven datasets were selected randomly from the database. For twenty-five of these patients cMRI and late gadolinium enhancement data was also available for comparison. Table 6.2 shows the demographics of the population and Table 6.3 the image properties of the 3D ultrasound data used. This study was performed according to the ethical principles for medical research involving human subjects of the World Medical Association's declaration of Helsinki.

6.3.2 Data analysis

The images were categorised by the authors between poor, fair and good quality according to the percentage of myocardium clearly visible (<60%, 60%-75% and >75% respectively), the contrast between blood pool and myocardium and between myocardium and surrounding tissues, and the presence of severe image artifacts.

Table 6.2: Population characteristics.

Age (years)[a]	63.6 ± 8.9
Male[b]	20 (74)
Heart Rate (bpm)[a]	52.9 ± 7.1
Body Mass Index (kg/m^2)[a]	27.7 ± 4.1
Hypertension[b]	20 (74)
Myocardial Infarction[b]	14 (52)
Scar (%)[a,†]	3.5 ± 4.9
ED Volume (EDV) (ml)[a,†]	166.8 ± 35.7
Ejection Fraction (EF) (%)[a,†]	59.9 ± 9.7

[a]Data are mean±standard deviation;[b]Data are count (%); [†]As given by cMRI.

Table 6.3: Description of the recordings.

Frame Rate (FR) (fps)[a]	30.9 ± 9.8
Depth (cm)[b]	14 [11; 19]
Opening Angles (°)[b]	60 [50; 75]
Stitching mode	
1-beat[c]	2 (7)
4-beat[c]	11 (41)
6-beat[c]	14 (52)

[a]Data are mean±standard deviation;[b]Data are median [minimum;maximum];[c]Data are count (%).

Table 6.4: Optimal hyper-parameters for each coupling strategy using the entire dataset.

Model	w_{in}	w_{out}
UN	0.9	0.8
2S	0.8	0.6
EB	0.7	0.8
MM	0.7	0.8

The percentage of poor, fair and good images was respectively 29.63%, 29.63% and 40.74%.

Each sequence was analyzed by a clinical expert, providing manual contouring of the endocardium and epicardium at end diastole (ED). The ED frame was defined based on the electrocardiogram (ECG) as well as the largest volume of the LV through visual assessment. The expert was previously provided with initial training in the software and guidance in a written protocol. The manual contouring was performed using an in-house developed software package - Speqle3D, KU Leuven. The first step in contouring was the LV LAx alignment, followed by annotation of the base and apex. These positions were used to compute five SAx and four LAx views in which the expert then performed manual contouring. The software then uses a least-squares surface fitting procedure with a fifth-order spherical harmonics expansion to get the final LV surface [229].

6.3.3 Similarity Metrics

To perform a quantitative comparison between different surfaces, three different distance measures were used: Mean absolute distance (MAD) [209], which measures the average distance at any point between the segmented and the reference mesh;

Hausdorff distance (HD) [210], which measures the maximum distance between the segmented and reference mesh; and modified Dice (Dice*= 1-Dice) [211], which is a measure of the overlap between the segmented and reference mesh. In addition to the quantitative measures described, clinical indices were also considered, namely the endocardial and myocardial volumes. One-sample or paired t-tests using a p-value of 0.05 were used to analyse the significance of differences and, when multiple comparisons were performed, this value was corrected using the Bonferroni method [230].

6.3.4 Cross-Validation

To estimate the performance of the different coupling strategies and select the optimal settings for parameters w_{in} and w_{out}, leave-one-out cross-validation was applied. Both parameters were varied between 0 and 2 in increments of 0.1 and the optimal combination of parameters was chosen according to a global ranking metric:

$$\begin{aligned} Rank = &\frac{1}{6}(\widehat{MAD}_{endo} + \widehat{HD}_{endo} + \widehat{Dice^*}_{endo} \\ &+ \widehat{MAD}_{epi} + \widehat{HD}_{epi} + \widehat{Dice^*}_{epi}), \end{aligned} \tag{6.22}$$

where the $\widehat{\ }$ above each distance metric symbolizes that this value was normalized according to the results obtained with parameters $w_{in} = 1$ and $w_{out} = 1$. For a given distance metric d this normalization is done according to:

$$\widehat{d} = \frac{d}{d_{w_{in}=1 \wedge w_{out}=1}}. \tag{6.23}$$

In practice, each of the twenty-seven images was tested using the remaining twenty-six as the training set. At each time, the optimal set of parameters for the training set was selected and used to segment the test image. By not splitting the data into a final training and test set, a biased estimate of the error due to an unfortunate split of the data is avoided. The optimal parameters for future use of each model are selected by finding the optimal set for all twenty-seven cases and these are shown in Table 6.4.

6.3.5 Parameter Sensitivity Analysis

Because active contour-based segmentation frameworks often involve a fair amount of fine tuning of the diverse parameters involved, it is crucial to study the robustness and stability of the framework with respect to these parameters. The parameters studied were the local neighborhood radius ρ, the matrix size for the angular discretization of the boundary representation and the regularization term weights w_t and w_κ. Each parameter was varied from their preset optimal value by 50% of its value and its impact was studied in terms of MAD, HD and Dice*. For the matrix

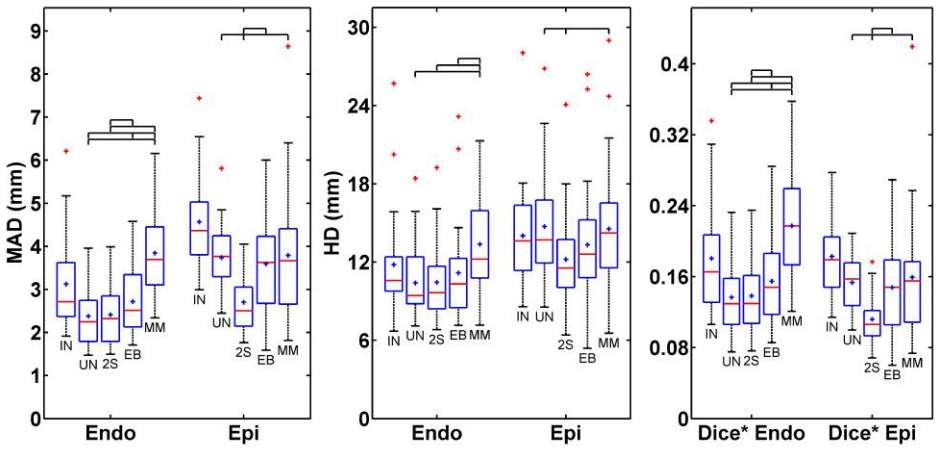

Figure 6.2: Distance metrics (MAD, HD and Dice*) results comparing BEAS for endo- and epicardial contours after cross-validation. Legends under the lower whiskers represent the coupling strategy (UN, 2S, EB or MM) and the first, labeled IN, corresponds to the initialization shapes. The ends of the whiskers represent the lowest and highest data point within 1.5 times the inter-quartile range of the lower and upper quartile respectively. Top black brackets denote that the difference between the two indicated coupling strategies was found significant (corrected for multiple comparisons). This t-test was performed exclusively between the different coupling strategies and not with the initialization.

size, this 50% variation was not feasible given that due to the multiscale operation involved in BEAS, the matrix sizes must be multiples of the largest scale h used, 2^3, and only possible variations were considered.

6.4 Results

6.4.1 Comparison of Coupling Strategies

Figure 6.2 shows the distance metrics obtained by comparing the automatic contours from all four coupling strategies to the manual contours. The distance metrics obtained from the initialization contours are also shown. It can be observed that the epicardial segmentation presents a larger error than the endocardial segmentation, as expected given the added difficulty of contouring the epicardium. Comparing the performance of the different coupling strategies, it becomes clear that, for the endocardium, the coupling strategies with the best results are the UN and 2S, with very similar performances, and also the EB model. For the epicardium however, both the UN and EB models behave worse than the 2S. The MM model has the worst performance, especially for the endocardium.

A regionwise comparison of the all models with the manual contours is shown in Figure 6.3.

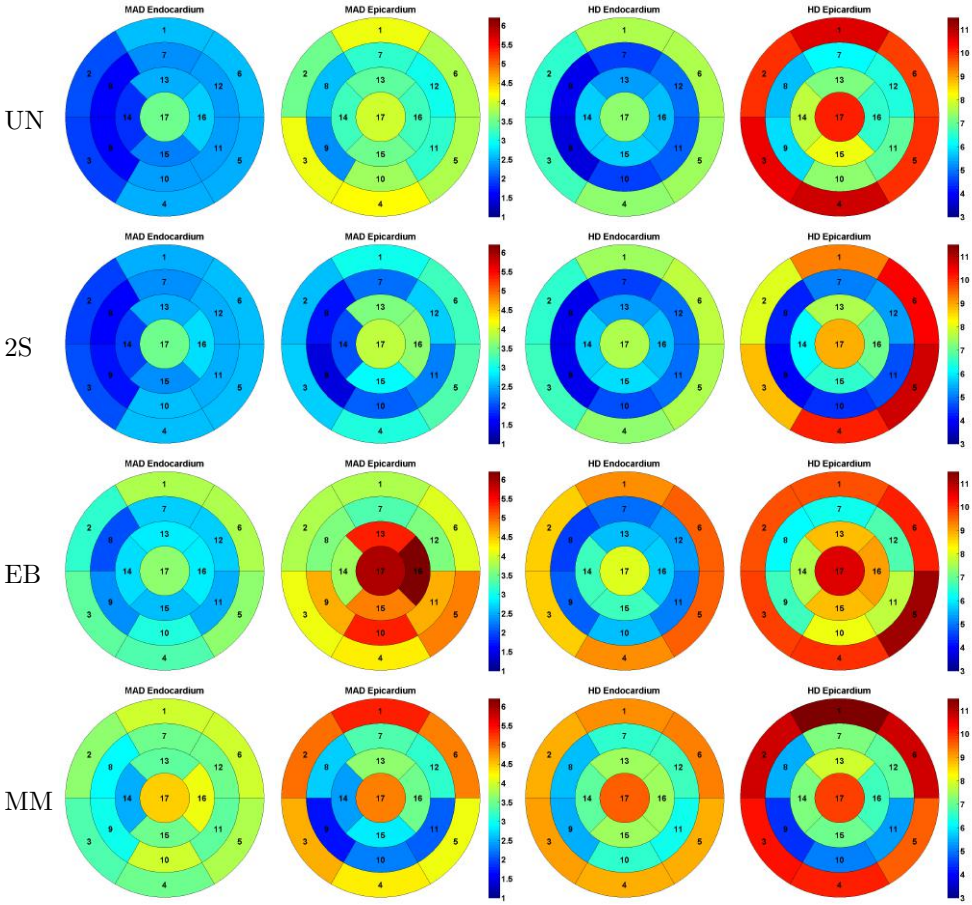

Figure 6.3: Bullseye plots of MAD and HD at every region for endo- and epicardial contours obtained with BEAS. All measures in mm.

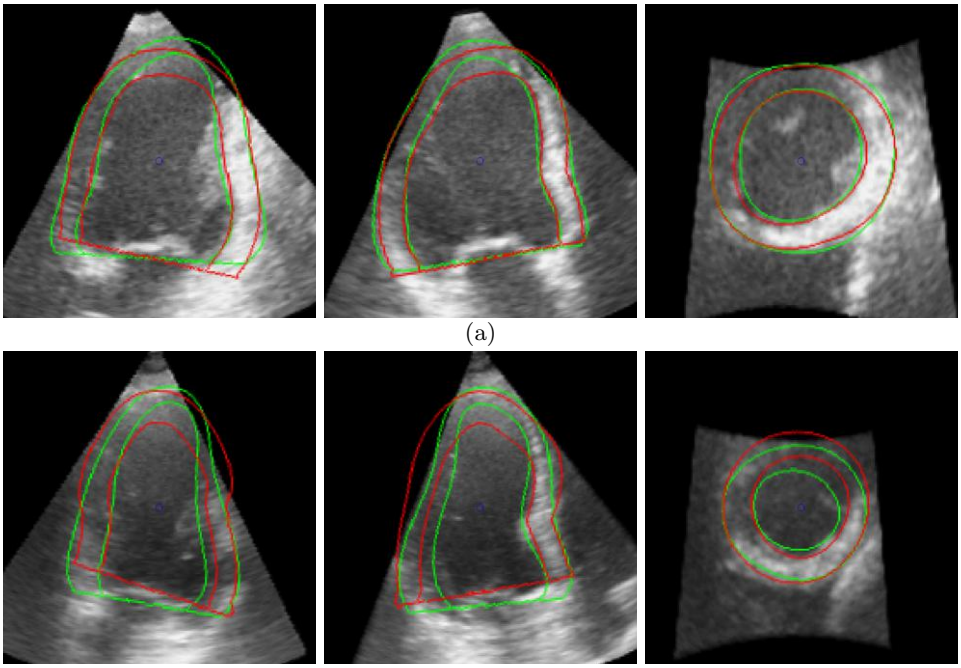

(a)

(b)

Figure 6.4: Best (a) and worst (b) automatic segmentation results with the 2S model (red) compared to manual contours by expert (green). The three orthogonal planes shown for each 3D image were chosen automatically according to the LAx defined upon BEAS initialization.

6.4.2 Performance of Proposed Coupling Strategy

Given the results shown on Section 6.4.1 the focus will, hereinafter, be set on the 2S model. Figure 6.4 shows the best and worst segmentation result for the 2S model compared to the manual contours. It can be observed that the greatest errors seem to occur near the apex and base and this can be confirmed in Figure 6.3 for the 2S model.

The clinical indices of endo- and myocardial volumes were also computed for the automatic segmentation results and compared to those obtained from the manual contours as shown in Figure 6.5. It can be observed that BEAS overestimates the endocardial volume when compared to the manual contouring. The cardiac volumes obtained with the 2S model were also compared with those from cMRI as shown in Figure 6.6. It can be seen that, compared to cMRI, the 2S model underestimates the endocardial volume and overestimates the myocardial volume.

The average time required for the myocardial segmentation was 1.58 ± 0.31s. For the automatic initialization the average time required was 0.93 ± 0.11s. All data was processed in a non-optimized MATLAB implementation.

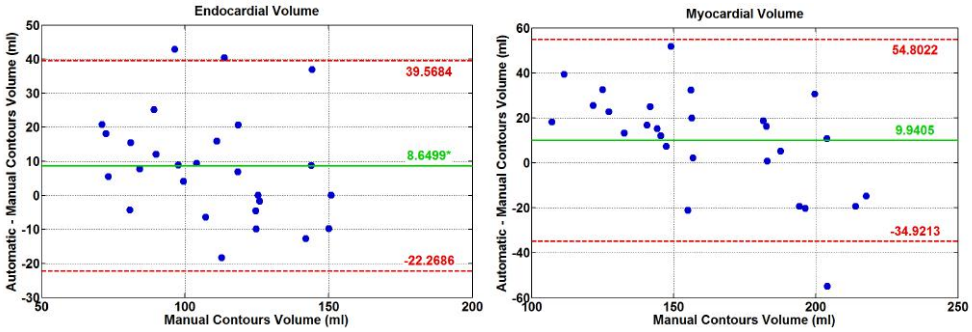

Figure 6.5: Bland-Altman plots of the cardiac volumes computed for the manual contours and the automatic contours obtained with the 2S model (green: bias (*, $p < 0.05$), red: limits of agreement ($\mu \pm 1.96\sigma$)).

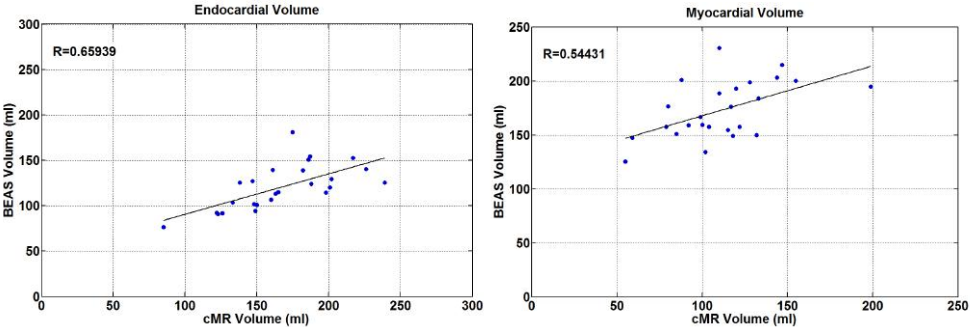

Figure 6.6: Correlation between the cardiac volumes computed for the manual contours in cMRI and the automatic contours obtained with the 2S model.

6.4.3 Parameter Sensitivity Analysis

Figure 6.7 shows the influence of each of the considered parameters on the segmentation results using the 2S coupling strategy. It can be observed that the neighborhood radius variation has an effect on the segmentation result, especially when considering smaller radius values. The variation of the matrix size determining the angular discretization strongly compromises the evolution for lower matrix sizes. Variations of the thickness regularization term weight w_t had no influence on the endocardial segmentation and little influence on the epicardial segmentation following no particular pattern. The variation of the curvature regularization term weight w_κ showed that lower values compromised the evolution (see HD), whereas higher values slightly improved performance.

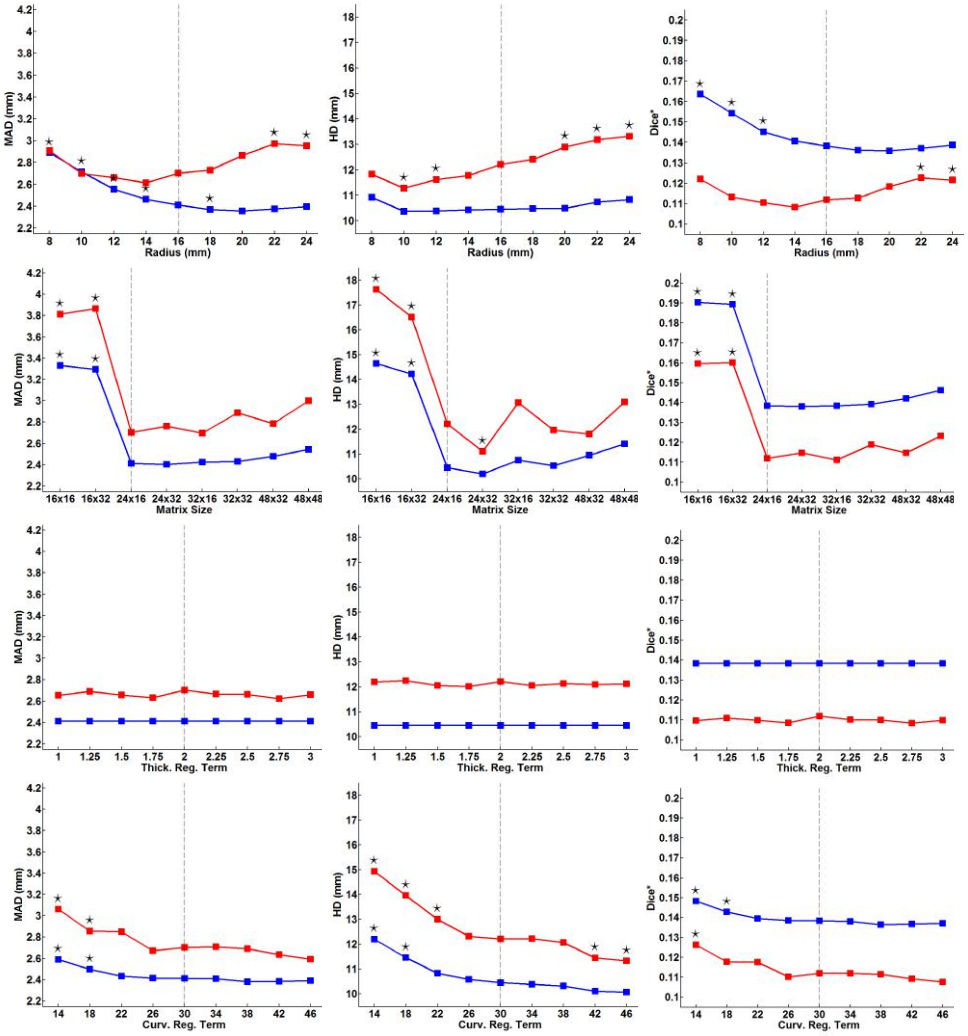

Figure 6.7: Influence of the variation of each of the considered parameters (neighborhood radius, matrix size, w_t and w_κ) in the distance metrics (MAD, HD and Dice*) for endo- and epicardial segmentation using the 2S coupling. Blue: endocardium; red: epicardium. Vertical dotted line indicates the preset parameter value. $\star$ indicates that the difference was found significant ($p < 0.05$) when compared to the results obtained with the preset parameters.

6.5 Discussion

6.5.1 Comparison of Coupling Strategies

Comparing the performance of the different coupling strategies for endocardial segmentation, it appears that the more independent the endocardial segmentation is, the better the performance. This reinforces the idea that the epicardial segmentation cannot give aid to the endocardial segmentation as its segmentation is more challenging. The fully independent endocardial strategies, UN and 2S, have thus the best results for endocardial segmentation. While both coupling strategies have the same underlying endocardial segmentation, the small resulting differences can be attributed to the cross validation. For the UN model, the cross validation is done separately for each surface as they are fully independent from each other. This assures the best result for each surface. For the 2S model, however, the best combination of weights for both surfaces is selected. As such, a compromise is made between endo- and epicardial results, thus justifying the slight difference in distance metrics observed and the differences in w_{in} for the UN and 2S models in Table 6.4.

In regard to the epicardial performance, it becomes clear that both coupling models 2S and EB perform much better compared to the UN strategy, therefore justifying a coupling strategy. The propagation of information from the endo- towards the epicardial surface helps the epicardial segmentation as this segmentation is more challenging. As such, it becomes clear that the 2S model joins both advantages - endocardial independence and coupled epicardium - thus appearing to be the best solution from those presented here.

6.5.2 Performance of Proposed Coupling Strategy

As for the specific results for the 2S model, namely the regionwise comparison, the apical region error can be explained by the near field noise inherent to the region close to the probe. Without any real information, the position of the apex has to be "guessed", thus leading to variability. The deviations at the base are most likely caused by differences in the base plane chosen. A different position and especially a different angle will give rise to a large HD and this is the case in Figure 6.4(b).

Turning to the Bland-Altman plots shown in Figure 6.5, both the endo- and myocardial volumes have small biases. While the observed limits of agreement may at first be considered large, one must take into account the number of factors that contribute to these final volumes, namely the segmentation of two complex objects in RT3DE which has its inherent noise characteristics and semi-objective methods such as the definition of the base plane. Furthermore, the current database has quite some challenging images as was seen in Section 6.3.2 and most with surfaces partially outside the image sector as can be observed in Figure 6.4.

In terms of the comparison between the volumes from cMRI and the volumes obtained with BEAS, an underestimation of the endocardial volume by RT3DE was expected as this has been reported multiple times in the past [231]. For myocardial

volume, there is only a limited number of small studies comparing cMRI and RT3DE but because the myocardial volume is dependent on the endocardial volume, the observed bias and correlation values are, to a big extent, a consequence of the endocardial error.

Finally, it should be noted that the results presented in this manuscript were obtained in a fully automatic manner, i.e. without any user interaction. For clinical use, it would be important however to enable correction of the contours in case the operator would not agree with the solution proposed by the algorithm. Such an interactive extension has been proposed in Barbosa et al. [206] for the original (endocardial) BEAS framework and could easily be adapted to the coupled BEAS framework proposed in this manuscript.

In terms of the computation time, the current application in MATLAB cannot perform real-time segmentation. However, it has been shown previously that in a C++ implementation of BEAS there is a significant speed-up being able to perform 3D endocardial segmentation in approximately 12.5ms which can already be considered real-time in a normal RT3DE acquisition [3].

6.5.3 Parameter Sensitivity Analysis

Overall, the parameter sensitivity analysis was able to show that the proposed framework is robust enough to support variation in its parameters. Furthermore, the observed variations can be justified by reasons related to the framework's inherent characteristics.

With respect to the neighborhood radius ρ, its influence had already been analyzed in [165] with the BEAS framework for endocardial segmentation. In [165], it was noted that a small ρ would limit the field of view (FOV) of the interface during its evolution whereas a large ρ would retrieve information beyond the ROI, thus compromising the segmentation. This is in agreement with the findings of the current study. The epicardial segmentation, however, seems not to be as affected by smaller ρ values. This is likely due to the dependence on the endocardial segmentation. Because the epicardial initialization will be closer to the final surface, a smaller radius, and thus a smaller basin of convergence will not negatively impact the results. Though in this study an equal value of ρ was considered for endo- and epicardium, the results point to a possible advantage of different ρ values for each surface.

The results of the variation of the matrix size determining the angular discretization show the balance between a smooth interface and a proper representation that needs to be achieved as had been shown in [165,227]. A small matrix size will result in a mesh which cannot capture the LV shape. Increasing the matrix size will make the B-spline support more local, compromising the smoothness of the mesh.

As for the variations in performance when varying w_t, these were expected given the framework characteristics. As the endocardial segmentation is independent from the epicardial no influence whatsoever was expected. For the epicardial segmentation, though an effect is present, this was not expected to have a large magnitude

or specific trend. Due to the fact that a change to the thickness regularization term will only have an impact on the strength of the force pulling the contours to plausible values of thickness, changing this value will not have a significant impact on the final result.

Finally, the results observed for the impact of w_κ can be caused by either E_κ, E_{κ_B} or both since both regularization terms are controlled by w_κ. However, given that this impact is much more significant for the HD and for the epicardium, it can be inferred that the base curvature is the main origin of these results as it has been shown that this is the region with the highest HD. According to the results on Figure 6.7, it seems that increasing the value of w_κ could improve the segmentation accuracy, especially for the epicardial segmentation.

6.5.4 Limitations and Future Work

In spite of the results shown in this study, there are some limitations that must be addressed in the future. In this study, only the ED frame was segmented. Segmentation of the end systolic (ES) frame would be extremely important not only to obtain important clinical values, such as EF, but also to further validate the proposed framework. Though the 2S endocardial segmentation is fully independent, and an approach for endocardial ES segmentation has been validated first in [165] and later in Chapters 3 and 5, the performance of the epicardial segmentation has not yet been tested and should be addressed in the future.

While the 2S model was the most successful for this population, one must take into account that under other populations another model might be more successful. This could be the case for example in hypertrabeculated hearts where the endocardial segmentation can be especially challenging. Similarly, some of the cases have parts of the epicardial surface outside the FOV which has an influence on the results. Nevertheless, the population considered in this study is representative of the greater part of the patients referred for echocardiography which strenghtens the conclusions of this study.

Furthermore, one might consider ways to improve the robustness of this segmentation approach. Given the very way that clinicians manually contour the LV, the definition of a base plane is required and differences between base planes give rise to large errors in both distance metrics and volume measurements. A method for automatic detection of specific landmarks such as the mitral annulus (MA) and/or the LV outflow tract (LVOT) could be of paramount importance to minimize the error in this region. The introduction of prior shape information through a myocardial SSM as was done in Chapter 5 for the endocardium could also help in making the segmentation more exact, especially near the base but also in the apex and low contrast regions where BEAS sometimes fails to segment correctly.

6.6 Conclusions

In conclusion, a framework to perform fully automatic segmentation of endo- and epicardium was proposed. It was shown that the use of a coupling strategy can be advantageous. In the case of apical RT3DE, the optimal coupling strategy was the 2S model, where an independent endocardial segmentation is performed followed by a coupled epicardial segmentation. In this way, information from the endocardial shape is propagated to the epicardium but not vice-versa. This result is a consequence of the inherent characteristics of 3D apical ultrasound images. Similarly to the original BEAS for endocardial segmentation, this approach would allow for the implementation of an optimized version of this algorithm in an online analysis tool to provide real-time functional measurements.

Chapter 7

Validation of Automatic 3D Myocardial Segmentation Using Coupled Shape-Based B-Spline Explicit Active Surfaces

This chapter is based on a paper submitted for publication in a peer-reviewed journal: **Pedrosa J.**, Duchenne J., Queirós S., Degtiarova G., Gheysens O., Claus P., Voigt J., D'hooge J.. Non-invasive myocardial performance mapping using 3D echocardiographic stress-strain loops: validation against PET.

Abstract

Cardiac assessment is a critical step in cardiology and real-time 3D echocardiography (RT3DE) plays an increasingly important role. While numerous approaches have been presented for left ventricle (LV) endocardial segmentation, myocardial segmentation (i.e. segmenting both endo- and epicardial surfaces) has received less attention. However, myocardial segmentation provides clinical information and is often essential in post-processing such as strain and classification approaches. In this chapter, a method for shape-based full-cycle myocardial segmentation is proposed fusing the advantages of B-spline Explicit Active Surfaces (BEAS) and statistical shape models (SSM) for a robust segmentation. The segmentation is propagated throughout the heart cycle using localized anatomical affine optical flow (lAAOF). The framework was validated on the CETUS challenge data, a publicly available multi-center multi-vendor dataset with manual endocardial contouring performed by 3 experts at end diastole (ED) and end systole (ES). One expert segmented the epicardium using the same protocol and image planes as those used for the endocardium to assure uniformity. It is shown that the proposed method achieves a mean absolute distance (MAD), Hausdorff distance (HD) and Dice of 2.49±0.60mm, 9.91±2.96mm and 0.908±0.029 at ED and 2.90±0.68mm, 12.02±3.28mm and 0.881±0.037 at ES for epicardial segmentation. The epicardial reference contours developed in this study were made available on the CETUS website thus allowing for future comparison studies on epicardial segmentation.

7.1 Introduction

LV volume and function assessment is an essential step in clinical cardiology where echocardiography plays a major role due to its low-cost, portability, non-invasiveness and good spatiotemporal resolution. While 2D echocardiography (2DE) is still the standard imaging mode used, RT3DE has several advantages as it allows to visualize the whole 3D LV geometry and avoids geometrical assumptions usually used in 2DE. Nevertheless, manual analysis of 3D imaging is challenging and time consuming making the development of automatic tools to help clinicians extremely important.

In spite of the challenges of RT3DE, numerous approaches have been proposed for automatic and semi-automatic LV segmentation, most of these focused on the endocardial surface [75, 214]. However, epicardial segmentation is also extremely useful to study clinical indices such as LV mass and thickness and is also an essential step in advanced post processing techniques such as strain and machine learning approaches through the definition of a region of interest (ROI). Nevertheless, 3D epicardial segmentation methods have received little attention, especially if considering automatic methods. Walimbe et al. [216] combined a deformable model with a generalized gradient vector field to perform 3D endo- and epicardial segmentation with promising results. Orderud et al. [217] proposed a Kalman filter tracking framework which linked endo- and epicardial segmentation by sharing position, size

and orientation between both surfaces, but this approach was only validated on simulated images. A semiautomated extension of this approach for biventricular segmentation has been validated in clinical images with promising results [232]. A tracking approach was proposed by Verhoek et al. [218], where optical flow is used to propagate the results of the single-frame random forest segmentation from Lempitsky et al. [219]. However, none of these approaches perform a full coupling of both endo- and epicardial surfaces to share both position and orientation but also shape. It was shown in Chapter 6 that a two-step (2S) coupling, where the endocardial segmentation provided information to the epicardial segmentation but not vice-versa, was the most advantageous.

In Chapter 5, a segmentation and tracking framework was proposed for full-cycle endocardial LV segmentation which was based on a combination of BEAS with an SSM to provide LV shape clues which was propagated throughout the cycle with lAAOF. This framework was shown to outperform all other proposed LV endocardial segmentation frameworks. In this work, this framework is extended for LV myocardial segmentation using the 2S model and a myocardial SSM to provide shape information on the LV myocardium.

7.2 Methodology

7.2.1 B-spline Explicit Active Surfaces

It was shown in Chapter 6 that the most efficient way to represent the myocardium using the BEAS framework was to perform a 2S approach where the endocardial segmentation was performed independently, followed by the epicardial segmentation represented as the thickness of the myocardium. This allowed the epicardium to take advantage of the information from the endocardial segmentation without the need for extensive and complicated constraints between the two surfaces. This same representation was chosen for the current study.

As in previous implementations for LV and myocardial segmentation, the angular discretization was set to 24×16 (elevation$\times$azimuth) and the B-spline scale to 2^1.

The evolution of the model is defined by the minimization of an energy criterion E. This energy is expressed by the sum of the data attachment term E_d and a regularization term E_r:

$$E = E_d + E_r. \tag{7.1}$$

The data attachment energy function E_d follows a variation of the localized Yezzi energy adapted for endocardial segmentation [165] detailed in Section 2.6. The neighborhood region limit ρ was set at 16 mm as in Barbosa et al. [115].

7.2.2 Statistical Shape Model

To give information on the shape variations of the myocardium, 289 cardiac magnetic resonance imaging (cMRI) datasets from the DOPPLER-CIP study were

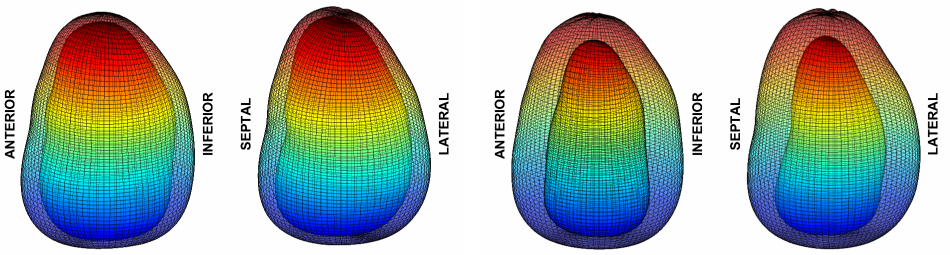

(a) (b)

Figure 7.1: SSM mean models at ED (a) and ES (b).

used [190]. The endo- and epicardium were contoured at ED and ES on both long axis (LAx) and short axis (SAx) slices and an iterative closest point (ICP) algorithm [205] was used to correct for misalignment between the slices. A 3D mesh was then interpolated from the aligned 2D contours at both time points. A more detailed description of this methodology can be found on Chapter 5.

As in Chapter 5, the SSM was built in the BEAS coordinate system. The SSM shapes will then be represented through their B-spline representation coefficients $c[\mathbf{k}]$. Following the method described in Chapter 5, singular value decomposition [208] was used to obtain the eigenvectors $\mathbf{p}_i$ through which any shape from the dataset can be approximated according to:

$$c[\mathbf{k}] \approx \bar{c}[\mathbf{k}] + \mathbf{Pb}, \tag{7.2}$$

where $\mathbf{P}$ is the matrix of the first t eigenvectors and $\mathbf{b}$ is a vector of t weights which for any given shape corresponds to $\mathbf{b} = \mathbf{P}^T (c[\mathbf{k}] - \bar{c}[\mathbf{k}])$.

Given the 2S approach chosen for the myocardial segmentation, two different SSMs are needed at ED and ES, one representing the endocardium for the first segmentation step and a second representing both the endocardium and the myocardial thickness for the second segmentation step. In this way, the first segmentation step remains fully independent of the epicardium, while the second segmentation step derives information from the endocardial shape to obtain clues about the expected epicardial surface. As such, the endocardial SSM was built from the endocardial B-spline coefficients $c[\mathbf{k}]$, while the myocardial SSM was built by concatenating both the endocardial and the myocardial thickness B-spline coefficients so that the shape variations regarding both surfaces are modelled together. The mean shapes for each of these models are shown in Figure 7.1. Note that since these models are scaled only shape variations can be observed in this figure.

The SSM-based regularization of BEAS was performed according to two regularization energies, hard and soft, as proposed by Queirós et al. [198]. The hard term restricts the segmented shape to the shape variability observed in the training set penalizes high values of b_i, following the rationale that it is much more probable

to find an average shape than a shape which is close to the variability limits. The regularization term E_r is thus defined as

$$E_r = \alpha E_{hard} + \beta E_{soft}, \tag{7.3}$$

where α and β are hyperparameters controlling the relative weight between the two terms.

7.2.3 Framework Description

A conceptual description of the proposed framework is shown in Figure 7.2 and is an adaptation of the framework for endocardial LV segmentation detailed in Chapter 5.

7.2.3.1 Automatic Initialization

The automatic initialization algorithm used was introduced in Barbosa et al. [165] and is detailed in Chapter 2. This initialization will provide the initial estimation of the LAx and center for BEAS and the SSM.

7.2.3.2 Automatic SAx Orientation

The SAx orientation method is detailed in Chapter 4 and is crucial to correctly position the SSM, given that different sides of the LV have different shape characteristics. However, this orientation algorithm depends on a previous estimate of the LV surface and the result from the initialization is too rough as it relies on the fitting of an ellipsoid. As such, the automatic SAx orientation is only applied after the initial stage of endocardial segmentation.

7.2.3.3 Segmentation at ED

The segmentation at ED is composed of three stages. Initially, an endocardial segmentation is performed without the SSM, so that the energy criterion E is equal to E_d, the data attachment term. This provides an initial segmentation of the LV, which is used for the SAx orientation estimation but also to refine the initial estimates of LAx orientation and center according to the centroid and direction of largest variance of the segmented mesh. With the center position and both the LAx and SAx orientation well defined, it is then possible to use BEAS with the endocardial SSM regularization according to equation 5.10 to further refine the segmentation. In a third stage, the epicardial surface is initialized and segmented using the myocardial SSM. As in the original 2S approach, the endocardial surface is not refined further at this point, being only a reference for the explicit function of myocardial thickness and the myocardial SSM.

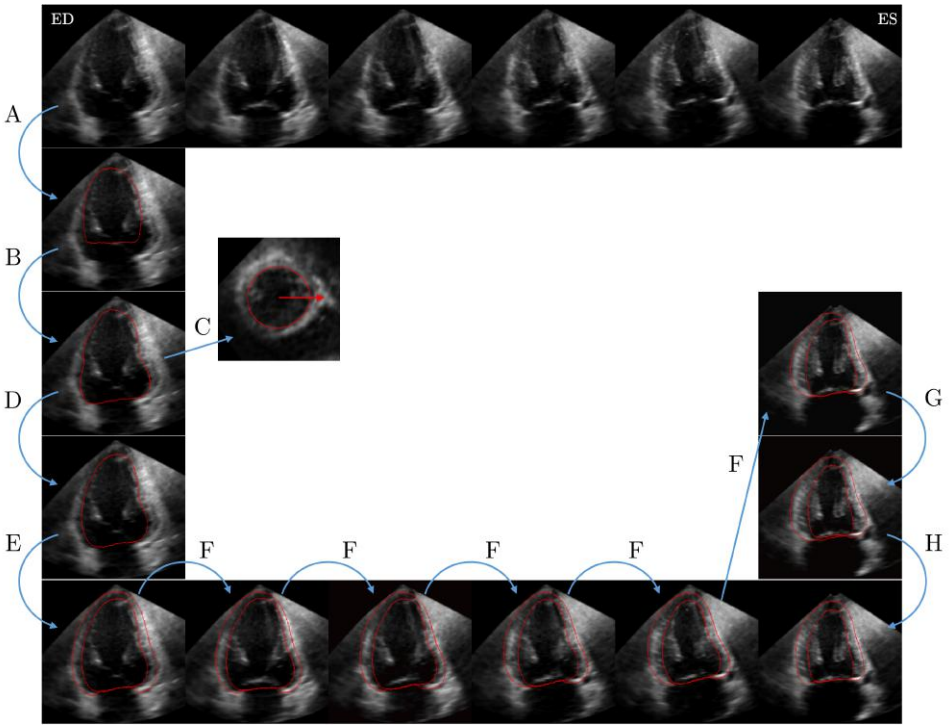

Figure 7.2: Conceptual description of the proposed segmentation and tracking framework. First, automatic initialization is applied to the ED frame (A). The first stage of segmentation is then performed using BEAS (B). The result from this segmentation is used to detect the SAx orientation (C) and this information is used to perform the second stage of segmentation using BEAS and the ED SSM (D). The epicardial surface is then initialized and the ED myocardial SSM is used to perform the myocardial segmentation (E). The final ED segmentation is then propagated frame to frame using the lAAOF (F) and a final refinement of the ES segmentation is performed using first the ES endocardial SSM (G) and then the ES myocardial SSM (H).

7.2.3.4 Localized Anatomical Affine Optical Flow

lAAOF is then used to propagate the result from ED to the remaining frames. The lAAOF method was proposed in Queirós et al. [199] and relies on an affine optical flow approach which independently estimates the motion at each point in the surface based on an anatomically constrained neighborhood. A detailed description of this method can be found in the original paper by Queirós et al. [199]. The parameters used to tune the lAAOF were replicated from [199].

7.2.3.5 Segmentation at ES

Segmentation at ES is used to further refine the result from the lAAOF, thus bringing together intensity and shape-based clues. In order to balance the contribution between tracking and segmentation clues, an energy term was added to penalize the deviation between the result of the lAAOF and the segmentation. Such an approach is similar to that detailed in Chapter 3. The regularization energy criterion is then expressed as:

$$E_r = \alpha E_{hard} + \beta E_{soft} + \gamma E_A, \tag{7.4}$$

where E_A is defined according to 3.11 and γ is a hyperparameter used to define the balance between tracking and intensity/shape-based information. As at ED, the 2S approach is used, so that the endocardium is refined first, followed by the epicardium using both the refined endocardial surface and the epicardial tracking result.

7.3 Experiments

Given the lack of a robust and validated database for epicardial segmentation in RT3DE, manual contouring of the epicardium was performed by an expert on the CETUS challenge database. The CETUS challenge database is a publicly available multi-center multi-vendor dataset with manual endocardial contouring performed by 3 experts at ED and ES until consensus was achieved between the three. It comprises 45 RT3DE datasets, divided into 15 training and 30 testing datasets.

To ensure uniformity between the endo- and epicardial contours, the same protocol that was used for the endocardial contours was followed for the epicardium [212]. In brief, the expert contoured the epicardium in pre-defined slices where the endocardial contours were also visible. The epicardial countours were defined as to observe the following requirements: a) located outside the endocardial contours; b) excluding the pericardium; c) keeping tissue consistency between ED and ES; d) contour up to the basal plane defined by the endocardial reference. This was performed at ED and ES and the contours at each time point were used to define a 3D reference mesh using a spherical harmonics interpolation [103]. The basal plane defined on the endocardial reference was used to define the basal plane of the epicardial reference.

The automatic segmentation was evaluated against the epicardial manual contouring with MAD, HD and Dice. Myocardial volumes at ED and ES were also compared. The results of the proposed framework were also compared to the same framework without the use of the SSM regularization to study the impact of this regularization on the segmentation accuracy. Results are presented in mean±standard deviation.

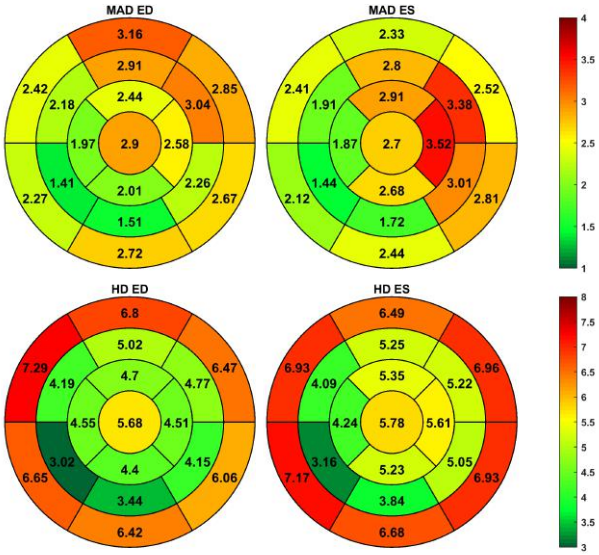

Figure 7.3: Bullseye plots of average MAD and HD at every region for ED and ES epicardial segmentation. Measures in mm.

7.4 Results

Table 7.1 shows the segmentation and tracking results for the proposed approach for the epicardium. Note that the endocardial segmentation performance is unaltered by the addition of the epicardial surface due to the nature of the 2S model. The endocardial segmentation results are thus the same as those described in Chapter 5. As in Chapter 5 the introduction of the SSM regularization has a strong positive effect on the segmentation leading to more accurate segmentation of the endo- and epicardial surfaces.

Figure 7.3 shows a regionwise analysis of error performed by analysing MAD and HD in each of the 17 segments of the LV according to [10]. It can be observed that the greatest errors are found for the basal segments, especially in HD. There seems to be a trend towards worst segmentation on the anterolateral side of the LV.

Figure 7.4 shows the best and worst epicardial segmentation results at ED and ES on the training dataset compared to the manual references by the expert.

A comparison between the manual and automatic myocardial volumes is shown in Figure 7.5. The myocardial volume bias was -18.6 ± 33.6ml at ED and 11.2 ± 25.6ml at ES, where the bias at ED was statistically significantly different from zero at $p < 0.05$.

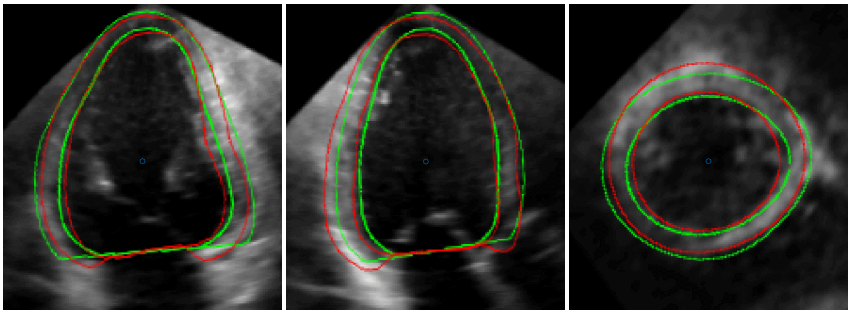

(a)

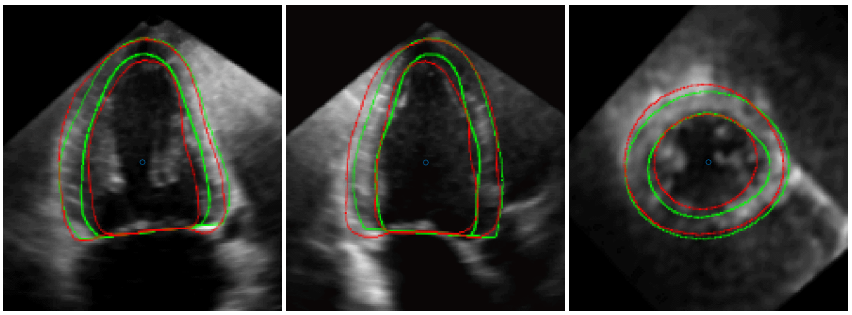

(b)

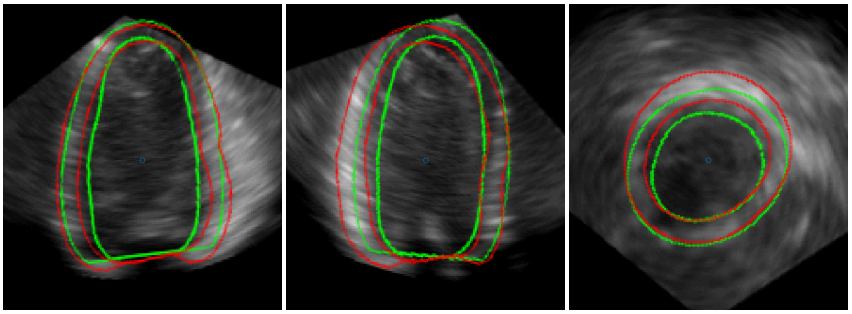

(c)

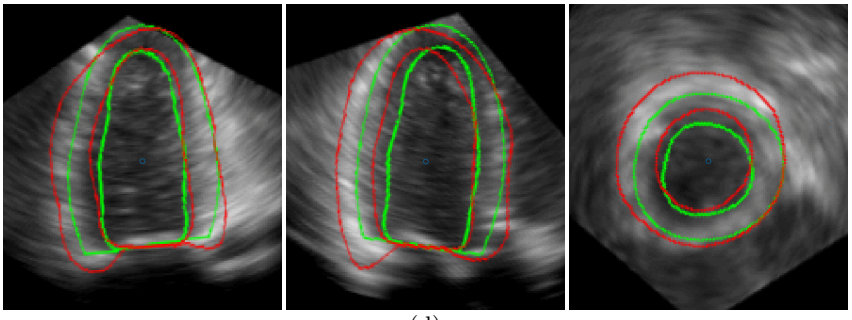

(d)

Figure 7.4: Best (a,b) and worst (c,d) endo- and epicardial automatic segmentation results (red) compared to manual contouring (green) at ED (a,c) and ES (b,d). The three orthogonal planes shown for each 3D image were chosen according to the automatically defined LAx/SAx orientation.

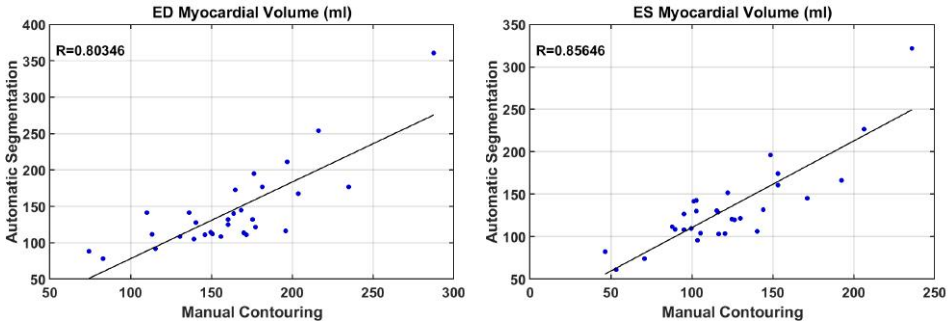

Figure 7.5: Correlation plots of myocardial volumes computed for the manual contours and the automatic contours at ED and ES.

7.5 Discussion

From Table 7.1 it is clear that the proposed framework presents an excellent segmentation and tracking performance for the epicardium. Given the inherent characteristics of the 2S model used for the epicardial segmentation, it can be concluded that the obtained segmentation performance for the epicardium takes advantage of the excellent performance for the endocardial segmentation shown in Chapter 5. The comparison with the same framework without the SSM also clearly demonstrates the importance of this regularization for both the endo- and epicardial segmentation. It remains true, however, that the epicardial segmentation performs worse than the endocardial segmentation and this is a direct consequence of the fact that the epicardial contour is more challenging to contour, especially in apical views [75].

Comparing with the state-of-the-art it appears that the current framework outperforms previously proposed 3D epicardial segmentation frameworks. In Chapter 5, the 2S ED epicardial segmentation with BEAS was proposed, achieving an MAD, HD and Dice of 2.70 ± 0.65mm, 12.2 ± 3.66mm and 0.112 ± 0.026. The semiautomated biventricular segmentation approach by Bersvendsen et al. [232] obtained an MAD of 3.1 ± 0.5mm for the LV epicardium. Nevertheless, a direct comparison between these studies is not straightforward as the datasets used for validation were not the same.

Regarding the regionwise analysis in Figure 7.3, the worst performance on the anterolateral side can be explained by inherent image characteristics, namely dropout which is common in this region due to the proximity to lung tissue. This has been verified both in comparison among manual endocardial contouring by different experts and in numerous 3D segmentation frameworks for the endocardium [114], including the BEAS framework presented in Chapter 5. It has also been observed in the original 2S ED epicardial segmentation framework using BEAS presented in Chapter 6. Regarding the basal segments, it seems that this is brought on mostly by the definition of a base plane in the manual reference as was reported in Chapter 6. Because in the manual references a base plane is defined and used to crop the

epicardium mesh, the same must be done for the automatic segmentation but even small errors in the position and angle of that plane can result in large HDs. This effect can be seen on Figure 7.4, especially for the worst case.

Regarding the myocardial volume, although a significant bias was obtained at ES the correlation values obtained are high, especially taking into account the number of factors that contribute to this final value of myocardial volume.

7.6 Conclusion

In this work, a fully automatic full-cycle LV myocardial segmentation and tracking framework is proposed. This framework is an extension of a previous work on LV endocardial segmentation and takes advantage of its excellent endocardial segmentation performance to obtain a promising epicardial segmentation performance through the 2S model coupling the endo- and epicardial surfaces and the use of a myocardial SSM to provide additional shape information. Furthermore, the current work is validated on a publicly available and robust database on which the epicardial contours were drawn by an expert in this study. The publication of these epicardial references on the same platform as the database will allow future studies direct comparisons to other state-of-the-art methods, accelerating meaningful research in the field.

Table 7.1: Performance on the CETUS testing datasets for endo- and epicardial surfaces. MAD, HD and Dice of the proposed shape-based myocardial segmentation framework compared to the same framework without using the SSM. All values in mean ± standard deviation. $\star$, † and ‡ indicate respectively that the difference to the proposed framework was statistically significant at a $p<0.05$, $p<0.01$ and $p<0.001$ level.

Method	Surface	**MAD (mm)**		**HD (mm)**		**Dice**	
		ED	**ES**	**ED**	**ES**	**ED**	**ES**
Proposed	Endocardium	1.81 ± 0.59	1.98 ± 0.66	6.31 ± 1.69	6.95 ± 2.14	0.909 ± 0.034	0.875 ± 0.046
	Epicardium	2.43 ± 0.69	2.51 ± 0.63	9.25 ± 2.69	9.86 ± 3.05	0.911 ± 0.031	0.896 ± 0.034
No SSM	Endocardium	$2.26 \pm 0.72^{\ddagger}$	$2.45 \pm 0.85^{\ddagger}$	$8.10 \pm 2.62^{\ddagger}$	$8.19 \pm 3.03^{\star}$	$0.894 \pm 0.040^{\ddagger}$	$0.861 \pm 0.054^{\star}$
	Epicardium	$3.05 \pm 0.69^{\ddagger}$	$3.35 \pm 0.84^{\ddagger}$	$11.09 \pm 2.69^{\dagger}$	$11.77 \pm 2.68^{\dagger}$	$0.885 \pm 0.027^{\ddagger}$	$0.856 \pm 0.042^{\ddagger}$

Part II

Applications

Chapter 8

Integration of Segmentation Methodologies in a Distributable User-Friendly Software Tool

Abstract

In this chapter, the integration of the tools developed and validated in the first part of this thesis is discussed. While previous chapters presented the tools developed and their validation, the availability of these tools in a distributable user-friendly software is of great importance to allow their application in the future. Speqle3D, an in-house developed software package, was thus chosen for this purpose. The tools presented in this thesis were implemented in a user-friendly way in this software environment.

8.1 Introduction

While the development and validation of novel segmentation and tracking tools is of value per se, it is equally important to make them available so that they can be applied in other studies. In the case of myocardial segmentation, these studies could be direct applicational studies, for example to obtain further insight on 4D myocardial geometry in a specific population, or studies where the myocardial segmentation acts as an initial step in a post processing chain such as strain or machine learning applications, where segmentation could be used to define the region of interest (ROI). Furthermore, the direct use of this technology in a clinical setting could be of much use by providing additional clinical information through an automated workflow. No matter the application, it thus becomes of great importance to make the tools developed available in a distributable software package that can be easily used by clinicians and/or researchers from different backgrounds.

8.2 Speqle3D

Speqle3D is an in-house developed software package to visualize and process 2D echocardiography (2DE) and real-time 3D echocardiography (RT3DE) datasets. Among other characteristics, Speqle3D allows for the slicing and orientation of 3D images in arbitrary planes and manual contouring of structures. Speqle3D relies on a graphical interface compiled in MATLAB, thus making it extremely simple from both the user point of view as it appears like a usual graphical interface but also from the programming point of view as changes can be easily incorporated in a MATLAB environment. Speqle3D is freely available for research purposes with a computer-based license so that it is possible to distribute it to researchers that want to use it. Figure 8.1 shows the basic interface of Speqle3D and an example of an RT3DE image as seen in the interface.

Three different tools were implemented in Speqle3D: the left ventricular (LV) myocardial segmentation described in Chapter 7, an adapted version of the LV myocardial segmentation for 2DE and the 3D mitral valve (MV) segmentation described in Appendix A. These tools complement those already implemented in

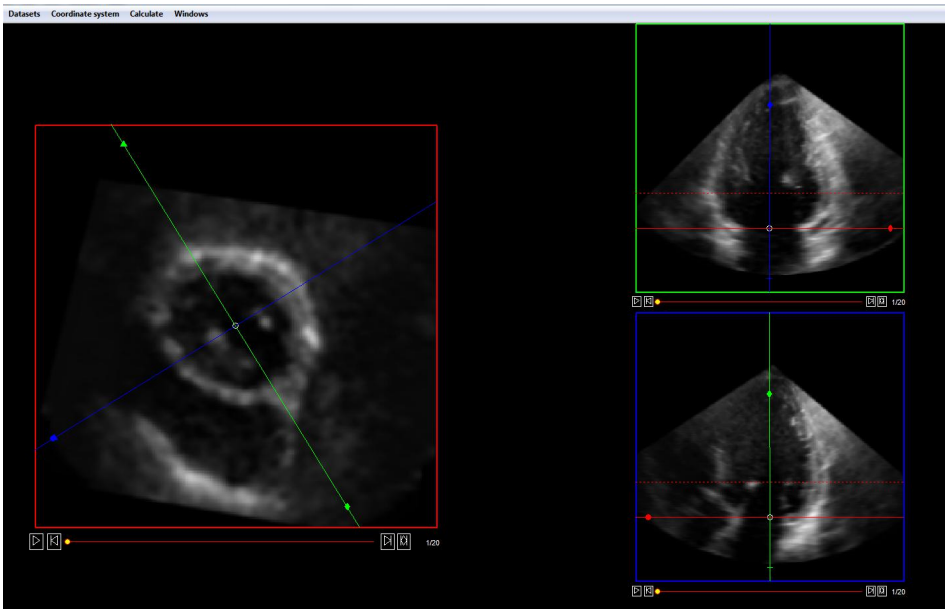

Figure 8.1: Speqle3D interface and example RT3DE dataset.

Speqle, namely 2D registration for myocardial deformation imaging [233], automatic aortic valve (AV) segmentation for aortic annular sizing [234] and left atrial (LA) appendix segmentation.

8.2.1 3D Myocardial Segmentation

The 3D myocardial segmentation framework described in Chapter 7 was implemented in Speqle3D so that a full cycle segmentation can be obtained in a fully automatic way. The workflow is as follows:

1. The user annotates end diastole (ED) and end systole (ES) by scrolling through time and selecting the correct frames. If ED and ES are not annotated, segmentation is performed only on the current frame.

2. Endocardial segmentation is performed by opening the B-spline Explicit Active Surfaces (BEAS) toolbox and clicking on 'Endocardium'. Initialization of the surface at ED is performed using the method proposed by Barbosa et al. in [165] and the LV is segmented according to the framework proposed in Chapter 5. Alternatively, a semi-automatic segmentation can be performed by first aligning the long axis (LAx) and short axis (SAx) manually. This can be helpful in images of low image quality or when the field of view (FOV) is not conventional, leading to a failure of the initialization algorithm. The segmentation is propagated from ED to ES using the localized anatomical affine

optical flow (lAAOF) proposed in [199] and the segmentation result is refined at ES using shape-based regularization.

3. Manual correction of the endocardial surface is then possible at any frame. This is possible in a separate window where the user is presented with a set of predefined LAx slices and their orientation in the 17 segment model [10]. The correction is performed by placing points in each of the slices. The point is then used to obtain a new contour on that slice through spline interpolation. To control the influence of each of the points placed, a sphere of influence is presented to the user for each point which determines the section of the original contour which is discarded before spline interpolation. In that manner, the user can control how local the influence of the point is. The manual correction interface is shown in Figure 8.2, showing the image slice being corrected and the 17-segment model for 3D orientation. When the user is satisfied with the corrected contours, the 3D mesh is interpolated leading to a new segmentation result for that frame. The corrected mesh is then propagated automatically throughout the heart cycle.

4. By clicking 'Epicardium' on the BEAS toolbox, myocardial segmentation is performed. The endocardial segmentation at ED is used to initialize the epicardial surface which is segmented according to the method described in Chapter 7. This segmentation is propagated from ED to ES using the lAAOF proposed in [199] and the segmentation result is refined at ES using shape-based regularization.

5. Epicardial manual correction is possible through the placing of user points within the same manual correction environment and methodology described for the endocardium and the corrected mesh is propagated automatically throughout the heart cycle.

An example of a segmented LV myocardium in Speqle3D is shown in Figure 8.3 and the complete workflow can be appreciated in the link given in the footnote.

8.2.2 2D Myocardial Segmentation

Although this thesis focused on RT3DE as potentially the standard echocardiographic examination of the future, 2DE is currently still the most used imaging technique both in clinical practice and research. As such, it was important to adapt the framework developed in this thesis to analyse 2DE LV images. This can easily be done in the BEAS framework by adapting the explicit function to a polar rather than a spherical domain and tuning the parameters. Given the much larger variability of views in 2DE than 3D, an adaptation of the automatic LAx initialization would not be able to have a satisfactory feasibility and, as such, manual initialization was implemented. The workflow is as follows:

https://kuleuven.box.com/s/bii3yf4o5v4rz3295ua6ctyijjokzy1k

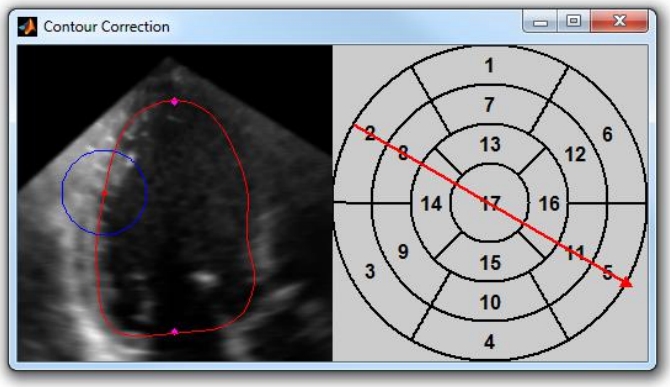

Figure 8.2: Speqle3D manual correction interface. User point shown in red with blue sphere of influence. Magenta points indicate intersections with LV contours from other LAx slices.

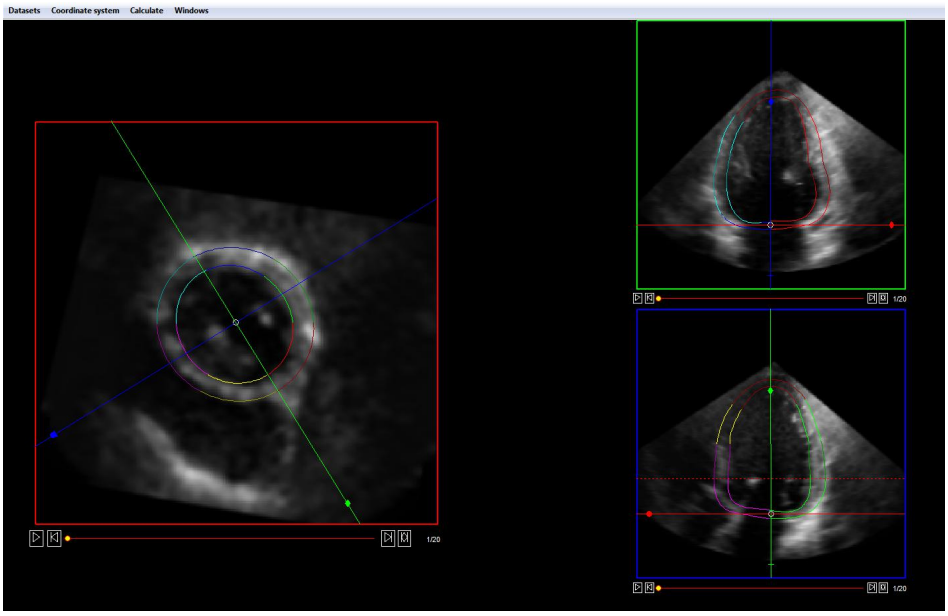

Figure 8.3: Automatic LV myocardial segmentation on RT3DE on Speqle3D environment.

1. The user annotates ED and ES by scrolling through time and selecting the correct frames. If ED and ES are not annotated, segmentation is performed only on the current frame.

2. The user places three points on the ED frame, at the mitral annulus (MA) and apex.

3. Endocardial segmentation is performed by opening the BEAS toolbox and clicking on 'Endocardium'. The three user points are used to initialize the endocardial surface through spline interpolation. LAx orientation is determined as the direction from the mid-basal point to the apex. Endocardial segmentation is performed in two stages as proposed in Chapter 5 for RT3DE. A first segmentation stage is performed using the modified Yezzi energy proposed in [165] and a second stage using the same data attachment term with a shape model regularization. This segmentation is propagated from ED to ES using the lAAOF proposed in [199] and the segmentation result is refined at ES using shape-based regularization.

4. Endocardial manual correction is possible through the placing of user points within the same manual correction environment and methodology described for 3D myocardial segmentation. The corrected mesh is then propagated automatically throughout the heart cycle.

5. By clicking 'Epicardium' on the BEAS toolbox, myocardial segmentation is performed. The endocardial segmentation at ED is used to initialize the epicardial surface which is segmented using a myocardial shape model according to the method described in Chapter 7. This segmentation is propagated from ED to ES using the lAAOF proposed in [199] and the segmentation result is refined at ES using shape-based regularization.

6. Epicardial manual correction is possible through the placing of user points within the same manual correction environment and methodology described for 3D myocardial segmentation and the corrected mesh is propagated automatically throughout the heart cycle.

The angular discretization of the boundary representation was set empirically at 48 points and the B-spline scale h at 2^1 for both endo- and epicardial surfaces. The neighborhood region limit ρ was set at 15mm. The endo- and myocardial shape models were built from a set of 2DE images from 500 patients collected in a clinical setting. This dataset emcompasses both 2- and 4-chamber images manually contoured at ED and ES. Following the methodology described in Chapter 5 and 7, the contours were scaled and aligned and principal component analysis is used to obtain a statistical shape model (SSM) representing the shape variability of the LV. As such, four different SSMs were obtained, at ED and ES for 2- and 4-chamber images. The 2- or 4-chamber set of SSMs is then selected based on the image metadata (if absent no SSM regularization is applied). The hard and soft regularization terms α and β were set empirically at 1 and 0.0002 for the endocardial

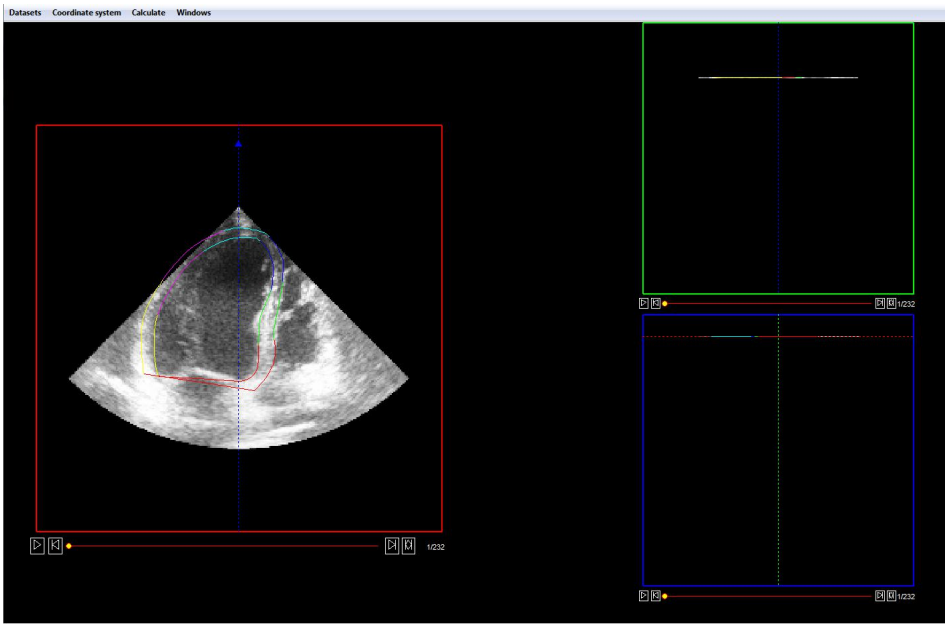

Figure 8.4: Semi-automatic LV myocardial segmentation of 4-chamber 2DE on Speqle3D environment.

SSM and at 1 and 0.002 for the myocardial SSM. The hyperparameter for ES shape-based regularization γ was set at 0.25 for both endo- and epicardial segmentation. An example of a segmented 2DE LV myocardium in Speqle3D is shown in Figure 8.4 and the complete workflow can be appreciated in the link given in the footnote.

8.2.3 3D Mitral Valve Segmentation

The 3D MV segmentation framework described in Appendix A was implemented in Speqle3D so that 4D MV geometry can be obtained. As the MV initialization depends on a previous LV segmentation at ED, 3D endocardial segmentation must first be performed. The workflow is as follows:

1. The user annotates ED and ES by scrolling through time and selecting the correct frames. If ED and ES are not annotated, segmentation is performed only on the current frame.

2. Endocardial segmentation is performed by opening the BEAS toolbox and clicking on 'Endocardium' as detailed in Section 8.2.1.

3. MV segmentation is performed by clicking on 'Mitral Valve' on the BEAS toolbox. MV initialization is performed according to the method described in Appendix A. Alternatively, a semi-automatic initialization can be performed

https://kuleuven.box.com/s/bii3yf4o5v4rz3295ua6ctyijjokzy1k

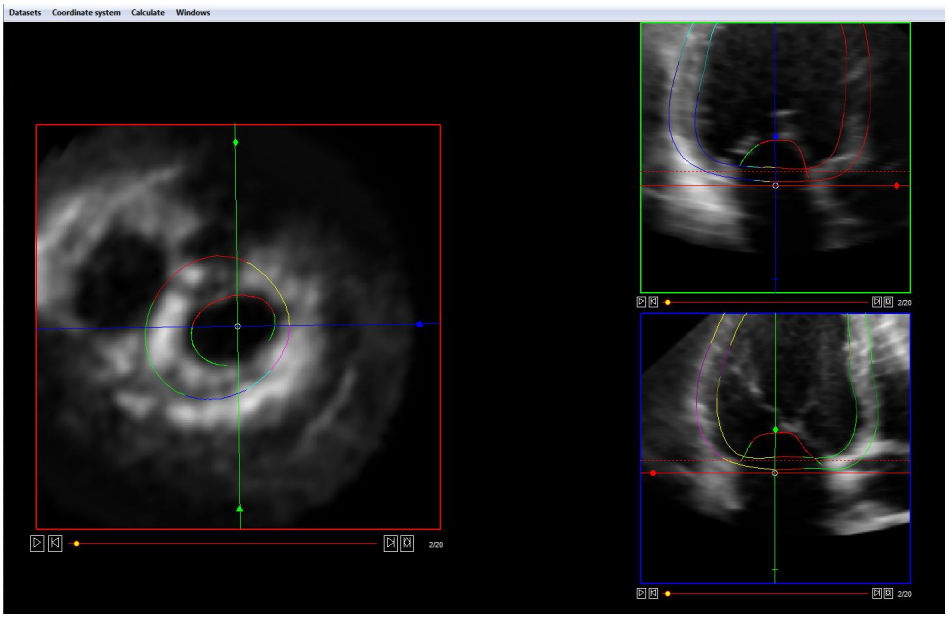

Figure 8.5: Automatic MV segmentation on RT3DE image on Speqle3D environment.

by orienting the LAx and SAx manually to the MV and LV outflow tract (LVOT). For this semi-automatic initialization the LV segmentation from step 2 is no longer needed and the MV is initialized as a half-sphere of radius equal to the length of the LAx defined by the user. Segmentation is performed at ED according to the method described in Appendix A and this segmentation is propagated from ED to ES using the lAAOF proposed in [199].

4. MV manual correction is possible through the placing of user points within the same manual correction environment and methodology described for 3D myocardial segmentation. Instead of the 17-segment model presented on the 3D myocardial segmentation tool, a schematic of the MV and LVOT is shown to aid the user in the 3D orientation of the 2D slices shown. The corrected mesh is propagated automatically throughout the heart cycle.

An example of a segmented MV in Speqle3D is shown in Figure 8.5 and the complete workflow can be appreciated in the link given in the footnote.

8.3 Conclusion

In conclusion, the tools developed in this thesis were implemented in a software application, Speqle3D, in an user-friendly way, enabling manual input and allowing for the extraction of 4D geometry of different anatomical structures. This then

https://kuleuven.box.com/s/bii3yf4o5v4rz3295ua6ctyijjokzy1k

facilitates the application of the tools developed in this thesis in a clinical setting. Furthermore, it enables the use of the tools developed in future studies, such as using the segmentation as an initial step in other postprocessing methods such as strain applications or machine learning tools or more clinical oriented studies trying to obtain more information regarding 4D geometry of the LV myocardium and the MV.

Chapter 9

Non-invasive Myocardial Performance Mapping Using 3D Echocardiographic Stress-Strain Loops

This chapter is based on a paper submitted for publication in a peer-reviewed journal: **Pedrosa J.**, Duchenne J., Queirós S., Degtiarova G., Gheysens O., Claus P., Voigt J., D'hooge J.. Non-invasive myocardial performance mapping using 3D echocardiographic stress-strain loops: validation against PET.

Abstract

Regional contribution to left ventricular (LV) ejection is of much clinical importance but its assessment is notably challenging. While deformation imaging is often used, this does not take into account loading conditions. Recently, a method for intraventricular pressure estimation was proposed, thus allowing for loading conditions to be taken into account in a non-invasive way. In this work, a method for 3D automatic myocardial performance mapping in echocardiography is proposed by performing 3D myocardial segmentation and tracking, thus giving access to local geometry and strain. This is then used to assess local LV stress-strain relationships which can be seen as a measure of local myocardial work. The proposed method was validated against 18F-fluorodeoxyglucose positron emission tomography (FDG-PET), the reference method to assess local metabolism clinically. Averaged over all patients, the mean correlation between FDG-PET and the proposed method was 0.67 ± 0.18. In conclusion, the proposed method shows promising results for fully automatic non-invasive estimation of regional myocardial performance.

9.1 Introduction

The assessment of the regional contribution to LV ejection has long been an object of interest in clinical cardiology and is clinically most often assessed through visual wall motion readings. However, such readings are subject to high intra- and inter-observer variability. More objective measurements of shortening indices through regional deformation imaging have thus been introduced to tackle this problem [102, 235, 236]. However, local deformation is highly dependent on loading conditions and to truly estimate myocardial performance, the relation between deformation and loading conditions must be taken into account [237]. Nevertheless, it is challenging to estimate loading conditions non-invasively and most studies thus resort to invasive intraventricular pressure measurements. Suga [238] first proposed such an approach by successfully correlating LV pressure-volume loop area to global myocardial oxygen consumption in a canine model and this approach was later validated in a clinical setting [239]. Following the same rationale, regional myocardial work was estimated by relating local myocardial deformation to pressure in several studies [240–244]. While these techniques have been proposed already decades ago, they have seen limited clinical application due to their complexity and the need for an invasive intraventricular pressure measurement. Recently, Russel et al. [245] have proposed a method for non-invasive estimation of intraventricular pressure, thus allowing for non-invasive estimation of myocardial work. Nevertheless, pressure remains a global loading parameter as local loading, expressed as myocardial stress, depends on LV geometry. Such an approach was followed in a recent study [246], where the authors used Laplace's law to estimate local stress from non-invasive pressure measurements and local geometry, which, related to local strain was equated to local myocardial work.

In spite of these recent advances, the methodology remains complex as obtaining

the full myocardial performance map requires 3 different long axis (LAx) views to be acquired and in each of the views the LV must be segmented and local strains computed. As such, the use of real-time 3D echocardiography (RT3DE) can play a role in decreasing the complexity of this method by decreasing the number of acquisitions needed. Although manual analysis of 3D images is more challenging than 2D, automatic methods can be used to obtain 3D local LV geometry and strains, further decreasing the complexity of the method. Moreover, the acquisition of RT3DE rather than 2D echocardiography (2DE) allows the analysis of the full 3D myocardial motion rather than being limited to in-plane motion as in [243,245,246] where only longitudinal strain-stress loop area was considered.

As such, in this study, a method for non-invasive myocardial performance mapping on RT3DE is proposed. A validated fully automatic method for myocardial segmentation and tracking presented in Chapter 7 was used to obtain 3D local LV geometry and strain. Intraventricular pressure was estimated according to the method by Russel et al. [245], which is used together with local geometry to estimate local LV stress. The proposed LV stress-strain loop areas were then validated against FDG-PET, the reference method to clinically assess local metabolism.

9.2 Methodology

9.2.1 3D Left Ventricular Myocardial Segmentation

3D LV myocardial segmentation was performed using B-spline Explicit Active Surfaces (BEAS) according to the framework proposed in Chapter 7. To extract local geometry and strain, the LV segmentation obtained was divided into 17 segments according to [10] and the extracted parameters averaged within each segment. At each frame, the local wall thickness h was computed, defined as the distance from the endo- to the epicardial surface along the endocardial surface normal. Longitudinal and circumferential curvatures, k_l and k_c, were also extracted taking advantage of the spherical domain on which the BEAS segmentation is defined:

$$k_l = \bar{k} - \sqrt{\bar{k}^2 - K}, \tag{9.1}$$

$$k_c = \bar{k} + \sqrt{\bar{k}^2 - K}, \tag{9.2}$$

where $\bar{k}$ and K are respectively the mean and gaussian curvatures obtained according to

$$\bar{k} = \frac{eG + gE}{2EG}, \tag{9.3}$$

$$K = \frac{eg - f^2}{EG}, \tag{9.4}$$

where E and G are coefficients of the first fundamental form and e, f and g are coefficients of the second fundamental form [228]. Segmental strain was computed throughout the heart cycle for all three components - longitudinal (ε_l), circumferential (ε_c) and radial (ε_r).

9.2.2 Left Ventricular Stress Estimation

In order to estimate LV stress, the equations proposed by Mirsky et al. [247] were used, thus:

$$\sigma_l = \frac{P.r_l}{h(2 + \frac{h}{r_l})}, \tag{9.5}$$

$$\sigma_c = \frac{P}{h(\frac{1}{r_c} + \frac{1}{r_c} + \frac{h}{r_l r_c})}, \tag{9.6}$$

where σ_l and σ_c are, respectively, the longitudinal and circumferential components of LV stress, P is the intraventricular pressure and $r_i = 1/k_i$ is the radius of curvature along direction i. For a more extensive reasoning of the assumptions behind the equations chosen, the reader is referred to the original paper by Mirsky et al. [247].

Intraventricular pressure was estimated according to the method by Russel et al. [245], which essentially scales a typical LV pressure trace based on valve opening/closing and measured systolic arterial cuff pressure. The valve events were manually annotated by visual inspection of the RT3DE images.

To estimate the radial LV stress σ_r, the generalized 3D Hooke's law was used, assuming that the myocardium is an elastic, isotropic and incompressible medium:

$$\varepsilon_r = \frac{1}{E}(\sigma_r - \mu(\sigma_l + \sigma_c)), \tag{9.7}$$

where E and μ are, respectively, the Young's modulus and Poisson coefficient of the medium. Given that the myocardium is assumed to be incompressible, $\mu = 0.5$.

9.2.3 Myocardial Performance Mapping

To obtain a map of myocardial performance, a stress-strain loop was calculated for each of the components (i.e. radial, longitudinal and circumferential). The sum of the area of each of these loops, hereinafter referred to as L+C+R loop area, was then taken as an estimate of the total local myocardial work.

It can be shown that the radial stress-strain loop area is independent of the Young's modulus E chosen given that:

$$\begin{aligned} A\{\varepsilon_r, \sigma_r\} &= \frac{1}{2}\int \sigma_r {\varepsilon_r}' - \varepsilon_r {\sigma_r}' dt \\ &= \frac{1}{2}\int (E\varepsilon_r + \mu(\sigma_l + \sigma_c)){\varepsilon_r}' - \varepsilon_r (E\varepsilon_r + \mu(\sigma_l + \sigma_c))' dt \\ &= \frac{\mu}{2}\int \sigma_l {\varepsilon_r}' - \varepsilon_r {\sigma_l}' dt + \frac{\mu}{2}\int \sigma_c {\varepsilon_r}' - \varepsilon_r {\sigma_c}' dt \\ &= \mu A\{\varepsilon_r, \sigma_l\} + \mu A\{\varepsilon_r, \sigma_c\}, \end{aligned} \tag{9.8}$$

where $A\{\varepsilon_i, \sigma_j\}$ is the area of the loop formed by stress component i and strain component j. For simplicity sake, the prime symbol was used to represent the derivative in t.

9.3 Experiments

12 non-ischemic and 7 ischemic patients were selected from the WORK-CRT study, which followed heart failure patients undergoing cardiac resynchronization therapy (CRT) at the University Hospitals Leuven (ClinicalTrials.gov Identifier: NCT02537782). The patients were selected based on showing acceptable RT3DE spatiotemporal resolution and image quality and FDG-PET analysis one week prior to CRT.

3D LV myocardial segmentation was performed for each patient and the myocardial performance maps estimated based on the method described above. A comparison to FDG-PET was performed by using the normalized tracer uptake (%). The LV segment with the highest tracer uptake was used as a reference (100%), and segmental values reported as percentages of this value.

For comparison to the proposed myocardial performance maps, pressure-strain loop areas as proposed in [245] were also computed.

9.4 Results

An example of the myocardial performance map and FDG-PET tracer uptake map obtained for one patient as well as the correlation between the two measurements is shown in Figure 9.1. Qualitatively, it can be observed that there is a good correspondence between the L+C+R stress-strain loop area in Figure 9.1(a) and the FDG-PET map in Figure 9.1(b). By plotting the segmental L+C+R stress-strain loop area values against the FDG-PET tracer uptake as in Figure 9.1(c), a correlation value can be obtained showing the agreement between both measures. Among all patients, the Pearson correlation coefficient was 0.67 ± 0.14.

A comparison of the performance of each of the components individually to the L+C+R stress-strain loop area is shown in Fig. 9.2. It can be seen that the contribution of all three spatial components outperforms any of the other individually considered components. The difference between the correlations using L+C+R stress-strain and pressure-strain loop areas was also statistically significant at $p < 0.05$.

9.5 Discussion

It is clear that the proposed methodology can successfully estimate LV myocardial work in a non-invasive way. Both local deformation and loading conditions are taken into account, thus using additional information in comparison to myocardial deformation imaging, which is essential for the estimation of myocardial performance. The proposed method is also of low complexity, as only one image needs to be acquired. Moreover, the LV myocardial segmentation is fully automatic and only the valve events need to be annotated manually.

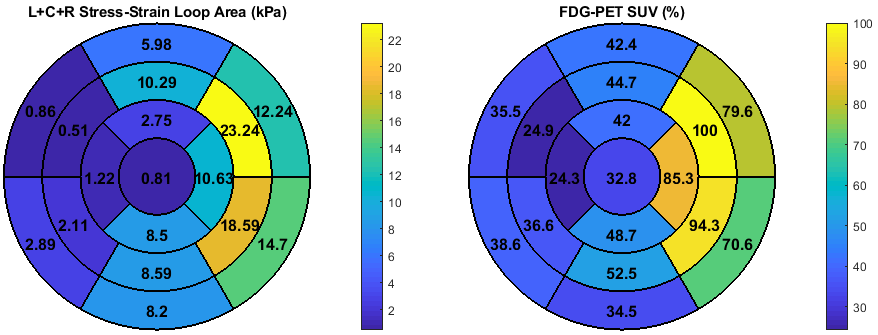

(a) (b)

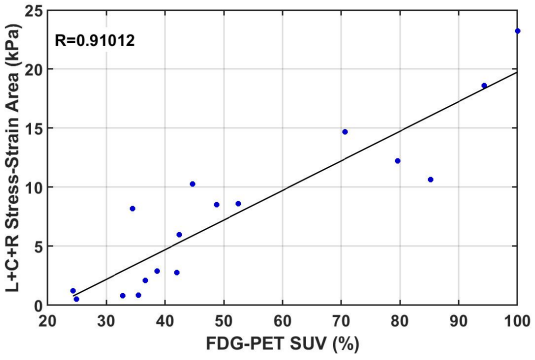

(c)

Figure 9.1: Myocardial performance map (a) and FDG-PET tracer uptake (b) for a given patient and correlation between the two (c).

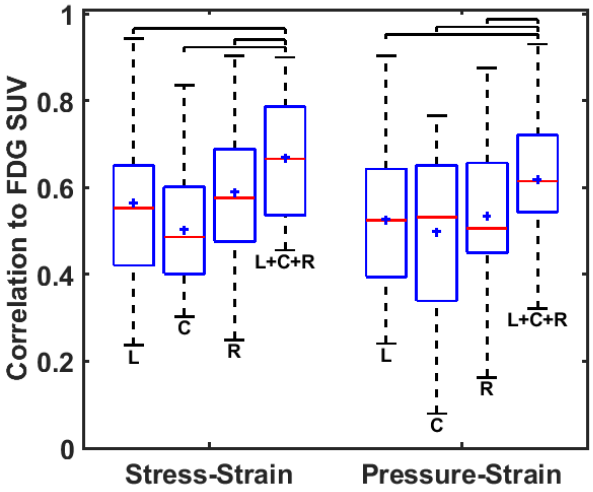

Figure 9.2: Correlation between FDG-PET tracer uptake and each stress-strain/pressure-strain loop area across all patients. Brackets indicate statistically significant differences at $p < 0.05$; only differences to L+C+R loop area within each group are shown.

Analysing Fig. 9.2, it becomes clear that the contribution of all three components of stress and strain is necessary in the final myocardial performance map, as the L+C+R loop area was statistically significantly better than any of the three components independently. Specifically, the longitudinal stress-strain and pressure-strain loop areas are equivalent to the approaches in [246] and [245] as in those studies LAx 2DE was used and thus only longitudinal components were assessed. In spite of the promising results of those studies, it is shown that RT3DE can provide additional information, thereby resulting in better correlation to FDG-PET tracer uptake.

Furthermore, it was shown that the correlation between the L+C+R stress-strain and FDG-PET tracer uptake was statistically significantly different and greater than using L+C+R pressure-strain. This highlights the importance of considering local, rather than global loading, through myocardial geometry for an accurate myocardial performance map.

Nevertheless, there are limitations to this study which must be considered. First, the number of patients is relatively small and a larger dataset would certainly strenghten the conclusions drawn in this study. Secondly, RT3DE is, in spite of the improvements in recent years, a more challenging technique than 2DE in terms of acquisition window and image quality in some patients, which might have an impact in the applicability of this method to the general population. However, the improvements to RT3DE's spatiotemporal resolution are expected to continue as more advanced beamforming techniques migrate to commercial systems, improving the quality of information that can be obtained with RT3DE and simultaneously

increasing the applicability of RT3DE based methods such as the one proposed in this study. Thirdly, given the fact that normalized FDG-PET tracer uptake was used as ground truth, a direct comparison between patients is not possible. This might have an effect on the final results as correlations are only possible within each patient. An alternative approach could be to use the FDG-PET standard uptake ratio as proposed in [248], which would allow for a more robust measurement of myocardial oxygen consumption and a comparison across all patients. However, this method could not be applied to this population in the scope of this study. Finally, the equations 9.5, 9.6 and 9.7 used to estimate LV stress present numerous assumptions which are known to be violated in the LV myocardium. While numerous forms of these equations exist, the most known being perhaps Laplace's law, these were chosen as they predict different longitudinal and circumferentail stress. Nevertheless, due to the assumption involved, it would be important to consider more complex analysis tools adapted to complex geometries as the LV myocardium, such as finite element methods. However, good correlation with FDG-PET, the reference method to clinically assess local metabolism, was obtained validating the proposed method.

In terms of future work, the automation of the annotation of the valve events would be of interest as it is currently the only step that requires user interaction. This would further simplify the method, rendering it fully automatic.

9.6 Conclusion

In conclusion, a novel non-invasive method for myocardial performance mapping in RT3DE is proposed. The fact that the proposed method relies on RT3DE not only simplifies the protocol, as only one image must be acquired and processed, but gives access to the full 3D information, leading to more accurate results than previous similar implementations in 2DE. Furthermore, the proposed method relies on an automatic segmentation framework, where only the valve events must be manually annotated making it simple to apply.

Chapter 10

Real-Time Anatomical Imaging of the Heart on an Experimental Ultrasound System

This chapter is based on a paper published in the proceedings of the *2017 IEEE International Ultrasonics Symposium (IUS)*: **Pedrosa J.**, Komini V., Duchenne J., D'hooge J.. Real-time anatomical imaging of the heart on an experimental ultrasound system. In *2017 IEEE International Ultrasonics Symposium (IUS) proceedings* Sep 6 (pp. 1-4).

Abstract

Fast echocardiography imaging requires a reduction of the number of transmit events. This can be achieved through advanced beamforming techniques but restricting the field of view (FOV) to the anatomically relevant domain, e.g. the myocardium, can increase frame rate (FR) further. In the present work, an anatomical scan sequence was implemented and tested experimentally by performing real-time segmentation of the myocardium on conventional B-mode and feeding this information back to the scanner in order to define a fast myocardial scan sequence. Ultrasound imaging was performed using HD-PULSE, an experimental fully programmable 256 channel ultrasound system equipped with a 3.5MHz phased array transducer. A univentricular polyvinyl alcohol (PVA) phantom was connected to a pump to simulate the cardiac cycle to perform *in vitro* validation of this approach. In addition, three volunteers were also imaged from an apical 4-chamber view to demonstrate the feasibility of this method *in vivo*. It is shown that this method is feasible to be applied in real-time and *in vivo* giving a minimum gain in FR of 1.5.

10.1 Introduction

Echocardiography is the modality of choice for routine diagnosis and assessment of cardiac function due to its low cost, wide availability and lack of ionizing radiation. Nevertheless, in spite of having good spatiotemporal resolution, traditional ultrasound cannot resolve the totality of cardiac mechanical events, especially when considering some very short lived events such as the mechanical activation of the left ventricle (LV) pre-ejection. As such, potentially important clinical information might be lost.

Recently, very high temporal resolution ultrasound imaging has been made possible through the development of more complex scan sequences such as multi-line acquisition (MLA), retrospective gating, diverging wave (DW) imaging and multi-line transmit (MLT) [59]. In MLA, multiple neighboring lines are reconstructed simultaneously for each transmit beam [47]. This technique is already implemented in most commercial scanners. Retrospective gating divides the sector into smaller subsectors and each of these subsectors is imaged at high FR using electrocardiogram (ECG) as a timing reference [46]. It is then possible to combine the different subsectors into a single high FR sector. Retrospective gating is also a standard technique for 3D imaging. However, this fusion process may fail if the cardiac cycles between the subsectors are markedly different or when the subject's heartbeat is irregular leading to stitching artifacts. DW imaging relies on the transmission of a single or a small number of DW to reconstruct the whole sector [55]. However, this technique significantly compromises spatial resolution and contrast-to-noise ratio, thus requiring coherent spatial compounding which in turn compromises the gain in FR [249]. Alternatively, MLT imaging relies on the simultaneous transmission of multiple focused beams [49]. In spite of the possibility of cross-talk between different beams, it has been shown that this effect is very limited when MLT is carefully

setup [183]. Furthermore, MLT maintains similar spatial resolution to traditional ultrasound as it uses focused beams. A more extensive review of the problematic of high FR imaging and potential solutions and applications can be found in subsection 2.3.3.

In spite of the substantial gain in FR provided by these fast imaging approaches, a significant portion of the image lines reconstructed using these techniques is of limited or no interest in the study of myocardial dynamics, as they cross the blood pool or are located outside the epicardium. A straightforward way to reduce the number of transmits and/or the number of image lines to be reconstructed would then be to limit the FOV to the anatomically relevant space only.

Lervik et al. have proposed a method for anatomical imaging by manually adjusting two wide transmit beams to cover the ventricular walls from the apical view [250]. In this way, the data from the blood pool is not acquired allowing for high FR imaging to be acquired and these authors showed that such a method can produce valuable clinical information. Nevertheless, the method proposed by Lervik et al. requires the user to select the myocardial walls which might not be practical in a clinical setting. Ortega et al. [251] have thus proposed to perform real-time segmentation of the myocardium on conventional B-scan mode images and feeding that information back to the scanner to define a fast myocardial scan sequence. In their work, real-time 3D echocardiography (RT3DE) images were obtained and the myocardium was segmented automatically using the B-spline Explicit Active Surfaces (BEAS) framework. This information was then used to obtain a coverage function, defining the percentage of myocardium covered by each line to be reconstructed, which was then used to set up an MLT sequence which could cover the associated FOV as fast as possible. It was shown by computer simulation that using such a technique would yield an FR gain around 2. By applying it with a 10MLT-4MLA configuration, a total FR gain of 80 was obtained.

As such, the aim of this study was to implement and validate the method proposed by Ortega et al. in an experimental ultrasound system. An *in vitro* setup using a univentricular phantom was first used to test the method. Subsequently, *in vivo* experiments were conducted to assess the feasibility of this method and the associated FR gain.

10.2 Methodology

10.2.1 Echocardiographic Acquisition

2D echocardiography (2DE) data was acquired using HD-PULSE, an experimental ultrasound system [252]. HD-PULSE is a fully programmable 256 channel experimental ultrasound system which allows controlling and reading-out of up to 1024 elements through 1:4 transmit and 4:1 receive multiplexing. It is a modular platform built on two National Instruments reconfigurable PXI systems, each containing 4 blocks of PCI Express cards controlling 32 channels. Each block is composed of a tri-level pulser with arbitrary pulse capability, a receiver card with

a low-noise pre-amplifier up to 32dB and two NI5752 analog-to-digital converters with 12-bit resolution and up to 50MS/s, allowing for real-time data processing and streaming on a field-programmable gate array (FPGA). All electronics can be controlled in a LabVIEW environment. A phased Samsung Medison P2-5AC probe with a center frequency of 3.5MHz was used for all acquisitions. Simultaneous ECG acquisition was performed on an external NI USB-7845R and real-time QRS detection performed on FPGA using the Pan-Tompkins algorithm [253].

10.2.2 Real-time Automatic Segmentation

Real-time segmentation of the myocardium was performed using the BEAS framework [3]. The method for shape-based myocardial segmentation detailed in Chapter 7 was adapted for 2D segmentation as detailed in Chapter 8. The endocardial surface was initialized automatically according to an adaptation of the method of LV long axis (LAx) detection proposed in [165] for 2DE. In brief, the intensity profile along equidistant lines parallel to the probe surface is extracted. It is assumed that the LV LAx is in the middle of the image and the LV wall on either side of the image is detected by finding the highest dark-to-bright gradient (from blood pool to LV wall). The estimated wall positions are used to define the LV LAx and the initial surface is defined through spline interpolation on the estimated wall positions. Additionally, a user point could be placed at the LV base to provide an anchor point for the LV LAx increasing the robustness of the method on lower quality images.

All methods were implemented in a LabVIEW environment thus allowing for real-time initialization and segmentation and user interaction.

10.2.3 Anatomical Imaging

Following the method proposed by Ortega et al. [251], the relevant FOV for functional cardiac imaging was defined as follows: first, real-time automatic myocardial segmentation is performed at end diastole (ED) through ECG triggering. This assures that the ventricle is captured at its larger dimension so that the outer wall is not excluded from the anatomical FOV. Secondly, a coverage function is built by calculating the percentage of each scan line that crosses the myocardium. Finally, the fast anatomical scan sequence is computed by excluding the scan lines of smaller myocardial coverage as given by the coverage function until a limit of total myocardial coverage T is achieved. This threshold T is defined prospectively by the user. Note that the resulting FOV is corrected to be spatially continuous in both walls, so that two small sectors are obtained covering each of the walls. The resulting anatomical scan sequence, computed in real-time, is then used to obtain high FR images of the LV.

10.2.4 Non-rigid Image Registration

In order to demonstrate the feasibility of anatomical imaging for functional myocardial imaging, a non-rigid image registration (NRIR) framework [233] was used to estimate the motion of the tissue in the image. In brief, the basic concept of NRIR is to deform a moving image I_M to align with a fixed image I_F. The displacement field $\mathbf{T}_\xi = (T_x, T_y)$ is computed at every pixel (x, y) and modeled as a tensor product of 2D cubic B-splines $\beta^3_\xi[\xi \in (x, y)]$ [254] such that

$$\mathbf{T}_\xi(x,y) = \sum_{i\in N_i}\sum_{i\in N_j} \mu_{\mathbf{ij}} \beta^3_x \left(\frac{x-\kappa^{ij}_x}{\sigma_x}\right) \beta^3_y \left(\frac{y-\kappa^{ij}_y}{\sigma_y}\right), \tag{10.1}$$

where N_ξ denotes the set of control grid points within the compact support of B-splines of intergrid position κ_ξ and spacing σ_ξ. The B-spline coefficients $\mu_{\mathbf{ij}}$ are then optimized in an iterative multiscale optimization process according to the sum of squared differences and a bending energy [254]. A detailed description of this method can be consulted in [233].

10.3 Experiments

In vitro

A univentricular homogeneous PVA phantom with realistic LV dimensions was manufactured and connected to a CardioFlow 5000MR pump (Shelley Medical Imaging Technologies, Ontario, Canada) as described in [255]. In brief, the phantom was submerged in a water tank and fixed so that apical scanning was possible. The pump was connected to the PVA phantom in a closed circulation so that the pump flow deforms the phantom through the increase/decrease of pressure. A sinusoidal flow waveform was used to cyclically (60bpm) inflate/deflate the phantom in order to simulate cardiac motion/contraction. To have an independent measure of tissue deformation, a digital ultrasonic measurement system (Sonometrics Corporation, London, Ontario, Canada) was used. Two ultrasonic microcrystals were attached to the wall in the same longitudinal direction to obtain reference longitudinal displacement. These microcrystals emit and detect ultrasonic pulses and thus the time of flight between the two microcrystals can be used to estimate the distance between them along time.

A 2MLT-2MLA approach was used to create a conventional B-scan of the phantom (FR 155Hz). BEAS was then used to perform segmentation in real-time at the moment of largest volume of the phantom. A total myocardial coverage value T of 85% was used to create an anatomical scan sequence from the obtained coverage function. A minimum of two seconds were captured for both conventional images and anatomical imaging and these were processed offline using NRIR to estimate the tissue motion. The longitudinal strain obtained with the ultrasonic microcrystals was then used as a reference by comparing it to the longitudinal strain obtained from NRIR at in the same wall region on both imaging modes.

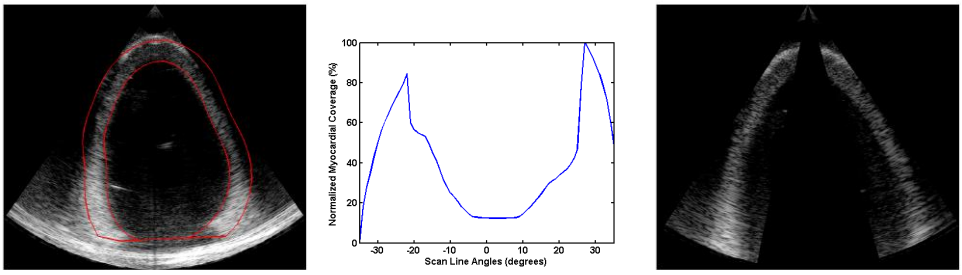

(a) (b) (c)

Figure 10.1: (a) Conventional B-mode obtained for the univentricular phantom at the moment of largest volume with BEAS segmentation imposed; (b) Normalized coverage function for phantom at the moment of largest volume (c) Anatomical B-mode obtained for the univentricular phantom.

In vivo

Three volunteers were imaged in an apical 4-chamber view using a single-line transmit 2MLA approach (FR 79Hz). BEAS was then used to perform segmentation in real-time at ED by using ECG gating to trigger the segmentation. A total myocardial coverage value T of 85% was used to create an anatomical scan sequence from the obtained coverage function.

To evaluate how much information is lost as the heart deforms, the myocardial coverage along the heart cycle was analysed. The LV was segmented at ED and end systole (ES) on the anatomical scan images by using the conventional B-mode as a reference. The segmented myocardium was then divided into segments according to the 17-segment model [10] so that the regional impact of this technique can be determined.

10.4 Results

In vitro

Figure 10.1(a) shows an example of a conventional B-scan of the PVA phantom with the real-time segmentation result obtained with BEAS. The corresponding coverage function is shown in Figure 10.1(b). The resulting anatomical imaging resulted in a FR gain of 1.64 thus giving an FR of 255Hz. An example of an anatomical image is shown on Figure 10.1(c).

Figure 10.2 shows the comparison between the reference longitudinal strain obtained with the ultrasonic microcrystals and the strain obtained through NRIR in the conventional and anatomical imaging. It can be observed that both conventional and anatomical imaging present excellent correlations to the reference longitunidal strain. In Figure 10.2(c) it can be seen that anatomical imaging presents peak longitudinal strain values closer to the reference in comparison to conventional imaging which overestimates strain by approximately 4%.

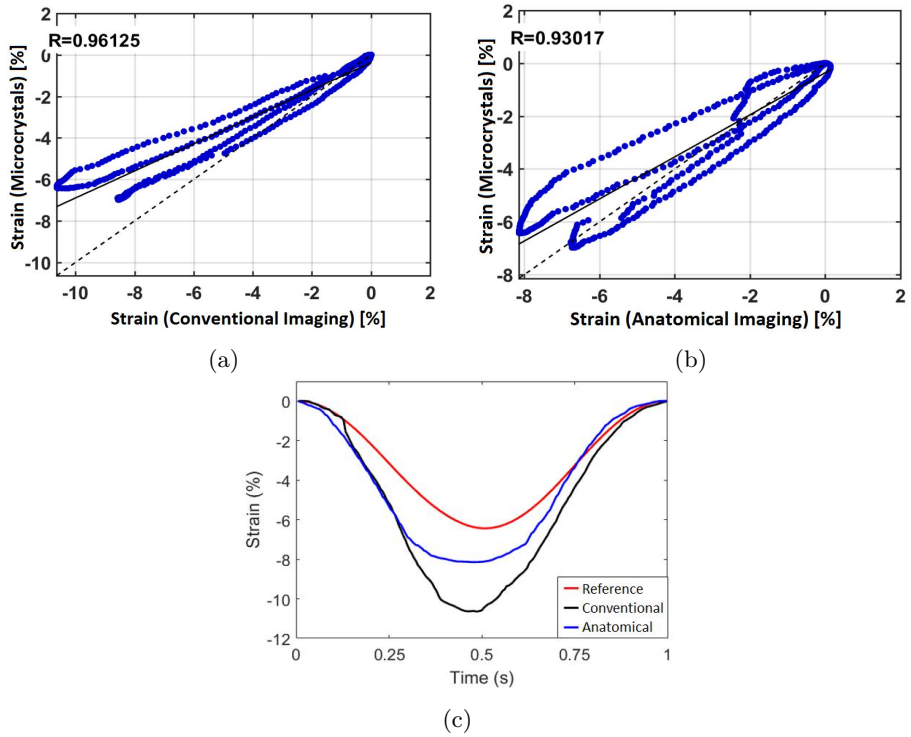

Figure 10.2: (a) Correlation between estimated strain on conventional imaging against reference method; (b) Correlation between estimated strain on anatomical imaging against reference method (c) Example strain curves for reference method and NRIR estimation on conventional and anatomical imaging.

In vivo

Figure 10.3(a) shows an example of a conventional B-scan of one of the volunteers with the real-time segmentation result obtained with BEAS. An example of the resulting anatomical imaging for this volunteer is shown in Figure 10.3(b). The FR gain for each of the volunteers was respecticely 1.54, 1.54 and 1.77, giving a final FR of 122, 122 and 140Hz. The global and segmental myocardial coverage obtained on the anatomical images at ED and ES are shown in Figure 10.4. It is shown that both at ED and ES the global myocardial coverage is over 85%, the value defined for T. Looking at the segmental analysis of myocardial coverage, it is clear that the most affected segment is the apical cap, with a coverage between 10% and 30%. The remaining segments, however, remain almost unaffected, except for the basal septal segment which was moderately affected in two of the volunteers at ES.

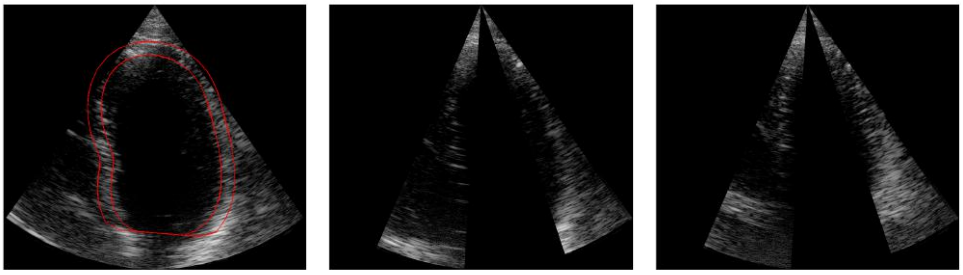

(a) (b) (c)

Figure 10.3: (a) Conventional B-mode obtained for one of the volunteers at ED with BEAS segmentation imposed; (b-c) Anatomical B-mode obtained for the same volunteer at ED and ES respectively.

10.5 Discussion

It is clear that the proposed approach is able to give a significant FR gain. For both the *in vitro* and *in vivo* setups a FR gain between 1.54 and 1.77 was obtained. These results are comparable to what had been obtained *in silico* in [251], where a FR gain of 2 was obtained using the same methodology but in RT3DE. Of course, the actual FR gain is dependent on patient physiology such as the size of the ventricular cavity, thickness of the walls, etc. as well as the positioning of the probe and distance to the apex, thus explaining the different results obtained *in vitro* and *in vivo*. When comparing to the *in silico* experiments, a higher gain was expected as a greater percentage of the volume is discarded when compared to a 2DE acquisition. Nevertheless, the results show that a minimum FR gain of 1.5 is realistic in an *in vivo* setup in 2DE. Compared to other techniques such as DW, this method has the advantage that it is able to maintain the spatial resolution and signal-to-noise ratio (SNR) and contrast-to-noise ratios of conventional ultrasound. Furthermore, this technique can be combined with an MLT-MLA sequence as done in the *in vitro* setup in this study, allowing for a further increase in FR enabling sequences with several hundred frames per second.

Figure 10.2 shows that, for the purpose of myocardial deformation imaging, the relevant motion information is preserved and state-of-the-art motion estimators such as NRIR can cope with the missing information in the center of the image to provide accurate strain data with excellent correlation to the reference data. Furthermore, given the higher FR, it can be expected that the information obtained through anatomical imaging is more representative of the true tissue motion, thus giving access to more accurate clinical information.

Of course, the approach used is intrisically limited, as sections of the myocardium are effectively discarded to obtain the observed FR gain. Nevertheless, as shown in Figure 10.4, this technique affects mainly the apical cap, which, even in conventional ultrasound contains little usable clinical information due to significant near field clutter. Furthermore, the global myocardial coverage can easily be controlled by changing the parameter T. This parameter is however, a compromise between FR

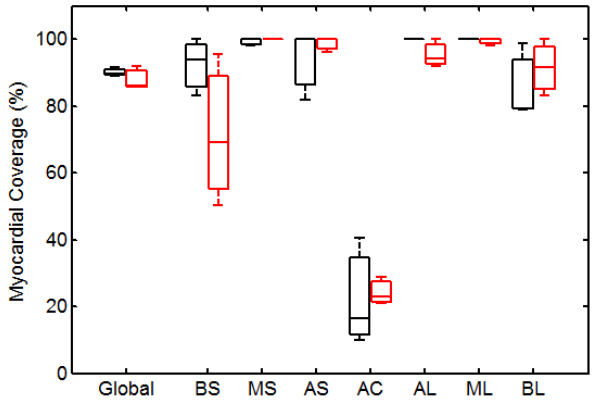

Figure 10.4: Percentage of myocardial coverage for all volunteers at ED (black) and ES (red). Global corresponds to the total myocardial coverage. BS, MS, AS correspond to basal, mid and apical septal segments, AC corresponds to apical cap and AL, ML and BL to apical, mid and basal lateral segments

gain and myocardial coverage and, from the authors' experience, a good compromise is obtained with the 85% value used in this work.

A limitation of this method is the fact that only a segmentation at ED is performed to obtain the anatomical scan sequence. This could lead to sections of the myocardium being lost in the remaining heart cycle, as the movement of the heart is not considered. However, in the experiments performed, the myocardial coverage at ED and ES are comparable, except for the basal septal segment in two of the volunteers. In non healthy cases however, the movement of the heart may be more unpredictable and as such, a dynamic anatomical imaging could be considered for future work by performing full cycle segmentation and dynamically adapting the scan sequence along the heart cycle.

10.6 Conclusion

Anatomical scanning in combination with MLT-MLA beamforming techniques can increase FR significantly while keeping information of the relevant structures for functional myocardial imaging. In the present work, it was shown that anatomical scanning is a feasible approach *in vivo* allowing for a minimum FR gain of 1.5. Furthermore, when combined with MLT/MLA techniques, the FR can be further increased without a compromise in spatial resolution and acceptable cross-talk.

Chapter 11

Final Remarks

11.1 Main Contributions

In this thesis, the topic of real-time 3D echocardiography (RT3DE) left ventricular (LV) assessment was addressed. This topic was approached both in a technical context in Part I of this thesis, developing novel image processing frameworks to extract valuable information from the image, and also in an applicational/clinical context in Part II, by applying the techniques developed to solve clinical problems.

In Chapter 2, a review of the most relevants topics for the contextualization of this work was given. Starting with anatomical and functional considerations on the cardiovascular system and particularly the LV, a review on the prognostic value of LV assessment in clinical practice was presented, highlighting the clinical importance of the LV and the maturity of this clinical field. The different cardiac imaging modalities were then explored as means to assess the LV and the focus was set on echocardiography due to its inherent advantages. Moreover, the importance of RT3DE was highlighted as it gives access to the true 3D geometry of the cardiac structures. The relevance of high frame rate (FR) imaging was also briefly described as an additional way of obtaining further information on the cardiac dynamics.

In Section 2.4, a review of the state-of-the-art of LV segmentation and tracking methodologies was presented, which showed the advanced maturity of the research field. Also the commercial solutions available were described as those are the ones commonly available to clinicians. Finally, a review on the validation of RT3DE LV volume assessment was presented, showing the validity of this modality as a clinical tool.

11.1.1 Technical Contributions

Given the topic of this thesis, the technical contributions were of course around the topic of 3D myocardial LV segmentation in RT3DE. The starting point of this thesis was, as described in Section 2.5, the B-spline Explicite Active Surfaces (BEAS) framework for 3D LV segmentation which had proven to be potentially real-time, fully automatic and accurate. The work developed during this thesis aimed then at improving this framework both in terms of its robustness and the clinical information it provides.

The first technical contribution of this thesis was heartBEATS, a hybrid energy framework for tracking of the LV from end diastole (ED) to end systole (ES) presented on Chapter 3. Though this framework was initially proposed in the PhD work of Daniel Barbosa, the author of this thesis played a determinant role in the finalization and publication of the validation results obtained. The heartBEATS framework allows the tracking of the LV segmentation throughout the heart cycle, balancing segmentation and tracking clues for an improved tracking result without compromising the feasibility of real-time.

The second technical contribution was an automatic method for short axis (SAx) orientation of the LV proposed in Chapter 4. This method is based on the detection of the inferior right ventricular (RV) insertion using image intensity and structural

information. SAx orientation allows to extract regional information from an LV segmentation and divide it into a 17 segment model for example.

The third technical contribution was a framework for full-cycle LV segmentation using a statistical shape model (SSM) obtained from cardiac magnetic resonance imaging (cMRI) images (Chapter 5). This approach couples the advantages of the BEAS framework, a purely image information approach, to those of SSMs to give prior information about the expected shape for an accurate segmentation. The segmentation is propagated throughout the heart cycle using localized anatomical affine optical flow (lAAOF). This framework was enabled by the contributions from previous chapters, namely the SAx orientation proposed in Chapter 4 to align the image to the LV SSM and the hybrid energy approach from Chapter 3 to refine the segmentation at ES. The proposed framework outperformed any other state-of-the-art method for ED/ES LV segmentation evaluated on the MICCAI CETUS challenge. Moreover, it outperforms other methods in terms of computational speed, being able to perform ED/ES segmentation and tracking in a few seconds in a non-optimized implementation and could thus be implemented to run real-time.

The fourth technical contribution focused on the way to couple endo- and epicardial segmentation for an optimal myocardial segmentation (Chapter 6). While these two surfaces are bound anatomically to the same structure, the myocardium, their mathematical definition can be done in a number of ways and plays a role in the final result. It was shown that the best approach was a two-step (2S) approach where the endocardial surface is segmented first and then used as a base for the epicardial segmentation by defining the epicardial surface as the thickness of the myocardium. This corroborates the idea that epicardial segmentation is more challenging, and can thus benefit from the additional shape and position information provided by the endocardial segmentation. In this way, a framework for LV myocardial segmentation was proposed, allowing for more information to be extracted, namely LV mass and myocardial thickness. Furthermore, myocardial segmentation is essential as a first step in post processing approaches such as strain analysis or definition of the region of interest (ROI) in machine learning approaches.

The fifth contribution was presented in Chapter 7 and was the adaptation of the framework from Chapter 5 for LV myocardial segmentation. This was possible by combining this framework to the coupling validated in Chapter 6 and through the creation of a myocardial SSM. Because epicardial segmentation datasets are not publicly available, an expert contoured the epicardium in the MICCAI CETUS challenge database and this data was made public on the challenge website, thus allowing the validation and direct comparison with other methods in the future. This framework for automatic and robust full-cycle LV myocardial segmentation/tracking allows for the extraction of LV volumes and local geometry throughout the heart cycle, thus giving important clinical information. 3D strains can also be extracted in the myocardium given the local characteristics of the lAAOF, enabling more advanced clinical analysis.

11.1.2 Applicational/Clinical Contributions

A first study, dedicated to facilitating the future application of the proposed technical contributions, was described in Chapter 8. The framework developed in Chapter 7 for 3D myocardial segmentation was implemented in a user-friendly distributable software application where echocardiographic images can be loaded, automatically segmented and manually corrected. An adapted version of this framework for 2D echocardiography (2DE) was also implemented. The framework for 3D mitral valve (MV) segmentation described in Appendix A was also implemented. The implementation of the frameworks developed in this thesis in a distributable software application enables their application in future studies, technical or clinical, and accessible to any user without the need for programming skills.

The second contribution was the introduction of a method for myocardial performance mapping in RT3DE in Chapter 9. By using the 3D LV myocardial segmentation framework in Chapter 7, 3D local myocardial deformation and geometry can be obtained. Intraventricular pressure can then be estimated based on the valve events and by using equations that link pressure and geometry to LV stress, LV stress-strain loops can be built. The area of these loops is shown to be a measure for myocardial work as validated by 18F-fluorodeoxyglucose positron emission tomography (FDG-PET), the reference method to assess local metabolism clinically.

The third contribution was the validation of a high FR imaging method, anatomical imaging, in an *in vivo* setting (Chapter 10). In this method, real-time myocardial segmentation is performed in 2DE on the ultrasound system and the resulting segmentation is used to define a fast myocardial scan sequence. This method was tested on HD-PULSE, an experimental ultrasound scanner. It was shown that a minimum FR gain of 1.5 was possible without a significant impact on spatial resolution, thus giving access to more information on wall motion dynamics. Moreover, the potential applications of real-time LV segmentation were highlighted, showing that they far outreach the direct extraction of clinical parameters.

11.2 Discussion

The literature review presented in this thesis has made it evident that echocardiographic image analysis is a mature field, especially when it comes to solutions for the LV. Analysis of RT3DE has particularly received attention in recent years as the perceived imaging technique of the future for LV analysis. Numerous solutions, both semi- and fully automated, have been proposed in the research community and are now gaining importance in commercial solutions. Nevertheless, there are still challenges to be solved that could be tackled in future work.

In spite of the extensive research conducted towards the development of automatic frameworks for LV segmentation in RT3DE image, there still seems to be no software platform providing a robust set of tools for LV assessment in RT3DE. The technical contributions made in this thesis aimed at providing fast, automatic and robust solutions for this problematic, going further than the endocardial surface at

a single time frame to obtain a full LV myocardial segmentation throughout the heart cycle, thus providing additional clinical information. Establishing links with emerging image processing techniques, as is lAAOF, and fusing these with BEAS in an elegant framework was extremely important for this objective, contributing to the promising results obtained. The inclusion of prior information through an SSM was also shown to be a major factor in increasing the robustness of the framework and directly contributing to the promising results obtained. Ultrasound is a challenging imaging modality and RT3DE especially so making the shape information provided by the SSM extremely useful, driving the segmentation when the image information is low or unreliable.

While it is not always straightforward to balance image and prior information on the final segmentation, it is expected that data driven solutions (thus powered by shape and/or appearance prior information) become the standard in RT3DE solutions, following the direction already observed in other computer vision fields. This trend can already be seen for the commercial players (as access to data is usually less of a constraint than in a research setting) in products such as Siemens' eSie LVA^{TM} or Philips' HeartModel^{AI}. It can be expected that data driven and specifically deep learning approaches will take the same path that mechanistic approaches treaded in the past years, starting with 2DE and then moving to 3D LV and eventually coming to 3D LV myocardial segmentation.

In the context of the framework for 3D LV myocardial segmentation developed in this thesis, data driven solutions can also come to play a major role further improving the results obtained and creating a more robust framework. The LV initialization proposed in [165] and used throughout this thesis is dependent on edge detection followed by Hough transform for circles (HTc) for long axis (LAx) detection and surface initialization and could therefore be replaced by a data driven approach. The influence of the initialization error was explored in Chapter 5 and it was shown that improving the initialization could increase the performance of the framework (mean absolute distance (MAD): 1.38 mm; Hausdorff distance (HD): 4.86 mm; Dice: 0.959 for the LV endocardial segmentation at ED). It would therefore be interesting to replace this initialization for an approach that would take into account shape, appearance and contextual information for a more accurate decision regarding LV pose and shape. Several machine learning algorithms already implemented for LV assessment in echocardiography [256, 257] could provide such an initialization through the creation of an edgemap for LV initialization. Moreover, such an edgemap could also be used to strenghten the segmentation by including an energy term designed for and driven by this map, either replacing or complementing the modified Yezzi energy term [165] currently used to extract image information.

The potential clinical application of the techniques developed in this work was a major concern throughout the thesis. The focus was set on the clinical indices that can be extracted and improved by the proposed framework and its improvements and clinicians were, naturally, an important source of input. Nevertheless, a major gap still exists preventing the widespread use of this, or other similar frameworks, in the clinic. In spite of the inherent advantages of RT3DE and its recent developments, providing better image quality and temporal resolution, clinical cardiology

still relies heavily on 2DE and RT3DE is reserved almost entirely to clinical research. This can be attributed, on one hand, to the gap between clinical and research image processing tools, a gap that now starts to be closed by the major commercial players. On the other hand, the average clinician must be focused on providing the best care to his/her patients and, consequently, follows the recommendations of higher entities such as the European Association of Cardiovascular Imaging. As such, research efforts towards validation of RT3DE and its associated processing frameworks are of utmost importance as they bring more evidence to strengthen what is still an emerging clinical tool.

Besides more accurate assessment of the clinical indices already in use today such as ED and ES volumes (EDV and ESV) and ejection fraction (EF), RT3DE LV assessment opens up new clinical possibilities by giving access to a greater amount of information in a more reliable way. The introduction of a novel framework for myocardial performance mapping in Chapter 9 has highlighted the wealth of information that can be retrieved from a single RT3DE acquisition in a totally automatic and non-invasive way. Myocardial performance mapping has long been a holy grail of clinical cardiology which has recently received new strenght with the method for non-invasive intraventricular pressure measurement by Russel et al. [245]. While the ideas applied in Chapter 9 have long been proposed, such a study using RT3DE and correlating it to a ground truth from FDG-PET had not yet been reported. Nevertheless, the number of patients in this study is limited and should be extended.

The application of the myocardial segmentation in a real-time application in Chapter 10 for anatomical imaging has shown the potential applications of this technology, straightening the gap between image processing and acquisition. While in this chapter an important step was given showing the feasibility of this technology *in vivo*, further efforts are needed to validate the clinical information obtained through this high FR imaging approach. Specifically, strain and/or strain rates could be extracted from such an approach and compared to those from other high FR imaging approaches such as diverging wave (DW) imaging within the same subject. This could validate the idea that anatomical imaging provides a better spatial resolution and signal-to-noise ratio (SNR) and consequently more reliable clinical information. However, this study was not possible within the scope of this thesis. An additional problematic could be that the current implementation of the method might prove challenging in more complex anatomies and heart motion due to the fact that only the position of the LV at ED is taken into account for the coverage function. This could lead to the LV moving out of the anatomical field of view (FOV) during the heart cycle. A straighforward improvement would then be to use lAAOF to track the LV along the heart cycle, thus creating a dynamic anatomical imaging, perfectly adapted to the LV along the whole heart cycle. Looking further into the future, an implementation of 3D anatomical imaging (thus implying real-time 3D LV myocardial segmentation) would lead to an even larger FR gain. An *in silico* implementation of this technique has yielded a FR gain of 80 times in a 10 multi-line transmit (MLT) - 4 multi-line acquisition (MLA) configuration without significant loss of image quality [251]. However, this was not possible within the

scope of this thesis due to hardware limitations on HD-PULSE which prevented the acquisition of RT3DE imaging.

Finally, the LV myocardial segmentation framework implemented in a distributable software application - Speqle3D (Chapter 8) allows for its application in future studies on further validation and extraction of clinical information. One important point of this implementation was the possibility of manual correction, in case the user disagreed with the segmentation result. This is especially important when image quality is lower or the view is not standard, to get the optimal segmentation result. However, a thorough validation of this manual correction would have been important to clearly assess how much and in what cases this type of input is perceived by the users as important.

11.3 Conclusion and Future Perspectives

Echocardiography is an indispensable tool for cardiac assessment and LV volume/function assessment has undeniable prognostic and diagnostic value as revealed by the existing extensive literature on the topic. Though currently still an emerging technology in the clinic, RT3DE gives access to the full 3D geometry of cardiac structures, thus presenting significant advantages over 2DE. However, the analysis of 3D images is particularly challenging and time consuming, making the development of automatic tools extremely important. Such tools would allow for easier analysis of RT3DE images, ultimately providing more information about the LV in a more robust and less user dependent way than current 2DE solutions.

In this thesis, several technical contributions were made with this goal in mind: a method for hybrid segmentation and tracking for more robust full-cycle segmentation; a method for SAx orientation of the LV giving additional local information; the addition of an SSM to the BEAS framework for a more robust segmentation; the coupling of endo- and epicardial surfaces for an efficient myocardial segmentation; and the framework for full-cycle 3D LV myocardial segmentation. It was shown that the proposed framework outperformed any other state-of-the-art framework on LV segmentation on the MICCAI CETUS challenge dataset. The application of the technical contributions made in this thesis was also considered, by implementing the proposed framework in a user-friendly distributable software application. The clinical value of the information that can be retrieved from RT3DE was further highlighted by proposing a method for myocardial performance mapping through the study of the stress-strain relationships in the LV, showing good correlation with FDG-PET. Finally, other applications were also considered by applying real-time segmentation in 2DE for anatomical imaging, as to obtain high FR imaging and study short lived myocardial dynamics.

The main challenge for the future remains the validation and acceptance of RT3DE LV assessment in a clinical setting. The research community plays an important role in the validation and benchmarking of new algorithms and it should be expected that more data driven methods and deep learning approaches are proposed. As large sets of data have become more accessible in recent years these tech-

niques have been implemented in a wide range of applications with very promising results. Though biomedical imaging is a particularly challenging field due to the difficulty of obtaining a reliable ground truth, it should be expected that deep learning approaches become the dominant framework in the future. A trend for more contextual information is also expected, e.g. multi-chamber segmentation frameworks, leading to more information to be extracted from a single image while at the same time making that information more reliable. This will likely have clinical implications as a wealth of information that was earlier infeasible or difficult to assess becomes available as was shown for the myocardial performance mapping in this thesis. The link between acquisition and processing will likely also be straightened in the future as real-time processing is made possible through faster processing and graphics processing unit implementations. An example of this is the anatomical imaging proposed in this thesis, linking acquisition and segmentation for high FR imaging. Besides high FR imaging, the optimization of the imaging settings based on the information being captured in real-time and the guidance of the clinician in positioning the probe would be extremely interesting to maximize image quality, thereby improving the quality of information that can be extracted. In conclusion, these technologies would have the potential for robust, unbiased and fast assessment of cardiac function, ultimately leading to better clinical care.

Appendix A

Fully Automatic Assessment of Mitral Valve Morphology from 3D Transthoracic Echocardiography

This chapter is based on a paper published in the proceedings of the *2018 IEEE International Ultrasonics Symposium (IUS)*: **Pedrosa J.**, Queirós S., Vilaça J., Badano L., D'hooge J.. Fully automatic assessment of mitral valve morphology from 3D transthoracic echocardiography. In *2018 IEEE International Ultrasonics Symposium (IUS) proceedings* Oct 22 (*accepted for publication*).

Abstract

Quantitative assessment of mitral valve (MV) morphology is important for diagnosing MV pathology and for planning of reparative procedures. Although this is typically done using 3D transesophageal echocardiography (TEE), recent advances in the spatiotemporal resolution of 3D transthoracic echocardiography (TTE) have enabled the use of this more patient friendly modality. However, manual data analysis is time consuming and operator dependent. In this study, a fully automatic method for MV segmentation and tracking in 3D TTE is proposed and validated. The proposed framework takes advantage of the left ventricle (LV) segmentation framework presented in Chapter 5 to localize the MV and performs segmentation based on the B-spline Explicit Active Surfaces (BEAS) framework. The orientation of the MV is obtained according to the automatically detected right ventricular (RV) insertion point and the LV outflow tract (LVOT). Following the segmentation, the MV surface is cropped to the mitral annulus (MA) and divided into posterior and anterior leaflets using a dynamic programming technique refined by consulting an atlas of manually contoured MVs. The segmented MV at end diastole (ED) is then propagated to end systole (ES) using localized anatomical affine optical flow (lAAOF). Because the orientation and leaflet division is known, relevant clinical parameters can then be extracted from the mesh at any time point. The proposed framework shows excellent segmentation results with a mean absolute distance (MAD) and Hausdorff distance (HD) of 1.19 ± 0.25mm and 5.79 ± 1.25mm at ED and 1.39 ± 0.32mm and 6.70 ± 1.97mm at ES against manual analysis. In conclusion, an automatic method for MV segmentation is proposed which could provide valuable clinical information in a more patient-friendly manner.

A.1 Introduction

The MV is a crucial structure of the left heart, playing a significant role in LV and left atrial (LA) function [258], and thus of great clinical importance. While the standard clinical tools for MV function assessment are mostly based on Doppler techniques [259, 260], quantitative assessment of the MV geometry plays an increasingly important role, allowing a better understanding of MV physiology and pathophysiology in mitral regurgitation [261–263] and mitral stenosis [264, 265], diagnosis of MV pathology [266, 267] and planning of reparative procedures [268, 269]. However, the fact that the MV is a 3D dynamic structure makes any quantitative assessment in standard 2D echocardiography (2DE) or cardiac magnetic resonance imaging (cMRI) challenging due to the need to define a correct imaging plane and to make geometric assumptions regarding the 3D structure of the MV [270]. Real-time 3D echocardiography (RT3DE), in specific RT3DE TEE (due to its better spatiotemporal resolution and optimal imaging window to the MV), has thus been proposed as an alternative to other 2D modalities. Furthermore, it has been shown that MV assessment by 3D TEE is not only in accordance to surgical measurements but also superior to 2D TEE [271]. Manual analysis of a 3D structure such as the MV throughout time is, however, quite challenging and time consuming, which has

motivated various studies on the automation of MV analysis through segmentation and/or tracking.

Schneider et al. [272] proposed a semiautomatic method for MV segmentation using a thin tissue detector and active contours based on a single point initialization. This approach was later extended to 4D MV assessment using optical flow and validated against manual contouring [273]. Burlina et al. [274] proposed a method using a combination of a thin tissue detector and a dynamic contour method, which is then refined by the user to obtain the final segmentation. Ionasec et al. [275] presented a comprehensive method based on probabilistic boosting trees and a model-based approach to perform both aortic valve (AV) and MV segmentation in computed tomography (CT) and TEE images. Pouch et al. [276] proposed a fully automatic segmentation method using a multi-atlas approach, the result of which is used to create a 3D geometric model of the MV. Sotaquira et al. [277] proposed a model-free graph-based approach, however this method required strong user interaction for initialization and coaptation line detection. Finally, De Veene et al. [278] proposed a method based on non-rigid registration to track the MV in 4D after manual segmentation of the MV on the first frame.

Nevertheless, TEE remains impractical as a routine or follow-up imaging modality due to the associated discomfort for the patient, added acquisition time and increased cost. TTE is therefore an attractive alternative. Recently, advances in the spatiotemporal resolution of RT3DE TTE have enabled the use of this more patient friendly technology for MV quantitative assessment. In a recent study by Mihăilă et al. [279] it was shown that manual analysis of MV geometry in RT3DE TTE was feasible and comparable to measurements from RT3DE TEE. In spite of the advances seen in TTE, it remains a challenging imaging modality for MV assessment due to the more difficult imaging window and overall lower image quality and higher variability in MV position in the image, all of which might render previously proposed automated MV assessment methodologies for TEE unusable in TTE. While manual or semiautomated methodologies such as TomTec's 4D-MV Assessment are still applicable, they can be quite time consuming due to the need for manual contouring or extensive landmarking of structures.

In this study, a novel fully automatic method for MV segmentation and tracking in RT3DE TTE is proposed. The proposed method is based on a previously validated method for 3D LV segmentation in TTE to localize the region of interest (ROI) in the image and the MV orientation. Segmentation of the MV is then performed using BEAS, which is propagated along time using lAAOF, allowing for 4D quantitative assessment of the MV.

A.2 Methodology

A.2.1 B-spline Explicit Active Surfaces

Given the nature of the object of interest, the B-spline representation of the MV was created on a half-spherical coordinate system thus defining the active geometric

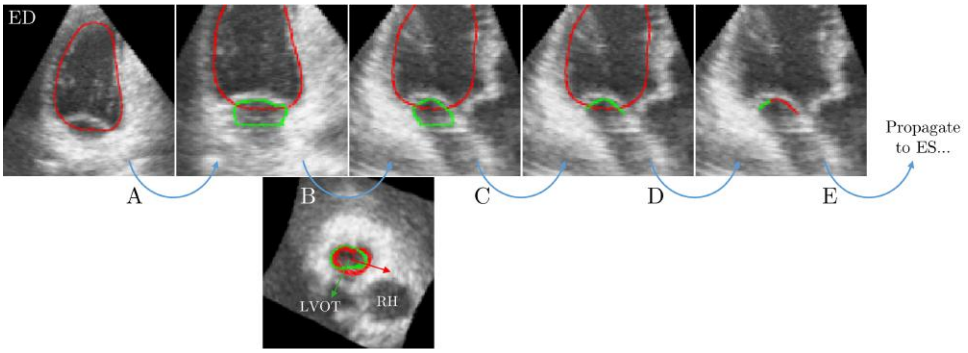

Figure A.1: Conceptual description of the proposed segmentation and tracking framework. After endocardial segmentation at ED, automatic initialization and segmentation of the MV is performed (A). LVOT detection is then performed to orient the MV (B). The lower frame shows the LV orientation according to the RV insertion point (red arrow) and MV orientation according to the LVOT (green arrow) as well as LVOT and right heart cavity (RH). After MV orientation the MV is outlined by detecting the MA (C). The coaptation line is then detected (D), separating the anterior and posterior leaflets (red and green). This segmentation is then propagated to ES (E).

functions as $r = \psi(\phi, \theta)$ for $\phi < 0$. The angular discretization of the boundary representation was empirically set to 24×16 (elevation×azimuth) and the B-spline scale to 2^2 for both angular coordinates.

A.2.2 Framework Description

A conceptual description of the proposed framework is shown in Figure A.1.

A.2.2.1 Mitral Valve Initialization

Due to the variability of the position and orientation of the MV in RT3DE TTE, its localization in an automatic way is often challenging. As such, the initialization used is based on the automatic LV segmentation framework presented in Chapter 5.

Taking advantage of the inherent BEAS structure of the segmented LV mesh, the localized image intensity outside the LV surface can be analyzed at any mesh point. This can be used to distinguish between LV mesh points that are close to the myocardium (and thus with relatively high image intensity) and those that separate the LV and LA blood pool (and thus with relatively low image intensity). An image intensity map in the spherical domain according to the LV BEAS coordinate system is shown in Figure A.2. Dynamic programming can then be used to find the separation between points adjacent to the myocardium and those adjacent to the blood pool according to the gradient of the image intensity map along the

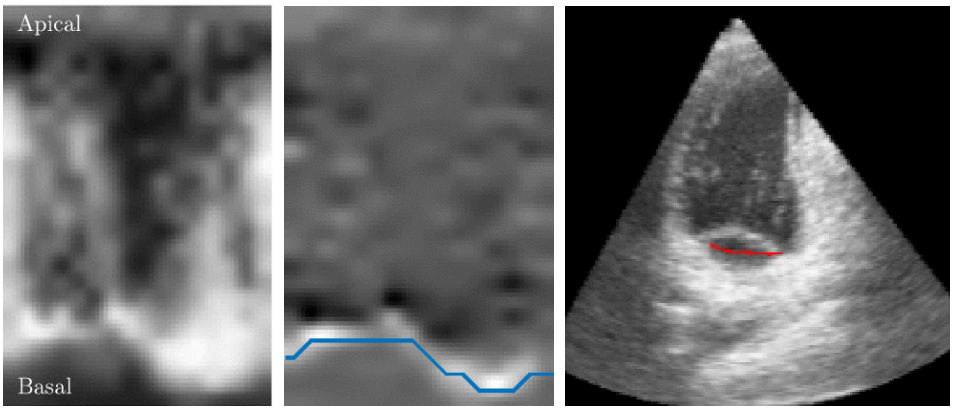

(a) (b) (c)

Figure A.2: MV initialization: (a) Map of mean intensity outside the LV mesh in spherical domain (b) Longitudinal gradient map and path obtained with dynamic programming. (c) Selected LV mesh section.

longitudinal direction. The base of the LV, as defined by dynamic programming, is then used as the initial surface of the MV. The origin of the MV BEAS coordinate system is defined 1cm below the LV base and oriented towards the LA roof (away from the LV).

A.2.2.2 Mitral Valve Segmentation

The MV segmentation is performed in two stages. First, a threshold-based evolution is performed given the fact that the MV initialization is based on the LV base and not the MV leaflets themselves. As in other BEAS implementations, the surface is evolved radially through equation 2.4 for

$$\bar{g}(\mathbf{x}^*) = \begin{cases} 1, & if \quad (u_{in} > u_{out} \wedge u_{in} > T) \vee u_{in} > 1 - T \\ 0, & otherwise \end{cases} \tag{A-1}$$

where u_{in} and u_{out} are the localized means inside and outside the MV surface and T is a fixed threshold. Since no energy equation is defined, the evolution stops when a maximum number of iterations N_{it} is reached or no further evolution of the surface is found. It is expected that by the end of this segmentation step the surface is on the LA side of the MV leaflets, preventing the surface from becoming trapped in local minima on the LV side of the MV during the second segmentation stage.

In the second stage the Yezzi localized energy adapted in [165] (equation 2.11) for endocardial segmentation is used to segment the MV leaflets since the blood pool is expected to be darker than the MV leaflets. An example of MV segmentation using BEAS is shown in Figure A.1 (second panel).

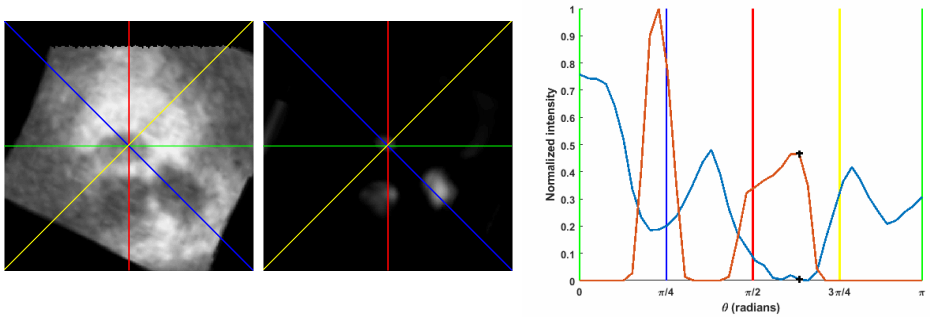

(a) (b) (c)

Figure A.3: LVOT detection: (a) RT3DE slice at MA level; (b) Frangi vesselness filter result at MA level; (c) Normalized average circumferential intensity profiles extracted from image (blue) and Frangi vesselness filter (red) and point chosen as LVOT (black cross). Angle θ is given from LV orientation at RV insertion point towards the right heart (clockwise in slices (a) and (b)). Vertical colored lines in (c) indicate the angular positions marked in slices (a) and (b).

A.2.2.3 Left Ventricle Outflow Tract Detection

To be able to extract clinical information from the segmented mesh, it is important to orient the mesh according to the surrounding anatomical structures. While an approximate orientation is obtained from the LV segmentation as the RV insertion point position is known (Chapter 4), the MV is more easily oriented according to the LVOT. Although typically the RV insertion point and LVOT are $\pi/2$ radians apart, patient variability is significant.

LVOT detection is therefore performed according to: i) the mean intensity outside u_{out} given that the blood pool in the LVOT is naturally dark; ii) a vesselness filter as introduced by Frangi et al. [280] suited for the average LVOT size, empirically set between 6 and 9mm. The circumferential direction between $\pi/3$ and π with maximum $\overline{vesselness} - \overline{u_{out}}$ (where $\overline{f}$ stands for the maximum-normalized value of f) is then selected as the LVOT direction as shown in Figure A.3.

A.2.2.4 Mitral Annulus Detection

Given the definition of BEAS in a half-spherical coordinate system it follows that the surface obtained will be defined for any $\phi < 0$. However, the MV is delineated by the MA, which is saddle shaped. It can be observed in Figure A.1 that the lower sections of the segmentation encompass the LA walls and the ascending aorta. These sections thus need to be discarded by finding the MA, where the MV leaflets are attached. Once again, the BEAS structure is used to retrieve u_{out}. It is expected that above the MA, where the u_{out} is extracted across the MV leaflets into the LV blood pool, the mean intensity will be low, whereas below the MA the u_{out} is

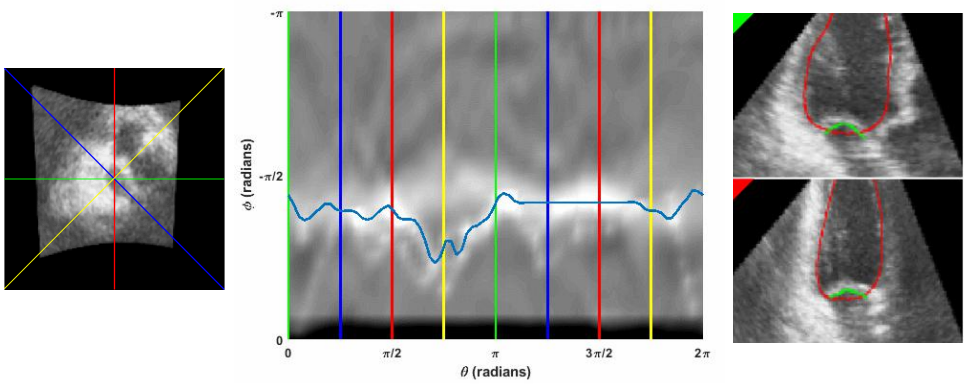

(a) (b) (c)

Figure A.4: MA detection example: (a) RT3DE slice at MA level; (b,c) Orthogonal long axis slices after MA cropping of the MV mesh; (d) u_{out} gradient map and path chosen after dynamic programming. Angle θ is given from the MV orientation at LVOT away from the right heart (clockwise in slice (a)). Colors of vertical lines in (b) and upper left triangles in (c) indicate the angular positions marked in slice (a).

extracted from the LA walls and thus of high intensity. Based on this assumption, dynamic programming can be used to separate these two regions based on the gradient along the longitudinal direction.

However, u_{out} is not a sufficiently reliable measure to delineate the MA, especially in the LVOT where the ascending aorta will also have low mean intensities and the MA is defined at the AV. Furthermore, artifacts might change the intensity profiles locally making this problem more challenging. As such, an intensive atlas based approach is used based on a set of reference meshes (excluding the reference from the patient being tested). The MV mesh is thus aligned to each of the reference meshes through an iterative closest point (ICP) algorithm taking into account the LVOT orientation. Mean square distance is used to score the alignment to each reference mesh and those with lower distance are selected. The reference MA path of each of these meshes is then projected into the MV BEAS space, thus creating a new map showing the reference MA paths. Summing this map to the u_{out} gradient map creates a single map representing both image intensity and shape-based information, penalizing paths away from the reference MA paths. The highest probability path is selected using dynamic programming and used to crop the segmented BEAS mesh and obtain the MV mesh as shown in Figure A.4.

A.2.2.5 Coaptation Line Detection

To extract further information on the MV anatomy it is important to separate the two leaflets by detecting the coaptation line, where the two leaflets meet. As proposed by Sotaquira et al. in [277], the distance of the mesh point to the MA

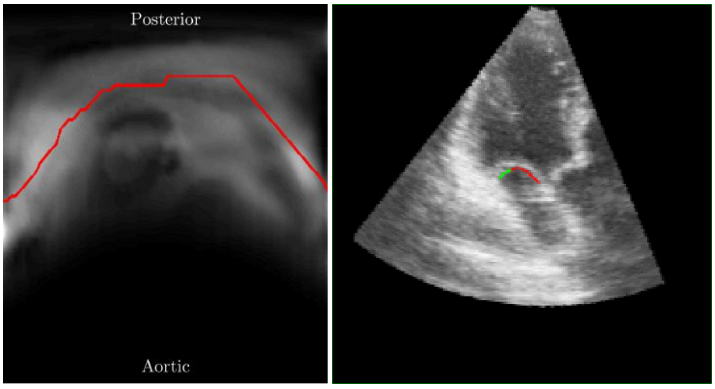

(a) (b)

Figure A.5: Coaptation line detection example: (a) Coaptation line feature map and path chosen after dynamic programming (b) Long axis slice after division into aortic (red) and posterior (green) leaflets.

plane (i.e. the tenting height) was used as the coaptation line usually shows high tenting values. Additionally, the mean intensity u_{out} up to 4mm from the mesh was found to be a good indicator of the coaptation as a slightly lower intensity region is formed where the two leaflets meet. Finally, the position of the coaptation line in the selected atlas meshes were also used by projection into the MV BEAS space and penalizing the distance from the reference coaptation lines. A feature map was created by multiplying normalized tenting height, normalized mean intensity and the reference coaptation line map and this was used to estimate the coaptation line using dynamic programming as shown in Figure A.5.

A.2.2.6 Mitral Valve Tracking

Finally, lAAOF is used to propagate the segmented MV across the systole allowing for dynamic MV assessment.

A.3 Experiments

The proposed framework was validated on a subset of the CETUS challenge data using manual MV references created in this study. Given that the CETUS data was not optimized for MV assessment, 15 datasets were selected based on adequate MV visualization. An expert contoured the MV in 8 longitudinal slices at ED and ES in Speqle3D and spline interpolation in a spherical coordinate system was used to generate a reference mesh. The automatic segmentation was evaluated with MAD and HD. Clinical indices were extracted from the manual references and automatic segmentation results for comparison, namely anterior-posterior (A-P)

Table A.1: Performance (MAD and HD) of the MV segmentation. Values in mean ± standard deviation.

Time frame	MAD (mm)	HD (mm)
ED	1.19 ± 0.25	5.79 ± 1.25
ES	1.39 ± 0.32	6.70 ± 1.97

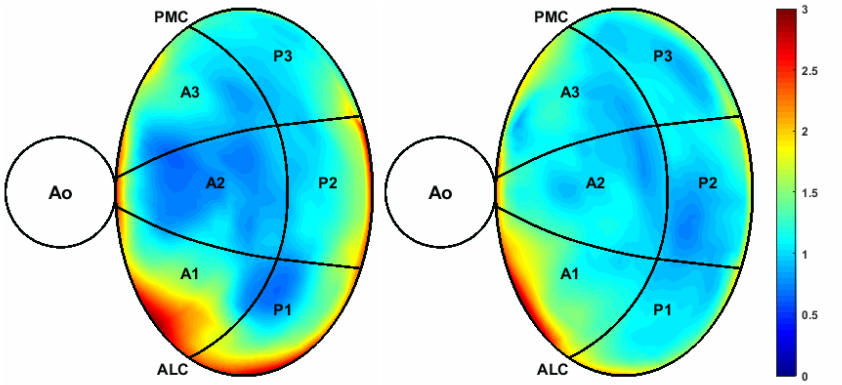

(a) (b)

Figure A.6: Regionwise plots of absolute distance for ED (a) and ES (b) MV segmentation. Ao indicates the aortic valve; PMC and ALC indicate the posteromedial and anterolateral commissures respectively; A1-3 and P1-3 indicate the anterior and posterior leaflet scallops. Measures in mm.

diameter, anterolateral-posteromedial diameter (AL-PM) diameter, MA circumference and MA area.

A.4 Results

Table A.1 shows the segmentation and tracking results for the proposed approach. Figure A.6 shows a regionwise analysis of error calculated as the absolute distance at each mesh point to the reference mesh and plotted according to the division of the MV into its two leaflets and the lateral, central and medial scallops. A trend for worse performance can be observed around the annulus, accentuated on the anterolateral side. Figure A.7 shows the best and worst MV segmentation results at ED and ES compared to the manual references by the expert. Finally, Figure A.8 shows the correlation between the clinical indices extracted from the automatic and manual MV meshes.

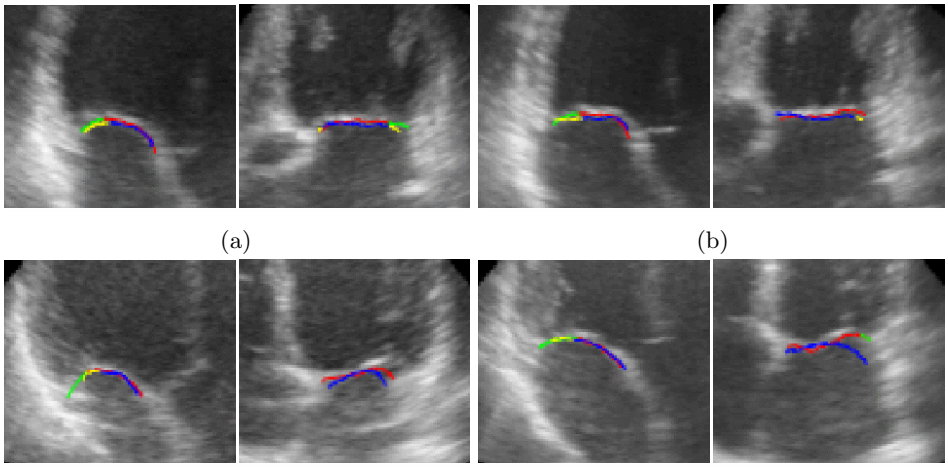

(a) (b)

(c) (d)

Figure A.7: Best (a,b) and worst (c,d) MV segmentation results compared to manual contouring at ED (a,c) and ES (b,d). Manual contours shown in red and green for the anterior and posterior leaflets respectively. Automatic segmentation results shown in blue and yellow for the anterior and posterior leaflets respectively. The two orthogonal planes shown for each RT3DE image were chosen according to the automatically defined LVOT orientation.

A.5 Discussion

From Table A.1 it is clear that the proposed framework presents an excellent MV segmentation and tracking performance. In the more specific regionwise analysis of Figure A.6 it becomes clear that the most challenging is the MA definition. This is a consequence not only of its very definition, which is prone to error, but of the fact that, because the MA defines the end of the mesh, different MA definitions in automatic and manual contours will directly lead to large absolute distances. The trend towards a larger error on the anterolateral side might be a consequence of the lower contrast observed in this region due to its proximity to the lungs. Nevertheless, it can be observed in Figure A.8 that overall a good correlation is found in the clinical indices considered with the exception of the A-P diameter at ES where only moderate correlation is found.

In spite of the promising results, this study presents some limitations which must be addressed in the future. First, the amount of data on which the framework was validated and on which the atlas is based is quite limited and a larger dataset should be considered to draw a more definite conclusion. Furthermore, populations with specific MV pathologies should be targeted to assess the feasibility of this method. Second, only the systolic phase is considered in this study. While MV dynamics are generally considered to be more important during systole [281], assessment of the complete MV dynamics would be interesting. However, the low frame rate (FR) often obtained in RT3DE TTE can be a limiting factor when tracking the MV

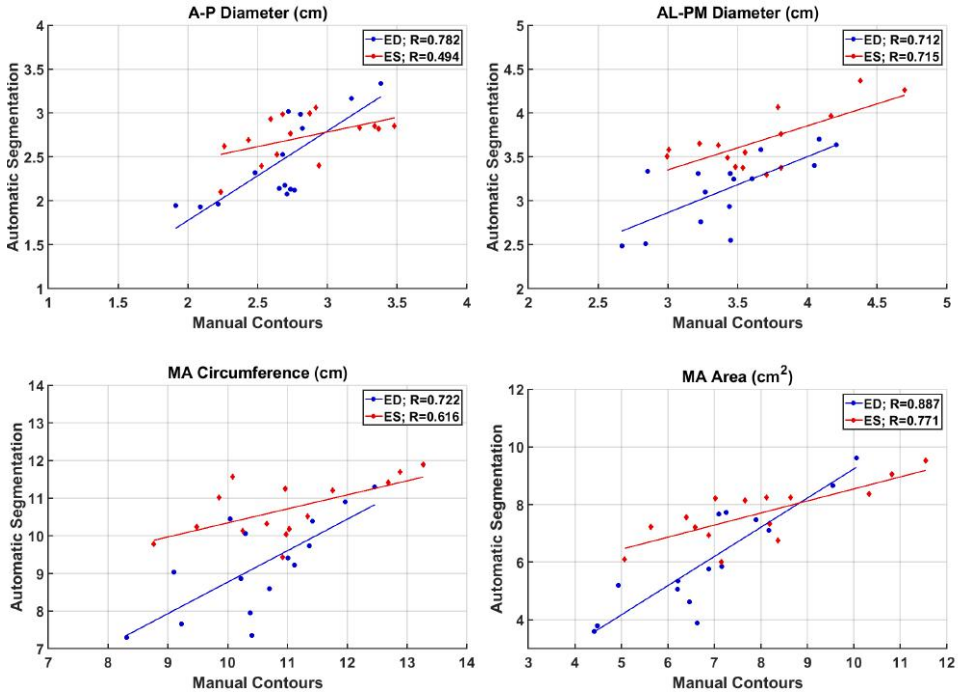

Figure A.8: Correlations between MV parameters at ED and ES obtained by manual contouring and automatic segmentation.

during diastole due to the very fast motion of the leaflets.

A.6 Conclusion

In this work, a novel automatic MV segmentation and tracking framework for RT3DE TTE based on BEAS and lAAOF is proposed and validated. This tool provides dynamic systolic MV assessment, allowing for the extraction of important clinical parameters with good correlation to those obtained from manual assessment.

Bibliography

[1] World Health Organization et al. Global status report on noncommunicable diseases 2014: attaining the nine global noncommunicable diseases targets; a shared responsability. In *Global status report on noncommunicable diseases 2014: attaining the nine global noncommunicable diseases targets; a shared responsability*. 2014.

[2] Colin D Mathers and Dejan Loncar. Projections of global mortality and burden of disease from 2002 to 2030. *PLoS medicine*, 3(11):e442, 2006.

[3] Daniel Barbosa, Thomas Dietenbeck, Joel Schaerer, Jan D'hooge, Denis Friboulet, and Olivier Bernard. B-spline explicit active surfaces: an efficient framework for real-time 3-D region-based segmentation. *IEEE Transactions on Image Processing*, 21(1):241–251, 2012.

[4] Qi Duan, Elsa D Angelini, and Andrew F Laine. Real-time segmentation by active geometric functions. *Computer methods and programs in biomedicine*, 98(3):223–230, 2010.

[5] Authors/Task Force members, Perry M Elliott, Aris Anastasakis, Michael A Borger, Martin Borggrefe, Franco Cecchi, Philippe Charron, Albert Alain Hagege, Antoine Lafont, Giuseppe Limongelli, et al. 2014 ESC guidelines on diagnosis and management of hypertrophic cardiomyopathy: the task force for the diagnosis and management of hypertrophic cardiomyopathy of the european society of cardiology (ESC). *European heart journal*, 35(39):2733–2779, 2014.

[6] Rick A Nishimura, Catherine M Otto, Robert O Bonow, Blase A Carabello, John P Erwin, Robert A Guyton, Patrick T O'Gara, Carlos E Ruiz, Nikolaos J Skubas, Paul Sorajja, Thoralf M Sundt, and James D Thomas. 2014 AHA/ACC guideline for the management of patients with valvular heart disease. *Journal of the American College of Cardiology*, 63(22):e57–e185, 2014.

[7] Clyde W Yancy, Mariell Jessup, Biykem Bozkurt, Javed Butler, Donald E Casey, Mark H Drazner, Gregg C Fonarow, Stephen A Geraci, Tamara Horwich, James L Januzzi, et al. 2013 ACCF/AHA guideline for the management of heart failure: executive summary. *Circulation*, 128(16):1810–1852, 2013.

[8] Paul A Iaizzo. *Handbook of cardiac anatomy, physiology, and devices*. Springer Science & Business Media, 2009.

[9] *By adh30 revised work by DanielChangMD who revised original work of DestinyQx; Redrawn as SVG by xavax (Wikimedia Commons: Wiggers Diagram.svg) CC BY-SA 4.0, via Wikimedia Commons)*, 2018. `https://upload.wikimedia.org/wikipedia/commons/9/91/Wiggers_Diagram_2.svg`.

[10] Manuel D Cerqueira, Neil J Weissman, Vasken Dilsizian, Alice K Jacobs, Sanjiv Kaul, Warren K Laskey, Dudley J Pennell, John A Rumberger, Thomas Ryan, and Mario S Verani. Standardized myocardial segmentation and nomenclature for tomographic imaging of the heart: a statement for healthcare professionals from the cardiac imaging committee of the council on clinical cardiology of the american heart association. *Journal of the American Society of Echocardiography*, 15(5):463–467, 2002.

[11] Joaquin F Pombo, Bart L Troy, and Richard O Russell. Left ventricular volumes and ejection fraction by echocardiography. *Circulation*, 43(4):480–490, 1971.

[12] James D Thomas and Zoran B Popović. Assessment of left ventricular function by cardiac ultrasound. *Journal of the American College of Cardiology*, 48(10):2012 – 2025, 2006. Focus Issue: Cardiac Imaging.

[13] Harvey D White, Robin M Norris, Michael A Brown, Peter W Brandt, Ralph ML Whitlock, and Christopher J Wild. Left ventricular end-systolic volume as the major determinant of survival after recovery from myocardial infarction. *Circulation*, 76(1):44–51, 1987.

[14] Robin M Norris, Harvey D White, David B Cross, Christopher J Wild, and Ralph ML Whitlock. Prognosis after recovery from myocardial infarction: the relative importance of cardiac dilatation and coronary stenoses. *European heart journal*, 13(12):1611–1618, 1992.

[15] Robert J Burns, Raymond J Gibbons, Qilong Yi, Robin S Roberts, Todd D Miller, Gary L Schaer, Jeffrey L Anderson, and Salim Yusuf. The relationships of left ventricular ejection fraction, end-systolic volume index and infarct size to six-month mortality after hospital discharge following myocardial infarction treated by thrombolysis. *Journal of the American College of Cardiology*, 39(1):30 – 36, 2002.

[16] The Multicenter Postinfarction Research Group. Risk stratification and survival after myocardial infarction. *New England Journal of Medicine*, 309(6):331–336, 1983. PMID: 6866068.

[17] Jean L Rouleau, Mario Talajic, Bruce Sussex, Louise Potvin, Wayne Warnica, Richard F Davies, Martin Gardner, Duncan Stewart, Sylvain Plante, Robert Dupuis, Claude Lauzon, John Ferguson, Etel Mikes, Vidoslav Balnozan, and Pierre Savard. Myocardial infarction patients in the 1990s - their risk factors, stratification and survival in canada: The canadian assessment of myocardial infarction (CAMI) study. *Journal of the American College of Cardiology*, 27(5):1119 – 1127, 1996.

[18] Maria Teresa La Rovere, Gian Domenico Pinna, Stefan H Hohnloser, Frank I Marcus, Andrea Mortara, Ryuji Nohara, J Thomas Bigger, A John Camm, and Peter J Schwartz. Baroreflex sensitivity and heart rate variability in the identification of patients at risk for life-threatening arrhythmias. *Circulation*, 103(16):2072–2077, 2001.

[19] Derek V Exner, Katherine M Kavanagh, Michael P Slawnych, L Brent Mitchell, Darlene Ramadan, Sandeep G Aggarwal, Catherine Noullett, Allie Van Schaik, Ryan T Mitchell, Mariko A Shibata, Sajad Gulamhussein, James McMeekin, Wayne Tymchak, Gregory Schnell, Anne M Gillis, Robert S Sheldon, Gordon H Fick, and Henry J Duff. Noninvasive risk assessment early after a myocardial infarction: The REFINE study. *Journal of the American College of Cardiology*, 50(24):2275 – 2284, 2007.

[20] Axel Bauer, Petra Barthel, Raphael Schneider, Kurt Ulm, Alexander Müller, Anke Joeinig, Raphael Stich, Antti Kiviniemi, Katerina Hnatkova, Heikki Huikuri, Albert Schömig, Marek Malik, and Georg Schmidt. Improved stratification of autonomic regulation for risk prediction in post-infarction patients with preserved left ventricular function (ISAR-Risk). *European Heart Journal*, 30(5):576–583, 2009.

[21] Eldrin F Lewis, Lemuel A Moye, Jean L Rouleau, Frank M Sacks, J Malcolm O Arnold, J Wayne Warnica, Greg C Flaker, Eugene Braunwald, and Marc A Pfeffer. Predictors of late development of heart failure in stable survivors of myocardial infarction: The CARE study. *Journal of the American College of Cardiology*, 42(8):1446 – 1453, 2003.

[22] Al Hallstrom, Craig M Pratt, H Leon Greene, Melissa Huther, Stephen Gottlieb, Anthony DeMaria, and James B Young. Relations between heart failure, ejection fraction, arrhythmia suppression and mortality: Analysis of the cardiac arrhythmia suppression trial. *Journal of the American College of Cardiology*, 25(6):1250 – 1257, 1995.

[23] Alfred E Buxton, Kerry L Lee, Gail E Hafley, Luis A Pires, John D Fisher, Michael R Gold, Mark E Josephson, Michael H Lehmann, and Eric N Prystowsky. Limitations of ejection fraction for prediction of sudden death risk in patients with coronary artery disease: Lessons from the MUSTT study. *Journal of the American College of Cardiology*, 50(12):1150 – 1157, 2007.

[24] Theophilus E Owan, David O Hodge, Regina M Herges, Steven J Jacobsen, Veronique L Roger, and Margaret M Redfield. Trends in prevalence and outcome of heart failure with preserved ejection fraction. *New England Journal of Medicine*, 355(3):251–259, 2006. PMID: 16855265.

[25] R Sacha Bhatia, Jack V Tu, Douglas S Lee, Peter C Austin, Jiming Fang, Annick Haouzi, Yanyan Gong, and Peter P Liu. Outcome of heart failure with preserved ejection fraction in a population-based study. *New England Journal of Medicine*, 355(3):260–269, 2006. PMID: 16855266.

[26] Jithendra B Somaratne, Colin Berry, John JV McMurray, Katrina K Poppe, Robert N Doughty, and Gillian A Whalley. The prognostic significance of heart failure with preserved left ventricular ejection fraction: a literature-based meta-analysis. *European journal of heart failure*, 11(9):855–862, 2009.

[27] Meta-analysis Global Group in Chronic Heart Failure (MAGGIC). The survival of patients with heart failure with preserved or reduced left ventricular ejection fraction: an individual patient data meta-analysis. *European Heart Journal*, 33(14):1750–1757, 2012.

[28] M Komadja, JP Jais, F Reeves, B Goldfarb, JB Bouhour, Y Juillieres, J Lanfranchi, P Peycelon, P Geslin, D Carrie, and Y Grosgogeat. Factors predicting mortality in idiopathic dilated cardiomyopathy. *European Heart Journal*, 11(9):824–831, 1990.

[29] CS Rihal, RA Nishimura, LK Hatle, KR Bailey, and AJ Tajik. Systolic and diastolic dysfunction in patients with clinical diagnosis of dilated cardiomyopathy. relation to symptoms and prognosis. *Circulation*, 90(6):2772–2779, 1994.

[30] Pantaleo Giannuzzi, Pier L Temporelli, Enzo Bosimini, Pedro Silva, Alessandro Imparato, Ugo Corrà, Michele Galli, and Amerigo Giordano. Independent and incremental prognostic value of doppler-derived mitral deceleration time of early filling in both symptomatic and asymptomatic patients with left ventricular dysfunction. *Journal of the American College of Cardiology*, 28(2):383 – 390, 1996.

[31] Shigeki Yamada, Hideki Ishii, Hiroshi Takahashi, Toru Aoyama, Yasuhiro Morita, Hirotake Kasuga, Keiko Kimura, Yutaka Ito, Ryo Takahashi, Takanobu Toriyama, Yoshinari Yasuda, Mutsuharu Hayashi, Hideki Kamiya, Yukio Yuzawa, Shoichi Maruyama, Seiichi Matsuo, Tatsuaki Matsubara, and Toyoaki Murohara. Prognostic value of reduced left ventricular ejection fraction at start of hemodialysis therapy on cardiovascular and all-cause mortality in end-stage renal disease patients. *Clinical Journal of the American Society of Nephrology*, 5(10):1793–1798, 2010.

[32] Tali Sharir, Guido Germano, Paul B Kavanagh, Shenhan Lai, Ishac Cohen, Howard C Lewin, John D Friedman, Michael J Zellweger, and Daniel S Berman. Incremental prognostic value of post-stress left ventricular ejection fraction and volume by gated myocardial perfusion single photon emission computed tomography. *Circulation*, 100(10):1035–1042, 1999.

[33] Janine Krivokapich, John S Child, Donald O Walter, and Alan Garfinkel. Prognostic value of dobutamine stress echocardiography in predicting cardiac events in patients with known or suspected coronary artery disease. *Journal of the American College of Cardiology*, 33(3):708 – 716, 1999.

[34] Nicholas G Bellenger, Malcolm I Burgess, Simon G Ray, Avijit Lahiri, Andrew JS Coats, John GF Cleland, and Dudley J Pennell. Comparison of left ventricular ejection fraction and volumes in heart failure by echocardiography, radionuclide ventriculography and cardiovascular magnetic resonance. Are they interchangeable? *European heart journal*, 21(16):1387–1396, 2000.

[35] Frans JT Wackers, Harvey J Berger, David E Johnstone, Lee Goldman, Lawrence A Reduto, Rene A Langou, Alexander Gottschalk, Barry L Zaret, Lenny Quartararo, and Linda Pytlik. Multiple gated cardiac blood pool imaging for left ventricular ejection fraction: Validation of the technique and assessment of variability. *The American Journal of Cardiology*, 43(6):1159 – 1166, 1979.

[36] Ronald G Schwartz, William B McKenzie, Jonathan Alexander, Philip Sager, Anthony D'Souza, Amita Manatunga, Peter E Schwartz, Harvey J Berger, John Setaro, Lee Surkin, et al. Congestive heart failure and left ventricular dysfunction complicating doxorubicin therapy: seven-year experience using serial radionuclide angiocardiography. *The American Journal of Medicine*, 82(6):1109–1118, 1987.

[37] Tom R Miller, Jerold W Wallis, Brian R Landy, Robert J Gropler, and Chander L Sabharwal. Measurement of global and regional left ventricular function by cardiac PET. *Journal of Nuclear Medicine*, 35(6):999–1005, 1994.

[38] Robert O Bonow, Vasken Dilsizian, Alberto Cuocolo, and Stephen L Bacharach. Identification of viable myocardium in patients with chronic coronary artery disease and left ventricular dysfunction. Comparison of thallium scintigraphy with reinjection and PET imaging with 18F-fluorodeoxyglucose. *Circulation*, 83(1):26–37, 1991.

[39] Thomas L Szabo. *Diagnostic ultrasound imaging: inside out*. Academic Press, 2004.

[40] Paul Suetens. *Fundamentals of medical imaging*. Cambridge University Press, 2002.

[41] Siddharth Singh and Abha Goyal. The origin of echocardiography: a tribute to Inge Edler. *Texas Heart Institute Journal*, 34(4):431, 2007.

[42] Richard L Popp, Stanley B Wolfe, Tsuneo Hirata, and Harvey Feigenbaum. Estimation of right and left ventricular size by ultrasound: A study of the echoes from the interventricular septum. *The American journal of cardiology*, 24(4):523–530, 1969.

[43] Harvey Feigenbaum, Richard L Popp, Stanley B Wolfe, Bart L Troy, Joaquin F Pombo, Charles L Haine, and Harold T Dodge. Ultrasound measurements of the left ventricle: a correlative study with angiocardiography. *Archives of Internal Medicine*, 129(3):461–467, 1972.

[44] Horace L Wyatt, Ming K Heng, Samuel Meerbaum, Pascal Gueret, John Hestenes, Eugene Dula, and Eliot Corday. Cross-sectional echocardiography. II. Analysis of mathematic models for quantifying volume of the formalin-fixed left ventricle. *Circulation*, 61(6):1119–1125, 1980.

[45] Horace L Wyatt, Samuel Meerbaum, Ming K Heng, Pascal Gueret, and Eliot Corday. Cross-sectional echocardiography III. Analysis of mathematic models for quantifying volume of symmetric and asymmetric left ventricles. *American heart journal*, 100(6):821–828, 1980.

[46] Shougang Wang, Wei-Ning Lee, Jean Provost, Jianwen Luo, and Elisa E Konofagou. A composite high-frame-rate system for clinical cardiovascular imaging. *IEEE transactions on ultrasonics, ferroelectrics, and frequency control*, 55(10), 2008.

[47] David P Shattuck, Marc D Weinshenker, Stephen W Smith, and Olaf T von Ramm. Explososcan: A parallel processing technique for high speed ultrasound imaging with linear phased arrays. *The Journal of the Acoustical Society of America*, 75(4):1273–1282, 1984.

[48] Toshio Shirasaka. Ultrasonic imaging apparatus, March 21 1989. US Patent 4,815,043.

[49] Raoul Mallart and Mathias Fink. Improved imaging rate through simultaneous transmission of several ultrasound beams. In *New Developments in Ultrasonic Transducers and Transducer Systems*, volume 1733, pages 120–131. International Society for Optics and Photonics, 1992.

[50] Alessandro Ramalli, Alessandro Dallai, Enrico Boni, Luca Bassi, Valentino Meacci, Matteo Giovannetti, Ling Tong, Jan D'hooge, and Piero Tortoli. Multi transmit beams for fast cardiac imaging towards clinical routine. In *Ultrasonics Symposium (IUS), 2016 IEEE International*, pages 1–4. IEEE, 2016.

[51] Alejandra Ortega, Jean Provost, Ling Tong, Pedro Santos, Brecht Heyde, Mathieu Pernot, and Jan D'hooge. A comparison of the performance of different multiline transmit setups for fast volumetric cardiac ultrasound. *IEEE transactions on ultrasonics, ferroelectrics, and frequency control*, 63(12):2082–2091, 2016.

[52] B Delannoy, R Torguet, C Bruneel, E Bridoux, JM Rouvaen, and H Lasota. Acoustical image reconstruction in parallel-processing analog electronic systems. *Journal of Applied Physics*, 50(5):3153–3159, 1979.

[53] Jesper Udesen, Fredrik Gran, Kristoffer Lindskov Hansen, Jørgen Arendt Jensen, Carsten Thomsen, and Michael Bachmann Nielsen. High frame-rate blood vector velocity imaging using plane waves: Simulations and preliminary experiments. *IEEE transactions on ultrasonics, ferroelectrics, and frequency control*, 55(8):1729–1743, 2008.

[54] Mathieu Couade, Mathieu Pernot, Mickael Tanter, Emmanuel Messas, Alain Bel, Maguette Ba, Albert-Alain Hagège, and Mathias Fink. Ultrafast imaging of the heart using circular wave synthetic imaging with phased arrays. In *Ultrasonics Symposium (IUS), 2009 IEEE International*, pages 515–518. IEEE, 2009.

[55] Hideyuki Hasegawa and Hiroshi Kanai. High-frame-rate echocardiography using diverging transmit beams and parallel receive beamforming. *Journal of medical ultrasonics*, 38(3):129–140, 2011.

[56] Jean Provost, Vu Thanh-Hieu Nguyen, Diégo Legrand, Stan Okrasinski, Alexandre Costet, Alok Gambhir, Hasan Garan, and Elisa E Konofagou. Electromechanical wave imaging for arrhythmias. *Physics in Medicine & Biology*, 56(22):L1, 2011.

[57] Clement Papadacci, Mathieu Pernot, Mathieu Couade, Mathias Fink, and Mickael Tanter. High-contrast ultrafast imaging of the heart. *IEEE transactions on ultrasonics, ferroelectrics, and frequency control*, 61(2):288–301, 2014.

[58] Gregg E Trahey and Levin F Nock. Synthetic receive aperture imaging with phase correction for motion and for tissue inhomogeneities. II. Effects of and correction for motion. *IEEE transactions on ultrasonics, ferroelectrics, and frequency control*, 39(4):496–501, 1992.

[59] Maja Cikes, Ling Tong, George R Sutherland, and Jan D'hooge. Ultrafast cardiac ultrasound imaging: technical principles, applications, and clinical benefits. *JACC: Cardiovascular Imaging*, 7(8):812–823, 2014.

[60] Mickael Tanter and Mathias Fink. Ultrafast imaging in biomedical ultrasound. *IEEE transactions on ultrasonics, ferroelectrics, and frequency control*, 61(1):102–119, 2014.

[61] Hiroshi Kanai and Yoshiro Koiwa. Myocardial rapid velocity distribution. *Ultrasound in Medicine and Biology*, 27(4):481–498, 2001.

[62] Mathieu Pernot and Elisa E Konofagou. Electromechanical imaging of the myocardium at normal and pathological states. In *Ultrasonics Symposium, 2005 IEEE*, volume 2, pages 1091–1094. IEEE, 2005.

[63] Jean Provost, Wei-Ning Lee, Kana Fujikura, and Elisa E Konofagou. Imaging the electromechanical activity of the heart in vivo. *Proceedings of the National Academy of Sciences*, 108(21):8565–8570, 2011.

[64] Aaron Fenster, Donal B Downey, and H Neale Cardinal. Three-dimensional ultrasound imaging. *Physics in medicine & biology*, 46(5):R67, 2001.

[65] Don L Dekker, Robert L Piziali, and Eugene Dong Jr. A system for ultrasonically imaging the human heart in three dimensions. *Computers and biomedical research*, 7(6):544–553, 1974.

[66] Jeffery C Bamber, Robert J Eckersley, P Hubregtse, Nigel L Bush, David S Bell, and Diane C Crawford. Data processing for 3-D ultrasound visualization of tumor anatomy and blood flow. In *Visualization in Biomedical Computing'92*, volume 1808, pages 651–664. International Society for Optics and Photonics, 1992.

[67] Donal B Downey and Aaron Fenster. Vascular imaging with a three-dimensional power doppler system. *AJR. American Journal of Roentgenology*, 165(3):665–668, 1995.

[68] Odd Helge Gilja, Nils Thune, Knut Matre, Trygve Hausken, Arnold Berstad, et al. In vitro evaluation of three-dimensional ultrasonography in volume estimation of abdominal organs. *Ultrasound in medicine & biology*, 20(2):157–165, 1994.

[69] Alain Delabays, Natesa G Pandian, Qi-Ling Cao, Lissa Sugeng, Gerald Marx, Achi Ludomirski, and Steven L Schwartz. Transthoracic real-time three-dimensional echocardiography using a fan-like scanning approach for data acquisition. *Echocardiography*, 12(1):49–59, 1995.

[70] Tracy L Elliot, Dónal B Downey, Shidong Tong, Carolyn A McLean, and Aaron Fenster. Accuracy of prostate volume measurements in vitro using three-dimensional ultrasound. *Academic radiology*, 3(5):401–406, 1996.

[71] Shidong Tong, Donal B Downey, H Neale Cardinal, and Aaron Fenster. A three-dimensional ultrasound prostate imaging system. *Ultrasound in medicine & biology*, 22(6):735–746, 1996.

[72] Stephen W Smith, Henry G Pavy, and Olaf T von Ramm. High-speed ultrasound volumetric imaging system. I. Transducer design and beam steering. *IEEE transactions on ultrasonics, ferroelectrics, and frequency control*, 38(2):100–108, 1991.

[73] Olaf T Von Ramm, Stephen W Smith, and Henry G Pavy. High-speed ultrasound volumetric imaging system. II. Parallel processing and image display. *IEEE transactions on ultrasonics, ferroelectrics, and frequency control*, 38(2):109–115, 1991.

[74] Judy Hung, Roberto Lang, Frank Flachskampf, Stanton K Shernan, Marti L McCulloch, David B Adams, James Thomas, Mani Vannan, and Thomas Ryan. 3D echocardiography: a review of the current status and future directions. *Journal of the American Society of Echocardiography*, 20(3):213–233, 2007.

[75] J Alison Noble and Djamal Boukerroui. Ultrasound image segmentation: a survey. *IEEE Transactions on medical imaging*, 25(8):987–1010, 2006.

[76] KY Esther Leung and Johan G Bosch. Automated border detection in three-dimensional echocardiography: principles and promises. *European journal of echocardiography*, 11(2):97–108, 2010.

[77] Olivier Gerard, Antoine Collet Billon, Jean-Michel Rouet, Miarie Jacob, Maxim Fradkin, and Cyril Allouche. Efficient model-based quantification of left ventricular function in 3-D echocardiography. *IEEE transactions on medical imaging*, 21(9):1059–1068, 2002.

[78] Johan Montagnat, Maxime Sermesant, Hervé Delingette, Grégoire Malandain, and Nicholas Ayache. Anisotropic filtering for model-based segmentation of 4D cylindrical echocardiographic images. *Pattern Recognition Letters*, 24(4-5):815–828, 2003.

[79] Vladimir Zagrodsky, Vivek Walimbe, Carlos R Castro-Pareja, Jian Xin Qin, Jong-Min Song, and Raj Shekhar. Registration-assisted segmentation of real-time 3-D echocardiographic data using deformable models. *IEEE Transactions on Medical Imaging*, 24(9):1089–1099, 2005.

[80] Maartje M Nillesen, Richard GP Lopata, Inge H Gerrits, Livia Kapusta, Henkjan J Huisman, Johan M Thijssen, and Chris L de Korte. Segmentation of the heart muscle in 3-D pediatric echocardiographic images. *Ultrasound in Medicine and Biology*, 33(9):1453–1462, 2007.

[81] Elsa D Angelini, Andrew F Laine, Shin Takuma, Jeffrey W Holmes, and Shunichi Homma. LV volume quantification via spatiotemporal analysis of real-time 3-D echocardiography. *IEEE Transactions on Medical Imaging*, 20(6):457–469, 2001.

[82] Xenophon Papademetris, Albert J Sinusas, Donald P Dione, and James S Duncan. Estimation of 3D left ventricular deformation from echocardiography. *Medical image analysis*, 5(1):17–28, 2001.

[83] Djamal Boukerroui, Olivier Basset, Atilla Baskurt, and Gérard Gimenez. A multiparametric and multiresolution segmentation algorithm of 3D ultrasonic data. *IEEE transactions on ultrasonics, ferroelectrics, and frequency control*, 48(1):64–77, 2001.

[84] Yun Zhu, Xenophon Papademetris, Albert Sinusas, and James S Duncan. Segmentation of myocardial volumes from real-time 3D echocardiography using an incompressibility constraint. In *International Conference on Medical Image Computing and Computer-Assisted Intervention*, pages 44–51. Springer, 2007.

[85] Xujiong Ye, J Alison Noble, and David Atkinson. 3-D freehand echocardiography for automatic left ventricle reconstruction and analysis based on multiple acoustic windows. *IEEE transactions on medical imaging*, 21(9):1051–1058, 2002.

[86] Elsa D Angelini, Shunichi Homma, Gregory Pearson, Jeffrey W Holmes, and Andrew F Laine. Segmentation of real-time three-dimensional ultrasound for quantification of ventricular function: a clinical study on right and left ventricles. *Ultrasound in Medicine and Biology*, 31(9):1143–1158, 2005.

[87] Cristiana Corsi, Giuseppe Saracino, Alessandro Sarti, and Claudio Lamberti. Left ventricular volume estimation for real-time three-dimensional echocardiography. *IEEE transactions on medical imaging*, 21(9):1202–1208, 2002.

[88] Ning Lin, Weichuan Yu, and James S Duncan. Combinative multi-scale level set framework for echocardiographic image segmentation. *Medical Image Analysis*, 7(4):529–537, 2003.

[89] Alessandro Sarti, Cristiana Corsi, Elena Mazzini, and Claudio Lamberti. Maximum likelihood segmentation of ultrasound images with Rayleigh distribution. *IEEE transactions on ultrasonics, ferroelectrics, and frequency control*, 52(6):947–960, 2005.

[90] Enrico G Caiani, Cristiana Corsi, Jose Zamorano, Lissa Sugeng, Peter MacEneaney, Lynn Weinert, Roberto Battani, Juan Luis Gutierrez, Rick Koch, Leopoldo Perez de Isla, et al. Improved semiautomated quantification of left ventricular volumes and ejection fraction using 3-dimensional echocardiography with a full matrix-array transducer: comparison with magnetic resonance imaging. *Journal of the American Society of Echocardiography*, 18(8):779–788, 2005.

[91] Meng Ma, Marijn van Stralen, Johan HC Reiber, Johan G Bosch, and Boudewijn PF Lelieveldt. Left ventricle segmentation from contrast enhanced fast rotating ultrasound images using three dimensional active shape models. In *International Conference on Functional Imaging and Modeling of the Heart*, pages 295–302. Springer, 2009.

[92] Meng Ma, Marijn van Stralen, Johan HC Reiber, Johan G Bosch, and Boudewijn PF Lelieveldt. Model driven quantification of left ventricular function from sparse single-beat 3D echocardiography. *Medical image analysis*, 14(4):582–593, 2010.

[93] Jøger Hansegård, Fredrik Orderud, and Stein I Rabben. Real-time active shape models for segmentation of 3D cardiac ultrasound. In *International Conference on Computer Analysis of Images and Patterns*, pages 157–164. Springer, 2007.

[94] Jøger Hansegård, Stig Urheim, Ketil Lunde, and Stein Inge Rabben. Constrained active appearance models for segmentation of triplane echocardiograms. *IEEE transactions on medical imaging*, 26(10):1391–1400, 2007.

[95] HS Wu, D Wang, L Shi, and CM Yu. Automatic segmentation of left ventricle in 3D echocardiography using a level set approach. *International Journal of Cardiology*, 164(2):S12–S13, 2013.

[96] KY Esther Leung, Marijn van Stralen, Marco M Voormolen, Nico de Jong, Antonius FW van der Steen, Johan HC Reiber, and Johan G Bosch. Improving 3D active

appearance model segmentation of the left ventricle with jacobian tuning. In *Medical Imaging 2008: Image Processing*, volume 6914, page 69143B. International Society for Optics and Photonics, 2008.

[97] Giuseppe Coppini, Riccardo Poli, and Guido Valli. Recovery of the 3-D shape of the left ventricle from echocardiographic images. *IEEE Transactions on Medical Imaging*, 14(2):301–317, 1995.

[98] Mingzhou Song, Robert M Haralick, Florence H Sheehan, and Richard K Johnson. Integrated surface model optimization for freehand three-dimensional echocardiography. *IEEE transactions on medical imaging*, 21(9):1077–1090, 2002.

[99] Bogdan Georgescu, Xiang Sean Zhou, Dorin Comaniciu, and Alok Gupta. Database-guided segmentation of anatomical structures with complex appearance. In *IEEE Computer Society Conference on Computer Vision and Pattern Recognition, 2005. CVPR 2005.*, volume 2, pages 429–436. IEEE, 2005.

[100] Xiaoguang Lu, Bogdan Georgescu, Yefeng Zheng, Joanne Otsuki, and Dorin Comaniciu. AutoMPR: Automatic detection of standard planes in 3D echocardiography. In *5th IEEE International Symposium on Biomedical Imaging: From Nano to Macro, 2008. ISBI 2008.*, pages 1279–1282. IEEE, 2008.

[101] Andriy Myronenko, Xubo Song, and David J Sahn. LV motion tracking from 3D echocardiography using textural and structural information. In *International Conference on Medical Image Computing and Computer-Assisted Intervention*, pages 428–435. Springer, 2007.

[102] An Elen, Hon Fai Choi, Dirk Loeckx, Hang Gao, Piet Claus, Paul Suetens, Frederik Maes, and Jan D'hooge. Three-dimensional cardiac strain estimation using spatio–temporal elastic registration of ultrasound images: A feasibility study. *IEEE transactions on medical imaging*, 27(11):1580–1591, 2008.

[103] Brecht Heyde, Daniel Barbosa, Piet Claus, Frederik Maes, and Jan D'hooge. Three-dimensional cardiac motion estimation based on non-rigid image registration using a novel transformation model adapted to the heart. In *International Workshop on Statistical Atlases and Computational Models of the Heart*, pages 142–150. Springer, 2012.

[104] Gemma Piella, Antonio R Porras, Mathieu De Craene, Nicolas Duchateau, and Alejandro F Frangi. Temporal diffeomorphic free form deformation to quantify changes induced by left and right bundle branch block and pacing. In *International Workshop on Statistical Atlases and Computational Models of the Heart*, pages 134–141. Springer, 2012.

[105] Leopoldo Pérez de Isla, David Vivas Balcones, Covadonga Fernández-Golfín, Pedro Marcos-Alberca, Carlos Almería, José Luis Rodrigo, Carlos Macaya, and Jose Zamorano. Three-dimensional-wall motion tracking: a new and faster tool for myocardial strain assessment: comparison with two-dimensional-wall motion tracking. *Journal of the American Society of Echocardiography*, 22(4):325–330, 2009.

[106] Patricia Reant, Laurence Barbot, Cecile Touche, Marina Dijos, Florence Arsac, Xavier Pillois, Mathieu Landelle, Raymond Roudaut, and Stephane Lafitte. Evaluation of global left ventricular systolic function using three-dimensional echocardiography speckle-tracking strain parameters. *Journal of the American Society of Echocardiography*, 25(1):68–79, 2012.

[107] Ken Saito, Hiroyuki Okura, Nozomi Watanabe, Akihiro Hayashida, Kikuko Obase, Koichiro Imai, Tomoko Maehama, Takahiro Kawamoto, Yoji Neishi, and Kiyoshi

Yoshida. Comprehensive evaluation of left ventricular strain using speckle tracking echocardiography in normal adults: comparison of three-dimensional and two-dimensional approaches. *Journal of the American Society of Echocardiography*, 22(9):1025–1030, 2009.

[108] Jonas Crosby, Brage H Amundsen, Torbjørn Hergum, Espen W Remme, Stian Langeland, and Hans Torp. 3-D speckle tracking for assessment of regional left ventricular function. *Ultrasound in Medicine and Biology*, 35(3):458–471, 2009.

[109] Yoshihiro Seo, Tomoko Ishizu, Yoshiharu Enomoto, Haruhiko Sugimori, and Kazutaka Aonuma. Endocardial surface area tracking for assessment of regional LV wall deformation with 3D speckle tracking imaging. *JACC: Cardiovascular Imaging*, 4(4):358–365, 2011.

[110] Lennart Tautz, Anja Hennemuth, and Heinz-Otto Peitgen. Quadrature filter based motion analysis for 3D ultrasound sequences. In *International Workshop on Statistical Atlases and Computational Models of the Heart*, pages 169–177. Springer, 2012.

[111] Martino Alessandrini, Hervé Liebgott, Daniel Barbosa, and Olivier Bernard. Monogenic phase based optical flow computation for myocardial motion analysis in 3D echocardiography. In *International Workshop on Statistical Atlases and Computational Models of the Heart*, pages 159–168. Springer, 2012.

[112] Oudom Somphone, Cecile Dufour, Benoît Mory, Loïc Hilpert, Sherif Makram-Ebeid, Nicolas Villain, Mathieu De Craene, Pascal Allain, and Eric Saloux. Motion estimation in 3D echocardiography using smooth field registration. In *International Workshop on Statistical Atlases and Computational Models of the Heart*, pages 151–158. Springer, 2012.

[113] Qi Duan, Elsa D Angelini, Susan L Herz, Christopher M Ingrassia, Kevin D Costa, Jeffrey W Holmes, Shunichi Homma, and Andrew F Laine. Region-based endocardium tracking on real-time three-dimensional ultrasound. *Ultrasound in Medicine and Biology*, 35(2):256–265, 2009.

[114] Olivier Bernard, Johan G Bosch, Brecht Heyde, Martino Alessandrini, Daniel Barbosa, Sorina Camarasu-Pop, Frederic Cervenansky, Sébastien Valette, Oana Mirea, Michel Bernier, et al. Standardized evaluation system for left ventricular segmentation algorithms in 3D echocardiography. *IEEE transactions on medical imaging*, 35(4):967–977, 2016.

[115] Daniel Barbosa, Denis Friboulet, Jan D'hooge, and Olivier Bernard. Fast tracking of the left ventricle using global anatomical affine optical flow and local recursive block matching. *Proceedings of the MICCAI Challenge on Endocardial Three-dimensional Ultrasound Segmentation-CETUS*, pages 17–24, 2014.

[116] Erik Smistad and Frank Lindseth. Real-time tracking of the left ventricle in 3D ultrasound using Kalman filter and mean value coordinates. *Medical Image Segmentation for Improved Surgical Navigation*, page 189, 2014.

[117] Denisa Muraru, Umberto Cucchini, Sorina Mihăilă, Marcelo Haertel Miglioranza, Patrizia Aruta, Giacomo Cavalli, Antonella Cecchetto, Seena Padayattil-Josè, Diletta Peluso, Sabino Iliceto, et al. Left ventricular myocardial strain by three-dimensional speckle-tracking echocardiography in healthy subjects: reference values and analysis of their physiologic and technical determinants. *Journal of the American Society of Echocardiography*, 27(8):858–871, 2014.

[118] Lawrence D Jacobs, Ivan S Salgo, Sascha Goonewardena, Lynn Weinert, Patrick Coon, Dianna Bardo, Olivier Gerard, Pascal Allain, Jose L Zamorano, Leopoldo P de Isla, et al. Rapid online quantification of left ventricular volume from real-time three-dimensional echocardiographic data. *European Heart Journal*, 27(4):460–468, 2005.

[119] Sebastiaan A Kleijn, Mohamed FA Aly, Caroline B Terwee, Albert C van Rossum, and Otto Kamp. Comparison between direct volumetric and speckle tracking methodologies for left ventricular and left atrial chamber quantification by three-dimensional echocardiography. *American Journal of Cardiology*, 108(7):1038–1044, 2011.

[120] Heartmodel AI. `https://www.philips.com.eg/healthcare/resources/feature-detail/anatomical-intelligence`. Accessed on: 2018-04-01.

[121] Francesco Maffessanti, Hans-Joachim Nesser, Lynn Weinert, Regina Steringer-Mascherbauer, Johannes Niel, Willem Gorissen, Lissa Sugeng, Roberto M Lang, and Victor Mor-Avi. Quantitative evaluation of regional left ventricular function using three-dimensional speckle tracking echocardiography in patients with and without heart disease. *American Journal of Cardiology*, 104(12):1755–1762, 2009.

[122] Ryo Kawamura, Yoshihiro Seo, Tomoko Ishizu, Akiko Atsumi, Masayoshi Yamamoto, Tomoko Machino-Ohtsuka, Hideki Nakajima, Satoshi Sakai, Yumiko Oishi Tanaka, Manabu Minami, et al. Feasibility of left ventricular volume measurements by three-dimensional speckle tracking echocardiography depends on image quality and degree of left ventricular enlargement: validation study with cardiac magnetic resonance imaging. *Journal of cardiology*, 63(3):230–238, 2014.

[123] Tomoyuki Takeguchi, Masahide Nishiura, Yasuhiko Abe, Hiroyuki Ohuchi, and Tetsuya Kawagishi. Practical considerations for a method of rapid cardiac function analysis based on three-dimensional speckle tracking in a three-dimensional diagnostic ultrasound system. *Journal of Medical Ultrasonics*, 37(2):41–49, 2010.

[124] Yefeng Zheng, Adrian Barbu, Bogdan Georgescu, Michael Scheuering, and Dorin Comaniciu. Fast automatic heart chamber segmentation from 3D CT data using marginal space learning and steerable features. In *Computer Vision, 2007. ICCV 2007. IEEE 11th International Conference on*, pages 1–8. IEEE, 2007.

[125] Lin Yang, Bogdan Georgescu, Yefeng Zheng, Peter Meer, and Dorin Comaniciu. 3D ultrasound tracking of the left ventricle using one-step forward prediction and data fusion of collaborative trackers. In *Computer Vision and Pattern Recognition, 2008. CVPR 2008. IEEE Conference on*, pages 1–8. IEEE, 2008.

[126] Victor Mor-Avi, Carly Jenkins, Harald P Kühl, Hans-Joachim Nesser, Thomas Marwick, Andreas Franke, Christian Ebner, Benjamin H Freed, Regina Steringer-Mascherbauer, Heidi Pollard, et al. Real-time 3-dimensional echocardiographic quantification of left ventricular volumes: multicenter study for validation with magnetic resonance imaging and investigation of sources of error. *JACC: Cardiovascular Imaging*, 1(4):413–423, 2008.

[127] Samuel C Siu, J Miguel Rivera, J Luis Guerrero, Mark D Handschumacher, Jean Paul Lethor, Arthur E Weyman, Robert A Levine, and Michael H Picard. Three-dimensional echocardiography. in vivo validation for left ventricular volume and function. *Circulation*, 88(4):1715–1723, 1993.

[128] Michal Hubka, Edward L Bolson, John A McDonald, Roy W Martin, Brad Munt, and Florence H Sheehan. Three-dimensional echocardiographic measurement of left

and right ventricular mass and volume: in vitro validation. *The international journal of cardiovascular imaging*, 18(2):111–118, 2002.

[129] Michael A Schmidt, Chikai J Ohazama, Kwabena O Agyeman, Raisa Z Freidlin, Michael Jones, Joy M Laurienzo, Cynthia L Brenneman, Andrew E Arai, Olaf T von Ramm, and Julio A Panza. Real-time three-dimensional echocardiography for measurement of left ventricular volumes. *American Journal of Cardiology*, 84(12):1434–1439, 1999.

[130] Doyal Lee, Anthon R Fuisz, Po-Hoey Fan, Tsui-Lieh Hsu, Chun-Pun Liu, and Hung-Tin Chiang. Real-time 3-dimensional echocardiographic evaluation of left ventricular volume: correlation with magnetic resonance imaging—a validation study. *Journal of the American Society of Echocardiography*, 14(10):1001–1009, 2001.

[131] Harald P Kühl, Andreas Franke, Marc W Merx, Rainer Hoffmann, David Puschmann, and Peter Hanrath. Rapid quantification of left ventricular function and mass using transoesophageal three-dimensional echocardiography: validation of a method that uses long-axis cutplanes. *European Journal of Echocardiography*, 3(1):213–221, 2000.

[132] Herman FJ Mannaerts, Johannes A Van Der Heide, Otto Kamp, Theano Papavassiliu, Johannes T Marcus, Aernout Beek, Albert C Van Rossum, Jos Twisk, and Cees A Visser. Quantification of left ventricular volumes and ejection fraction using freehand transthoracic three-dimensional echocardiography: comparison with magnetic resonance imaging. *Journal of the American Society of Echocardiography*, 16(2):101–109, 2003.

[133] Harald P Kühl, Marcus Schreckenberg, Dierk Rulands, Markus Katoh, Wolfgang Schäfer, Georg Schummers, Arno Bücker, Peter Hanrath, and Andreas Franke. High-resolution transthoracic real-time three-dimensional echocardiography: quantitation of cardiac volumes and function using semi-automatic border detection and comparison with cardiac magnetic resonance imaging. *Journal of the American College of Cardiology*, 43(11):2083–2090, 2004.

[134] Carly Jenkins, Kristen Bricknell, Lizelle Hanekom, and Thomas H Marwick. Reproducibility and accuracy of echocardiographic measurements of left ventricular parameters using real-time three-dimensional echocardiography. *Journal of the American College of Cardiology*, 44(4):878–886, 2004.

[135] Lissa Sugeng, Victor Mor-Avi, Lynn Weinert, Johannes Niel, Christian Ebner, Regina Steringer-Mascherbauer, Frank Schmidt, Christian Galuschky, Georg Schummers, Roberto M Lang, et al. Quantitative assessment of left ventricular size and function: side-by-side comparison of real-time three-dimensional echocardiography and computed tomography with magnetic resonance reference. *Circulation*, 114(7):654–661, 2006.

[136] Annemien E van den Bosch, Danielle Robbers-Visser, Boudewijn J Krenning, Marco M Voormolen, Jackie S McGhie, Wim A Helbing, Jolien W Roos-Hesselink, Maarten L Simoons, and Folkert J Meijboom. Real-time transthoracic three-dimensional echocardiographic assessment of left ventricular volume and ejection fraction in congenital heart disease. *Journal of the American Society of Echocardiography*, 19(1):1–6, 2006.

[137] Carly Jenkins, Jonathan Chan, Lizelle Hanekom, and Thomas H Marwick. Accuracy and feasibility of online 3-dimensional echocardiography for measurement of left ventricular parameters. *Journal of the American Society of Echocardiography*, 19(9):1119–1128, 2006.

[138] Osama II Soliman, Boudewijn J Krenning, Marcel L Geleijnse, Attila Nemes, Robert-Jan van Geuns, Timo Baks, Ashraf M Anwar, Tjebbe W Galema, Wim B Vletter, and Folkert J Ten Cate. A comparison between QLAB and TomTec full volume reconstruction for real time three-dimensional echocardiographic quantification of left ventricular volumes. *Echocardiography*, 24(9):967–974, 2007.

[139] Osama II Soliman, Boudewijn J Krenning, Marcel L Geleijnse, Attila Nemes, Johan G Bosch, Robert-Jan van Geuns, Sharon W Kirschbaum, Ashraf M Anwar, Tjebbe W Galema, Wim B Vletter, et al. Quantification of left ventricular volumes and function in patients with cardiomyopathies by real-time three-dimensional echocardiography: a head-to-head comparison between two different semiautomated endocardial border detection algorithms. *Journal of the American Society of Echocardiography*, 20(9):1042–1049, 2007.

[140] Jøger Hansegård, Stig Urheim, Ketil Lunde, Siri Malm, and Stein Inge Rabben. Semi-automated quantification of left ventricular volumes and ejection fraction by real-time three-dimensional echocardiography. *Cardiovascular ultrasound*, 7(1):18, 2009.

[141] Denisa Muraru, Luigi P Badano, Gianluca Piccoli, Pasquale Gianfagna, Lorenzo Del Mestre, Davide Ermacora, and Alessandro Proclemer. Validation of a novel automated border-detection algorithm for rapid and accurate quantitation of left ventricular volumes based on three-dimensional echocardiography. *European journal of echocardiography*, 11(4):359–368, 2010.

[142] Sebastiaan A Kleijn, Wessel P Brouwer, Mohamed FA Aly, Iris K Rüssel, Gerben J de Roest, Aernout M Beek, Albert C van Rossum, and Otto Kamp. Comparison between three-dimensional speckle-tracking echocardiography and cardiac magnetic resonance imaging for quantification of left ventricular volumes and function. *European Heart Journal–Cardiovascular Imaging*, 13(10):834–839, 2012.

[143] Christopher A Miller, Keith Pearce, Peter Jordan, Rachel Argyle, David Clark, Martin Stout, Simon G Ray, and Matthias Schmitt. Comparison of real-time three-dimensional echocardiography with cardiovascular magnetic resonance for left ventricular volumetric assessment in unselected patients. *European Heart Journal–Cardiovascular Imaging*, 13(2):187–195, 2011.

[144] Paaladinesh Thavendiranathan, Shizhen Liu, David Verhaert, Anna Calleja, Adrien Nitinunu, Thomas Van Houten, Nathalie De Michelis, Orlando Simonetti, Sanjay Rajagopalan, Thomas Ryan, et al. Feasibility, accuracy, and reproducibility of real-time full-volume 3D transthoracic echocardiography to measure LV volumes and systolic function: a fully automated endocardial contouring algorithm in sinus rhythm and atrial fibrillation. *JACC: Cardiovascular Imaging*, 5(3):239–251, 2012.

[145] Quan Bin Zhang, Jing Ping Sun, Rui Feng Gao, Alex Pui-Wai Lee, Yan Lin Feng, Xiao Rong Liu, Wei Sheng, Feng Liu, and Cheuk-Man Yu. Novel single-beat full-volume capture real-time three-dimensional echocardiography and auto-contouring algorithm for quantification of left ventricular volume: validation with cardiac magnetic resonance imaging. *International journal of cardiology*, 168(3):2946–2948, 2013.

[146] Sung-A Chang, Sang-Chol Lee, Eun-Young Kim, Seung-Hee Hahm, Shin Yi Jang, Sung-Ji Park, Jin-Oh Choi, Seung Woo Park, Yeon Hyeon Choe, and Jae K Oh. Feasibility of single-beat full-volume capture real-time three-dimensional echocardiography and auto-contouring algorithm for quantification of left ventricular volume: validation with cardiac magnetic resonance imaging. *Journal of the American Society of Echocardiography*, 24(8):853–859, 2011.

[147] Kentaro Shibayama, Hiroyuki Watanabe, Nobuo Iguchi, Shunsuke Sasaki, Keitaro Mahara, Jun Umemura, and Tetsuya Sumiyoshi. Evaluation of automated measurement of left ventricular volume by novel real-time 3-dimensional echocardiographic system: validation with cardiac magnetic resonance imaging and 2-dimensional echocardiography. *Journal of cardiology*, 61(4):281–288, 2013.

[148] Wendy Tsang, Ivan S Salgo, Lyubomir Zarochev, Scott Settlemier, Nicole Bhave, Juergen Weese, Irina Waechter-Stehle, Michael Cardinale, Aldo Prado, Lynn Weinert, et al. Fully automated quantification of left ventricular and left atrial volumes from transthoracic 3D echocardiography: a validation study. *Journal of the American College of Cardiology*, 61(10 Supplement):E904, 2018.

[149] Yuichi J Shimada and Takahiro Shiota. A meta-analysis and investigation for the source of bias of left ventricular volumes and function by three-dimensional echocardiography in comparison with magnetic resonance imaging. *American Journal of Cardiology*, 107(1):126–138, 2011.

[150] Jennifer L Dorosz, Dennis C Lezotte, David A Weitzenkamp, Larry A Allen, and Ernesto E Salcedo. Performance of 3-dimensional echocardiography in measuring left ventricular volumes and ejection fraction: a systematic review and meta-analysis. *Journal of the American College of Cardiology*, 59(20):1799–1808, 2012.

[151] Thomas H Marwick. Application of 3D echocardiography to everyday practice: Development of normal ranges is step 1∗, 2012.

[152] Erlend Aune, Morten Bækkevar, Olaf Rødevand, and Jan Erik Otterstad. Reference values for left ventricular volumes with real-time 3-dimensional echocardiography. *Scandinavian Cardiovascular Journal*, 44(1):24–30, 2010.

[153] Kyoko Kaku, Masaaki Takeuchi, Kyoko Otani, Lissa Sugeng, Hiromi Nakai, Nobuhiko Haruki, Hidetoshi Yoshitani, Nozomi Watanabe, Kiyoshi Yoshida, Yutaka Otsuji, et al. Age-and gender-dependency of left ventricular geometry assessed with real-time three-dimensional transthoracic echocardiography. *Journal of the American Society of Echocardiography*, 24(5):541–547, 2011.

[154] Shota Fukuda, Hiroyuki Watanabe, Masao Daimon, Yukio Abe, Akihiro Hirashiki, Kumiko Hirata, Hiroshi Ito, Masumi Iwai-Takano, Katsuomi Iwakura, Chisato Izumi, et al. Normal values of real-time 3-dimensional echocardiographic parameters in a healthy japanese population. *Circulation Journal*, 76(5):1177–1181, 2012.

[155] Navtej S Chahal, Tiong K Lim, Piyush Jain, John C Chambers, Jaspal S Kooner, and Roxy Senior. Population-based reference values for 3D echocardiographic LV volumes and ejection fraction. *JACC: Cardiovascular Imaging*, 5(12):1191–1197, 2012.

[156] Denisa Muraru, Luigi P Badano, Diletta Peluso, Lucia Dal Bianco, Simona Casablanca, Gonenc Kocabay, Giacomo Zoppellaro, and Sabino Iliceto. Comprehensive analysis of left ventricular geometry and function by three-dimensional echocardiography in healthy adults. *Journal of the American Society of Echocardiography*, 26(6):618–628, 2013.

[157] Katrina K Poppe, Robert N Doughty, and Gillian A Whalley. Redefining normal reference ranges for echocardiography: a major new individual person data meta-analysis. *European Heart Journal–Cardiovascular Imaging*, 14(4):347–348, 2012.

[158] Gillian Whalley. A meta-analysis of echocardiographic measurements of the left heart for the development of normative reference ranges in a large international cohort: the echonormal study. 2014.

[159] Daniel Barbosa, Olivier Bernard, Oana Savu, Thomas Dietenbeck, Brecht Heyde, Piet Claus, Denis Friboulet, and Jan D'hooge. Coupled B-spline active geometric functions for myocardial segmentation: A localized region-based approach. In *Ultrasonics Symposium (IUS), 2010 IEEE*, pages 1648–1651. IEEE, 2010.

[160] Michael Unser. Splines: A perfect fit for signal and image processing. *IEEE Signal processing magazine*, 16(6):22–38, 1999.

[161] Shawn Lankton and Allen Tannenbaum. Localizing region-based active contours. *IEEE transactions on image processing*, 17(11):2029–2039, 2008.

[162] Jan Kybic and Michael Unser. Fast parametric elastic image registration. *IEEE transactions on image processing*, 12(11):1427–1442, 2003.

[163] Tony F Chan and Luminita A Vese. Active contours without edges. *IEEE Transactions on image processing*, 10(2):266–277, 2001.

[164] Daniel Barbosa, Brecht Heyde, Thomas Dietenbeck, Helene Houle, Denis Friboulet, Olivier Bernard, and Jan D'hooge. Quantification of left ventricular volume and global function using a fast automated segmentation tool: validation in a clinical setting. *The international journal of cardiovascular imaging*, 29(2):309–316, 2013.

[165] Daniel Barbosa, Thomas Dietenbeck, Brecht Heyde, Helene Houle, Denis Friboulet, Jan D'hooge, and Olivier Bernard. Fast and fully automatic 3-D echocardiographic segmentation using B-spline explicit active surfaces: feasibility study and validation in a clinical setting. *Ultrasound in Medicine and Biology*, 39(1):89–101, 2013.

[166] Marijn van Stralen, KY Esther Leung, Marco M Voormolen, Nico de Jong, Antonius FW van der Steen, Johan HC Reiber, and Johan G Bosch. Time continuous detection of the left ventricular long axis and the mitral valve plane in 3-D echocardiography. *Ultrasound in medicine and biology*, 34(2):196–207, 2008.

[167] Mehmet Üzümcü, Rob J van der Geest, Cory Swingen, Johan HC Reiber, and Boudewijn PF Lelieveldt. Time continuous tracking and segmentation of cardiovascular magnetic resonance images using multidimensional dynamic programming. *Investigative radiology*, 41(1):52–62, 2006.

[168] Daniel Barbosa, Olivier Bernard, Brecht Heyde, Thomas Dietenbeck, Helene Houle, Denis Friboulet, and Jan D'hooge. B-spline explicit active tracking of surfaces (BEATS): Application to real-time 3D segmentation and tracking of the left ventricle in 3D echocardiography. In *Ultrasonics Symposium (IUS), 2012 IEEE International*, pages 224–227. IEEE, 2012.

[169] Engin Dikici and Fredrik Orderud. Generalized step criterion edge detectors for kalman filter based left ventricle tracking in 3D+T echocardiography. In *International Workshop on Statistical Atlases and Computational Models of the Heart*, pages 261–269. Springer, 2012.

[170] Fredrik Orderud, Jøger Hansegård, and Stein I Rabben. Real-time tracking of the left ventricle in 3D echocardiography using a state estimation approach. In *International Conference on Medical Image Computing and Computer-Assisted Intervention*, pages 858–865. Springer, 2007.

[171] KY Esther Leung, Marijn van Stralen, Gerard van Burken, Nico de Jong, and Johan G Bosch. Automatic active appearance model segmentation of 3D echocardiograms. In *Biomedical Imaging: From Nano to Macro, 2010 IEEE International Symposium on*, pages 320–323. IEEE, 2010.

[172] KY Esther Leung, Mikhail G Danilouchkine, Marijn van Stralen, Nico de Jong, Antonius FW van der Steen, and Johan G Bosch. Left ventricular border tracking using cardiac motion models and optical flow. *Ultrasound in medicine & biology*, 37(4):605–616, 2011.

[173] Lin Yang, Bogdan Georgescu, Yefeng Zheng, Yang Wang, Peter Meer, and Dorin Comaniciu. Prediction based collaborative trackers (PCT): A robust and accurate approach toward 3D medical object tracking. *IEEE Transactions on Medical Imaging*, 30(11):1921–1932, 2011.

[174] Ruta Jasaityte, Brecht Heyde, and Jan D'hooge. Current state of three-dimensional myocardial strain estimation using echocardiography. *Journal of the American Society of Echocardiography*, 26(1):15–28, 2013.

[175] Mathieu De Craene, Stéphanie Marchesseau, Brecht Heyde, Hang Gao, Martino Alessandrini, Olivier Bernard, Gemma Piella, AR Porras, Lennart Tautz, Anja Hennemuth, et al. 3D strain assessment in ultrasound (Straus): A synthetic comparison of five tracking methodologies. *IEEE transactions on medical imaging*, 32(9):1632–1646, 2013.

[176] Michael Sühling, Muthuvel Arigovindan, Patrick Hunziker, and Michael Unser. Multiresolution moment filters: Theory and applications. *IEEE Transactions on Image Processing*, 13(LIB-ARTICLE-2004-013):484–495, 2004.

[177] Daniel Barbosa, Brecht Heyde, Thomas Dietenbeck, Denis Friboulet, Jan D'hooge, and Olivier Bernard. Fast left ventricle tracking in 3D echocardiographic data using anatomical affine optical flow. In *International Conference on Functional Imaging and Modeling of the Heart*, pages 191–199. Springer, 2013.

[178] Bruce D Lucas and Takeo Kanade. An iterative image registration technique with an application to stereo vision. 1981.

[179] Berthold KP Horn and Brian G Schunck. Determining optical flow. *Artificial Intelligence*, 17(1):185 – 203, 1981.

[180] Jean-Yves Bouguet. Pyramidal implementation of the affine Lucas Kanade feature tracker description of the algorithm. *Intel Corporation*, 5(1-10):4, 2001.

[181] Fredrik Orderud and Stein Inge Rabben. Real-time 3D segmentation of the left ventricle using deformable subdivision surfaces. In *IEEE Conference On Computer Vision and Pattern Recognition, 2008. CVPR 2008.*, pages 1–8. IEEE, 2008.

[182] Kashif Rajpoot, Vicente Grau, J Alison Noble, Harald Becher, and Cezary Szmigielski. The evaluation of single-view and multi-view fusion 3D echocardiography using image-driven segmentation and tracking. *Medical image analysis*, 15(4):514–528, 2011.

[183] Ling Tong, Hang Gao, and Jan D'hooge. Multi-transmit beam forming for fast cardiac imaging-a simulation study. *IEEE transactions on ultrasonics, ferroelectrics, and frequency control*, 60(8):1719–1731, 2013.

[184] Honghai Zhang, Ademola K Abiose, Dipti Gupta, Dwayne N Campbell, James B Martins, Milan Sonka, and Andreas Wahle. Novel indices for left-ventricular dyssynchrony characterization based on highly automated segmentation from real-time 3-D echocardiography. *Ultrasound in medicine & biology*, 39(1):72–88, 2013.

[185] Brecht Heyde, Daniel Barbosa, Ana-Maria Daraban, Ruta Jasaityte, Piet Claus, Frederik Maes, and Jan D'hooge. An automated pipeline for regional cardiac strain estimation from volumetric ultrasound data. In *Ultrasonics Symposium (IUS), 2013 IEEE International*, pages 1248–1251. IEEE, 2013.

[186] Mahdi Tabassian, Martino Alessandrini, Peter Claes, Luca De Marchi, Dirk Vandermeulen, Guido Masetti, and Jan D'hooge. Automatic detection of myocardial infarction through a global shape feature based on local statistical modeling. In *Statistical Atlases and Computational Models of the Heart. Imaging and Modelling Challenges*, volume 9534 of *Lecture Notes in Computer Science*, pages 208–216. Springer International Publishing, 2016.

[187] Fredrik Orderud, Hans Torp, and Stein Inge Rabben. Automatic alignment of standard views in 3D echocardiograms using real-time tracking. In *SPIE Medical Imaging 2009*, page 72650D, March 2009.

[188] Kiryl Chykeyuk, Mohammad Yaqub, and J Alison Noble. Class-specific regression random forest for accurate extraction of standard planes from 3D echocardiography. In *Medical Computer Vision. Large Data in Medical Imaging*, volume 8331 of *Lecture Notes in Computer Science*, pages 53–62. Springer International Publishing, 2014.

[189] João S Domingos, Eduardo Lima, Paul Leeson, and J Alison Noble. Local phase-based fast ray features for automatic left ventricle apical view detection in 3D echocardiography. In *Medical Computer Vision. Large Data in Medical Imaging*, volume 8331 of *Lecture Notes in Computer Science*, pages 119–129. Springer International Publishing, 2014.

[190] Frank Rademakers, Jan Engvall, Thor Edvardsen, Mark Monaghan, Rosa Sicari, Eike Nagel, Jose Zamorano, Heikki Ukkonen, Tino Ebbers, Vitantonio Di Bello, Jens-Uwe Voigt, Lieven Herbots, Piet Claus, and Jan D'hooge. Determining optimal noninvasive parameters for the prediction of left ventricular remodeling in chronic ischemic patients. *Scandinavian Cardiovascular Journal*, 47(6):329–334, December 2013.

[191] Nuno Almeida, Denis Friboulet, Sebastian Imre Sarvari, Olivier Bernard, Daniel Barbosa, Eigil Samset, and Jan D'hooge. Left-atrial segmentation from 3-D ultrasound using B-spline explicit active surfaces with scale uncoupling. *IEEE transactions on ultrasonics, ferroelectrics, and frequency control*, 63(2):212–221, 2016.

[192] Xulei Qin, Zhibin Cong, and Baowei Fei. Automatic segmentation of right ventricular ultrasound images using sparse matrix transform and a level set. *Physics in medicine and biology*, 58(21):7609, 2013.

[193] Michael Bernier, Pierre-Marc Jodoin, and Alain Lalande. Automatized evaluation of the left ventricular ejection fraction from echocardiographic images using graph cut. *Proceedings MICCAI Challenge on Echocardiographic Three-Dimensional Ultrasound Segmentation (CETUS), Boston, MIDAS Journal*, pages 25–32, 2014.

[194] Ozan Oktay, Wenzhe Shi, Kevin Keraudren, Jose Caballero, and Daniel Rueckert. Learning shape representations for multi-atlas endocardium segmentation in 3D echo images. *Proceedings MICCAI Challenge on Echocardiographic Three-Dimensional Ultrasound Segmentation (CETUS), Boston, MIDAS Journal*, pages 57–64, 2014.

[195] Chunliang Wang and Örjan Smedby. Model-based left ventricle segmentation in 3D ultrasound using phase image. In *MICCAI Workshop" Grand Challenge on Endocardial Three-dimensional Ultrasound Segmentation", Boston, US, 2014.*, 2014.

[196] Ozan Oktay, Alberto Gomez, Kevin Keraudren, Andreas Schuh, Wenjia Bai, Wenzhe Shi, Graeme Penney, and Daniel Rueckert. *Probabilistic Edge Map (PEM) for 3D Ultrasound Image Registration and Multi-atlas Left Ventricle Segmentation*, pages 223–230. Springer International Publishing, Cham, 2015.

[197] Marijn van Stralen, Alexander Haak, KY Esther Leung, Gerard van Burken, Clemens Bos, and Johan G Bosch. Full-cycle left ventricular segmentation and tracking in 3D echocardiography using active appearance models. In *Ultrasonics Symposium (IUS), 2015 IEEE International*, pages 1–4. IEEE, 2015.

[198] Sandro Queirós, Alexandros Papachristidis, Daniel Barbosa, Konstantinos C Theodoropoulos, Jaime C Fonseca, Mark J Monaghan, João L Vilaça, and Jan D'hooge. Aortic valve tract segmentation from 3D-TEE using shape-based B-spline explicit active surfaces. *IEEE transactions on medical imaging*, 35(9):2015–2025, 2016.

[199] Sandro Queirós, João L Vilaça, Pedro Morais, Jaime C Fonseca, Jan D'hooge, and Daniel Barbosa. Fast left ventricle tracking using localized anatomical affine optical flow. *International journal for numerical methods in biomedical engineering*, 33(11):e2871, 2017.

[200] Jyrki Lötjönen, Mika Pollari, Sari Kivistö, and Kirsi Lauerma. *Correction of Movement Artifacts from 4-D Cardiac Short- and Long-Axis MR Data*, pages 405–412. Springer Berlin Heidelberg, Berlin, Heidelberg, 2004.

[201] Adam G Chandler, Richard J Pinder, Thomas Netsch, Julia A Schnabel, David J Hawkes, Derek LG Hill, and Reza Razavi. Correction of misaligned slices in multi-slice cardiovascular magnetic resonance using slice-to-volume registration. *Journal of Cardiovascular Magnetic Resonance*, 10(1):13, 2008.

[202] Piotr J Slomka, David Fieno, Amit Ramesh, Vaibhav Goyal, Hidetaka Nishina, Louise EJ Thompson, Rola Saouaf, Daniel S Berman, and Guido Germano. Patient motion correction for multiplanar, multi-breath-hold cardiac cine MR imaging. *Journal of Magnetic Resonance Imaging*, 25(5):965–973, 2007.

[203] Maria Chiara Carminati, Francesco Maffessanti, and Enrico Gianluca Caiani. Nearly automated motion artifacts correction between multi breath-hold short-axis and long-axis cine CMR images. *Computers in Biology and Medicine*, 46:42 – 50, 2014.

[204] An Elen, Jeroen Hermans, Javier Ganame, Dirk Loeckx, Jan Bogaert, Frederik Maes, and Paul Suetens. Automatic 3-D breath-hold related motion correction of dynamic multislice MRI. *IEEE Transactions on Medical Imaging*, 29(3):868–878, 2010.

[205] Paul J Besl and Neil D McKay. Method for registration of 3-D shapes. In *Sensor Fusion IV: Control Paradigms and Data Structures*, volume 1611, pages 586–607. International Society for Optics and Photonics, 1992.

[206] Daniel Barbosa, Brecht Heyde, Maja Cikes, Thomas Dietenbeck, Piet Claus, Denis Friboulet, Olivier Bernard, and Jan D'hooge. Real-time 3D interactive segmentation of echocardiographic data through user-based deformation of B-spline explicit active surfaces. *Computerized Medical Imaging and Graphics*, 38(1):57 – 67, 2014.

[207] Timothy F Cootes, Christopher J Taylor, David H Cooper, and Jim Graham. Active shape models - their training and application. *Computer vision and image understanding*, 61(1):38–59, 1995.

[208] Ian Jolliffe. *Principal Component Analysis*. John Wiley & Sons, Ltd, 2014.

[209] Vikram Chalana, David T Linker, David R Haynor, and Yongmin Kim. A multiple active contour model for cardiac boundary detection on echocardiographic sequences. *IEEE Transactions on Medical Imaging*, 15(3):290–298, 1996.

[210] Daniel P Huttenlocher, Gregory A Klanderman, and William J Rucklidge. Comparing images using the Hausdorff distance. *IEEE Transactions on pattern analysis and machine intelligence*, 15(9):850–863, 1993.

[211] Lee R Dice. Measures of the amount of ecologic association between species. *Ecology*, 26(3):pp. 297–302, 1945.

[212] Alexandros Papachristidis, Marcel Geleijnse, Elena Galli, Brecht Heyde, Martino Alessandrini, Daniel Barbosa, Erwan Donal, Marc Monaghan, Olivier Bernard, Jan D'hooge, et al. Clinical expert delineation of 3D left ventricular echocardiograms for the CETUS segmentation challenge. In *Proceedings MICCAI challenge on echocardiographic three-dimensional ultrasound segmentation (CETUS)*, pages 9–16, 2014.

[213] Marijn Van Stralen, Alexander Haak, KY Esther Leung, Gerard van Burken, and Johan G Bosch. Segmentation of multi-center 3D left ventricular echocardiograms by active appearance models. *Proceedings MICCAI Challenge on Echocardiographic Three-Dimensional Ultrasound Segmentation (CETUS), Boston, MIDAS Journal*, pages 73–80, 2014.

[214] KY Esther Leung and Johan G Bosch. Automated border detection in three-dimensional echocardiography: principles and promises. *European Heart Journal - Cardiovascular Imaging*, 11(2):97–108, 2010.

[215] Masaaki Takeuchi, Tomoko Nishikage, Victor Mor-Avi, Lissa Sugeng, Lynn Weinert, Hironi Nakai, Ivan S Salgo, Olivier Gerard, and Roberto M Lang. Measurement of left ventricular mass by real-time three-dimensional echocardiography: Validation against magnetic resonance and comparison with two-dimensional and M-mode measurements. *Journal of the American Society of Echocardiography*, 21(9):1001 – 1005, 2008.

[216] Vivek Walimbe, Vladimir Zagrodsky, and Raj Shekhar. Fully automatic segmentation of left ventricular myocardium in real-time three-dimensional echocardiography. In *Medical Imaging 2006: Image Processing*, volume 6144, page 61444H. International Society for Optics and Photonics, 2006.

[217] Fredrik Orderud, Gabriel Kiss, and Hans Torp. Automatic coupled segmentation of endo-and epicardial borders in 3D echocardiography. In *Ultrasonics Symposium, 2008. IUS 2008. IEEE*, pages 1749–1752. IEEE, 2008.

[218] Michael Verhoek, Mohammad Yaqub, John McManigle, and J Alison Noble. Learning optical flow propagation strategies using random forests for fast segmentation in dynamic 2D & 3D echocardiography. In Kenji Suzuki, Fei Wang, Dinggang Shen, and Pingkun Yan, editors, *Machine Learning in Medical Imaging*, volume 7009 of *Lecture Notes in Computer Science*, pages 75–82. Springer Berlin Heidelberg, 2011.

[219] Victor Lempitsky, Michael Verhoek, J Alison Noble, and Andrew Blake. Random forest classification for automatic delineation of myocardium in real-time 3D echocardiography. In Nicholas Ayache, Hervé Delingette, and Maxime Sermesant, editors, *Functional Imaging and Modeling of the Heart*, volume 5528 of *Lecture Notes in Computer Science*, pages 447–456. Springer Berlin Heidelberg, 2009.

[220] Jie Feng, Wei-Chung Lin, and Chin-Tu Chen. Epicardial boundary detection using fuzzy reasoning. *IEEE Transactions on Medical Imaging*, 10(2):187–199, Jun 1991.

[221] José MB Dias and José MN Leitão. Wall position and thickness estimation from sequences of echocardiographic images. *IEEE Transactions on Medical Imaging*, 15(1):25–38, 1996.

[222] Enrico G Caiani, Cristiana Corsi, Lissa Sugeng, Peter MacEneaney, Lynn Weinert, Victor Mor-Avi, and Roberto M Lang. Improved quantification of left ventricular mass based on endocardial and epicardial surface detection with real time three dimensional echocardiography. *Heart*, 92(2):213–219, 2006.

[223] Christopher D Garson, Bing Li, Scott T Acton, and John A Hossack. Guiding automated left ventricular chamber segmentation in cardiac imaging using the concept of conserved myocardial volume. *Computerized Medical Imaging and Graphics*, 32(4):321 – 330, 2008.

[224] Yun Zhu, Xenophon Papademetris, Albert J Sinusas, and James S Duncan. A coupled deformable model for tracking myocardial borders from real-time echocardiography using an incompressibility constraint. *Medical Image Analysis*, 14(3):429 – 448, 2010.

[225] Thomas Dietenbeck, Martino Alessandrini, Daniel Barbosa, Jan D'hooge, Denis Friboulet, and Olivier Bernard. Detection of the whole myocardium in 2D-echocardiography for multiple orientations using a geometrically constrained level-set. *Medical image analysis*, 16(2):386–401, 2012.

[226] Constantine Butakoff, Simone Balocco, Federico M Sukno, Corné Hoogendoorn, Catalina Tobon-Gomez, Gustavo Avegliano, and Alejandro F Frangi. Left-ventricular epi- and endocardium extraction from 3D ultrasound images using an automatically constructed 3D ASM. *Computer Methods in Biomechanics and Biomedical Engineering: Imaging & Visualization*, 4(5):265–280, 2016.

[227] Sandro Queirós, Daniel Barbosa, Brecht Heyde, Pedro Morais, João L Vilaça, Denis Friboulet, Olivier Bernard, and Jan D'hooge. Fast automatic myocardial segmentation in 4D cine CMR datasets. *Medical Image Analysis*, 18(7):1115 – 1131, 2014.

[228] Elsa Abbena, Simon Salamon, and Alfred Gray. *Modern Differential Geometry of Curves and Surfaces with Mathematica, Third Edition.* Textbooks in Mathematics. Taylor & Francis, 2006.

[229] Piet Claus, Hon Fai Choi, Jan D'hooge, and Frank E Rademakers. On the calculation of principle curvatures of the left-ventricular surfaces. In *30th Annual International Conference of the IEEE Engineering in Medicine and Biology Society*, pages 961–964, Aug 2008.

[230] Olive Jean Dunn. Multiple comparisons among means. *Journal of the American Statistical Association*, 56(293):52–64, 1961.

[231] Peter W Wood, Jonathan B Choy, Navin C Nanda, and Harald Becher. Left ventricular ejection fraction and volumes: It depends on the imaging method. *Echocardiography*, 31(1):87–100, 2014.

[232] Jørn Bersvendsen, Fredrik Orderud, Øyvind Lie, Richard John Massey, Kristian Fosså, Raúl San José Estépar, Stig Urheim, and Eigil Samset. Semiautomated biventricular segmentation in three-dimensional echocardiography by coupled deformable surfaces. *Journal of Medical Imaging*, 4(2):024005, 2017.

[233] Bidisha Chakraborty, Zhi Liu, Brecht Heyde, Jianwen Luo, and Jan D'hooge. 2-D myocardial deformation imaging based on RF-based nonrigid image registration. *IEEE transactions on ultrasonics, ferroelectrics, and frequency control*, 65(6):1037–1047, 2018.

[234] Sandro Queirós, Pedro Morais, Christophe Dubois, Jens-Uwe Voigt, Wolfgang Fehske, Andreas Kuhn, Tobias Achenbach, Jaime C Fonseca, João L Vilaça, and Jan D'hooge. Validation of a novel software tool for automatic aortic annular sizing in three-dimensional transesophageal echocardiographic images. *Journal of the American Society of Echocardiography*, 31(4):515–525, 2018.

[235] Jan D'hooge, Andreas Heimdal, Fadi Jamal, Tomasz Kukulski, Bart Bijnens, Frank Rademakers, Liv Hatle, Paul Suetens, and George R Sutherland. Regional strain and strain rate measurements by cardiac ultrasound: principles, implementation and limitations. *European Journal of Echocardiography*, 1(3):154–170, 2000.

[236] Jan D'hooge, Elisa Konofagou, Fadi Jamal, Andreas Heimdal, Laurentino Barrios, Bart Bijnens, Jan Thoen, Frans Van de Werf, George Sutherland, and Paul Suetens. Two-dimensional ultrasonic strain rate measurement of the human heart in vivo. *IEEE transactions on ultrasonics, ferroelectrics, and frequency control*, 49(2):281–286, 2002.

[237] Frank Rademakers, Frans Werf, Luc Mortelmans, Guy Marchal, and Jan Bogaert. Evolution of regional performance after an acute anterior myocardial infarction in humans using magnetic resonance tagging. *The Journal of physiology*, 546(3):777–787, 2003.

[238] Hiroyuki Suga. Total mechanical energy of a ventricle model and cardiac oxygen consumption. *American Journal of Physiology-Heart and Circulatory Physiology*, 236(3):H498–H505, 1979.

[239] Hideyuki Takaoka, Motoshi Takeuchi, Michio Odake, and Mitsuhiro Yokoyama. Assessment of myocardial oxygen consumption (Vo2) and systolic pressure–volume area (PVA) in human hearts. *European heart journal*, 13:85–90, 1992.

[240] Ryuichi Hisano and George Cooper. Correlation of force-length area with oxygen consumption in ferret papillary muscle. *Circulation Research*, 61(3):318–328, 1987.

[241] John V Tyberg, James S Forrester, Horace L Wyatt, Steven J Goldner, William W Parmley, and Harold JC Swan. An analysis of segmental ischemic dysfunction utilizing the pressure-length loop. *Circulation*, 49(4):748–754, 1974.

[242] James S Forrester, John V Tyberg, Horace L Wyatt, Steven Goldner, William W Parmely, and Harold JC Swan. Pressure-length loop: a new method for simultaneous measurement of segmental and total cardiac function. *Journal of applied physiology*, 37(5):771–775, 1974.

[243] Stig Urheim, Stein Inge Rabben, Helge Skulstad, Erik Lyseggen, Halfdan Ihlen, and Otto A Smiseth. Regional myocardial work by strain doppler echocardiography and LV pressure: a new method for quantifying myocardial function. *American Journal of Physiology-Heart and Circulatory Physiology*, 288(5):H2375–H2380, 2005.

[244] Jürgen Duchenne, Piet Claus, Efstathios D Pagourelias, Razvan O Mada, Joeri Van Puyvelde, Kathleen Vunckx, Eric Verbeken, Olivier Gheysens, Filip Rega, and Jens-Uwe Voigt. Sheep can be used as animal model of regional myocardial remodelling and controllable work. *Cardiology Journal*, 2014.

[245] Kristoffer Russell, Morten Eriksen, Lars Aaberge, Nils Wilhelmsen, Helge Skulstad, Espen W Remme, Kristina H Haugaa, Anders Opdahl, Jan Gunnar Fjeld, Ola Gjesdal, et al. A novel clinical method for quantification of regional left ventricular pressure–strain loop area: a non-invasive index of myocardial work. *European heart journal*, 33(6):724–733, 2012.

[246] Marta Cvijic, Jürgen Duchenne, Serkan Ünlü, Blazej Michalski, Marit Aarones, Stefan Winter, Svend Aakhus, Wolfgang Fehske, Ivan Stankovic, and Jens-Uwe Voigt. Timing of myocardial shortening determines left ventricular regional myocardial work and regional remodelling in hearts with conduction delays. *European Heart Journal-Cardiovascular Imaging*, 2017.

[247] Israel Mirsky, William J Corin, Tomoyuki Murakami, Joerg Grimm, Otto M Hess, and Hans P Krayenbuehl. Correction for preload in assessment of myocardial contractility in aortic and mitral valve disease. application of the concept of systolic myocardial stiffness. *Circulation*, 78(1):68–80, 1988.

[248] Jörg van den Hoff, Liane Oehme, Georg Schramm, Jens Maus, Alexandr Lougovski, Jan Petr, Bettina Beuthien-Baumann, and Frank Hofheinz. The PET-derived tumor-to-blood standard uptake ratio (SUR) is superior to tumor SUV as a surrogate parameter of the metabolic rate of FDG. *EJNMMI research*, 3(1):77, 2013.

[249] Mickael Tanter, Jeremy Bercoff, Laurent Sandrin, and Mathias Fink. Ultrafast compound imaging for 2-D motion vector estimation: Application to transient elastography. *IEEE transactions on ultrasonics, ferroelectrics, and frequency control*, 49(10):1363–1374, 2002.

[250] Lars Christian Naterstad Lervik, Birger Brekke, Svein Arne Aase, Mai Tone Lønnebakken, Dordi Stensvåg, Brage H Amundsen, Hans Torp, and Asbjorn Støylen. Myocardial strain rate by anatomic doppler spectrum: First clinical experience using retrospective spectral tissue doppler from ultra-high frame rate imaging. *Ultrasound in Medicine & Biology*, 43(9):1919–1929, 2017.

[251] Alejandra Ortega, João Pedrosa, Brecht Heyde, Ling Tong, and Jan D'hooge. Automatic definition of an anatomic field of view for volumetric cardiac motion estimation at high temporal resolution. *Applied Sciences*, 7(7):752, 2017.

[252] Alejandra Ortega, Dave Lines, João Pedrosa, Bidisha Chakraborty, Vangjush Komini, Hans Gassert, and Jan D'hooge. HD-PULSE: High channel Density Programmable ULtrasound System based on consumer Electronics. In *Ultrasonics Symposium (IUS), 2015 IEEE International*, pages 1–3, Oct 2015.

[253] Jiapu Pan and Willis J Tompkins. A real-time QRS detection algorithm. *IEEE transactions on biomedical engineering*, (3):230–236, 1985.

[254] Daniel Rueckert, Luke I Sonoda, Carmel Hayes, Derek LG Hill, Martin O Leach, and David J Hawkes. Nonrigid registration using free-form deformations: application to breast MR images. *IEEE transactions on medical imaging*, 18(8):712–721, 1999.

[255] Brecht Heyde, Szymon Cygan, Hon Fai Choi, Beata Lesniak-Plewinska, Daniel Barbosa, An Elen, Piet Claus, Dirk Loeckx, Krzysztof Kaluzynski, and Jan D'hooge. Regional cardiac motion and strain estimation in three-dimensional echocardiography: A validation study in thick-walled univentricular phantoms. *IEEE transactions on ultrasonics, ferroelectrics, and frequency control*, 59(4):668–682, 2012.

[256] Sarah Leclerc, Thomas Grenier, Florian Espinosa, and Olivier Bernard. A fully automatic and multi-structural segmentation of the left ventricle and the myocardium on highly heterogeneous 2D echocardiographic data. In *Ultrasonics Symposium (IUS), 2017 IEEE International*, pages 1–4. IEEE, 2017.

[257] Ozan Oktay, Enzo Ferrante, Konstantinos Kamnitsas, Mattias Heinrich, Wenjia Bai, Jose Caballero, Stuart A Cook, António de Marvão, Timothy Dawes, Declan P O'Regan, et al. Anatomically constrained neural networks (ACNNs): application to cardiac image enhancement and segmentation. *IEEE transactions on medical imaging*, 37(2):384–395, 2018.

[258] Tomasz A Timek and D Craig Miller. Experimental and clinical assessment of mitral annular area and dynamics: what are we actually measuring? *The Annals of thoracic surgery*, 72(3):966–974, 2001.

[259] William A Zoghbi, David Adams, Robert O Bonow, Maurice Enriquez-Sarano, Elyse Foster, Paul A Grayburn, Rebecca T Hahn, Yuchi Han, Judy Hung, Roberto M Lang, et al. Recommendations for noninvasive evaluation of native valvular regurgitation: a report from the american society of echocardiography developed in collaboration with the society for cardiovascular magnetic resonance. *Journal of the American Society of Echocardiography*, 30(4):303–371, 2017.

[260] Helmut Baumgartner, Judy Hung, Javier Bermejo, John B Chambers, Arturo Evangelista, Brian P Griffin, Bernard Iung, Catherine M Otto, Patricia A Pellikka, and Miguel Quiñones. Echocardiographic assessment of valve stenosis: EAE/ASE recommendations for clinical practice. *Journal of the American Society of Echocardiography*, 22(1):1–23, 2009.

[261] Nozomi Watanabe, Yasuo Ogasawara, Yasuko Yamaura, Nozomi Wada, Takahiro Kawamoto, Eiji Toyota, Takashi Akasaka, and Kiyoshi Yoshida. Mitral annulus flattens in ischemic mitral regurgitation: geometric differences between inferior and anterior myocardial infarction. *Circulation*, 112(9 suppl):I–458, 2005.

[262] Jasmine Grewal, Rakesh Suri, Sunil Mankad, Akiko Tanaka, Douglas W Mahoney, Hartzell V Schaff, Fletcher A Miller, and Maurice Enriquez-Sarano. Mitral annular dynamics in myxomatous valve disease: new insights with real-time 3-dimensional echocardiography. *Circulation*, 121(12):1423–1431, 2010.

[263] Starr R Kaplan, Gerard Bashein, Florence H Sheehan, Malcolm E Legget, Brad Munt, Xiang-Ning Li, Murali Sivarajan, Edward L Bolson, Merrilinn Zeppa, M Archa, et al. Three-dimensional echocardiographic assessment of annular shape changes in the normal and regurgitant mitral valve. *American heart journal*, 139(3):378–387, 2000.

[264] Jorina Langerveld, Gabriel Valocik, HW Thijs Plokker, Sjef MPG Ernst, Herman FJ Mannaerts, Johannes C Kelder, Otto Kamp, and Wybren Jaarsma. Additional value of three-dimensional transesophageal echocardiography for patients with mitral valve stenosis undergoing balloon valvuloplasty. *Journal of the American Society of Echocardiography*, 16(8):841–849, 2003.

[265] Dominik Schlosshan, Gunjan Aggarwal, Gita Mathur, Roger Allan, and Greg Cranney. Real-time 3D transesophageal echocardiography for the evaluation of rheumatic mitral stenosis. *JACC: Cardiovascular Imaging*, 4(6):580–588, 2011.

[266] Alex Pui-Wai Lee, Ming C Hsiung, Ivan S Salgo, Fang Fang, Jun-Min Xie, Yan-Chao Zhang, Qing-Shan Lin, Jen-Li Looi, Song Wan, Randolph HL Wong, et al. Quantitative analysis of mitral valve morphology in mitral valve prolapse using real-time three-dimensional echocardiography: importance of annular saddle-shape in pathogenesis of mitral regurgitation. *Circulation*, page 112, 2012.

[267] Karima Addetia, Victor Mor-Avi, Lynn Weinert, Ivan S Salgo, and Roberto M Lang. A new definition for an old entity: improved definition of mitral valve prolapse using three-dimensional echocardiography and color-coded parametric models. *Journal of the American Society of Echocardiography*, 27(1):8–16, 2014.

[268] Feroze Mahmood, Balachundhar Subramaniam, Joseph H Gorman, Robert M Levine, Robert C Gorman, Andrew Maslow, Peter J Panzica, Robert M Hagberg, Swaminathan Karthik, and Kamal R Khabbaz. Three-dimensional echocardiographic assessment of changes in mitral valve geometry after valve repair. *The Annals of thoracic surgery*, 88(6):1838–1844, 2009.

[269] Feroze Mahmood, Joseph H Gorman, Balachundhar Subramaniam, Robert C Gorman, Peter J Panzica, Robert C Hagberg, Adam B Lerner, Philip E Hess, Andrew Maslow, and Kamal R Khabbaz. Changes in mitral valve annular geometry after repair: saddle-shaped versus flat annuloplasty rings. *The Annals of thoracic surgery*, 90(4):1212–1220, 2010.

[270] Gary P Foster, Adam K Dunn, Selwin Abraham, Naser Ahmadi, and Guilda Sarraf. Accurate measurement of mitral annular dimensions by echocardiography: importance of correctly aligned imaging planes and anatomic landmarks. *Journal of the American Society of Echocardiography*, 22(5):458–463, 2009.

[271] Patric Biaggi, Sean Jedrzkiewicz, Christiane Gruner, Massimiliano Meineri, Jacek Karski, Annette Vegas, Felix C Tanner, Harry Rakowski, Joan Ivanov, Tirone E David, et al. Quantification of mitral valve anatomy by three-dimensional transesophageal echocardiography in mitral valve prolapse predicts surgical anatomy and the complexity of mitral valve repair. *Journal of the American Society of Echocardiography*, 25(7):758–765, 2012.

[272] Robert J Schneider, Douglas P Perrin, Nikolay V Vasilyev, Gerald R Marx, J Pedro, and Robert D Howe. Mitral annulus segmentation from 3D ultrasound using graph cuts. *IEEE Transactions on Medical Imaging*, 29(9):1676–1687, 2010.

[273] Robert J Schneider, Neil A Tenenholtz, Douglas P Perrin, Gerald R Marx, J Pedro, and Robert D Howe. Patient-specific mitral leaflet segmentation from 4D ultrasound. In *International Conference on Medical Image Computing and Computer-Assisted Intervention*, pages 520–527. Springer, 2011.

[274] Philippe Burlina, Chad Sprouse, Daniel DeMenthon, Anne Jorstad, Radford Juang, Francisco Contijoch, Theodore Abraham, David Yuh, and Elliot McVeigh. Patient-specific modeling and analysis of the mitral valve using 3D-TEE. In *International Conference on Information Processing in Computer-Assisted Interventions*, pages 135–146. Springer, 2010.

[275] Razvan Ioan Ionasec, Ingmar Voigt, Bogdan Georgescu, Yang Wang, Helene Houle, Fernando Vega-Higuera, Nassir Navab, and Dorin Comaniciu. Patient-specific modeling and quantification of the aortic and mitral valves from 4-D cardiac CT and TEE. *IEEE transactions on medical imaging*, 29(9):1636–1651, 2010.

[276] Alison M Pouch, Hongzhi Wang, Manabu Takabe, Benjamin M Jackson, Joseph H Gorman, Robert C Gorman, Paul A Yushkevich, and Chandra M Sehgal. Fully automatic segmentation of the mitral leaflets in 3D transesophageal echocardiographic images using multi-atlas joint label fusion and deformable medial modeling. *Medical image analysis*, 18(1):118–129, 2014.

[277] Miguel Sotaquira, Mauro Pepi, Laura Fusini, Francesco Maffessanti, Roberto M Lang, and Enrico G Caiani. Semi-automated segmentation and quantification of mitral annulus and leaflets from transesophageal 3-D echocardiographic images. *Ultrasound in Medicine and Biology*, 41(1):251–267, 2015.

[278] Henri De Veene, Philippe B Bertrand, Natasa Popovic, Pieter M Vandervoort, Piet Claus, Matthieu De Beule, and Brecht Heyde. Automatic mitral annulus tracking in volumetric ultrasound using non-rigid image registration. In *Engineering in Medicine and Biology Society (EMBC), 2015 37th Annual International Conference of the IEEE*, pages 1985–1988. IEEE, 2015.

[279] Sorina Mihăilă, Denisa Muraru, Eleonora Piasentini, Marcelo Haertel Miglioranza, Diletta Peluso, Umberto Cucchini, Sabino Iliceto, Dragoş Vinereanu, and Luigi P

Badano. Quantitative analysis of mitral annular geometry and function in healthy volunteers using transthoracic three-dimensional echocardiography. *Journal of the American Society of Echocardiography*, 27(8):846–857, 2014.

[280] Alejandro F Frangi, Wiro J Niessen, Koen L Vincken, and Max A Viergever. Multiscale vessel enhancement filtering. In *International Conference on Medical Image Computing and Computer-Assisted Intervention*, pages 130–137. Springer, 1998.

[281] Jun Kwan, Min-Jae Jeon, Dae-Hyeok Kim, Keum-Soo Park, and Woo-Hyung Lee. Does the mitral annulus shrink or enlarge during systole? A real-time 3D echocardiography study. *Journal of Korean medical science*, 24(2):203–208, 2009.

List of publications

International Journals

João Pedrosa, Daniel Barbosa, Nuno Almeida, Olivier Bernard, Johan Bosch, and Jan D'hooge. Cardiac chamber volumetric assessment using 3D ultrasound - a review. *Current Pharmaceutical Design*, 2016.

Alejandra Ortega, **João Pedrosa**, Brecht Heyde, Ling Tong, and Jan D'hooge. Automatic definition of an anatomic field of view for volumetric cardiac motion estimation at high temporal resolution. *Applied Sciences*, 7(7):752, 2017.

Daniel Barbosa, **João Pedrosa**, Brecht Heyde, Thomas Dietenbeck, Denis Friboulet, Olivier Bernard, and Jan D'hooge. heartBEATS: A hybrid energy approach for real-time B-spline explicit active tracking of surfaces. *Computerized Medical Imaging and Graphics*, 2017.

João Pedrosa, Daniel Barbosa, Brecht Heyde, Frédéric Schnell, Assami Rösner, Piet Claus, and Jan D'hooge. Left ventricular myocardial segmentation in 3-D ultrasound recordings: Effect of different endocardial and epicardial coupling strategies. *IEEE transactions on ultrasonics, ferroelectrics, and frequency control*, 64(3):525 536, 2017.

João Pedrosa, Sandro Queirós, Olivier Bernard, Jan Engvall, Thor Edvardsen, Eike Nagel, and Jan D'hooge. Fast and fully automatic left ventricular segmentation and tracking in echocardiography using shape-based B-spline explicit active surfaces. *IEEE Transactions on Medical Imaging*, 2017.

Assami Rösner, Tigran Khalapyan, **João Pedrosa**, Håvard Dalen, Doff B. McElhinney, Mark K. Friedberg, George K. Lui. Ventricular mechanics in adolescent and adult patients with a Fontan circulation: Relation to geometry and wall stress. *Echocardiography*, 2018.

João Pedrosa, Jürgen Duchenne, Sandro Queirós, Ganna Degtiarova, Piet Claus, Jens-Uwe Voigt, Jan D'hooge. Non-invasive myocardial performance mapping using 3D echocardiographic stress-strain loops: validation against PET. *(submitted for publication).*

Pedro Santos, Aniela Petrescu, **João Pedrosa**, Marta Orlowska, Vangjush Komini, Jens-Uwe Voigt, Jan D'hooge. Natural shear wave imaging in the human heart: normal values, feasibility and reproducibility. *(submitted for publication).*

Aniela Petrescu, Pedro Santos, Marta Orlowska, **João Pedrosa**, Stéphanie Bézy, Bidisha Chakraborty, Marta Cvijic, Monica Dobrovie, Michel Delforge, Jan D'hooge, Jens-Uwe Voigt. Velocity of naturally occurring myocardial shear waves to assess myocardial stiffness. *(submitted for publication)*.

Bidisha Chakraborty, **João Pedrosa**, Oana Mirea, Brecht Heyde, Jens-Uwe Voigt, Jan D'hooge. Clinical validation of 2D non-rigid image registration and estimation of accuracy in assessment of global and regional dysfunctionality in cardiac images. *(submitted for publication)*.

International Conference Proceedings

Alejandra Ortega, **João Pedrosa**, Brecht Heyde, Ling Tong, and Jan D'hooge. An automatic method for determining the anatomical relevant space for fast volumetric cardiac imaging. In *2015 IEEE International Ultrasonics Symposium (IUS)*, pages 14, Oct 2015.

Alejandra Ortega, Dave Lines, **João Pedrosa**, Bidisha Chakraborty, Vangjush Komini, Hans Gassert, and Jan D'hooge. HD-PULSE: High channel Density Programmable ULtrasound System based on consumer Electronics. In *2015 IEEE International Ultrasonics Symposium (IUS)*, pages 1-3, Oct 2015.

João Pedrosa, Brecht Heyde, Laurens Heeren, Jan Engvall, Jose Zamorano, Alexandros Papachristidis, Thor Edvardsen, Piet Claus, and Jan D'hooge. Automatic short axis orientation of the left ventricle in 3D ultrasound recordings. In *SPIE Medical Imaging 2016: Ultrasonic Imaging and Tomography*, volume 9790, pages 97900E, 2016.

João Pedrosa, Vangjush Komini, Jürgen Duchenne, and Jan D'hooge. Real-time anatomical imaging of the heart on an experimental ultrasound system. In *2017 IEEE International Ultrasonics Symposium (IUS)*, Sep 2017.

Pedro Santos, Nadezhda Koriakina, Bidisha Chakraborty, **João Pedrosa**, Vangjush Komini, and Jan D'hooge. Phase coherence beamforming to enhance myocardial speckle tracking performance. In *2017 IEEE International Ultrasonics Symposium (IUS)*, Sep 2017.

Pedro Santos, **João Pedrosa**, and Jan D'hooge. High frame rate multi-plane echocardiography using multi-line transmit beamforming: First experimental findings. In *2017 IEEE International Ultrasonics Symposium (IUS)*, Sep 2017.

Bidisha Chakraborty, **João Pedrosa**, Vangjush Komini, Brecht Heyde, and Jan D'hooge. RF-NRIR for motion estimation in fast cardiac anatomical imaging. In *2017 IEEE International Ultrasonics Symposium (IUS)*, Sep 2017.

João Pedrosa, Sandro Queirós, João Vilaça, Luigi Badano, Jan D'hooge. Fully automatic assessment of mitral valve morphology from 3D transthoracic echocardiography. In *Ultrasonics Symposium (IUS), 2018 IEEE International*, Oct 2018 *(accepted for publication)*.

Acknowledgement, Personal Contribution and Conflicts of Interest

Scientific Acknowledgment

This thesis was supported by the European Research Council under the European Union's Seventh Framework Program (HeartMAPAS; FP7/2007-2013/ERC) under Grant 281748.

Personal Contribution

I hereby assert that the personal contributions to this thesis included but were not limited to:

- Conception, implementation and validation of the frameworks detailed in Chapters 4-7 and Appendix A;
- Implementation of the tools described in Chapters 8;
- Implementation of the framework in real-time for ECG triggering, LV segmentation and anatomical scan sequence generation and processing of the data acquired in Chapter 10;
- Patient selection, processing of RT3DE data and conception and validation of the framework used in Chapter 9;
- Writing of the papers included in this thesis and the remaining chapters.

Conflicts of Interest

I hereby assert that there are no conflicts of interest (both personal and institutional) regarding specific financial interests that are relevant to the work reported in this thesis.